Influence des propriétés mécaniques et géométriques de nanoparticules sur leur inges- tion par les cellules cancéreuses

Sarah Iaquinta

To cite this version:

Sarah Iaquinta. Influence des propriétés mécaniques et géométriques de nanoparticules sur leur ingestion par les cellules cancéreuses. Autre. Nantes Université, 2022. Français. NNT : 2022NANU4088 . tel-04368913

HAL Id: tel-04368913
https://theses.hal.science/tel-04368913v1
Submitted on 2 Jan 2024

THÈSE DE DOCTORAT DE

NANTES UNIVERSITÉ

ÉCOLE DOCTORALE N° 602
Sciences pour l'Ingénieur
Spécialité : *Mécanique des Solides*

Par
Sarah IAQUINTA

« Influence des propriétés mécaniques et géométriques des nanoparticules sur leur ingestion par les cellules cancéreuses »

Thèse présentée et soutenue à Saint Nazaire, le 15/12/2022
Unité de recherche : Institut de recherche en Génie Civil et Mécanique (GeM) – UMR CNRS 6183

Rapporteurs avant soutenance :

Aline BEL-BRUNON	Maître de conférences HDR, INSA Lyon
Régis COTTEREAU	Chargé de recherche, CNRS, Aix-Marseille Université

Composition du Jury :

Président :	Jean-Michel CROS	Professeur des Universités, Université d'Evry
Examinatrice :	Aline BEL-BRUNON	Maître de conférences HDR, INSA Lyon
Examinateur :	Régis COTTEREAU	Chargé de recherche, CNRS, Aix-Marseille Université
Dir. de thèse :	Sylvain FRÉOUR	Professeur des Universités, Nantes Université
Co-dir. de thèse :	Frédéric JACQUEMIN	Professeur des Universités, Nantes Université
Co-encadrant :	Shahram KHAZAIE	Maître de conférences, Nantes Université

ACKNOWLEDGEMENT - REMERCIEMENTS

Le travail présenté dans ce mémoire a été réalisé au sein de l'Institut de Recherche en Génie Civil et Mécanique (GeM), sur le site de l'IUT de Saint Nazaire. Cette thèse a été financée par l'initiative NExT.

Je souhaite tout d'abord remercier les membres de mon jury de thèse, Aline Bel-Brunon et Régis Cottereau, pour avoir rapporté mon travail, ainsi que Jean-Michel Cros, qui m'a fait l'honneur de présider le jury.

Je remercie ensuite les membres de mon équipe d'encadrement, Frédéric Jacquemin, Sylvain Fréour et Shahram Khazaie, pour leur présence et implication tout au long du travail de thèse. Je remercie par ailleurs Christophe Blanquart et Éléna Ishow pour leur accompagnement dans le cadre du consortium lié au projet METCIN.

Il est aussi important pour moi de remercier mes enseignants et encadrants de l'ENSTA Bretagne, tout particulièrement Sylvain Calloch, Yann Marco, Morgane Broudin et Romain Créac'hcadec, pour m'avoir menée vers la recherche et m'y avoir donné goût.

Ces trois années de thèse ont été égayées par la bonne ambiance au sein de l'équipe du GeM de Saint Nazaire, et notamment grâce aux doctorants, avec qui j'ai passé de bons moments et à qui je souhaite tout le meilleur. Un grand merci à Quentin (à prononcer Quentaing), d'une bienveillance exceptionnelle, qui a toujours été présent, mais surtout pour regarder et reregarder des petits Hobbits joufflus partir à l'aventure.

Il me faut bien sûr remercier mes amis, amies, amigos et amigas, qui ont rendu la vie plus douce grâce aux moments partagés et aux liens qui durent. Inès et Constance, mes copines que j'admire énormément et avec qui j'espère faire encore beaucoup de restos. Os velhos de Versailles, merci pour le pagode, les bières et les pudim. Pas merci pour les pizzas aux brocolis avec du ketchup. Je ne peux évidemment pas remercier mes amis sans remercier mon meilleur ami et amorzinho, qui a eu la tâche ingrate de relire toute la thèse. Son soutien indéfectible et inconditionnel m'ont permis de donner le meilleur au

cours de ces trois années.

Je ne pourrais conclure ces remerciements sans adresser une pensée à ma famille et surtout à mes parents, qui ont tout fait pour m'offrir la possibilité de m'épanouir dans mes études, alors qu'eux-même n'ont pas eu cette chance. J'adresse une pensée émue à mon grand-père, à qui je dédie ce mémoire, qui nous disait toujours de bien travailler à l'école, parce que c'était le plus important. Et de faire attention, surtout.

Ciao, ciao, Papi.

TABLE OF CONTENTS

LIST OF FIGURES

LIST OF TABLES

INTRODUCTION

1 Context of this thesis

In 2017, the ambition of gathering the universities of the metropolitan area of Nantes has emerged, as a way of promoting the quality of the research, teaching and engineering of the region. As such, the Université de Nantes, the École Centrale Nantes, the Centre Hopitalier Universitaire (CHU) of Nantes, the Institut National de la Santé et de la Recherche Médicale (INSERM), the École des Beaux-Arts de Nantes Saint-Nazaire (EBANSN), the École Nationale Supérieure d'Architecture de Nantes (ENSA Nantes) and the Institut de Recherche Technologique (IRT) Jules Verne have united themselves to create Nantes Université in 2022. This new entity gathers 43000 students, 7800 employees and 42 research laboratories.

In order to reinforce the strategy of Nantes Université, the i-site NExT[1] (Nantes Excellence Trajectory) was created in 2019. It is an initiative in research, teaching and industry, which aims at developing the excellence of Nantes Université through two fields: the health of the future and the industry of the future. NExT yielded the increase of the scientific production of Nantes Université by 2.5, while 5.5 times more research contracts and 9 times more industrial pulpits have been created compared to 10 years ago. In addition, collaborations within Nantes Université have been made easier thanks to this initiative, which contributed to the funding of intern projects, among them METCIN[2] (Mechanical Exploration for Tackling Cellular Interactions of Nanoparticles at the Nanoscale), to which this thesis belongs. The former is presented in the following section.

2 Presentation of the METCIN research project

The METCIN project involves a consortium of researchers in mechanics, biology and chemistry from three distinct laboratories which are part of Nantes Université: the Institut de Recherche en Génie Civil et Mécanique UMR CNRS 6183 (GeM), the Cen-

---

[1] More information available at `https://next-isite.fr`.

[2] More information available at `https://next-isite.fr/metcin`.

tre de Recherche en Cancérologie et Immunologie de Nantes-Angers Unité Inserm U1232 (CRCI2NA) and the Chimie Et Interdisciplinarité, Synthèse, Analyse, Modélisation UMR CNRS 6230 (CEISAM) laboratory. Their contributions to the METCIN project are illustrated in Figure 1.

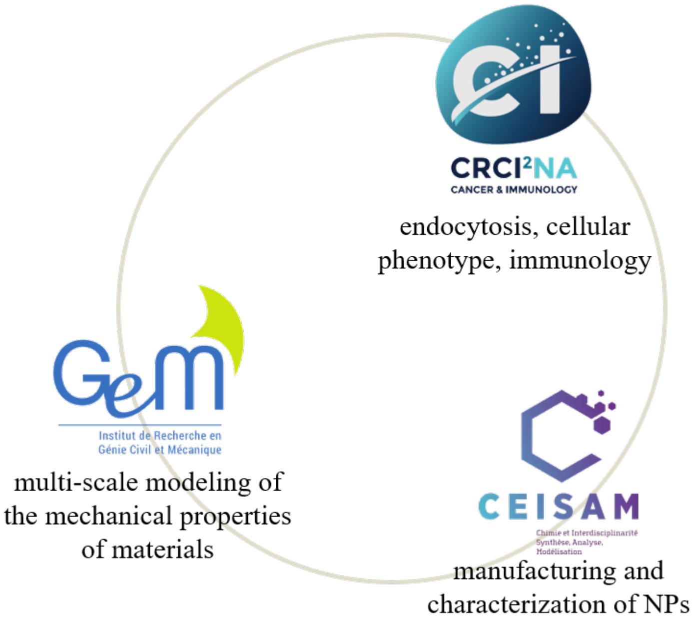

Figure 1: Scientific corsortium involved in the METCIN project.

The objective of this project is to provide a multidisciplinary understanding of the effect of the mechanical properties of nanoparticles (NPs) on the mechanisms relative to their cellular internalization, along with the consequences of the entry of such NPs on the cellular phenotype. As such, this project is divided into three work packages, to be achieved within 4 years. One of them involves the development of a multiscale and multiphysics model of the entry of NPs into cells (endocytosis), which is the subject of this thesis. Indeed, in this work, we develop a model for the cellular uptake of rigid elliptic NPs, which are used to investigate the influence of the aspect ratio of the NPs on their internalization by cells with different phenotypes. As such, we developed a model able to account for the differences between the mechanical properties of healthy and cancer cells. This thesis was conducted at the GeM laboratory, where the mechanics of materials, dynamics of structure, durability of composite materials and biomechanics, via both experimental and numerical approaches, are some of the main research domains. This project contributes to the development of the newly created research group, Biomechanics and Health of the Future[1] in the laboratory, and was therefore presented to the HCÉRES (Haut Conseil de l'Évaluation de la Recherche et de l'Enseignement Supérieur) evaluation committee in 2021.

3 Presentation of this thesis

In France, two out of three women and one out of two men are affected by cancer before the age of 85. Among them, 40 % do not heal [1]. Furthermore, the existing treatments have the drawback of causing side effects, mostly due to poor accuracy in the targeting of cancer cells [2]. This targeting is based on heterogeneous chemical properties between these cells. However, recent advances from literature highlight the existence of discrepancies also between their mechanical behavior. The focus is thus put on the possibility to mechanically target cancer cells, which would lead to a more efficient delivery of drugs with a reduction of the side effects for the patients.

This thesis, entitled "Influence des propriétés mécaniques et géométriques des nanoparticules sur leur ingestion par les cellules cancéreuses" (Influence of the mechanical and geometrical properties of nanoparticles on their uptake by cancer cells), focuses on the use of NPs as vectors to deliver anti cancer agents to cancer cells that would be engulfed by the latter through endocytosis. Previous studies, both experimental and numerical, have investigated the influence of the mechanical and geometrical properties of the NPs on their cellular uptake. However, experimental studies have limitations. Indeed, they do not enable to easily isolate a parameter from others and the observation of the phenomena at such scale requires sophisticated experimental facilities and may be impaired by a poor reproducibility. For this reason, numerical investigations have emerged as a suitable alternative to study the cellular uptake of NPs. The objective of the present work is to build a model for the cellular uptake of NPs that will enable to determine the optimal mechanical and geometrical properties of NPs so that they would enter cancer cells, while avoiding healthy counterparts.

For this purpose, an existing model of the wrapping of NPs by a cell membrane, based on an energetic approach, is used. This approach consists in investigating the variation of the total potential energy of the system, composed of an elliptical rigid NP and a portion of membrane, during the wrapping of the NP. The model is henceforth enriched by the description of the membrane mechano-adaptation during the interaction with the NP,

---

[1] More information available at `https://gem.ec-nantes.fr/en/utr-biomec-2-2`.

which is introduced mathematically based on the behavior described in the literature. The influence of this novelty on the outcome of the model is subsequently investigated and compared to the influence of the aspect ratio of the NP and along with the initial membrane properties, via sensitivity analyses. Limitations due to the computational cost of such methods are overcome using surrogate models.

4 Outline of the manuscript

This manuscript is organized as follows: Chapter 1 provides an overview of the context of this study, along with a presentation of the materials that are investigated, *e.g.* the cell, its membrane and the NPs. The existing experimental and numerical investigations of the cellular uptake of NPs are briefly presented. Then, Chapter 2 justifies the choice of the preferred approach for this study and presents it in details. After, Chapter 3 aims at comparing the influence of the adhesion between the NP and the membrane, the membrane tension and the aspect ratio of the NP on the predictions of cellular uptake. This is performed through a sensitivity analysis applied on surrogate models, whose implementation is presented in details. Then, the modeling of the mechanical adaptation of the membrane is justified by literature review in Chapter 4, in which the influence of this enrichment of the model is studied via sensitivity analysis, for the case of the uptake of a circular NP. The similar study is conducted for an elliptical NP in Chapter 5. Last, an application of the model to breast cancer, based on real experimental data, is presented in Chapter 6. Indeed, an extensive literature study is conducted in order to identify a range of values for the mathematical parameters introduced in this new model in order to differentiate healthy from cancerous mammary cells. By computing the model with the measured cell properties, the aspect ratios of the NP that enable it to enter preferably in cancer cells were found. Finally, the results are summarized and discussed at the end of the document.

The outline of this thesis is illustrated in Figure 2.

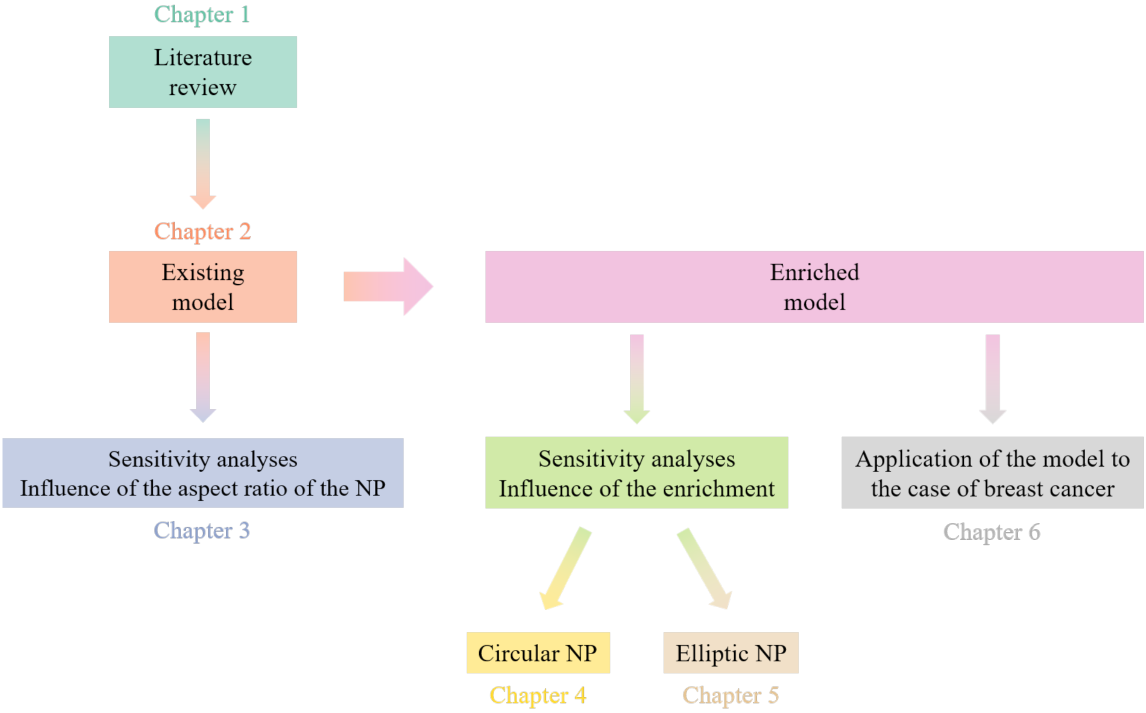

Figure 2: Graphical outline of the thesis.

CHAPTER 1

LITERATURE REVIEW

1 Introduction

The aim of this first chapter is to introduce the context of this thesis, to provide a description of the elements involved in this study and to present the current state of art on the modeling of the cellular uptake of NPs. Hence, an overview of the existing cancer treatments is given in Section 2, which introduces the interest of using NPs in the field of medicine, while emphasizing the ways to enhance their effectiveness. To do so, it is necessary to study the process through which these NPs enter the cell. This process, called endocytosis and presented in Section 3, involves the cell membrane, which is subsequently introduced in Section 4, along with generalities on the cell itself and the main differences between healthy and cancer cells that can lead to disparities in their ability of endocytosis. Last, the investigations that have already been conducted on the cellular uptake of NPs are summarized in Section 5.

2 Cancer treatments

2.1 Overview

Cancer is a disease whose occurrence has been increasing since the beginning of the 20th century [3]. The treatments have evolved since then, from the improvement of the diagnosis methods to the development of innovative remedies [4, 5]. The former differ depending on the location and the stage of cancer. Indeed, when the tumorous cells are easily reachable and have not spread to the rest of the organism, it is possible to remove them surgically or with local treatments such as radiotherapy [6]. Otherwise, non-local (also called systemic) treatments are used alone or as a complement to local treatments. Among the most commonly used, chemotherapy, hormonotherapy, immunotherapy and the most recent targeted therapy are briefly presented hereinafter.

Chemotherapy treatments have been introduced for the first time in the 1940s [7] and consist in inhibiting the division of rapidly growing cells by destroying their DNA during replication. However, side effects are caused in healthy tissues such as bone marrow, hairs or the reproductive system [8], which are also rapidly growing and therefore hit by the treatment. In addition, some chemotherapeutic agents can induce an increased risk of secondary malignancies like leukemia (blood cancer) or peripherical neuropathy (nerves damaging). Hormonotherapy is used for hormone-related cancer, such as breast or prostate cancer, which are among the most frequent cancer types [3]. These treatments consist in reducing the hormone levels in the organism by injecting hormone agonists [9]. They cause side effects such as osteoporosis or arthralgia [10]. Immunotherapy consists in generating a response of the host's immune system against the tumor by introducing antibodies into the organism [11]. A more recent approach for cancer treatment is the targeted therapy, which has been developed for the past 20 years [12]. It consists in targeting specific molecules that contribute to the growth of tumors and to block their action. Thus, cancer cells are more efficiently targeted than with conventional chemotherapy agents that usually affect indifferently both cancer and healthy cells based on the condition to be rapidly growing cells. Still, some of the targeted molecules are also present in other healthy cells. The interference of the treatment with these may subsequently block their reproduction and hence lead to unwanted side effects.

Chemotherapy and targeted therapy have in common that they reach out to specific cells through targeting. This targeting can be used on Drug Delivery Systems (DDS), which can take the form of NPs, as presented in Section 2.2.

2.2 Nanoparticles for cancer treatments

Some cancer treatments consist in delivering molecules that cannot directly be injected to the patient. In this particular case, these molecules need to be encapsulated [13]. The system subsequently obtained is called a nanovector. After avoiding clearance mechanisms, the nanovector can reach the desired cells, thanks to a targeting similar to those described in Section 2.1. Thus, the drug is eventually released to the cell of interest. Nanovectors of several types exist, *e.g.* NPs and virus-like particles or nanovesicles. In the scope of the present work, only NPs will be considered. They are used as an emerging cancer treatment tool as DDS but also for photothermal and radiotherapy [14]. In the case of photothermal therapy, metallic (*e.g.* gold) NPs are used to kill the cell they are into once an electromagnetic radiation is applied. In radiotherapy, metal NPs are used to detect the position of cancer cells via X-ray in order to identify the location where the radiotherapy should be applied.

NPs are of two types: organic or inorganic. Organic NPs can be lipid-based or are formed of a combination of lipids and macromolecules such as proteins [13]. Inorganic NPs [15] are for instance made of metals, silica or carbon. They are usually easier to manufacture and more stable than their organic counterpart. Still, they tend to have a stronger toxicity for the organism [16] and to be less biodegradable [13].

Recalling that the objective of the METCIN project is to identify the influence of the mechanical properties of NPs of various nature, and mostly those manufactured by the CEISAM laboratory, which are fluorescent and photo-cross-linkable. Details on these NPs and their fabrication are provided in [17]. However, the modeling of such NPs with a purely mechanical approach is challenging due to their complex behavior. As such, since the objective of the present thesis is to provide a mechanical modeling of the uptake of NPs in order to identify the influential mechanical parameters, only the inorganic NPs will be investigated here. The adaptation of the model to NPs with complex behaviors is a perspective of future work, once we are able to investigate the uptake of rigid NPs.

The mechanical properties of inorganic NPs vary according to their composition, size and shape. For instance, the elastic modulus of NPs range from a few MPa up to a few GPa, while their size can vary from around 10 nm to 1 μm [18]. Furthermore, a variety of shapes exist and NPs can, for instance, be circular, elliptical, disc-like or tubular [15, 19]. They enter the cell through a phenomenon called endocytosis, that will be introduced in Section 3.

3 Endocytosis

3.1 Overview

In order to feed itself and to satisfy some of its functions, the cell exchanges elements such as gases, ions, hormones, liquids or solids with the extra-cellular medium (ECM) [20]. The transport of small penetrants *e.g.* gases, ions and simple molecules, takes place via diffusion between the intra- and extra-cellular media, while large penetrants like NPs enter the cell via a mechanism called endocytosis [16]. The phenomenon of endocytosis was observed for the first time in 1883 [21] and has been widely investigated since then [22]. The endocytosis of an object takes place in three steps: (i) the cell determines, based on the presence of opsonins (proteins that belong to the bloodstream that aim at tagging objects to make them visible by the cells), whether the former can be internalized and adhesion between the cell membrane and the surface of the object takes place. If so, (ii) the cell membrane deforms around the object and last, (iii) the membrane forms a vesicle around the object that is further uptaken by the cell. These phases are schematically illustrated in Figure 1.1. Nonetheless, after its entry into the host cell, several steps may remain for the object to reach its destination inside the cell [23]. Furthermore, the object may also spontaneously be expelled from the cell via a phenomenon called exocytosis.

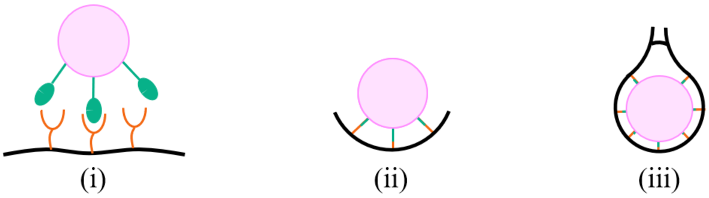

Figure 1.1: Steps of endocytosis: (i) initiation of the contact between the object and the membrane through the interaction of specific molecules, (ii) deformation of the membrane around the object to wrap it and (iii) formation of a vesicle after the fusion of the two sides of the membrane.

As introduced above, endocytosis takes place with several kinds of objects. For this reason, several types of endocytosis do exist to adapt to the variety of the objects involved. For large solid elements, the process is called *phagocytosis*, while one calls *pinocytosis* the cellular uptake of liquid and small solid objects [24]. Phagocytosis is often performed by cells that are part of the immune system, such as macrophages, for instance [25]. In the specific case of the present study, the NPs are not supposed to enter such cells, as they may lead to their death, and consequently to a weakening of the patient immune system. For this reason, phagocytosis will not be detailed in this thesis.

3.2 Endocytosis of nanoparticles

The endocytosis of NPs is the subject of several studies for their application to DDS. The objective of these studies is to investigate the influence of the physico-chemical properties of both the NP and the cell membrane on the likelihood for the NP to be uptaken by the cell. The results of these studies are synthesized in Table 1.1. Some of the notions, introduced in this table, refer to the composition of the cell membrane, which is described in Section 4.

Table 1.1: Influence of the properties of the NP, the cell and the ECM on the endocytosis of NPs. Note that many of the references used to do this literature review involve the study of phagocytosis as they are easier to observe than the endocytosis of benign cells. However, the results from these studies can be used to provide an overview of the influential parameters on endocytosis.

Concerns	**Type**	**Parameter**	**Influence**	**Reference**
The NP	Geometry	Size	- Minimal size under which the endocytosis is impossible; - Existence of an optimal size that contributes to endocytosis.	[26–29]
		Shape at contact	- Endocytosis is more likely to happen if the NP touches the membrane with its tip than with its flat side.	[30, 31]
		Shape	- No influence	[19]
	Chemical composition of the surface	Hydrophobicity	- Hydrophilic NPs are more likely to adhere to the hydrophilic membrane; - The presence of hydrophobic regions in the NP facilitates the binding with the hydrophobic tails of the phospholipids.	[16, 32–35]
		Electric charge	- Depending on its charge, the NP is more likely to bind to certain regions of the cell membrane.	[16, 36, 37]
	Mechanical properties	Stiffness	- Stiff NPs are more likely to be endocytosed than soft ones.	[30, 38–40]
The cell	Chemical composition	Membrane molecules	- Insaturated fatty acids are more mobile and thus increase the deformability of the membrane.	[41, 42]
	Physiology	Cell type	- The adhesion depends on the distribution of the types of phospholipids in the membrane, which differs according to the cell type.	[20, 25]
	Mechanical properties	Membrane tension	- Cells with low membrane tension are more likely to have endocytosis.	[43–49]
The ECM	Chemical composition	pH	- Endocytosis is more likely when the pH is close to 7.	[25, 50]
	Mechanical properties	Stiffness	- Stiff media facilitate endocytosis.	[51, 52]

4 Cells and cell membrane

To better understand the objects that are involved in this study, the microstructure of the cell wall is presented in Section 4.1 and an overview of the main differences between healthy and cancer cells is provided in Section 4.2.

Animal bodies are organized in several levels, among them: (i) the organs, (ii) the tissues, and (iii) the cells. Indeed, organs *e.g.* the liver or the brain, are composed of tissues *e.g.* muscles, glands, themselves composed of cells [53]. Two kinds of cells exist: the prokaryote and the eukaryote [20]. Prokaryotes, often bacteria, are organisms composed of a single cell, that have no nucleus. The remaining of the existing cells are eukaryotes. Their diameter is between 10 and 100 μm and differs according to the type of the cell. Around 200 types of cells exist in the human body, which belong to 5 main tissues: the epithelial, connective, nervous, muscle tissue and blood. Cells from epithelial, connective and muscle tissues are organized in leaflets while blood and nervous cells are separated from each other and evolve in the ECM. These tissues are illustrated in Figure 1.2.

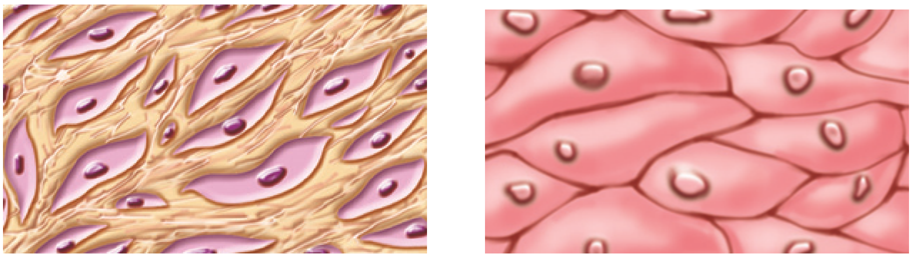

(a) connective (b) epithelial

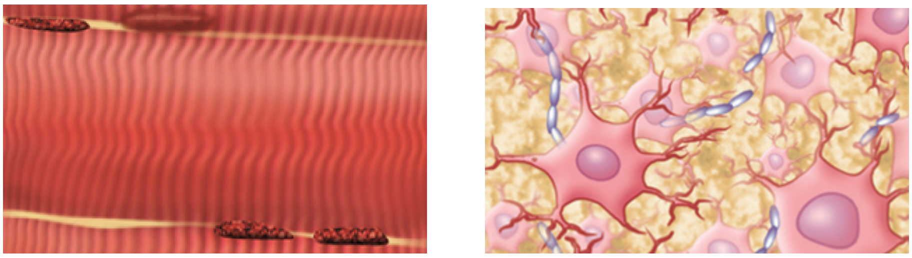

(c) muscle (d) nervous

Figure 1.2: Illustration of common tissues in the human body, reproduced from [54].

Cells contain organelles, which are substructures that ensure specific functions of the cell. These cells are also composed of a cytoskeleton, which is a network of proteins filaments that enables cell movement. An illustration of the structure of an eukaryote cell is provided in Figure 1.3, where several organelles are represented. For details on their role, the reader is referred to [20, 53, 55]. The inner components of the cell are separated from the ECM thanks to the cell membrane.

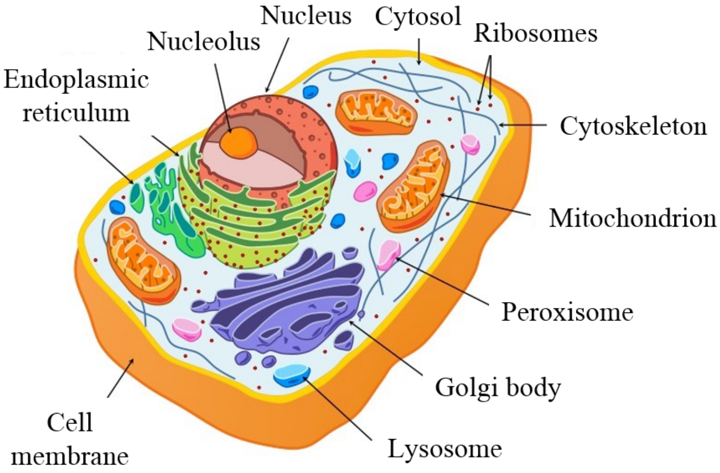

Figure 1.3: Illustration of the composition of a an eukaryote cell, reproduced from [56].

Since this study aims at understanding the first steps of endocytosis (described in Figure 1.1), a particular attention is given to the cell membrane, whose structure is presented in Section 4.1.

4.1 The cell membrane

This section is mainly based on Cooper *et al.* [20] and Anthony [53]. The cell membrane, also called plasma membrane, is the protective layer of the cell, as it ensures a waterproof separation between the inner and outer sides of the cell. The membrane also plays the role of an interface, since elements transit to and from the cell through it. A simplified illustration of the structure of the cell membrane is provided in Figure 1.4. The cell membrane is mainly composed of phospholipids, proteins, cholesterol and sugar [57, 58]. These elements are respectively presented in Sections 4.1.1, 4.1.2, 4.1.3 and 4.1.4.

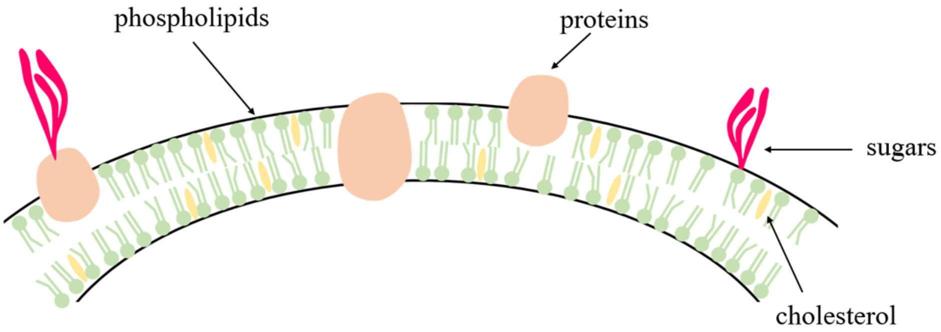

Figure 1.4: Illustration of the structure of the cell membrane.

4.1.1 Phospholipids

As illustrated in Figure 1.4, the cell membrane is formed of a bilayer of lipids that are all composed of a head and a tail [20]. The head can contain amino acids, alcohol, phosphate, glycerol or sphingosine. These lipids are called phospholipids and depending on their composition, a suffix is added, *e.g.* glycerophospholipids or sphyngophospholipids. The electric charge of the head of the lipids depends on the amino acid of which it is constituted. The charge can hence either be negative, neutral or positive. The tail contains two chains of fatty acids with between 14 and 24 carbon atoms each. The fatty acids can be saturated or unsaturated, depending on the presence of simple and double bonds. The head of a phospholipid is hydrophilic (polar), while its two tails are hydrophobic (apolar). For this reason, they spontaneously arrange themselves as bilayers. Indeed, hydrophilic heads are gathered together, as well as hydrophobic tails, as illustrated in Figure 1.5.

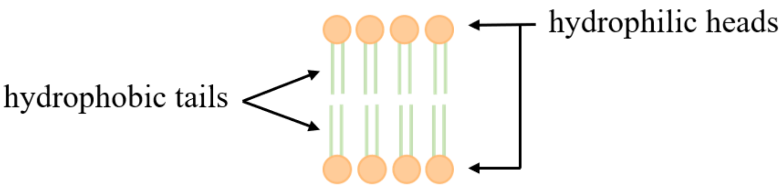

Figure 1.5: Arrangement of lipids in a bilayer, tails in the middle and heads on the opposite sides.

Furthermore, the two layers face each other. As such, the polar heads at the outer side of the membrane, *i.e.* in contact with the aqueous intra and extracellular media, while the fatty acid chains are inside the membrane. The adhesion between the phospholipids is ensured by van der Waals and hydrophobic interactions. Both leaflets are not symmetric in composition and differ by the kind of phospholipids they are composed of. The phospholipid layers have a fluid-like behavior. Indeed, the presence of unsaturated fatty acids causes alignment flaws in the bilayer and hence induces a mobility in the membrane. In addition, phospholipids have several degrees of freedom. They can, for instance, switch their position with their neighbor, rotate, bend their tail or even move to the other layer [59]. Some of these degrees of freedom are schematically illustrated in Figure 1.6.

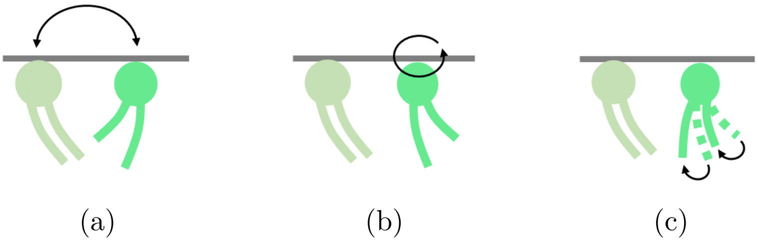

Figure 1.6: Illustration of some of the degrees of freedom of phospholipids, such as (a) an exchange of position, (b) the rotation of a phospholipid or (c) the random movement of the tails of a phospholipid. The horizontal line represents the boundary of the membrane.

4.1.2 Proteins

Proteins have several functions [20]. They contribute to the passive transport of small elements through the membrane. They also play a major role in the adhesion to the ECM. Last, they enable the reception of external signals and stimuli. The proteins are either located on the outside of the membrane (peripheral proteins) or through the bilayer (integral proteins), as illustrated in Figure 1.4. The polar side of such proteins is located on the outside of the membrane, as shown in Figure 1.7.

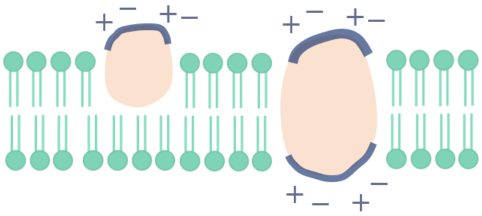

Figure 1.7: Peripheral (left) and integral (right) proteins. The polar side of the proteins is located outside of the bilayer.

4.1.3 Cholesterol

Like phospholipids, cholesterol is a kind of lipid [20]. Between 20 % and 30 % of the membrane lipids are cholesterol. These molecules are mainly hydrophobic and thus located inside the membrane, as illustrated in Figure 1.4. Cholesterol contributes to the stiffness of the membrane by influencing the organization of the phospholipids, as illustrated in Figure 1.8.

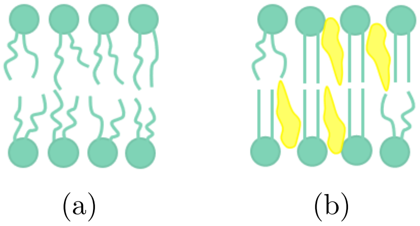

Figure 1.8: Organization of the phospholipids (a) without and (b) with cholesterol, represented in yellow.

4.1.4 Sugar

As illustrated in Figure 1.4, sugars are located on the outer side of the membrane, at the interface with the ECM [20]. These molecules are hydrophilic and associated to lipids or proteins, leading to the formation of complexes, respectively called glycolipids and glycoproteins. These sugars form a fibrous coat called glycocalix, also known as cell coat or fuzzy coat. Glycocalix provides an anti adhesive barrier, in order to protect the cell from possible aggressions from the ECM. The thickness of this coat varies between cells from similar and different kinds [60, 61]. Figure 1.9 shows a microscopic observation of glycocalix on intestinal cells.

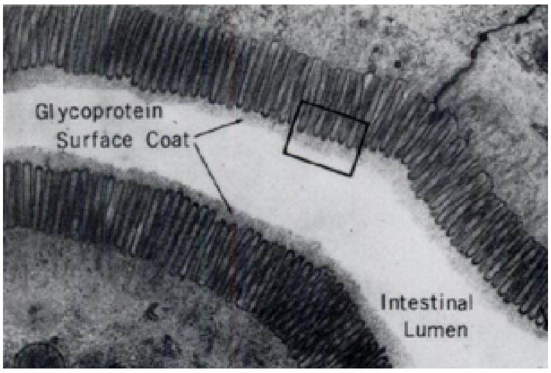

Figure 1.9: Observation of glycocalix on intestine rat cells, reproduced from [60].

4.2 Differences between cancer and healthy cells

4.2.1 Definition of a cancer cell

More than 100 types of cancer have already been described in anatomical pathology. Despite this variety, cancer cells share common features. Indeed, Hanahan and Weinberg [62] highlighted six common functional capabilities in cancer cells. Hence, such cells are insensitive to anti-growth signal and they are self sufficient in growth signals. In addition, they present a limitless replicative potential and are able to spread to other tissues. They are also able to sustain themselves thanks to the development of their own vascularities, also called as angiogenesis. Last, most of the processes that cause the death of the cell, also called as apoptosis, do not apply to cancer cells. These properties are summarized in Figure 1.10.

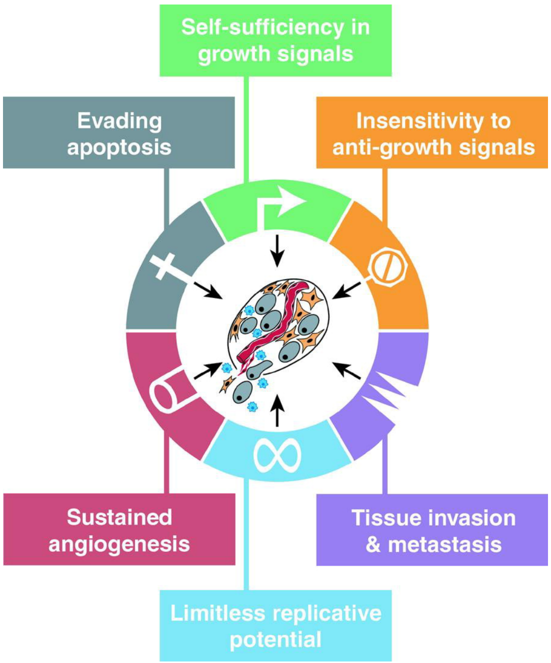

Figure 1.10: Common properties of cancer cells, reproduced from [62].

Observations of healthy and cancer mammalian cells in *in vitro* cultures, represented in Figure 1.11, illustrate the fact that cancer cells do not regulate their reproduction, which takes place until there is no space left in the medium, while healthy cells are not as aggregated. Furthermore, healthy cells form flat monolayers with well defined borders, while cancer cells borders are fuzzier, with a more abundant cytoskeleton, as illustrated in Figure 1.12.

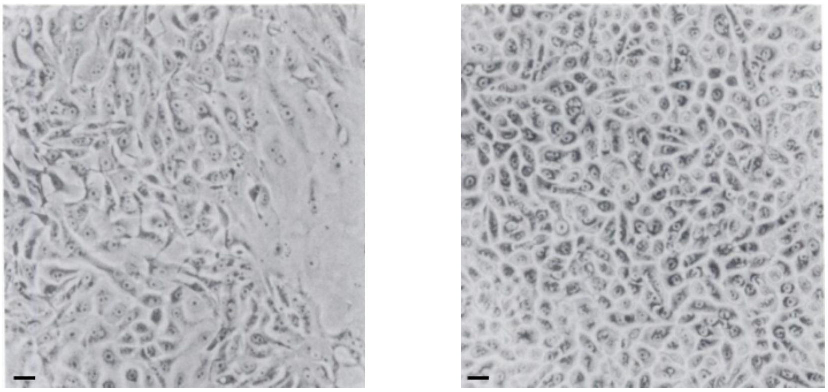
(a) (b)

Figure 1.11: *in vitro* culture of (a) healthy and (b) cancer mammalian cells. The black line represents a scale of 15 μm. Adapted from [63].

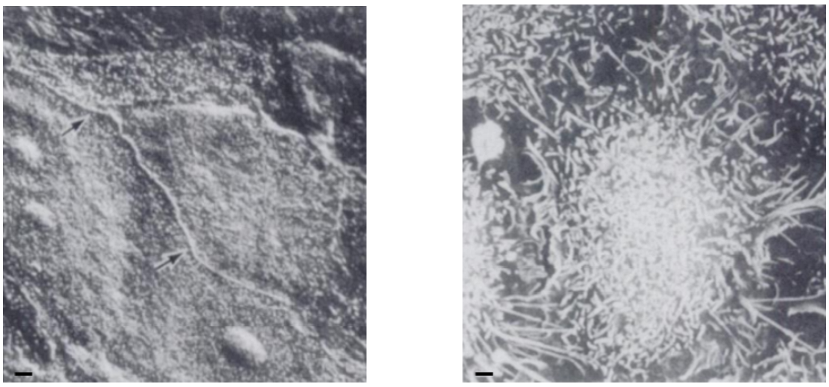
(a) (b)

Figure 1.12: Scanning electron microscopy of (a) healthy and (b) cancer mammalian cells. The arrows in (a) show the cell borders. The black line represents a scale of 1 μm. Adapted from [63].

In addition to the functional capabilities that differ between cancer and healthy cells, differences in their mechanical properties have also been observed. These heterogeneities play a key role in the context of this thesis, as they will be used in order determine the aspect ratio of NPs so that they are internalized by cancer cells preferably. These differences are described in Section 4.2.2 below.

4.2.2 Mechanical differences

Differences in the mechanical properties have been observed between healthy and cancer cells. For instance, the progression of cancer induces a reorganization of the cytoskeleton, which often leads to a reduction of the stiffness of the cell [64–67]. Mechanical measurements, such as Atomic Force Microscope (AFM) [68–70], bio-Micro-Electro-Mechanical Systems (MEMS) [71, 72] or tweezers [73, 74], performed on bladder, colon, breast and prostate cancer and healthy cells show lower Young moduli for cancer cells. Furthermore, the glycocalix coat tends to be thicker on cancer cells compared to healthy ones [61, 75–77]. As introduced in Section 4.1.4, the thicker the glycocalix, the smaller the adhesion between the cell and extra-cellular objects. Hence, one can infer that the adhesion of cancer cells is lower than that of healthy cells. These differences are summarized in Figure 1.13.

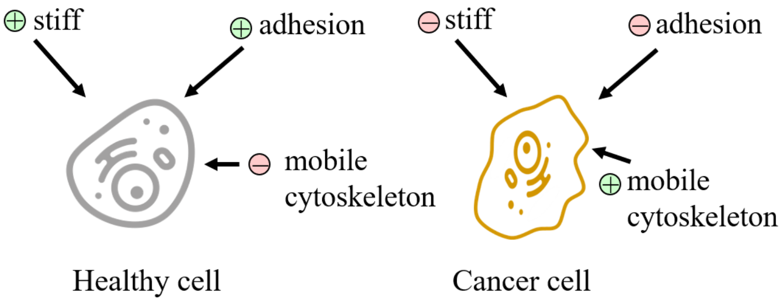

Figure 1.13: Illustration of the main mechanical discrepancies between healthy and cancer cells.

In order to investigate the entry of NPs into cells and to account for the mechanical differences between healthy and cancer cells on the corresponding process, experimental and numerical studies have been conducted. They are presented in Section 5.

5 Previous works on the understanding of the cellular uptake of NPs

5.1 Experimental investigations

In order to observe tendencies on the cellular uptake of NPs, this phenomenon has widely been investigated experimentally [22, 78, 79]. Still, the use of such methods has limitations regarding the investigation of the influence of the mechanical and geometrical properties of the NP on its cellular uptake. First, many of these studies are focused on phagocytosis [19, 30], as it is easier to observe. Second, it is complicated to identify the individual influence of a given property because of the difficulty to alter one of them without changing the others. For instance, it is known that a cell with a high concentration in cholesterol is stiffer. Moreover, increasing the amount of cholesterol also alters the charge at the surface of the cell and consequently the adhesion with extracellular objects. In addition, it is challenging to accurately control the mechanical properties of a cell. It is especially the case for the bending rigidity of the cell and the adhesion [64, 80–83], which are of main interest in the study of the cellular uptake of NPs. Furthermore, as introduced in Section 4, the cells evolve in a fluid medium in which they move due to the activity of their cytoskeleton. The observation of the cellular uptake of a single NP is henceforth limited, due to the cell movement, as it is experimentally challenging to develop such an observation facility. In addition, experimental settings usually consist in introducing several NPs in a cell culture, often with several cells, and then compare the rate of engulfed NPs, without prioritizing a region in the cell membrane. Last, discoveries made on *in vitro* observations in artificial environment are not easy to translate to *in vivo* behaviors [67]. For this reason, even though experimental observations may seem more representative of the actual behaviors of the investigated systems, they are still limited. In addition, the application of external perturbations, *e.g.* temperature or change in the composition or pH of the ECM, is challenging. These parameters influence the endocytosis process, as previously presented in Table 1.1.

Because of the aforementioned reasons, models have been developed to provide a complementary tool to experimental studies in order to overcome the challenges mentioned in this section. These models may focus on the scale of the elements of the membrane (Section 5.2) or on the scale of the NP (Section 5.3).

5.2 Models at the scale of the membrane constituents

The endocytosis of NPs is a complicated process which is induced by several phenomena happening at the molecular scale. For this reason, molecular approaches [84] have been used to numerically investigate the cellular uptake of NPs [30, 85–89]. In such approaches, the microscopic elements of the NP-membrane system can be modeled with several degrees of precision. For instance, possible representations of membrane phospholipids are displayed in Figure 1.14. In addition, molecular dynamics approaches enable to follow processes with a time scale [90]. Previous molecular dynamics models of the cellular uptake of NPs investigated the influence of the shape of the NP and aspect ratio on endocytosis [91] and showed that elliptic NPs are more likely to be engulfed by the cell if they enter in contact with it from their sharpest side (by the tip of the NP). Otherwise, they tend to rotate to enter the cell in this position [85, 88, 92]. An example of the modeling of the cellular uptake of a NP is provided in Figure 1.15.

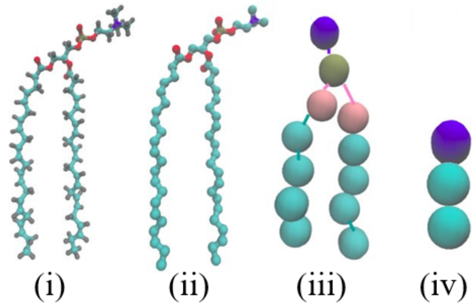

Figure 1.14: Illustration of the possible representation of phospholipids: (i): representation of all the atoms; (ii): representation of all the atoms except hydrogens; (iii) and (iv): example of coarse grained models. Reproduced from [93].

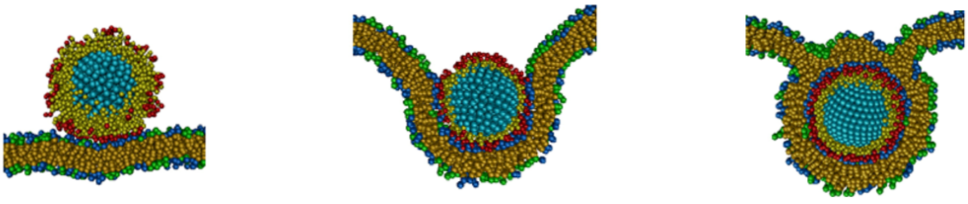

Figure 1.15: Example of a molecular dynamics simulation of the cellular uptake of a NP with a coarse grained model, reproduced from [94].

Such models are, due to their level of discretization, highly computationally expensive. Furthermore, their implementation is based on the knowledge about small scale interactions, such as the interactions between the atoms of each molecule, for instance. They are consequently highly dependent on the accuracy of the composition of the membrane, *i.e.* the distribution of the kind of lipids in each layer or their mobility. For this reason, they are not well suited for parametric studies, as they yield non affordable total computation times because of the required accuracy of their input parameters. Last, to the best of our knowledge, the existing molecular dynamics models only account for rigid NPs [30]. Indeed, modeling the deformation of the NP, even with a simple linear elastic constitutive law, would lead to highly complex models.

For these reasons, molecular dynamics approaches do not suit well to purely mechanical investigations of the cellular uptake of NPs, especially when parametric studies are aimed to be conducted. In this case, models at the scale of the NP are preferred. Such models are presented in Section 5.3.

5.3 Models at the scale of the NP

Models of the cellular uptake at the scale of the NP have first been introduced by Yi *et al.* in 2011 [40]. These models are built based on a simple energetic approach, that will be detailed in Chapter 2, while the present section only aims at introducing the main principles of such an approach.

Models at the scale of the NP consist in modeling the cell membrane as a homogeneous line, based on the scale ratio between the radius of the NP and the membrane thickness. Hence, the constituents of the membrane, as well as the molecular-scale interactions between them, are not modeled. This system is illustrated in Figure 1.16, in which three regions are defined: the inner free region (1), that is the part of the NP which is not yet wrapped by the membrane, the outer free region (2), part of the membrane that is not (yet) in contact with the NP, and the adhesion region (3), that corresponds to the contact region between the NP and the membrane. The ensemble is described by several variables, as well as a coordinate system (r, z), in order to follow the curvature of the membrane (through the angle ψ) depending on the arclength, denoted as s in regions (1) and (3) or by t in region (2).

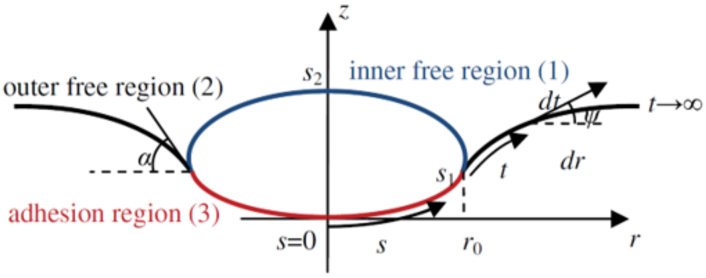

Figure 1.16: Representation of the wrapping of a NP by the cellular membrane, as defined in [40].

In this approach, the variation of potential energy of the system is described by the Canham-Helfrich Halmitonian [59, 95–98] and is minimized with the Euler Lagrange equations in order to determine the equilibrium state of the system. A parametric study, in order to investigate the influence of the mechanical and geometrical properties of the system on the equilibrium state, can hence be conducted. Such approaches have been utilized in other studies of the cellular uptake of NPs or the adhesion of vesicles to substrate or between two vesicles (whose results can be generalized to the uptake of NPs), such as in [99–107], and even more recently in [108, 109]. Last, despite their advantages, it is worth noting that such simplified models involve the use of strong hypotheses which may not apply properly to all real cases. Hence, even though these approaches enable to perform complex investigations with a reasonable computational cost, one needs to be careful in their interpretation.

6 Summary of Chapter 1

This chapter provided the context needed for this thesis. As such, the systems to be investigated as well as an overview of the state of the art have been presented, while considering the inherent complexity involved when dealing with living systems. Hence, from each section of this chapter, conclusions are drawn to specify the scope of the study, and are summarized as follows:

- **Cancer treatments** are evolving and new cancer therapies have been recently developed. Part of them consist in using NPs that are able to target cancer cells in order to avoid healthy cells and consequently to reduce the side effects of the currently commonly used cancer treatments. These NPs use mostly chemical differentiation to target cancer cells, which has not proven to be an accurate method for the moment, often also being responsible for the undesired destruction of healthy cells. In the meantime, mechanical differentiation has been emerging in the past few years as a promising alternative to target unhealthy cells more accurately than with chemical differentiation only. As such, this thesis focuses on studying the parameters involved in the mechanical differentiation in order to identify the mechanical and geometrical properties of a NP that optimize its efficiency on targeting cancer cells only.
- **Endocytosis** is then presented since it is the process through which NPs enter the cells. An overview of the main observations of the endocytosis of NPs is given and the mechanical and geometrical influential parameters are emphasized, showing that the curvature of the NP at the contact region with the membrane plays a crucial role on their engulfment, along with the electrical charge of the membrane, for instance.
- **The variety of cells** was then highlighted, showing that it is difficult to generalize the results to all types of cells, given the fundamental discrepancies involved. In addition, significant variations in the cell composition are observed between two cells

from the same type. Hence, accounting for this variability is important for understanding the cellular uptake of NPs, especially given that experimental observations performed on few cells may not generalize well.

- **The cell membrane** has a fluid structure and is composed of lipids, proteins and sugars. The local composition of the membrane changes along the circumference of the cell, which leads to a variation of the mechanical properties with respect to the location along the membrane.
- **Investigations on the cellular uptake of NPs** have mostly been conducted experimentally. However, such studies present limitations such as the generalization of the observations, due to the variety of the properties that can be observed even between two cells of the same type, and also within the cell itself. It is also difficult to determine the influence of a single parameter of the cell on the uptake of NPs as these parameters are likely to change during the process, since the cell is a living system. Furthermore, the measurement of such mechanical properties is also challenging, due to the accuracy needed to reach such scale.
- **Numerical investigations** thus appear as an alternative to experiments as they enable to easily perform parametric studies on the models that have been developed. Models at the scale of either the constituents of the membrane or the NP are commonly used to investigate the cellular uptake of NPs. However, models at the molecular scale apply better to chemical investigations and have large computational costs due to the amount of degrees of freedom that are modeled, depending on the discretization applied. On the contrary, models at the scale of the NP offer the possibility to conduct investigations, while focusing on a mechanical approach, with a limited computation time. Details and justifications on the preferred approach are provided in Chapter 2.

The literature review, presented in this chapter, is non exhaustive and aimed at providing an overview of the main topics related to this thesis. The goal was to offer a succinct presentation, while remaining intelligible for readers who do not possess a background in cell biology. Moreover, complementary information are provided throughout the document, when needed.

Chapter 2

PRESENTATION OF THE MECHANICAL MODEL OF ENDOCYTOSIS

1 Introduction

This chapter aims at presenting which of the approaches introduced in Chapter 1 was preferred to model the cellular uptake of a NP in this work. This choice is justified by the scale of the phenomena that will be represented, as introduced in Section 1.1. The post-processing applied to this model, in order to identify the influence of the input parameters, is presented in Section 1.2.

1.1 Scale of the model

In order to perform a purely mechanical-based approach in the developed model, the study focuses on NPs whose diameter is around 100 nm, while that of the cell is around 10 μm. An illustration of the difference of scale between the NP and the cell is provided in Figure 2.1. These dimensions were set based on the literature [18, 20], in order to represent a range of NPs effectively used for medical applications while limiting the complexity of our approach. Indeed, with smaller NPs, (*i.e.* whose size is in the same order of magnitude as some constituents of the membrane), the model would need to account for those constituents and consequently for the chemical phenomena that can take place between them, which is out of the scope of the present study. With NPs of size around 100 nm, the membrane, whose thickness is in the order of 10 nm, will be represented as a horizontal line in 2D or a horizontal plane in 3D, as in [40, 95, 102, 110]. Last, modeling at the scale of the NP also allows to neglect the curvature of the cell compared to that of the NP.

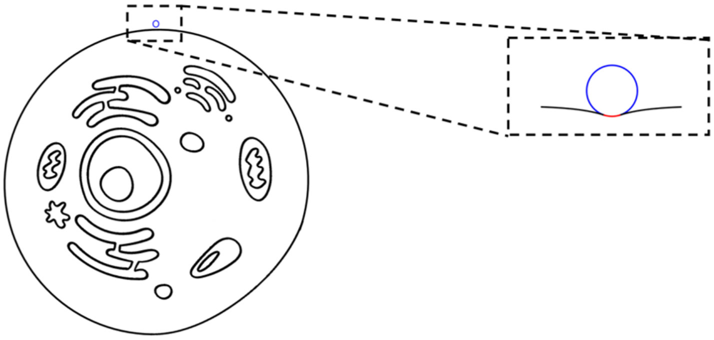

Figure 2.1: Schematic illustration of the scale ratio between the NP and the cell.

1.2 Investigation steps

Following [40, 95, 102, 110], the system is investigated via the evaluation of its total potential energy, in order to identify the equilibrium state. Then, parametric studies are performed in order to understand the influence of the input parameters on the equilibrium. The analytical evaluation of the potential energy of the system is presented in Section 2. Different approaches to determine the equilibrium state are subsequently compared in Section 3.

2 Evaluation of the total potential energy of the system

2.1 Presentation of the system

The system, composed of an elliptic NP and a portion of the cell membrane, is illustrated in Figure 2.2. It is divided into four regions: region 1, in blue, is the free part of the NP, regions $2r$ and $2l$, in black, are the free parts of the membrane, respectively on the right and left side of the NP, and region 3, in red, is the part of the membrane in contact with the NP. The spatial coordinates are denoted with (r, z), wherein the origin O is located at the intersection between the regions 1, $2l$ and 3. Each region $i \in \{1, 2l, 2r, 3\}$ is parametrized by its arclength $s_i \in [0; l_i]$, where l_i is the length of the region i, along with the angle ϕ_i, used to calculate the curvature and subsequently the bending energy. This angle is defined as the angle between the tangent to the region and the horizontal (colinear to the r axis), as illustrated in Figure 2.2. The system is symmetric, therefore the length of the two free parts of the membrane are considered equal and will henceforth be denoted as l_2, where $l_{2l} = l_{2r} = l_2$.

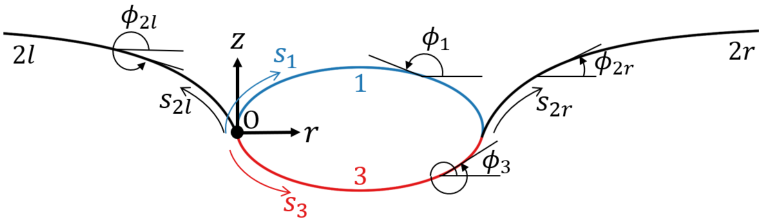

Figure 2.2: Illustration of the parametrization of the NP-membrane interaction.

The lengths l_1 and l_3 are defined in terms of the wrapping degree f, which corresponds to the fraction of the circumference p of the NP wrapped by the membrane. Hence, $l_3 = pf$, $l_1 = p(1-f)$ and the wrapping degree reads:

$$f = \frac{l_3}{l_1 + l_3}. \tag{2.1}$$

Due to the size of the NP compared to that of the cell, the membrane is supposed to be flat far from the contact region. This implies that

$$\lim_{s_{2r}\to\infty} \phi_{2r}(s_{2r}) = 0 \quad \text{and} \quad \lim_{s_{2l}\to\infty} \phi_{2l}(s_{2l}) = 2\pi.$$

2.2 Analytical form of the total potential energy of the system

The objective of this section is to provide the analytical form of the potential energy of the system. For this purpose, the hypotheses are presented in Section 2.2.1. Then, the variation of the potential energy of the system, in terms of the wrapping degree f, is described in Section 2.2.2.

2.2.1 Hypotheses

Rigid NP In this work, the focus is put on rigid NPs as they lead to a model with reasonable complexity, enabling us to subsequently carry out post-processing with a sustainable computational cost, thanks to a moderate number of influencing parameters. Nonetheless, given that the rigidity of the NP is typically at least 2 orders of magnitude greater than that of the cell membrane [88, 111, 112], the assumption of a rigid NP is convenient in most cases.

Elastic membrane The assumption that the behavior of cell membranes is elastic was made in the 1970s by Helfrich [59] and his work is the foundation of all energy-based approaches for modeling endocytosis [40, 97–99, 109].

2D model Most of the existing NPs being symmetric [19], a 2D model of the system is used for the sake of simplicity and to decrease the computational costs. Furthermore, this model has already been investigated with a 2D approach by Yi *et al.* in a more recent paper [105], which allow us to use the results as a basis for our study. In such case, the energy per unit length in the out-of-plane direction (see Figure 2.3) is investigated.

Symmetry The system, presented in Figure 2.2, being symmetric, only half of it is used to calculate the energy and the reduced system is illustrated in Figure 2.3.

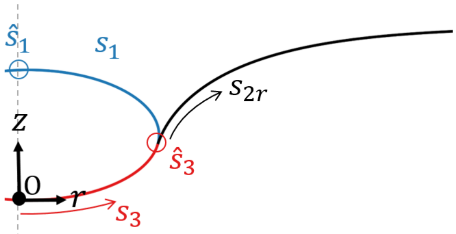

Figure 2.3: Illustration of the reduced system because of the symmetry.

For this reduced system, the origin of the coordinates system (r, z) is located in region 3, where $s_3 = 0$. The total arclength of region $j \in \{1, 3\}$ is denoted by $\hat{s}_j$ and equals $l_j/2$. At the intersection between the regions 1, $2r$ and 3 (red circle), $s_3 = \hat{s}_3$ and one has $s_1 = 0$ and $s_{2r} = 0$ (origin of the arclength for the regions 1 and $2r$). Due to symmetry, $r(s_1 = \hat{s}_1) = 0$ (blue circle). One can also note that the length of the region $2r$ is asymptotically larger than the circumference of the NP, *i.e.* $l_2 \gg p$.

2.2.2 Description of the variation of the potential energy

The variation of the total potential energy of the system per unit length in the out-of-plane direction, that will further be referred to as potential energy for brevity, investigated in this section, corresponds to the variation of the potential energy between a given state and the initial state. The latter is defined as the instant at which the contact between the cell and the NP initiates. As such, initially, $\hat{s}_3$ is near to zero.

The variation of the potential energy between the initial and a given state at which the wrapping degree of the NP equals f can be decomposed to the following three contributions: (i) the bending energy of the membrane $\Delta E_b(f)$, (ii) the energy due to the adhesion between the NP and the membrane $\Delta E_\gamma(f)$ and (iii) the membrane tension energy $\Delta E_\sigma(f)$, due to the stretching of the membrane [40, 59]. Hence, the former reads:

$$\Delta E(f) = \Delta E_b(f) + \Delta E_\gamma(f) + \Delta E_\sigma(f). \tag{2.2}$$

For the sake of clarity, the dependence on f is henceforth omitted. The variation of the bending energy of the membrane ΔE_b is the following functional [59]:

$$\Delta E_b = \underbrace{\frac{1}{2}\int_0^\infty \kappa_{2r}(s_{2r})[\dot{\phi}_{2r}(s_{2r}) - \widetilde{c}_{2r}(s_{2r})]^2 ds_{2r}}_{\text{region 2r}} + \underbrace{\frac{1}{2}\int_0^{\hat{s}_3} \kappa_3(s_3)[\dot{\phi}_3(s_3) - \widetilde{c}_3(s_3)]^2 ds_3}_{\text{region 3}}, \tag{2.3}$$

where the overdot denotes the derivative with respect to the arclength. In Equation 2.3, the bending rigidity and the initial curvature of the region $i \in \{2r, 3\}$ are denoted by κ_i and $\widetilde{c}_i$, respectively. The heterogeneity in mechanical and geometrical properties, as introduced in Chapter 1, implies a dependence of the latter to the arclength s_i. However, in order to simplify further calculations, we assume that the membrane is homogeneous, which means that the bending rigidity of the regions $2r$ and 3 (membrane) are equal and will be denoted as κ in the following. In addition, since the membrane is considered initially flat, its initial curvature equals zero regardless of the arclength, yielding $\widetilde{c}_{2r} = \widetilde{c}_3 = 0$. Finally, ΔE_b reads:

$$\Delta E_b = \frac{1}{2}\kappa \left(\int_0^\infty \dot{\phi}_{2r}^2 ds_{2r} + \int_0^{\hat{s}_3} \dot{\phi}_3^2 ds_3 \right). \tag{2.4}$$

The adhesion energy ΔE_γ is defined as:

$$\Delta E_\gamma = -\int_0^{\hat{s}_3} \gamma(s_3) ds_3, \tag{2.5}$$

where γ, also assumed constant, *i.e.* $\gamma(s_3) := \gamma$, is the linear adhesion energy.

Finally, the tension energy ΔE_σ reads:

$$\Delta E_\sigma = \sigma \Delta l, \tag{2.6}$$

where Δl is the change of the length of the membrane, defined as the difference between the deformed and the initial states and σ is the linear membrane tension. The membrane being initially flat, its initial length is equal to the projection of the deformed state over the r axis. Hence, Equation 2.6 can be written as:

$$\Delta E_\sigma = \sigma \left(\int_0^\infty (ds_{2r} - dr_{2r}) + \int_0^{\hat{s}_3} (ds_3 - dr_3) \right). \tag{2.7}$$

Equation 2.7 can be simplified by applying the geometrical relation between ds_i and dr_i, *i.e.* $dr_i = \cos(\phi_i) ds_i$, illustrated in Figure 2.4.

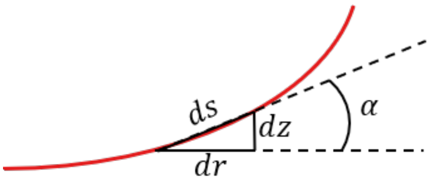

Figure 2.4: Relation between the infinitesimal lengths ds, dr, dz and α, which is the angle between ds and dr.

Hence:

$$\Delta E_\sigma = \sigma \left(\int_0^\infty [1 - \cos\phi_{2r}] ds_{2r} + \int_0^{\hat{s}_3} [1 - \cos\phi_3] ds_3 \right). \tag{2.8}$$

The variation of the potential energy ΔE of the system thus reads:

$$\begin{aligned} \Delta E(s_{2r}, \phi_{2r}, \dot{\phi}_{2r}, s_3, \phi_3, \dot{\phi}_3) = & \int_0^\infty \left(\frac{\kappa}{2} \dot{\phi}_{2r}^2 + \sigma[1 - \cos\phi_{2r}] \right) ds_{2r} \\ & + \int_0^{\hat{s}_3} \left(\frac{\kappa}{2} \dot{\phi}_3^2 + \sigma[1 - \cos\phi_3] - \gamma \right) ds_3. \end{aligned} \tag{2.9}$$

3 Determination of the equilibrium state

ΔE in Equation 2.9 represents the variation of the potential energy between a given state (wrapping degree f) and the initial state (wrapping degree $f \to 0$). In order to analytically determine the equilibrium state of the system, *i.e.* the wrapping degree f at which the system is at equilibrium, denoted by $\tilde{f}$, ΔE should be minimized. For this purpose, an analytical minimization is first performed using the Euler-Lagrange (EL) formalism, presented in Section 3.1. Numerical difficulties related to the solution of the obtained system, that will be presented in the following, did not enable us to determine $\tilde{f}$ using this approach. The strategies tested to overcome these issues are then fully described in Section 3.1.4. We consequently opted for a numerical determination of $\tilde{f}$ based on assumptions made in the literature, which consists in computing $\Delta E(f)$ for values of f ranging between 0 and 1 and to identify the local minima and hence determine $\tilde{f}$. Details on this approach are provided in Section 3.2.

3.1 Determination of the equilibrium state based on Euler Lagrange equations

The minimization of the potential energy $DEbar$ is equivalent to solving the corresponding EL equations. This analytical minimization leads to the equilibrium state equations that involve ϕ_i, r_i and z_i in each region $i \in \{2r, 3\}$. Solving these equations enables to determine the value of $\tilde{f}$ using Equation 2.1, as f is related to $\hat{s}_3$. First, the constraint and boundary conditions of the problem are introduced in Section 3.1.1. Then, the theory involving EL equations is fully described in Section 3.1.2 and used in Section 3.1.3. Last, the procedure to solve the subsequently obtained equations is presented in Section 3.1.4.

3.1.1 Constraints and boundary conditions

Constraints The minimization of ΔE is performed under constraints. These constraints are relative to the relation between r, z and ϕ, illustrated in Figure 2.4, as follows:

$$\dot{r}_i - \cos\phi_i = 0,\ i \in \{2r, 3\} \tag{2.10a}$$

$$\dot{z}_i - \sin\phi_i = 0,\ i \in \{2r, 3\} \tag{2.10b}$$

Boundary conditions The boundary conditions, partially presented in Section 2.2.1, are reminded in Table 2.1.

Table 2.1: Boundary conditions for ϕ_i, $\dot{\phi}_i$, r_i and z_i for $i \in \{2r, 3\}$. The empty cells correspond to unknown boundary conditions.

ϕ	$\dot{\phi}$	r	z
$\phi_{2r}(s_{2r} \to \infty) = 0$	$\dot{\phi}_{2r}(s_{2r} \to \infty) = 0$		
$\phi_3(0) = 0$		$r_3(0) = 0$	$z_3(0) = 0$

Furthermore, the geometrical continuity at the intersection of the regions $2r$ and 3 leads to:

$$r_{2r}(0) = r_3(\hat{s}_3); \tag{2.11a}$$

$$z_{2r}(0) = z_3(\hat{s}_3). \tag{2.11b}$$

The EL formalism, that will be applied using the boundary conditions presented in this section, will be introduced below.

3.1.2 Euler-Lagrange theoritical approach

Let J be a definite integral over the interval $[x_1, x_2]$ (where x_1 and x_2 can be unknown) as $J[y] = \int_{x_1}^{x_2} \mathcal{F}(x, y, \dot{y})dx$. J is a functional that takes the function y as an input and returns a scalar $J[y] \in \mathbb{R}$.

According to the EL approach, minimizing J under the equality constraint $\mathcal{G}$, defined as $\mathcal{G}(x, y, \dot{y}) = 0$, is equivalent to solving the unconstrained minimization of the functional $K = \int_{x_1}^{x_2} \mathcal{L}(x, y, \dot{y})dx$, in which $\mathcal{L}(x, y, \dot{y})$ is the so called Lagrangian, that reads:

$$\mathcal{L}(x, y, \dot{y}) = \mathcal{F}(x, y, \dot{y}) + \lambda(x)\mathcal{G}(x, y, \dot{y}), \tag{2.12}$$

wherein the function $\lambda(x)$ is called the Lagrange multiplier and is to be determined. Minimizing K is equivalent to solving the differential Equation 2.13 with the boundary conditions given in Equations 2.14 and 2.15.

$$\frac{\partial \mathcal{L}(x, y, \dot{y})}{\partial y} - \frac{\partial}{\partial \dot{x}} \frac{\partial \mathcal{L}(x, y, \dot{y})}{\partial \dot{y}} = 0, \tag{2.13}$$

$$\left. \frac{\partial \mathcal{L}(x, y, \dot{y})}{\partial \dot{y}} \delta y \right|_{x_1}^{x_2} = 0, \tag{2.14}$$

$$\left. \left(\mathcal{L}(x, y, \dot{y}) - \frac{\partial \mathcal{L}(x, y, \dot{y})}{\partial \dot{y}} \dot{y} \right) \delta x \right|_{x_1}^{x_2} = 0, \tag{2.15}$$

in which the delta operator $\delta X(\hat{x})$ of a dependent or independent variable X, evaluated at $\hat{x}$, yields zero if the value of $X(\hat{x})$ or that of $\hat{x}$ is known, and is strictly different from zero otherwise [113]. As a result, if the bounds of integration in J are known, the boundary condition in Equation 2.15 can be disregarded.

3.1.3 Application of the EL approach

Equation 2.9 can be written as follows:

$$\Delta E = \int_0^{\infty} \mathcal{F}_{2r}(s_{2r}, \phi_{2r}, \dot{\phi}_{2r})ds_{2r} + \int_0^{\hat{s}_3} \mathcal{F}_3(s_3, \phi_3, \dot{\phi}_3)ds_3, \tag{2.16}$$

where:

$$\mathcal{F}_{2r}(s_{2r}, \phi_{2r}, \dot{\phi}_{2r}) = \frac{\kappa}{2}\dot{\phi}_{2r}^2 + \sigma(1 - \cos\phi_{2r}), \tag{2.17}$$

$$\mathcal{F}_3(s_3, \phi_3, \dot{\phi}_3) = \frac{\kappa}{2}\dot{\phi}_3^2 + \sigma(1 - \cos\phi_3) - \gamma. \tag{2.18}$$

The integrands $\mathcal{F}_{2r}$ and $\mathcal{F}_3$ depend on different variables and functions, that are independent of each other. As such, ΔE is minimized when $\mathcal{F}_{2r}$ and $\mathcal{F}_3$ are individually minimized. Hence, two modified functionals K_{2r} and K_3, defined in Equation 2.19, are to be minimized to account for the constraints that have been introduced in Equations 2.10:

$$K_{2r} = \int_0^{\hat{s}_{2r}} \underbrace{\Big(\mathcal{F}_{2r}(s_{2r}, \phi_{2r}, \dot{\phi}_{2r}) + \lambda_{2r}(\dot{r}_{2r} - \cos\phi_{2r}) + \mu_{2r}(\dot{z}_{2r} - \sin\phi_{2r})\Big)}_{\mathcal{L}_{2r}(s_{2r}, \phi_{2r}, \dot{\phi}_{2r})} ds_{2r}, \tag{2.19a}$$

$$K_3 = \int_0^{\hat{s}_3} \underbrace{\Big(\mathcal{F}_3(s_3, \phi_3, \dot{\phi}_3) + \lambda_3(\dot{r}_3 - \cos\phi_3) + \mu_3(\dot{z}_3 - \sin\phi_3)\Big)}_{\mathcal{L}_3(s_3, \phi_3, \dot{\phi}_3)} ds_3, \tag{2.19b}$$

in which λ_i and $\mu_i, i \in \{2r, 3\}$ are Lagrange multiplier functions of s_i. The dependencies on the arclengths are dropped for the sake of clarity in the equations above and in the following. The application of the EL Equations 2.13 to the Lagrangians $\mathcal{L}_i(s_i, y_i, \dot{y}_i), i \in \{2r, 3\}$, where y_i and $\dot{y}_i$ are respectively defined as $y_i = (\phi_i, r_i, z_i)^\top$ and $\dot{y}_i = (\dot{\phi}_i, \dot{r}_i, \dot{z}_i)^\top$, yields:

$$\frac{\partial \mathcal{L}_i(s_i, y_i, \dot{y}_i)}{\partial \phi_i} - \frac{\partial}{\partial s_i}\frac{\partial \mathcal{L}_i(s_i, y_i, \dot{y}_i)}{\partial \dot{\phi}_i} = 0, \tag{2.20a}$$

$$\frac{\partial \mathcal{L}_i(s_i, y_i, \dot{y}_i)}{\partial r_i} - \frac{\partial}{\partial s_i}\frac{\partial \mathcal{L}_i(s_i, y_i, \dot{y}_i)}{\partial \dot{r}_i} = 0, \tag{2.20b}$$

$$\frac{\partial \mathcal{L}_i(s_i, y_i, \dot{y}_i)}{\partial z_i} - \frac{\partial}{\partial s_i}\frac{\partial \mathcal{L}_i(s_i, y_i, \dot{y}_i)}{\partial \dot{z}_i} = 0. \tag{2.20c}$$

First, the boundary conditions based on Equation 2.14 read:

$$\left.\frac{\partial \mathcal{L}_{2r}(s_{2r}, y_{2r}, \dot{y}_{2r})}{\partial \dot{\phi}_{2r}}\delta\phi_{2r}\right|_0^\infty = 0, \tag{2.21a}$$

$$\left.\frac{\partial \mathcal{L}_{2r}(s_{2r}, y_{2r}, \dot{y}_{2r})}{\partial \dot{r}_{2r}}\delta r_{2r}\right|_0^\infty = 0, \tag{2.21b}$$

$$\left.\frac{\partial \mathcal{L}_{2r}(s_{2r}, y_{2r}, \dot{y}_{2r})}{\partial \dot{z}_{2r}}\delta z_{2r}\right|_0^\infty = 0, \tag{2.21c}$$

and

$$\frac{\partial \mathcal{L}_3(s_3, y_3, \dot{y}_3)}{\partial \dot{\phi}_3}\delta\phi_3\bigg|_0^{\hat{s}_3} = 0, \tag{2.22a}$$

$$\frac{\partial \mathcal{L}_3(s_3, y_3, \dot{y}_3)}{\partial \dot{r}_3}\delta r_3\bigg|_0^{\hat{s}_3} = 0, \tag{2.22b}$$

$$\frac{\partial \mathcal{L}_3(s_3, y_3, \dot{y}_3)}{\partial \dot{z}_3}\delta z_3\bigg|_0^{\hat{s}_3} = 0. \tag{2.22c}$$

Second, the boundary conditions, introduced in Equation 2.15, are considered in the following expressions:

$$\left(\mathcal{L}_{2r}(s_{2r}, y_{2r}, \dot{y}_{2r}) - \frac{\partial \mathcal{L}_{2r}(s_{2r}, y_{2r}, \dot{y}_{2r})}{\partial \dot{\phi}_{2r}}\dot{\phi}_{2r}\right)\delta s_{2r}\bigg|_0^{\infty} = 0, \tag{2.23a}$$

$$\left(\mathcal{L}_{2r}(s_{2r}, y_{2r}, \dot{y}_{2r}) - \frac{\partial \mathcal{L}_{2r}(s_{2r}, y_{2r}, \dot{y}_{2r})}{\partial \dot{r}_{2r}}\dot{r}_{2r}\right)\delta s_{2r}\bigg|_0^{\infty} = 0, \tag{2.23b}$$

$$\left(\mathcal{L}_{2r}(s_{2r}, y_{2r}, \dot{y}_{2r}) - \frac{\partial \mathcal{L}_{2r}(s_{2r}, y_{2r}, \dot{y}_{2r})}{\partial \dot{z}_{2r}}\dot{z}_{2r}\right)\delta s_{2r}\bigg|_0^{\infty} = 0, \tag{2.23c}$$

and

$$\left(\mathcal{L}_3(s_3, y_3, \dot{y}_3) - \frac{\partial \mathcal{L}_3(s_3, y_3, \dot{y}_3)}{\partial \dot{\phi}_3}\dot{\phi}_3\right)\delta s_3\bigg|_0^{\hat{s}_3} = 0, \tag{2.24a}$$

$$\left(\mathcal{L}_3(s_3, y_3, \dot{y}_3) - \frac{\partial \mathcal{L}_3(s_3, y_3, \dot{y}_3)}{\partial \dot{r}_3}\dot{r}_3\right)\delta s_3\bigg|_0^{\hat{s}_3} = 0, \tag{2.24b}$$

$$\left(\mathcal{L}_3(s_3, y_3, \dot{y}_3) - \frac{\partial \mathcal{L}_3(s_3, y_3, \dot{y}_3)}{\partial \dot{z}_3}\dot{z}_3\right)\delta s_3\bigg|_0^{\hat{s}_3} = 0. \tag{2.24c}$$

According to Equations 2.9 and 2.16, the Lagrangians can be written as:

$$\mathcal{L}_{2r}(s_{2r}, y_{2r}, \dot{y}_{2r}) = \frac{\kappa}{2}\dot{\phi}_{2r}^2 + \sigma(1 - \cos\phi_{2r}) + \lambda_{2r}(\dot{r}_{2r} - \cos\phi_{2r}) + \mu_{2r}(\dot{z}_{2r} - \sin\phi_{2r}), \tag{2.25a}$$

$$\mathcal{L}_3(s_3, y_3, \dot{y}_3) = \frac{\kappa}{2}\dot{\phi}_3^2 + \sigma(1 - \cos\phi_3) + \lambda_3(\dot{r}_3 - \cos\phi_3) + \mu_3(\dot{z}_3 - \sin\phi_3) - \gamma. \tag{2.25b}$$

Inserting these Lagrangians into the EL equations leads to the following set of equations:

$$(\sigma + \lambda_{2r})\sin\phi_{2r} - \mu_{2r}\cos\phi_{2r} - \kappa\ddot{\phi}_{2r} = 0, \tag{2.26a}$$

$$\dot{\lambda}_{2r} = 0, \tag{2.26b}$$

$$\dot{\mu}_{2r} = 0, \tag{2.26c}$$

and

$$(\sigma + \lambda_3)\sin\phi_3 - \mu_3\cos\phi_3 - \kappa\ddot{\phi}_3 = 0, \tag{2.27a}$$

$$\dot{\lambda}_3 = 0, \tag{2.27b}$$

$$\dot{\mu}_3 = 0. \tag{2.27c}$$

Based on Equations 2.26 and 2.27, the Lagrange multipliers are constant functions.

Analogously, inserting the Lagrangians in the boundary conditions defined in Equations 2.21 and 2.22 leads to:

$$\kappa\dot{\phi}_{2r}\delta\phi_{2r}\Big|_0^\infty = 0, \tag{2.28a}$$

$$\lambda_{2r}\delta r_{2r}|_0^\infty = 0, \tag{2.28b}$$

$$\mu_{2r}\delta z_{2r}|_0^\infty = 0, \tag{2.28c}$$

and

$$\kappa\dot{\phi}_3\delta\phi_3\Big|_0^{\hat{s}_3} = 0, \tag{2.29a}$$

$$\lambda_3\delta r_3|_0^{\hat{s}_3} = 0, \tag{2.29b}$$

$$\mu_3\delta z_3|_0^{\hat{s}_3} = 0. \tag{2.29c}$$

The boundaries of the region $2r$ being known, the Equations 2.28 yield trivial equations. On the contrary, $\hat{s}_3$ is unknown, leading to the following relations:

$$\delta s_3(\hat{s}_3) \neq 0 \qquad \delta\phi_3(\hat{s}_3) \neq 0 \qquad \delta r_3(\hat{s}_3) \neq 0 \qquad \delta z_3(\hat{s}_3) \neq 0 \tag{2.30a}$$

Hence, the boundary conditions for the region 3 yield:

$$\kappa\dot{\phi}_3(\hat{s}_3)\delta\phi_3(\hat{s}_3) = 0 \Rightarrow \dot{\phi}_3(\hat{s}_3) = 0, \tag{2.31a}$$

$$\lambda_3\delta r_3(\hat{s}_3) = 0 \Rightarrow \lambda_3 = 0, \tag{2.31b}$$

$$\mu_3\delta z_3(\hat{s}_3) = 0 \Rightarrow \mu_3 = 0. \tag{2.31c}$$

Then, the Lagrangians in the boundary conditions presented in Equations 2.23 and 2.24 lead to the following equations:

$$\left[-\frac{\kappa}{2}\dot{\phi}_{2r}^2 + \sigma(1-\cos\phi_{2r}) + \lambda_{2r}(\dot{r}_{2r} - \cos\phi_{2r}) + \mu_{2r}(\dot{z}_{2r} - \sin\phi_{2r})\right]\delta s_{2r}\Big|_0^\infty = 0, \tag{2.32a}$$

$$\left[\frac{\kappa}{2}\dot{\phi}_{2r}^2 + \sigma(1-\cos\phi_{2r}) - \lambda_{2r}\cos\phi_{2r} + \mu_{2r}(\dot{z}_{2r} - \sin\phi_{2r})\right]\delta s_{2r}\Big|_0^\infty = 0, \tag{2.32b}$$

$$\left[\frac{\kappa}{2}\dot{\phi}_{2r}^2 + \sigma(1-\cos\phi_{2r}) + \lambda_{2r}(\dot{r}_{2r} - \cos\phi_{2r}) - \mu_{2r}\sin\phi_{2r}\right]\delta s_{2r}\Big|_0^\infty = 0, \tag{2.32c}$$

and

$$\left[-\frac{\kappa}{2}\dot{\phi}_3^2 + \sigma(1-\cos\phi_3) - \gamma + \lambda_3(\dot{r}_3 - \cos\phi_3) + \mu_3(\dot{z}_3 - \sin\phi_3)\right]\delta s_3\Big|_0^{\hat{s}_3} = 0, \tag{2.33a}$$

$$\left[\frac{\kappa}{2}\dot{\phi}_3^2 + \sigma(1-\cos\phi_3) - \gamma + \lambda_3(\dot{r}_3 - \cos\phi_3) - \mu_3\sin\phi_3\right]\delta s_3\Big|_0^{\hat{s}_3} = 0, \tag{2.33b}$$

$$\left[\frac{\kappa}{2}\dot{\phi}_3^2 + \sigma(1-\cos\phi_3) - \gamma - \lambda_3\cos\phi_3 + \mu_3(\dot{z}_3 - \sin\phi_3)\right]\delta s_3\Big|_0^{\hat{s}_3} = 0. \tag{2.33c}$$

Equations 2.32 for the region $2r$ lead to trivial equations, and Equations 2.33 for the region 3 yield:

$$\left[-\frac{\kappa}{2}\dot{\phi}_3^2 + \sigma(1-\cos\phi_3) - \gamma\right]\delta s_3(\hat{s}_3) = 0 \Rightarrow \sigma(1-\cos\phi_3(\hat{s}_3)) - \gamma = 0 \tag{2.34}$$

Finally, the EL shape equations, along with the boundary conditions, obtained with the previous system of equations, are summarized below:

$$\ddot{\phi}_{2r}(s_{2r}) = \frac{\sigma}{\kappa}\sin\phi_{2r}(s_{2r}), \tag{2.35}$$

$$\ddot{\phi}_3(s_3) = \frac{\sigma}{\kappa}\sin\phi_3(s_3), \tag{2.36}$$

$$\phi_{2r}(s_{2r}\to\infty) = 0, \tag{2.37}$$

$$\dot{\phi}_{2r}(s_{2r}\to\infty) = 0, \tag{2.38}$$

$$\phi_3(0) = 0, \tag{2.39}$$

$$\phi_3(\hat{s}_3) = \cos^{-1}\left(1 - \frac{\gamma}{\sigma}\right), \tag{2.40}$$

$$\dot{\phi}_3(\hat{s}_3) = 0. \tag{2.41}$$

Note that the boundary condition presented in Equation 2.40 is the well-known Young-Dupré equation [114, 115]. The value of $\hat{s}_3$ can be calculated by solving the Equation 2.36 and then determining the value of s_3 at which $\phi(s_3) = \phi(\hat{s}_3)$, so that it satisfies the boundary condition presented in Equation 2.40. The numerical procedure to solve the

Equation 2.36 is detailed in the following section.

3.1.4 Solution of the equilibrium equation

Equation 2.36 is a second order nonlinear differential equation for which there is no analytical solution [116]. However, it is possible to solve it numerically using finite differences approximation for instance [117].

These techniques require the knowledge of initial conditions $\phi_3(s_3 = 0)$ and $\phi_3(s_3 = \delta s_3)$ for a forward integration scheme or that of the final conditions $\phi_3(s_3 = \hat{s}_3)$ and $\phi_3(s_3 = \hat{s}_3 - \delta s_3)$ for a backward integration scheme [117], where δs_3 is an infinitesimal variation of s_3. Based on our own conditions, *i.e.* $\phi_3(s_3 = 0)$ and $\phi_3(s_3 = \hat{s}_3)$, a boundary value problem needs to be solved. The numerical integration of the second order Equation 2.36 is thus impossible in our case.

Still, it is possible to reduce the order of the Equation 2.36 by multiplying both sides with $\dot{\phi}_3$ and integrating. This gives:

$$\begin{aligned}
&\ddot{\phi}_3(s_3) = \frac{\sigma}{\kappa}\sin\phi_3(s_3) \Rightarrow \ddot{\phi}_3(s_3)\dot{\phi}_3(s_3) = \frac{\sigma}{\kappa}\sin\phi_3(s_3)\dot{\phi}_3(s_3)\\
\Rightarrow &\int_0^{\hat{s}_3} \ddot{\phi}_3(s_3)\dot{\phi}_3(s_3)ds_3 = \frac{\sigma}{\kappa}\int_0^{\hat{s}_3} \sin\phi_3(s_3)\dot{\phi}_3(s_3)ds_3\\
\Rightarrow &\dot{\phi}_3^2(s_3) = -\frac{2\sigma}{\kappa}\cos\phi_3(s_3) + C,
\end{aligned} \tag{2.42}$$

in which C is an integration constant, that is determined by evaluating the above expression at $s_3 = \hat{s}_3$. Recalling that $\dot{\phi}_3(\hat{s}_3) = 0$ and that $\phi_3(\hat{s}_3) = \cos^{-1}\left(1 - \frac{\gamma}{\sigma}\right)$ (Equation 2.40), one obtains:

$$C = \frac{2}{\kappa}(\sigma - \gamma). \tag{2.43}$$

Equation 2.36 thus becomes:

$$\dot{\phi}_3^2(s_3) = \frac{2}{\kappa}\Big(\sigma\left[1 - \cos\phi_3(s_3)\right] - \gamma\Big). \tag{2.44}$$

This first order ODE is still nonlinear and an analytical solution is hard to find. Still, it is possible to numerically determine the values of ϕ_3 by approximating $\dot{\phi}_3$ using a finite difference scheme [118]. Indeed, for a given function $y(x)$, discretized with a small step in x, Δx, a first order finite difference approximation (backward Euler) for $\dot{y}$ at $x = x_0$ reads:

$$\dot{y}(x_0) = \frac{y(x_0) - y(x_0 - \Delta x)}{\Delta x}. \tag{2.45}$$

This method requires the knowledge of $y(x_0 - \Delta x)$. In our case, $\phi_3(0)$ is known and equals zero, meaning that the finite differences method can be applied to numerically solve the Equation 2.44, as follows:

$$\begin{aligned}\left(\frac{\phi_3(s_3) - \phi_3(s_3 - \Delta s_3)}{\Delta s_3}\right)^2 &= \frac{2}{\kappa}\Big(\sigma\left[1 - \cos\phi_3(s_3)\right] - \gamma\Big) \\ \Rightarrow \phi_3(s_3) &= \pm \Delta s_3 \sqrt{\frac{2}{\kappa}\Big(\sigma\left[1 - \cos\phi_3(s_3)\right] - \gamma\Big)} + \phi_3(s_3 - \Delta s_3) \qquad (2.46)\end{aligned}$$

The convergence of the approximation of $\phi_3(s_3)$ depends on the discretization of the domain of definition of s_3 [118]. Using this method, it is possible to compute ϕ_3 for a range of values of s_3 and to subsequently determine $\hat{s}_3$ as being the arclength s_3 for which ϕ_3 equals $\cos^{-1}\left(1 - \frac{\gamma}{\sigma}\right)$. Finally, the value of $\tilde{f}$ is related to $\hat{s}_3$ and to the circumference p of the ellipse as $f = 2\hat{s}_3 p^{-1}$.

3.1.5 Conclusion on the EL equations based approach

The method to determine the equilibrium state of the system, presented in this section, enables to numerically determine the wrapping degree at equilibrium with a reasonable computational cost. Nonetheless, the analytical developments that have been introduced make the hypothesis that γ and σ remain constant during the wrapping of the NP. However, this hypothesis will be challenged in this thesis so that these mechanical parameters will further be modeled as functions of the wrapping degree, *i.e.* a function of $\hat{s}_3$, in Chapter 4. The aforementioned technique, used to determine the value of $\hat{s}_3$ based on the evolution of ϕ_3, does consequently not apply as $\phi_3(s_3)$ would therefore be a function of the unknown $\hat{s}_3$. Thus, a different approach, which consists in computing the variation of the total potential energy ΔE of the system, for a range of values of the wrapping degree, and subsequently infer the equilibrium state according to the evolution of ΔE with respect to f, is then preferred. More details on this approach are provided in the following.

3.2 Definition of the equilibrium state

In this section, the potential energy of the system, $\Delta E(f)$, is computed for a range of values of the wrapping degree f between 0 and 1. The approach used to compute ΔE is presented in Section 3.2.1. Observations of $\Delta E(f)$ are provided in Section 3.2.2. The hypotheses to define the equilibrium state of our system are subsequently introduced and applied in Section 3.2.3.

The model, presented in this section, applies to rigid elliptic NPs. For the same reasons as those presented in the previous section, the membrane is supposed elastic and the system is studied in two dimensions only.

3.2.1 Computation of the potential energy

The variation of the potential energy of the system is defined in Equation 2.9. In order to numerically evaluate ΔE, minor changes are applied to this equation. For instance, the value of Δl, the change in the length of the membrane, is computed as follows:

$$\Delta l = 2l_2 + l_3 - (r_{2r}(l_2) - r_{2l}(l_2)), \tag{2.47}$$

in which $r_i, i \in \{2r, 2l\}$ is the r-coordinate in region i. Hence, Equation 2.9 can be rewritten as:

$$\Delta E = \underbrace{\overbrace{\frac{\kappa}{2}\int_0^{l_2} \dot{\phi}_{2r}^2 ds_{2r}}^{\Delta E_{b_{2r}}} + \overbrace{\frac{\kappa}{2}\int_0^{l_2} \dot{\phi}_{2l}^2 ds_{2l}}^{\Delta E_{b_{2l}}} + \overbrace{\frac{\kappa}{2}\int_0^{l_3} \dot{\phi}_3^2 ds_3}^{\Delta E_{b_3}}}_{\Delta E_b} \underbrace{-\gamma l_3}_{\Delta E_\gamma} + \underbrace{\sigma(2l_2 + l_3 - r_{2r}(l_2) + r_{2l}(l_2))}_{\Delta E_\sigma}. \tag{2.48}$$

Note that this equation does not account for the symmetry and represents the variation of energy of the entire system, *i.e.* the one initially presented in Figure 2.2. Furthermore, we have $\phi_{2l} = 2\pi - \phi_{2r}$. As such, Equation 2.48 becomes:

$$\Delta E = \underbrace{\overbrace{\kappa\int_0^{l_2} \dot{\phi}_{2r}^2 ds_{2r}}^{\Delta E_{b_2}} + \overbrace{\frac{\kappa}{2}\int_0^{l_3} \dot{\phi}_3^2 ds_3}^{\Delta E_{b_3}}}_{\Delta E_b} \underbrace{-\gamma l_3}_{\Delta E_\gamma} + \underbrace{\sigma(2l_2 + l_3 - r_{2r}(l_2) + r_{2l}(l_2))}_{\Delta E_\sigma}. \tag{2.49}$$

Then, in order to compute the bending energy of the free part of the membrane ΔE_{b_2}, it is necessary to know the evolution of $\phi_{2r}(s_2)$. As such, the order of the shape equation $\ddot{\phi}_{2r}(s_{2r}) = \frac{\sigma}{\kappa}\sin\phi_{2r}(s_{2r})$ is reduced, similar to what we did for ϕ_3. Using the boundary conditions $\dot{\phi}_{2r}(s_{2r} \to \infty) = 0$ and $\phi_{2r}(s_{2r} \to \infty) = 0$ yields the first order shape equation:

$$\dot{\phi}_{2r}^2(s_{2r}) = \frac{2\sigma}{\kappa}\Big(1 - \cos\phi_{2r}(s_{2r})\Big). \tag{2.50}$$

This equation was solved by Muller *et al.* [119], yielding:

$$\phi_{2r}(s_{2r}) = 4\arctan\left[t\exp\left(-s_{2r}\frac{\sigma}{\kappa}\right)\right], \tag{2.51}$$

where $t = \tan\left(\frac{\phi_{2r}(0)}{4}\right)$. This equation is simplified introducing the adimensional variable $\overline{\sigma} = \sigma\frac{2a^2}{\kappa}$, where a is the relative radius of the ellipse, defined as the ratio between the circumference of the NP p and 2π. Hence, Equation 2.51 becomes:

$$\phi_{2r}(s_{2r}) = 4\arctan\left[t\exp\left(-\frac{s_{2r}}{a}\sqrt{\frac{\bar{\sigma}}{2}}\right)\right]. \tag{2.52}$$

The spatial coordinates (r, z) of the region $2r$ are then evaluated using the relations $dr_i = \cos\phi_i(s_i)ds_i$ and $dz_i = \sin\phi_i(s_i)ds_i, i \in \{2r, 2l\}$, as follows [105]:

$$r_{2r}(s_{2r}) = r_{2r}(0) + s_{2r} - \sqrt{\frac{\bar{\sigma}}{2}}\frac{1-\cos\left(\phi_{2r}(0)\right)}{\coth\left(\sqrt{\frac{\bar{\sigma}}{2}}s_{2r}\right) + \cos\left(\frac{\phi_{2r}(0)}{2}\right)}, \tag{2.53a}$$

$$z_{2r}(s_{2r}) = z_{2r}(0) + \sqrt{\frac{8}{\bar{\sigma}}}\sin\left(\frac{\phi_{2r}(0)}{2}\right)\left[1 - \frac{\operatorname{csch}\left(\sqrt{\frac{\bar{\sigma}}{2}}s_2\right)}{\coth\left(\sqrt{\frac{\bar{\sigma}}{2}}s_2\right) + \cos\left(\frac{\phi_{2r}(0)}{2}\right)}\right]. \tag{2.53b}$$

Based on the symmetry, the coordinates relative to the region $2l$ can be calculated as $r_{2l}(s_{2l}) = r_{2r}(s_{2l}) - r_{2r}(s_{2l})$ and $z_{2l}(s_{2l}) = z_{2r}(s_{2l})$. In the equations that have been introduced above, $\phi_2(0)$ is the value of ϕ_2 at the intersection between the regions 3 and $2r$, where the points $(s_{2r} = 0)$ and $(s_3 = l_3)$ are coincident. Consequently, $\phi_{2r}(s_2 = 0)$ can be calculated from $\phi_3(s_3 = l_3)$, which is well known from the definition of the ellipse (as well as ϕ_1, r_1, z_1, r_3 and z_3). Then, ΔE_{b_2} can be readily computed.

Finally, in order to ease further comparisons, the adimensional energy variation $\overline{\Delta E}$ is introduced as $\overline{\Delta E} = \Delta E\frac{2a}{\kappa_2}$. Thus, Equation 2.49 is reformulated in terms of adimensional variables $\bar{\gamma}$, defined as $\bar{\gamma} = \gamma\frac{2a^2}{\kappa_2}$ and $\bar{\sigma}$:

$$\overline{\Delta E} = \underbrace{\overbrace{\frac{a}{4}\int_0^{l_3}\dot{\phi}_3^2 ds_3}^{\overline{\Delta E}_{b_3}} + \overbrace{\frac{a}{2}\int_0^{l_2}\dot{\phi}_{2r}^2 ds_{2r}}^{\overline{\Delta E}_{b_2}}}_{\overline{\Delta E}_b} \underbrace{-\frac{1}{4a}\bar{\gamma}l_3}_{\overline{\Delta E}_{\bar{\gamma}}} + \underbrace{\frac{1}{4a}\bar{\sigma}\left(2l_2 + l_3 - r_{2r}(l_2) + r_{2l}(l_2)\right)}_{\overline{\Delta E}_{\bar{\sigma}}}. \tag{2.54}$$

The adimensional bending energy of the free part of the membrane $\overline{\Delta E}_{b_2}$ can be calculated by integrating $\dot{\phi}_{2r}^2$ over s_{2r}, leading to:

$$\overline{\Delta E}_{b_2} = -\sqrt{2\overline{\sigma}}t^2\left(\frac{1}{t^2 + \exp\sqrt{2\overline{\sigma}}\frac{l_2}{a}} - \frac{1}{t^2+1}\right). \tag{2.55}$$

A convergence study was conducted on $\phi_{2r}(s_{2r})$ to verify that setting $l_2 = 20a$ satisfies the hypothesis of membrane flatness at both extremities (see [105] for more details). Integrating $\dot{\phi}_3^2$ yields the bending energy of the region 3, $\overline{\Delta E}_{b_3}$. This integration is performed using the Simpson integration rule implemented in the Scipy library of Python. Furthermore, the discretization of the region 3 was determined after a convergence study in order to limit the computation time, while keeping accurate results. The result of this study led to a discretization with 300 points to describe the entire circular NP (regions 1 and 3) and consequently $300p(2\pi a_r)^{-1}$ points for describing an elliptic NP, where a_r is the semi-minor axis of the NP. Like its circumference, the number of points to discretize the region 3 is proportional to the wrapping degree. As such, $300f$ points are used.

The model presented in this section involves parameters whose values are set based on experimental results from the literature: $\kappa_2 \approx 10^{-18}$ N.m, $\gamma \approx 10^{-3}$ N.m^{-1} and $\sigma \approx 10^{-5}$ N.m^{-1} [30, 59, 104, 110, 120]. The units commonly used for these variables are k$_\mathrm{B}$T or erg for κ_2, k$_\mathrm{B}$T.nm^{-2} or erg.cm^{-2} for γ and dyne.cm^{-1} for σ [30, 110, 121] but it was chosen to convert them to the SI units to simplify the understanding by an unfamiliar audience.

3.2.2 Observation of the evolution of the energy of the system

An example of the contributions of $\overline{\Delta E}_b$, $\overline{\Delta E}_{\overline{\gamma}}$ and $\overline{\Delta E}_{\overline{\sigma}}$ on the total energy variation $\overline{\Delta E}$ for a circular NP is presented in Figure 2.5. With the particular set of parameters used to generate this figure, it appears that the energy due to the NP-membrane adhesion contributes more to the total potential energy than the energies of the bending and tension of the membrane, whose contributions are close. Nonetheless, it is worth noting that the membrane tension $\overline{\sigma}$ contributes to both $\overline{\Delta E}_{\overline{\sigma}}$ and $\overline{\Delta E}_{b_2}$. The influence of $\overline{\gamma}$ and $\overline{\sigma}$ on the shape of the membrane are illustrated in Figure 2.6 for a circular NP.

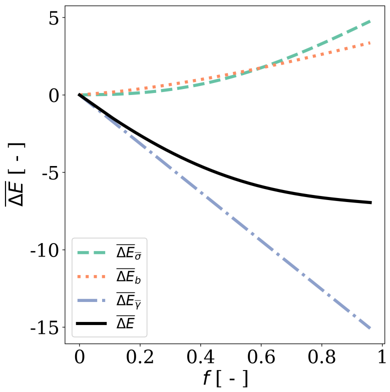

Figure 2.5: Contribution of the bending $\overline{\Delta E}_b$, tension $\overline{\Delta E}_{\overline{\sigma}}$ and adhesion $\overline{\Delta E}_{\overline{\gamma}}$ on the total energy $\overline{\Delta E}$, for a circular NP with $\overline{\gamma} = 10$ and $\overline{\sigma} = 2$.

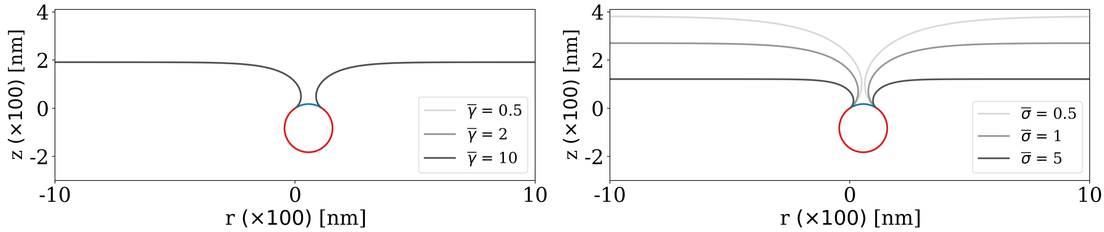

(a) (b)

Figure 2.6: Effect of (a) adhesion $\bar{\gamma}$ with $\bar{\sigma} = 2$ and (b) membrane tension $\bar{\sigma}$ with $\bar{\gamma} = 10$ on the wrapping for $f = 0.8$. The r axis is truncated to $[-10; 10]$. For a same wrapping degree f, the NP is fully wrapped by the cell only for $\bar{\sigma} = 0.5$.

This figure shows that $\overline{\gamma}$ does not influence the shape of the membrane, contrary to $\overline{\sigma}$. Indeed, for a same wrapping degree f, a variation in $\overline{\sigma}$ leads to different shapes for the membrane. Thus, a membrane with a low tension $\overline{\sigma}$ is more likely to close on top of the NP and hence to trap the NP in the cell, consequently leading to the internalization of the NP by the cell. This matches the analytical formulation of ψ_{2r} introduced previously, which is independent of γ. Still, as illustrated in Figure 2.7, the adhesion $\overline{\gamma}$ influences the evolution of $\overline{\Delta E}(f)$ and hence the value of the wrapping degree at equilibrium $\tilde{f}$. The membrane tension $\overline{\sigma}$ also influences $\tilde{f}$. In this particular case, a large value of $\overline{\gamma}$ combined with a small value of $\overline{\sigma}$ yields values of $\tilde{f}$ close to 1, *i.e.* full wrapping. Nonetheless, as illustrated in Figure 2.6, the value of $\tilde{f}$ does not necessarily determine the wrapping state. More details on the definition of the full wrapping are provided in Section 4. The aforementioned observations match the results from similar models published in the literature [40, 99].

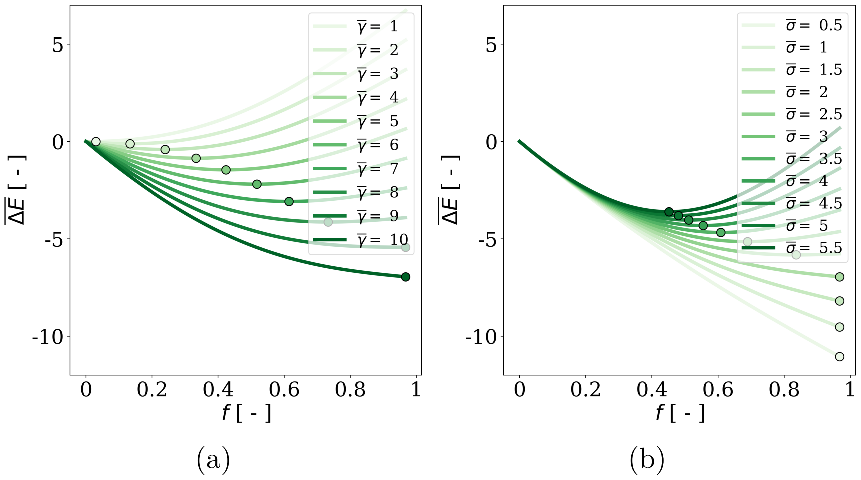

Figure 2.7: Influence of (a) $\overline{\gamma}$ with $\overline{\sigma} = 2$ and (b) $\overline{\sigma}$ with $\overline{\gamma} = 10$ on $\overline{\Delta E}(f)$ for a circular NP. The markers correspond to the equilibrium positions ($f = \tilde{f}$).

3.2.3 Practical computation of the equilibrium state

The equilibrium state of a system is attained when its potential energy reaches a minimum value. For circular NPs, $\overline{\Delta E}(f)$ only presents a single minimum, meaning that the equilibrium is reached for this position. On the contrary, in the case of elliptic NPs, $\overline{\Delta E}(f)$ may present several local minima. Examples of evolutions of $\overline{\Delta E}$ with respect to f are provided in Chapter 3. In this case, it is necessary to provide a clear definition of the equilibrium. According to Deserno *et al.* [97, 98], there is no mechanism that could contribute to overcome the energy barriers following a local minimum, except the energy due to thermal fluctuations, which are too weak to overcome the energy barriers we meet in this study. Consequently, the equilibrium is defined as the first local minimum, since the system is not able to leave this state.

To evaluate the location of the local minima, $\overline{\Delta E}$ is computed for a range of values of f and the Scipy built-in function *argrelmin* is used to get the local minima of $\overline{\Delta E}$. The first local minimum is subsequently extracted. The discretization of f was determined after a convergence study on the value of the minimum provided by the *argrelmin* function, yielding a discretization step of 0.003125, which leads to convergence regardless of the range of aspect ratios of the NP that have been investigated in this thesis. Note that $\overline{\Delta E}$ is calculated for $f \in [0.03, 0.97]$, in order to avoid the limit cases $f = 0$ and $f = 1$ since the wrapping is not initiated for $f = 0$ and the case $f = 1$ is never reached in practice as it requires an extreme bending of the membrane.

4 Accounting for the mechanical properties

The observations of $\overline{\Delta E}$, provided in Section 3.2.2, enable to find $\tilde{f}$ for a given set of mechanical properties $(\overline{\sigma}, \overline{\gamma})$. However, the challenge of the present work is to set a range of values for the mechanical properties of such a system due to the lack of experimental data [122]. Furthermore, these parameters should have wide ranges of values in practice, due to the variety of cell types and the diversity of their membrane composition [25, 57]. Section 4.1 introduces the strategy, that we suggest, to cope with the lack of experimental data, while it is detailed and applied in Sections 4.2 and 4.3.

4.1 Investigations using parametric studies

In order to overcome the lack of experimental data, $\tilde{f}$ is calculated for a range of values of mechanical parameters. Trends are subsequently observed using the phase diagrams, which are presented in Section 4.2. Based on the literature [40, 43, 99, 105, 110, 123] and considering a relative radius of the NP $a = 100$ nm, the ranges of mechanical parameters considered are $\bar{\sigma} \in [0.5, 5.5]$ and $\bar{\gamma} \in [1, 8]$. For each pair of $\overline{\sigma}$ and $\overline{\gamma}$, the final state of the system is determined (configuration at equilibrium). The possible states are presented in Section 4.2.

4.2 Wrapping phases and phase diagrams

The use of phases to differentiate the final state of the system is introduced in [98, 124]. Three phases, with their corresponding final configuration, are schematically depicted in Figure 2.8.

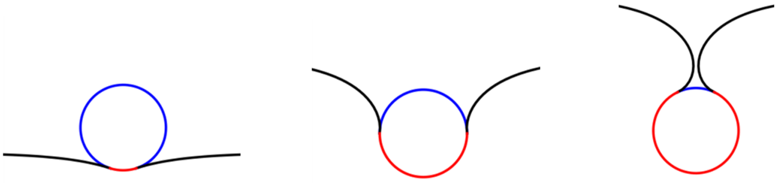

Figure 2.8: Illustration of the three wrapping phases: (left) no wrapping (phase 1), (middle) partial wrapping (phase 2) and (right) full wrapping (phase 3).

The first phase (no wrapping) gathers the configurations in which the endocytosis aborts soon after the NP touches the cell. As such, it corresponds to equilibrium wrapping degree close to 0. For numerical reasons and as introduced earlier, our model always initiate when the NP is in contact with the membrane and therefore the wrapping degree f is slightly higher than zero. For this reason, an arbitrary small value of $\tilde{f}$, equal to 0.2, is set as the threshold below which the system is deemed to end in phase 1. The phase 3 is defined as the scenarios where a full wrapping happens, which we define as the cases where the two sides of the free membrane cross, trapping the NP, *i.e.* $\max r_{2l}(s_{2l}) \geq \min r_{2r}(s_{2r})$. The phase 2 is composed of all the intermediate configurations, which lead to partial wrapping.

To browse the ranges of mechanical parameters defined in Section 4.1, a phase diagram is plotted. For this purpose, the final phase is computed for each combination of $\overline{\sigma}$ and $\overline{\gamma}$ and the results are displayed in a plot whose axes are $\overline{\gamma}$ and $\overline{\sigma}$, similar to the work presented in [40, 99] for instance. The phase diagram, obtained for a circular NP, is presented in Figure 2.9. The trends, observed in this phase diagram, clearly corroborate the preliminary observations made in Section 3.2.2. Indeed, only large values of $\overline{\gamma}$ and small values of $\overline{\sigma}$ lead to a full wrapping of the NP. The phase diagram, presented in Figure 2.9, which was obtained with our model, matches the one provided in [40], allowing us to validate the code we have implemented.

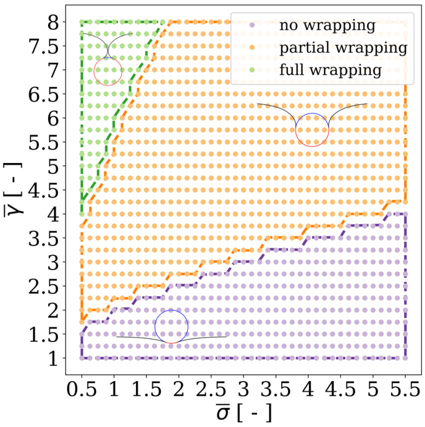

Figure 2.9: Phase diagram for a circular NP.

4.3 Phase proportion

Phase diagrams enable to observe the influence of the mechanical properties of the system on the final wrapping state of a NP. Nonetheless, to investigate the influence of the shape of the NP, *i.e.* to understand whether the effect of the mechanical properties on the NP varies depending on its aspect ratio, it is necessary to compute a phase diagram for each NP. To compare these diagrams, the proportion of each phase, denoted by ψ_i for $i \in \{1, 2, 3\}$, is computed. The value of ψ_i is calculated as the number of points in phase i divided by the total number of points. Thus, the phase proportions are compared for different shapes of NP. An example of a phase proportion plot is given in Figure 3.10 of Chapter 3. The number of points of the phase diagram was determined after a convergence study on the phase proportion and it was concluded that 280 points, being 14 and 20 to discretize $\overline{\sigma}$ and $\overline{\gamma}$ respectively, are sufficient to reach the convergence of the phase proportions[1]. It takes around 5 minutes, using an Intel core i7-9850H processor with 32 Gb of RAM, for the model to generate a phase diagram and thus a phase proportion for a circular NP. Applications of these tools are presented in the next chapters.

5 Discussion

The model presented in this chapter is based on several hypotheses that are worth to be discussed, such as:

- **A rigid NP** is investigated in this model in order to ease the approach compared to a deformable NP, since solely the deformation of the membrane is considered. As explained in the hypotheses section, it appears to be a reasonable hypothesis for many of the existing NPs. However, NPs whose bending rigidity is of the same order of magnitude as the membrane exist as well [88]. Moreover, studies have demonstrated that the rigidity of the NP is a prominent parameter of endocytosis [40, 105]. Consequently, additional investigations should be conducted by accounting for the rigidity of the NP, to provide results adapted to a larger range of NPs.
- **This model does not apply to phagocytes**. Indeed, the latter have a physiology that is specific to engulf objects from the extra-cellular medium [16]. As such, several assumptions, *e.g.* the hypothesis of an elastic membrane that passively uptakes the extracellular objects that touch it, may not hold for this kind of cells whose function is to actively internalize them as part of the immune system.
- **The membrane is considered homogeneous** since the investigated NPs are about 100 times smaller than the cell and the system is set at the scale of the NP (around 100 nm). However, the membrane contains trans-membrane proteins, which can reach 16 nm [125] and could consequently play a role in this process by directly

---

[1] Figure 2.9 contains more points for the quality of the illustration.

interacting with the NP. Moreover, the membrane is highly heterogeneous and is composed of various constituents, mainly carbohydrates, proteins and lipids [57, 58]. The outer part of the membrane is also covered by a sugar layer called glycocalix (see Chapter 1), which alters the interaction with the extra-cellular medium by reducing the adhesion. The presence of glycocalix is usually more significant in cancer cells than in healthy ones [126], meaning that it is a parameter to take into account to differentiate the adhesion of such cells. In addition, the composition of the cell membrane may change alongside its circumference. For instance, the presence of lipid rafts (regions with higher concentrations in cholesterol) locally increases the bending rigidity κ of the membrane [25, 127]. These observations about the structure of the cell membrane challenge the modeling of the region 3 as homogeneous. However, since the study is performed for a range of $\bar{\gamma}$ and $\bar{\sigma}$, the results remain valid as they account for the variability of the properties of the membrane. Last, due to the heterogeneity of the latter, the implementation of mechanical properties that depend on the arclength may provide more accurate predictions. A recent article [128] presents a model with a membrane whose bending rigidity varies along its arclength. Still, this variation is actually not well characterized and requires the implementation of stochastic behavior laws.

- **The model investigates the entry of a NP in a cell**. However, NPs are used for many other medical purposes. Indeed, they can be used as markers for radiotherapy or even for imaging to diagnose cancers [129, 130]. They may also be used to deliver drugs as in chemotherapy for instance [131]. For the NPs to achieve their goal, they first need to reach the target cell. However, depending on their physico-chemical properties, these NPs may be cleared by defense mechanisms, *e.g.* immunity cells, the liver or the kidneys [132]. Supposing that the NPs avoid these clearance processes, they still have to be internalized by the target cell. However, the cellular wrapping of the NP is actually the very first step of endocytosis [23]. Indeed, it is not sure that the NP will not be rejected (via exocytosis) before reaching its target inside the cell [25]. Finally, the NP being a foreign object in the body, it remains essential to consider the potential hazards and toxicity it could cause [133].
- **The model considers constant mechanical properties during endocytosis**, while they could actually vary with respect to f, as explained in [32, 106, 112, 134–140]. Indeed, the cell tends to adapt to the phenomenon by increasing the amount

of interactions at the contact region (and consequently increasing the adhesion) and the presence of membrane reservoirs may contribute in helping the membrane deformation (consequently reducing the tension). Accounting for the mechanical adaptation of the membrane is the subject of Chapter 4.

6 Conclusions of Chapter 2

This chapter presented and justified the modeling approach selected in this study. In order to remain on a purely mechanical-based approach, the system is modeled at the scale of the NP and depends on the adhesion between the NP and the membrane and on the membrane tension. The analytical approach was presented and its usefulness will be challenged in Chapter 4 after the introduction of additional parameters to the model. As such, the method to determine the equilibrium state of the system consists in defining it as the first local minimum of energy as the energy barrier cannot be overcome. The implementation of this method is detailed and several results are presented:

- **A preliminary observation of the variation of the total potential energy** illustrates some of the system behaviors and enables to conclude from qualitative observations that a large adhesion combined with a small tension yield wrapping degree close to 1 at equilibrium. Still, the adhesion does not influence the shape of the free membrane, while a small membrane tension makes the membrane more likely to trap the NP.

- **Phase diagrams** can be used to draw quantitative conclusions on the influence of the mechanical properties of the NP on its faculty to be engulfed by the cell.

- **Phase proportions** are presented as a mean of condensing the information into a single scalar, which will make easier comparing the effect of the mechanical properties of the systems among NPs of different shapes.

- **Comparison of the model with the literature** shows that our implementation matches the results from previous studies. Indeed, the evolution of the total potential energy, the shape of the membrane, as well as the phase diagrams obtained for a circular NP, are comparable with the results from the literature for similar configurations, allowing us to validate our numerical tool. This enables to further enrich the model with more realistic characteristics such as elliptical NPs (in Chapter 3) or mechanical properties that evolve as a function of the wrapping degree (in Chapter 4).

Chapter 3

INFLUENCE OF THE GEOMETRICAL AND MECHANICAL PARAMETERS ON THE ENDOCYTOSIS OF AN ELLIPTIC NANOPARTICLE

1 Introduction

This chapter investigates the influence of the aspect ratio of the NP and of the mechanical properties of the NP-membrane interface on the wrapping of the NP by the membrane. This is achieved by performing sensitivity analyses on the model introduced in Chapter 2. Sensitivity analyses are methods that consist in determining the influence of inputs of a system on the variability of its output(s) using a large amount of data. However, due to computational costs, it is often necessary to use surrogate models in order to faster estimate these outputs. This chapter is therefore organized as follows: an overview of the sensitivity analysis techniques is provided in Section 2, then some of the most commonly used surrogate models are introduced in Section 3. The process to perform sensitivity analysis on a surrogate model of the cellular uptake of a NP is presented in details in Section 4, where the influence of the aspect ratio $\overline{r}$ of the NP on the wrapping degree at equilibrium $\tilde{f}$ is compared to that of the membrane tension $\overline{\sigma}$ and the NP-membrane adhesion $\overline{\gamma}$. The content of the present chapter is a fully detailed version of the article that was published in the International Journal for Numerical Methods in Biomedical Engineering [141].

2 Sensitivity analysis

2.1 Overview

Sensitivity analysis is a field of computational mathematics that aims at determining the model input parameters that influence the most a quantity of interest (QoI) [142, 143]. It can be performed to achieve many objectives, among which the simplification of the model or to guide the research efforts as their results can be used to optimize the resources necessary for experimental investigations, for instance. Applications of sensitivity analyses particularly in biomechanics can be found in [144, 145].

Three distinct types of sensitivity analysis exist: the screening methods, the local sensitivity analysis and the variance-decomposition-based methods [146, 147]. Screening and variance-decomposition-based methods are branches of global sensitivity analysis [142]. Screening methods consists in screening out unimportant input parameters with a limited number of calls to the model. The local sensitivity analysis techniques consist in evaluating the influence of small variations of an input around a given point on the output of the model. This method provides quick results with few data points, but does not work well in case of a nonlinear or nonmonotonic model, for instance. Variance-decomposition-based sensitivity analyses study the influence of the variability of an input on the output, by investigating the contribution of each input on the variance of the output, by sweeping the entire domains of definition of the input parameters. Due to the nonlinearities and likely nonmonotonicities of the response of the model, global sensitivity analyses have been preferred over local techniques in this work. The principles of global sensitivity analysis will be introduced in Section 2.2, where variance-decomposition-based techniques will be detailed. For an in depth review of these methods, refer to [142, 148, 149] and references therein.

2.2 Global sensitivity analysis

2.2.1 Overview

Contrary to the local approaches, global sensitivity analysis aims at investigating the sensitivity of the model over its entire domain of definition [150]. The amount of data necessary to perform these analyses is thus substantial and depends on the dimension of the model M, *i.e.* the number of input parameters. Thus, screening methods are usually performed as a first step in order to classify the input parameters as important or unimportant. This enables to set constant values for less important variables so that the dimensionality of the model is reduced, which is usually needed when several variables are present. Figure 3.1 illustrates the variety of the screening and variance-decomposition methods according to the complexity and regularity of the model. This graph also provides an order of magnitude of the number of model evaluations required for each method, which is proportional to the dimension of the problem [142]. This further justifies the application of a preliminary screening method before having recourse to the variance-decomposition-based analyses, as it enables to reduce the dimension of the problem with only $10 \times M$ evaluations of the model. However, the dimension of our problem being already small (three input parameters, namely $\overline{\sigma}$, $\overline{\gamma}$ and $\overline{r}$), it is not crucial to perform screening method to further reduce the dimension. Thus, only the variance-based methods will be used in this work. In complement to Figure 3.1, the reader can follow the decision tree provided by Rocquigny *et al.* [151], for further heuristics on when to use each method.

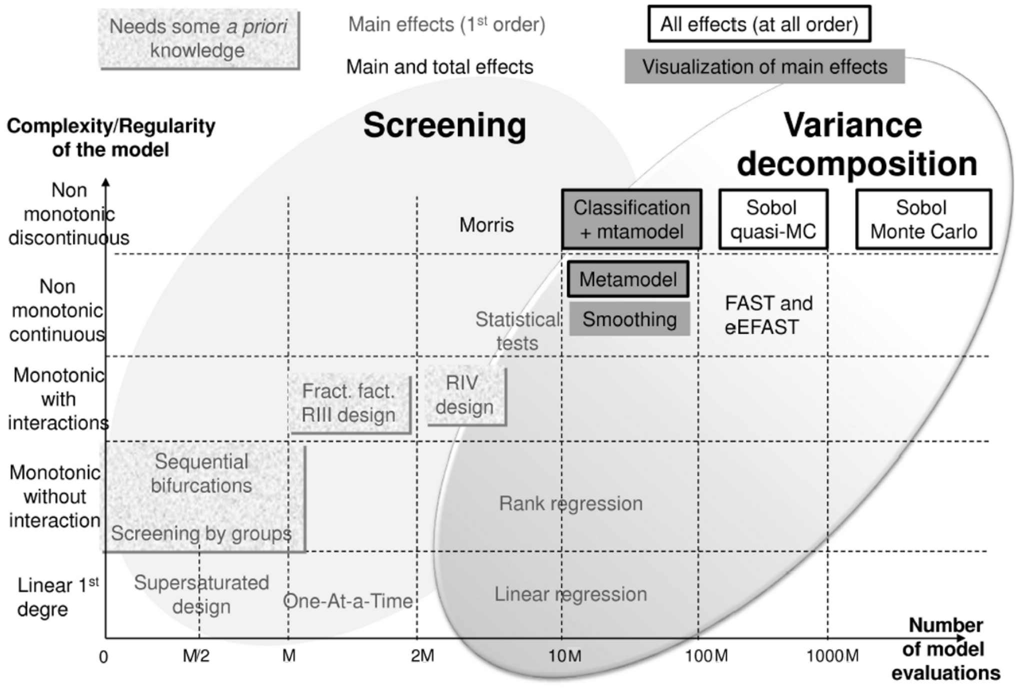

Figure 3.1: Graphical synthesis of global sensitivity analysis methods, adapted from [142]. M is the number of input parameters of the model.

2.2.2 Variance-decomposition-based sensitivity analysis

According to Figure 3.1, several variance-decomposition-based sensitivity analysis techniques can be used in the case of nonmonotonic models. Still, only two of them provide information on the effects at all orders, *i.e.* related to the effect of a variable only (first order) along with its interactions with one (second order) or all the other parameters (total). These are the Sobol indices, estimated using either Monte Carlo or quasi Monte Carlo sampling techniques. Both of which are presented in details in Section 3.4. The estimation of the Sobol indices is also referred to as ANOVA (ANalysis Of VAriance) in the literature. Sobol indices apply well to studies with independent parameters solely. For dependent ones, other approaches can be used to evaluate the sensitivity of the model, such as the ANalysis of COVAriance (ANCOVA) [152]. Since the variables involved in our work are independent (as fully introduced in Chapter 2), only the Sobol indices will be presented in this manuscript.

General definition of the Sobol indices The Sobol sensitivity indices [153] are used to estimate the contribution of an input random variable on the variance of the output. The first order and total Sobol indices for a variable X_i are defined in Equations 3.1, in which $X_i, i \in \{1, 2, ..., M\}$ is the set of M input variables and Y is an output QoI. The first order index S_i estimates the part of the variance of Y due to X_i only. Moreover, the total index ST_i also accounts for the effect of the interactions with other variables $X_{j, j \neq i}$.

$$S_i = \frac{\mathrm{Var}[\mathbb{E}[Y|X_i]]}{\mathrm{Var}[Y]}, \tag{3.1a}$$

$$ST_i = 1 - \frac{\mathrm{Var}[\mathbb{E}[Y|X_1, ..., X_{i-1}, X_{i+1}, ...X_M]]}{\mathrm{Var}[Y]}, \tag{3.1b}$$

in which $\mathbb{E}$ and Var respectively denote the expectation and the variance of a random variable. It is also possible to calculate the second order Sobol indices, which estimate the contribution of the interaction between two input variables X_i and X_j on the variance of Y. This index is denoted as $S_{i,j}$ and reads:

$$S_{i,j} = \frac{\mathrm{Var}[\mathbb{E}[Y|X_i, X_j] - \mathbb{E}[Y|X_i] - \mathbb{E}[Y|X_j]]}{\mathrm{Var}[Y]}. \tag{3.2}$$

Practical computation of the Sobol indices Several approaches exist to numerically compute the Sobol indices, *i.e.* to estimate different terms involving the evaluation of the variance [152]. For instance, Saltelli [154], Mauntz-Kucherenko [155], Martinez [156] and Jansen [157] have developed techniques to estimate these terms. Those are implemented in tools such as the open-source Python library OpenTURNS [158], UQlab [152] and SALib [159, 160]. In depth explanations on the existing techniques to compute the Sobol indices are presented in Appendix A. In this thesis, the Sobol indices are computed using OpenTURNS, developed for Python, which is the programing language used to implement our numerical models. In addition, OpenTURNS has an active community and a detailed documentation for different features of the library. Furthermore, it is also possible to determine the Sobol indices using the Polynomial Chaos Expansion (PCE) metamodel [161], as presented in Section 3.2.2.

Convergence of the Sobol indices The computation of the Sobol indices depends on the number of samples that are used to estimate the variance. It is henceforth necessary to ensure that enough samples are used. In this specific case, where the QoI (*i.e.* the Sobol indices) can be very close to zero (case of a non influential parameter), the usual convergence techniques based on the study of an absolute normalized gradient of the QoI cannot be applied. The latter, for a function y depending on a variable x, is defined as $|y(x+1) - y(x)|/|y(x)|$. Alternative criteria for the convergence of sensitivity indices have therefore been proposed in the literature, such as that of Vanrolleghem *et. al* [162] which consists in the evaluation of the variability of the sum of the sensitivity indices generated with two samples of different size. An inconvenience of this criterion is that the convergence of each sensitivity index is not investigated separately. In addition, Herman *et al.* [163] considered a threshold for the percentage of the sensitivity index of the most influential input parameter, which does not investigate the convergence of each indices either. Then, Sarrazin *et al.* [164] proposed a convergence study based on the range of the 95 % confidence intervals (CIs) of the indices, and concluded that the convergence is reached when the latter is smaller than 0.05. This criterion needs to be fulfilled for all the indices. In this work, we will therefore use the latter criterion to study the convergence of the Sobol indices.

3 Surrogate modeling

3.1 Overview

Surrogate models, or metamodels, can be regarded as mathematical approximations of a model. They are built using samples of input data, with their corresponding outputs and can be used to evaluate the model for any input value within its domain of definition with a near-to-zero computation time [165]. Thus, metamodels enable to perform sensitivity analyses – which often require large input datasets – thanks to affordable computation times [166]. Nonetheless, the estimations made by these surrogates leads to errors that need to be considered. This point will be discussed later in this chapter. Most of the surrogate models are distinguished based on the functions they use to approximate an output QoI: *e.g.* polynomial or Gaussian. An alternative to these models is for instance neural networks [167]. In this work, only two popular surrogate models will be presented: Gaussian process regression, also referred to as Kriging [168–174] and Polynomial Chaos Expansion (PCE) [175–178]. A comparative study [179], involving 14 test problems, with different shapes of non linearity and number of inputs, showed that the choice of the metamodel should be influenced by the behavior of the model that is being approximated. This is why preliminary observations are always necessary, as also highlighted in [180]. The conclusions of the comparative study were that Kriging performs well for nonlinear problems with the drawback of having a higher computational cost, due to its complex optimization process, while polynomial-based methods are easier to construct but also less accurate, in this case. The mathematical definition of both metamodels is presented in Section 3.2. The implementation and validation methods are subsequently detailed in Section 3.3. Last, the importance of the design of the input dataset in the elaboration of the metamodel is highlighted in Section 3.4, along with a brief presentation of commonly used sampling techniques.

3.2 Mathematical definition

3.2.1 Kriging

Kriging [168–174] is an interpolation model based on the decomposition of a random variable Y into a deterministic mean (trend) and a residual Gaussian process, which reads:

$$\Xi^{\mathrm{Kri}}(\boldsymbol{x}) = \mu(\boldsymbol{x}) + W(\boldsymbol{x}). \tag{3.3}$$

In this equation, $\boldsymbol{x}$ is one of the N realizations of the random input vector $\mathbf{X} = (\boldsymbol{x_1}, ..., \boldsymbol{x_N})^\top$ of dimension M and μ is a function defined as:

$$\mu(\boldsymbol{x}) = \sum_{j=1}^{n} a_j g_j(\boldsymbol{x}), \tag{3.4}$$

where $\boldsymbol{g}(\boldsymbol{x}) = (g_1(\boldsymbol{x}), ..., g_n(\boldsymbol{x}))^\top$ are the n trend functions and $\boldsymbol{a} = \{a_1, ..., a_n\}^\top$ the trend coefficients. The trend functions can be of different types, *e.g.* constant, linear or quadratic. $W(\boldsymbol{x})$ is a standard Gaussian field with zero mean. The covariance function C of W is defined as $C = C_{\ell,\sigma}$, where ℓ and σ are the lengthscale and signal variance parameters. An example of covariance function is the squared exponential (Gaussian) function, defined as:

$$C_{\ell,\sigma}(\boldsymbol{x_1}, \boldsymbol{x_2}) = \sigma^2 \exp\left(-\frac{1}{2\ell^2}\left\|\boldsymbol{x_1} - \boldsymbol{x_2}\right\|_2^2\right). \tag{3.5}$$

Once the type of the trend and covariance functions defined, the coefficients $\boldsymbol{a} = \{a_1, ..., a_n\}^\top$ are estimated via maximum likelihood optimization so that the metamodel interpolates the data contained in a training dataset $\mathbf{Y}$, as $\boldsymbol{a} = (\boldsymbol{G}^\top \boldsymbol{C}^{-1} \boldsymbol{G})^{-1} \boldsymbol{G}^\top \boldsymbol{C}^{-1} \mathbf{Y}$ in which the $N \times n$ matrix $\boldsymbol{G}$ is defined as $G_{ij} = g_j(\boldsymbol{x_i})$, $i \in \{1, ..., N\}$, $j \in \{1, ..., n\}$ and $\boldsymbol{C}$ is the $N \times N$ correlation matrix, whose components are $C_{ij} = C_{\ell,\sigma}(\boldsymbol{x}_i, \boldsymbol{x}_j)$, $i, j \in \{1, ..., N\}$.

As such, the first step for the implementation of Kriging consists in choosing the n trend functions g. Then, a model for the covariance function is selected and its parameters are identified. After, using the experimental design $\mathbf{X}$ and the corresponding responses $\mathbf{Y}$, a maximum likelihood optimization problem is solved to estimate the coefficients $\boldsymbol{a}$ of the trend. Refer to [158, 181] for more details and application examples.

3.2.2 Polynomial Chaos Expansion

PCE is a functional representation of the random QoI, wherein the latter is written as an infinite linear combination of some orthogonal polynomials, with respect to the Probability Density Functions (PDFs) of input parameters [182–184]. The exact infinite expansion is then truncated up to some degree p as:

$$\Xi_p^{PCE}(\boldsymbol{x}) = \sum_{i=0}^{P-1} a_i \Psi_i(\boldsymbol{\zeta}) = \boldsymbol{a}^\top \boldsymbol{\Psi}(\boldsymbol{\zeta}), \tag{3.6}$$

in which $\boldsymbol{x}$ is a realization of the random input vector $\mathbf{X} = (\boldsymbol{x_1}, ..., \boldsymbol{x_N})^\top$ of dimension M, $P = \binom{p+M}{M}$ polynomial basis functions $\boldsymbol{\Psi}$ and deterministic coefficients $\boldsymbol{a}$ are used. An isoprobabilistic transformation $\mathcal{T}$ links the standard random vector $\boldsymbol{\zeta} = (\zeta_1, ..., \zeta_M)$

to the random input vector $\boldsymbol{x}$, *i.e.* $\boldsymbol{x} = \mathcal{T}(\boldsymbol{\zeta})$. The type of polynomials is determined based on the PDFs of the input random parameters. For instance, Legendre, Hermite and Jacobi polynomials, defined over $[-1, 1]$, are used for uniform, Gaussian and beta random variables. The basis functions are then constructed by multiplying the one-dimensional bases. After, the expansion coefficients are calculated using a least squares approach via $\boldsymbol{a} = (\boldsymbol{G}^\top\ \boldsymbol{G})^{-1}\ \boldsymbol{G}^\top\ \mathbf{Y}$, wherein the $N \times P$ information matrix $\boldsymbol{G}$ is defined as $G_{ij} = \Psi_j(\boldsymbol{\zeta}_i)$. A rule of thumb to avoid the singularity of the matrix $\boldsymbol{G}^\top\ \boldsymbol{G}$ is that the dataset used to build the metamodel should contain more than $(M-1)P$ samples [178], leading to:

$$N > (M-1)\binom{p+M}{M}, \tag{3.7}$$

in which N is the number of samples. The mean and variance of the estimations of the output variable $\mathbf{Y}$ can be subsequently calculated in terms of the expansion coefficients via $\mathbb{E}[\Xi_p^{PCE}] = a_0$ and $\text{Var}[\Xi_p^{PCE}] = \sum_{i=1}^{P-1}\ a_i^2$, respectively. Note that PCE also enables to analytically evaluate the Sobol sensitivity indices directly from the expansion coefficients. Details on the calculation of the Sobol indices with these coefficients are provided in [152, 161, 185]. OpenTURNS built-in methods make it possible to compute the Sobol indices [158] with this approach.

3.3 Validation of the metamodel

The hyperparameters of the metamodels, *i.e.* the coefficients of the trend functions along with the parameters of the correlation function (ℓ and σ for the squared exponential model) of Kriging and the expansion coefficients of PCE, are optimized in order to maximize the accuracy of their predictions, which is quantified using the predictivity factor, denoted by Q_2. The latter can be estimated using validation techniques. Among them, one can mention the holdout validation, the cross validation and the Leave-One-Out validation [186]. These techniques are presented in the following.

3.3.1 Optimization of the hyperparameters

Holdout validation techniques consist in dividing the dataset into a training and testing subsets. The training set is used to train the model and the remaining testing dataset is used to validate the model. As such, the predictions of the model, made with the test dataset, are compared with the true values, which are the values contained in the testing dataset. The training of the metamodel consists in optimizing its hyperparameters introduced in Section 3. The true and predicted values can be compared in a true vs predicted plot. If the distribution of the points is close to the line $y = x$, the model is accurate, as the predictions are close to the true values. The predictivity factor Q_2 enables to quantify the accuracy of the metamodel by comparing the least squared error between the predicted and true values, normalized by the variance of the predicted values, to 1. Hence, the closer Q_2 gets to 1, the closer the predictions are to the true values. The predictivity factor is defined as:

$$Q_2 = 1 - \frac{\sum_{i=1}^{N}(Y_i - \hat{Y}_i)^2}{N\mathrm{Var}(\hat{Y})} \tag{3.8}$$

In this equation, Y_i is the i^{th} true value of the test subset and $\hat{Y}_i$ is the corresponding prediction. To be accurate, this method requires the test subset to be representative of the dataset, meaning that it has to contain enough samples to depict the behavior of the whole dataset. A rule of thumb is to consider that the size of the test subset should represent 30 % of the size of the dataset [187]. The holdout validation may thus require large datasets to provide accurate results. The split of the test and train subdatasets for the holdout validation is schematically illustrated in Figure 3.2a.

Cross validation (CV) consists in applying the holdout validation several times to the dataset. It is split in k subsets, called folds, and the holdout validation is performed by using one fold for testing and the rest of the dataset (the remaining $k - 1$ folds) for training. CV is henceforth also referred to as k-fold validation. The metamodel is therefore evaluated k times, and the predictions versus true values are stored. Thus, N_j predictions $\hat{Y}_i^j (i \in \{1, ..., N_j\},\ j \in \{1, ...k\})$ and their associate true values Y_i^j are compared, in which N_j is the number of samples in the j^{th} fold. This technique is used as an alternative to the holdout validation when the size of the dataset is not sufficient to train the metamodel with a representative dataset. Training using CV techniques provides more accurate predictions than those obtained with the holdout validation [186]. Nonetheless, the computational cost of such a method is larger, as the optimization process needs to be repeated k times.

The true versus predicted plot is generated with the predictions and true values of the k folds. The predictivity factor Q_2 is subsequently computed using Equation 3.9, which evaluates the mean of the predictivity factors obtained for each fold.

$$Q_2^{CV} = \frac{1}{k}\sum_{j=1}^{k} Q_2^j, \tag{3.9}$$

in which Q_2^j is the predictivity factor of the j^{th} fold, itself computed as:

$$Q_2^j = 1 - \frac{\sum_{i=1}^{N^j}(Y_i^j - \hat{Y}_i^j)^2}{N^j \mathrm{Var}(\hat{Y}^j)}, \tag{3.10}$$

where Y^j is the j^{th} testing subdataset, while $\hat{Y}_i^j$ is the prediction of the i^{th} sample and Y_i^j is the associate true value. An example of a possible split of the test and train subdataset for an 8-fold validation is illustrated in Figure 3.2b. The division of the folds can be defined in various ways. Numerical experiments revealed that setting $k = 10$ generally provides accurate estimations of the model, while limiting overfitting [188]. This value can be used as a rule of thumb but the value of k can be adapted accordingly to the behavior of the model being approximated by the metamodel [189].

Leave-One-Out (LOO) cross validation method is preferred over the k-fold in the case of a very small dataset [190]. Indeed, this method is equivalent to a k-fold cross validation in which the amount of folds k is equal to the size of the dataset N. In this case, each fold only contains one sample in the test set, in order to use for training the largest subset available. This technique is therefore more computationally expensive than the classical k-fold method, as it requires more rounds of training to be computed [188]. The split of the train and test subdataset for the LOO cross validation is shown in Figure 3.2c.

Synthesis on the validation methods The validation methods, that have been introduced, are compared in Figures 3.2, in which the separation of the training and testing subdataset is presented. Regardless of the validation technique used, the objective is always to find the parameters of the metamodel for which the predictivity factor Q_2 is as close as possible to 1.

In this thesis, the optimization of the hyperparameters using OpenTURNS is carried out using the LOO validation for both Kriging and PCE techniques. Indeed, although it may not be the most efficient in terms of the computation time, it remains reasonable, as the maximum CPU time for the optimization of the hyperparameters a metamodel encountered in this thesis is around 10 minutes. As such, this validation technique is used to take better advantage of the samples that are available.

3.3.2 Final validation

After optimization of the hyperparameters, the accuracy of the metamodel is calculated with an additional dataset, that is used only for this purpose [186]. This is consequently unseen data that has not been used to train the metamodel. The predictivity factor, obtained for this dataset, is then used to quantify the accuracy of the metamodel after optimization.

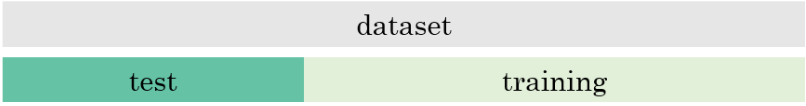

(a) Holdout

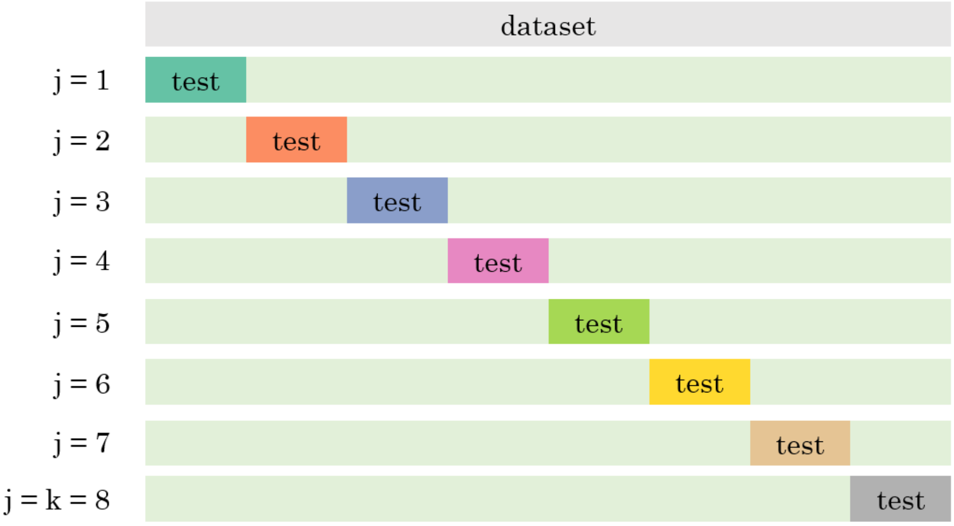

(b) 8-fold CV

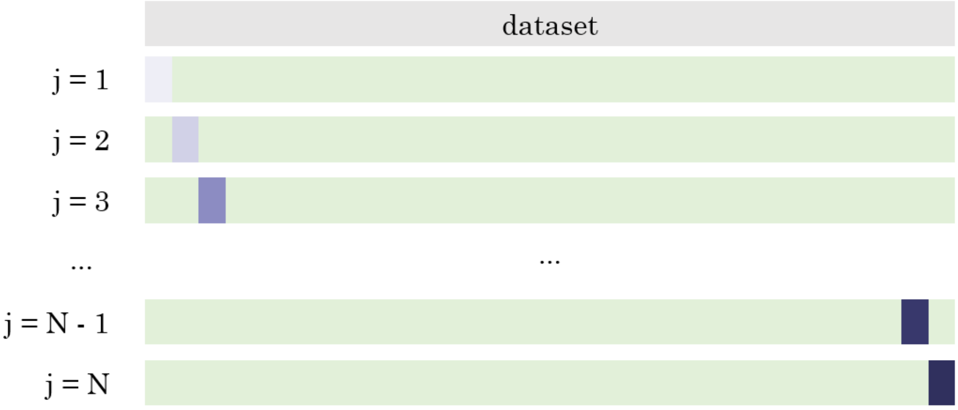

(c) LOO

Figure 3.2: Illustration of the division between the training and testing subdatasets for the holdout (a), cross-validation (b) and LOO (c) validations, where k is the number of folds and N is the size of the dataset. Light green regions stand for the training subdatasets, while the colored ones are the testing ones.

3.4 Sample definition

3.4.1 Importance of sampling on surrogate modeling and sensitivity analysis

Metamodels require observations of the model to be able to emulate it and, in general, the more complex the model is, the more resources it requires to generate the observation samples. However, the generation of these samples may be computationally expensive, depending on the computational cost of the model. This is why their size needs to be minimized while being representative of the behavior of the model [180]. The number of samples necessary to create a metamodel depends on the number of input parameters, their distributions and the nonlinearity of the model. Some of the well-known sampling techniques will be succinctly presented in Section 3.4.2 and compared in Section 3.4.3, in order to identify the one that will be the most suitable for our upcoming investigations. The reader can refer to [191] for detailed information on the existing sampling techniques.

3.4.2 Common sampling techniques

Regular sampling, also called as grid sampling, consists in sampling each input parameter in a regular manner [192]. This method suits well for variables that require only a few points to be described, since the total number of tuples of the M input variables can be calculated as the product of the amount of points used to describe each variable.

Monte Carlo (MC), also known as simple random sample, consists in an experimental design in which each sample (*i.e.* tuple of the M input variables) is generated independently of the others [166, 191].

Stratified sampling consists in splitting the domain of definition of the input variables into equal-size subdomains (also called strates) and to generate random samples for each one of them. This kind of sampling ensures that every chunk of the domain is sampled [192] and they may thus require a lot of samples, depending on the discretization.

Latin Hypercubes Sampling (LHS) derives from stratified sampling, with the attempt to reduce the amount of data. In this technique, the domains of the M input parameters are divided in the number of the expected samples, say 5×10^3 here. Then, 5×10^3 strates will be created. Among these, only one value is randomly taken for each variable, constituting thus one tuple which is the first sample. To generate the next tuple, the same process is repeated, but none of the previously used values of the parameters can be reused. Thus, LHS is called a *memory approach*, since the samples are generated by taking into account the ones that have already been set. Regular sampling, MC and LHS for two independent and uniformly distributed variables over $[0, 1]$ are compared in Figure 3.3.

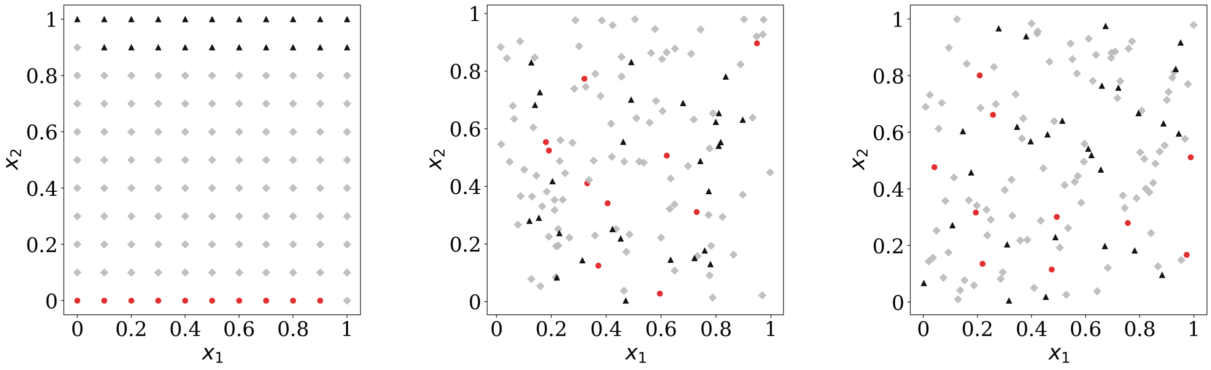

(a) Regular (b) Monte Carlo (c) Latin Hypercube

Figure 3.3: Example of (a) regular sampling with 121 points, (b) Monte Carlo and (c) Latin Hypercube sampling with $2^7 = 128$ points, computed using OpenTURNS. The red dots correspond to the first 10 points, the grey diamonds represent the following 11 to 100 points, and the black triangles stand for the remaining points.

Quasi Monte Carlo (qMC), also known as quasi-random or low-discrepancy [193] sampling method is similar to MC, as the tuples are generated independently from each other. However, they are not generated randomly but using a low discrepancy sequence [191, 194–197]. The latter is deterministic and well distributed across the domain of definition. The discrepancy of a sequence is the distance between its values and those of a uniformly distributed sequence. Examples of such sequences are Halton's [198], Sobol's [199, 200] or Faure's [201]. The samples obtained using these sequences for the same independent uniform variables over $[0, 1]$ are compared in Figure 3.4. This approach enables to generate samples that cover the domain of definition of the variables, contrary to MC, which might let some parts of the domain uncovered if the number of sample is not large enough [195].

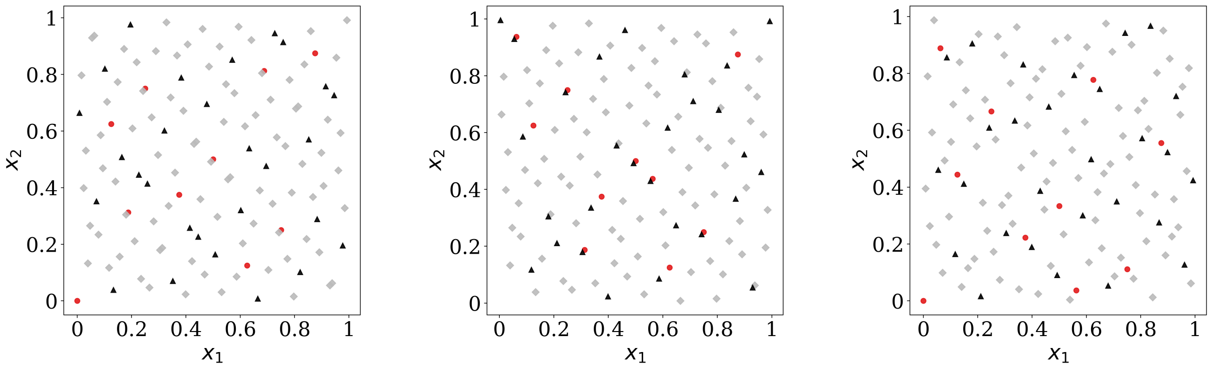

(a) Sobol's sequence (b) Faure's sequence (c) Halton's sequence

Figure 3.4: Example of low discrepancy sequences with $2^7 = 128$ points, computed with OpenTURNS. The red dots correspond to the first 10 points, the grey diamonds represent the following 11 to 100 points, and the black triangles stand for the remaining points.

3.4.3 Sampling technique used in this study

Preliminary observations on the behavior of our model showed that its response is nonlinear. Consequently, the samples need to fairly cover the domains of definition of the input parameters. Hence, the regular sampling method is discarded from the potential candidates, as well as the stratified sampling, which would require a very large number of samples. In our case, the computation time is about 1 second to compute $\tilde{f}$, *i.e.* one single point of a phase diagram. The aforementioned methods are hence not suitable to create metamodels or to perform parametric studies or any sensitivity analysis that depend on the number of samples. Thus, the choice needs to be made among MC, LHS and qMC methods. Comparative studies [195, 202] showed that qMC requires less samples to converge to the actual behavior of the data and to minimize the error in the integral quadrature compared to LHS, while MC requires the most. Consequently, the metamodel and the sensitivity analyses presented in this thesis will be performed using qMC-based samples. None of the three low discrepancy sequences that have been introduced in the previous section seems more adapted to our study than the others. Thus, our samples will be built using Sobol's sequences[1], as they are implemented in the most commonly used numerical open-source tools for the design of experiments, such as OpenTURNS or UQlab, among others.

---

[1] Note the difference between the Sobol indices and the Sobol sequences, which are different quantities. The Sobol indices are calculated for sensitivity analyses, while Sobol's sequences are used to create samples.

4 Influence of the aspect ratio of a rigid elliptic NP on its cellular uptake

In this section, the influence of the mechanical properties of the NP-membrane interface (*i.e.* the adhesion $\overline{\gamma}$ between the membrane and the NP and the membrane tension $\overline{\sigma}$), as well as the aspect ratio $\overline{r}$ of the NP, on the wrapping degree at equilibrium $\tilde{f}$, are compared. This investigation aims at providing guidelines to NP manufacturers regarding the characteristics they need to accurately reproduce. For instance, the control on the shape of the NP is currently a challenging task [111], because of the manufacturing limitations relative to the production of objects at such scales. Another objective of this chapter is to provide a quantitative comprehension of the influence of the aforementioned properties on the cellular uptake of the NP, which has already been investigated qualitatively, as introduced in Chapter 1. To fulfil this objective, we need to identify which of the investigated parameters is dominant on the prediction of the cellular uptake of the NPs.

4.1 Preliminary observations

In order to get a grasp of the influence of $\overline{r}$ on the wrapping degree at equilibrium $\tilde{f}$, the behavior of the variation of the total potential energy $\overline{\Delta E}(f)$ is observed in Figure 3.5 for several values of $\overline{r}$ and a cell with the following properties: $(\overline{\gamma}, \overline{\sigma}) = (10, 2)$.

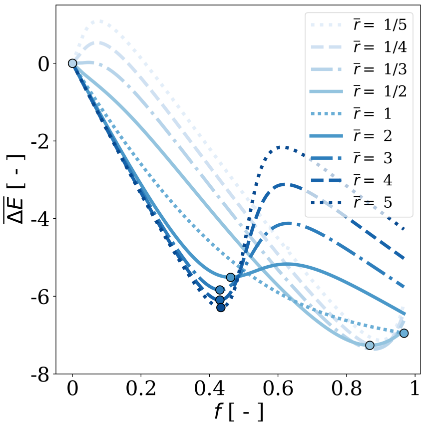

Figure 3.5: Influence of the aspect ratio $\overline{r}$ on the variation of the total potential energy in terms of the wrapping degree f for $(\overline{\gamma}, \overline{\sigma}) = (10, 2)$. The dots correspond to the equilibrium position.

Note that although $\overline{\gamma} = 10$ is out of the interval of definition considered in this study, this value is taken to inflate the effect of $\overline{\gamma}$ in energy plots. This choice was also made in a similar study [40]. Figure 3.5 shows that except for the cases of circular ($\overline{r} = 1$) and slightly vertical NPs ($\overline{r} \in [1/2, 1]$), an energy barrier occurs for low values of f for vertical NPs and around $f \approx 0.5$ for horizontal ones. The geometry of the membrane with $\overline{r} = 1/5$ for the wrapping degrees close to the energy barrier is displayed in Figure 3.6.

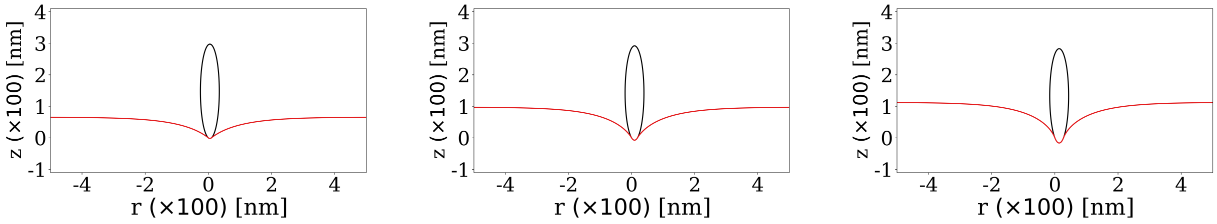

(a) $f = 0.05$ (b) $f = 0.10$ (c) $f = 0.15$

Figure 3.6: Geometry of the membrane during the wrapping of a vertical NP ($\overline{r} = 1/5$) for f close to the energy barrier and a cell with $(\overline{\gamma}, \overline{\sigma}) = (10, 2)$.

The same plot for $\overline{r} = 5$ are also presented in Figure 3.7. The values of f, at which the geometry is represented, are chosen to display the evolution of the geometry, before and after the energy barriers, that can be observed in Figure 3.8.

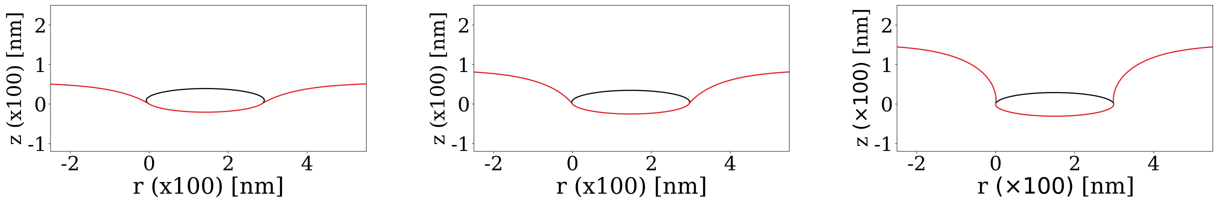

(a) $f = 0.40$ (b) $f = 0.45$ (c) $f = 0.50$

Figure 3.7: Geometry of the membrane during the wrapping of a horizontal NP ($\overline{r} = 5$) for f close to the energy barrier and a cell with $(\overline{\gamma}, \overline{\sigma}) = (10, 2)$.

Figure 3.7 shows that the shape of the membrane remains nearly untouched for a wrapping degree smaller than $f = 0.45$, and then an abrupt change happens between $f = 0.45$ and $f = 0.5$. The energy barrier, observed in the dotted dark blue line in Figure 3.8 for this range of f, is indeed due to the sharp change in curvature of the membrane, necessary to reach $f = 0.5$. The abrupt change in the curvature generates an increase the bending energy of the membrane $\overline{\Delta E_b}$ in Equation 2.54. The phenomenon at the origin of the energy barrier of vertical NP is similar, even though less significant. Indeed, vertical NPs have a small contact radius with the membrane, since the contact occurs at the tip of the ellipse. The energy barrier takes place for small wrapping degrees, as the steepest change in the bending of the membrane takes place during the wrapping of the tip of the NP. Once the latter is wrapped, the total energy keeps decreasing with f, as illustrated in Figure 3.5. These conclusions, from the evolution of $\overline{\Delta E}$ with respect to $\overline{r}$, show that the aspect ratio of the NP influences the bending energy $\overline{\Delta E_b}$ and therefore the total potential energy $\overline{\Delta E}$.

However, this understanding, for fixed values of $\overline{\sigma}$ and $\overline{\gamma}$, might be misleading. Indeed, Figure 2.7 highlighted the effect of the mechanical parameters $(\overline{\gamma}, \overline{\sigma})$ on $\overline{\Delta E}$, in the case of a circular NP ($\overline{r} = 1$). In order to determine if this effect remains notable for elliptic NPs, $\overline{\Delta E}(f)$ is plotted for a range of values of $\overline{\gamma}$ and $\overline{\sigma}$ in the case of NPs with $\overline{r} = 5$ and $\overline{r} = 1/5$ in Figure 3.8.

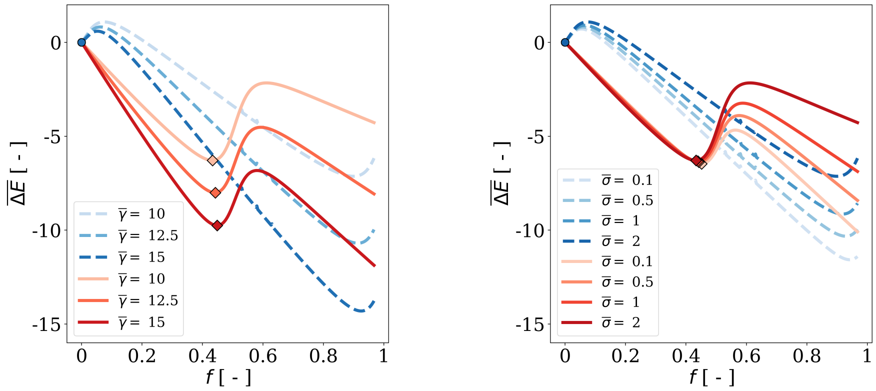

(a) (b)

Figure 3.8: Influence of (a) $\overline{\gamma}$ with $\overline{\sigma} = 2$ and (b) $\overline{\sigma}$ with $\overline{\gamma} = 10$ on $\overline{\Delta E}(f)$ for vertical ($\overline{r} = 1/5$, blue dashed lines) and horizontal ($\overline{r} = 5$, solid red lines) NPs. The equilibrium positions are shown by the markers.

The latter shows that the energy barrier for vertical ellipses is reduced for lower $\bar{\sigma}$ and higher $\bar{\gamma}$, while the one for horizontal ellipses is only slightly reduced by lowering $\bar{\sigma}$. Hence, the adhesion between the NP and the membrane, as well as the membrane tension, compensate the effect of the bending of the membrane on the total variation of potential energy $\overline{\Delta E}$.

Both of these observations lead to the conclusion that $\overline{r}$, $\overline{\gamma}$ and $\overline{\sigma}$ influence $\tilde{f}$ in different ways. For a better understanding of the influence of $\overline{r}$ and to generalize these observations to a large range of values of $\bar{\gamma}$ and $\bar{\sigma}$, *i.e.* a range of cells, phase diagrams are generated for all aspect ratios. Only the phase diagrams obtained for $\overline{r} = 1/4$, $\overline{r} = 1$ and $\overline{r} = 4$ are presented in Figure 3.9. The reader can refer to Appendix B for more phase diagrams for $\overline{r} \in [1/5, 5]$.

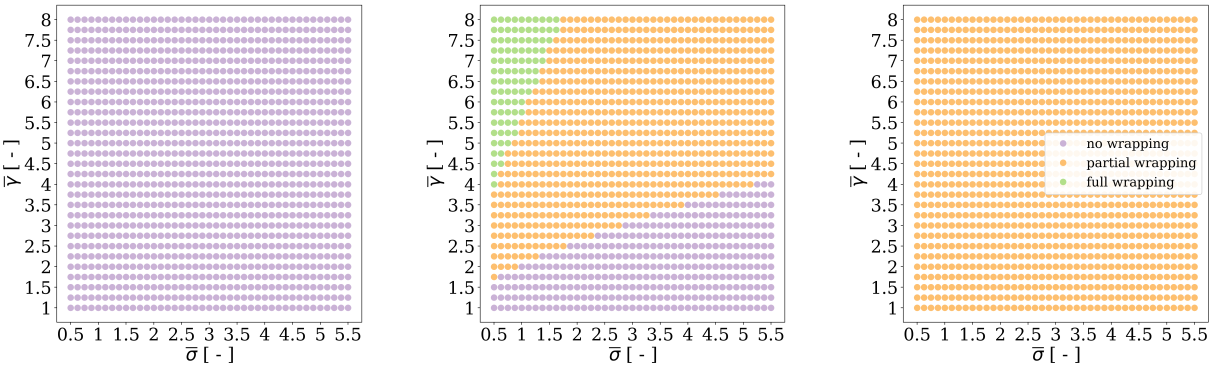

(a) vertical NP (b) circular NP (c) horizontal NP

Figure 3.9: Phase diagrams for (a) $\overline{r} = 1/4$, (b) $\overline{r} = 1$ and (c) $\overline{r} = 4$.

These phase diagrams show that the influence of $\overline{\gamma}$ and $\overline{\sigma}$ is not the same depending on the value of $\overline{r}$. Indeed, for very elongated NPs, *i.e.* $\overline{r} \gg 1$ or $\overline{r} \ll 1$, the phase diagrams do not change with $\overline{r}$, meaning that $\overline{\gamma}$ and $\overline{\sigma}$ do not influence the phase as they are not able to compensate the energy barrier due to the bending of the membrane. On the contrary, this is not the case for slightly elongated NPs. These observations are summarized in Figure 3.10, which presents the proportion of phases 1, 2 and 3 (denoted as ψ_1, ψ_2 and ψ_3), on the phase diagrams, in terms of $\overline{r}$.

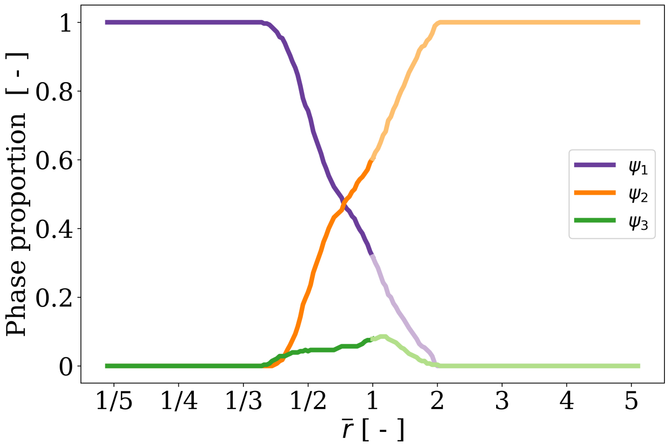

Figure 3.10: Phase proportions with respect to the aspect ratio of the NP. The dark (resp. light) lines correspond to vertical (resp. horizontal) NPs.

From this figure, one can observe that horizontal particles with $\overline{r} > 2$ barely surpass phase 2, while the vertical ones tend to remain in the the phase 1 for $\overline{r} < 1/3$. For highly elongated NPs ($\overline{r} \gg 1$), neither the vertical nor the horizontal particles reach phase 3, *i.e.* $\psi_3(\overline{r} > 2) = 0$ and $\psi_3(\overline{r} < 1/3) = 0$. Thus, the particles that are more likely to be engulfed by the cell are the ones that are slightly elongated, and especially the circular NPs, as ψ_3 is maximized for $\overline{r} \approx 1$.

The preliminary observations, presented in this section, qualitatively show that $\overline{r}$, $\overline{\gamma}$ and $\overline{\sigma}$ influence the outcome of the endocytosis of the NPs. The next section focuses on the quantitative evaluation of these influences.

4.2 Quantification of the influence of the aspect ratio on the uptake of the NPs

4.2.1 Preliminary considerations

The results of the preliminary observations presented in Section 4.1 do not enable to draw any striking conclusion, as all the parameters appear to play a role on the wrapping degree at equilibrium $\tilde{f}$. Furthermore, the behavior of the model does neither look monotonic nor linear. Thus, according to the introduction to sensitivity analysis provided in Section 2, the influence of each one of the input parameters $\overline{\gamma}$, $\overline{\sigma}$ and $\overline{r}$ and of their potential interactions on $\tilde{f}$, will be quantified by evaluating the Sobol indices. The description of the domains of definition of the input parameters is presented in Section 4.2.2. Then, the evaluation of the representativeness of the dataset will be discussed in Section 4.2.3. Thus, PCE and Kriging metamodels will be compared in Section 4.2.4. Once validated, they will be used to generate estimations of the model, which in turn will be used to compute the Sobol indices in Section 4.2.5. Note that the Python script used to build the metamodels and to conduct the sensitivity analyses is available in the Github repository[1] associated to this thesis.

4.2.2 Domains of definition of the variables

The variables related to the mechanical behavior of the system, $\overline{\gamma}$ and $\overline{\sigma}$, are set following the domains of definition presented in Section 2.1 from Chapter 2. Having recourse to the maximum entropy principle [203], since the only available information about these variables are their lower and upper bounds, the best candidate for their PDF is the uniform distribution. It is worth noting that this non-parametric approach to model the probabilistic content of a random variable is used since parametric approaches, based on real data, cannot be used in this work because of the lack of experimental data. However,

---

[1] `https://github.com/SarahIaquinta/PhDthesis`

recalling that the aspect ratio $\overline{r}$ of the NP ranges from 1/6 to 6, blindly applying a uniform distribution for $\overline{r}$ would result in realizations that are skewed towards more horizontal NPs, as they span over a larger interval than the vertical samples. To overcome this issue, we used a piecewise-uniform distribution, *i.e.* a distribution that is uniform over two disjoint intervals. In our case, the distribution is uniform between 1/6 and 1, and again between 1 and 6. Hence, the PDF of the random variable $\bar{R}$ is defined as:

$$f_{\bar{R}}(x) = \begin{cases} \frac{1}{2}\frac{1}{1-\frac{1}{6}} = \frac{3}{5} & \text{for } x \in [\frac{1}{6}, 1[\\ \frac{1}{2}\frac{1}{6-1} = \frac{1}{10} & \text{for } x \in]1, 6] \\ 0 & \text{otherwise,} \end{cases}$$

in which the weight 1/2 is added to each one of the two distributions to ensure that $\overline{r} = 1$ is the median of the distribution, *i.e.* $\mathsf{P}(\bar{R} < 1) = \mathsf{P}(\bar{R} > 1) = 1/2$. This distribution will be denoted as $\mathcal{U}^P(1/6, 1; 1, 6)$. As such, the input parameters are modeled as three independent random variables $\bar{\Gamma} \sim \mathcal{U}(1, 8)$, $\bar{\Sigma} \sim \mathcal{U}(0.5, 5.5)$ and $\bar{R} \sim \mathcal{U}^P(1/6, 1; 1, 6)$, where the intervals of definition have been described in Section 4.2 from Chapter 2. Figure 3.11 shows the histograms of the input variables based on a dataset of 10^3 random samples.

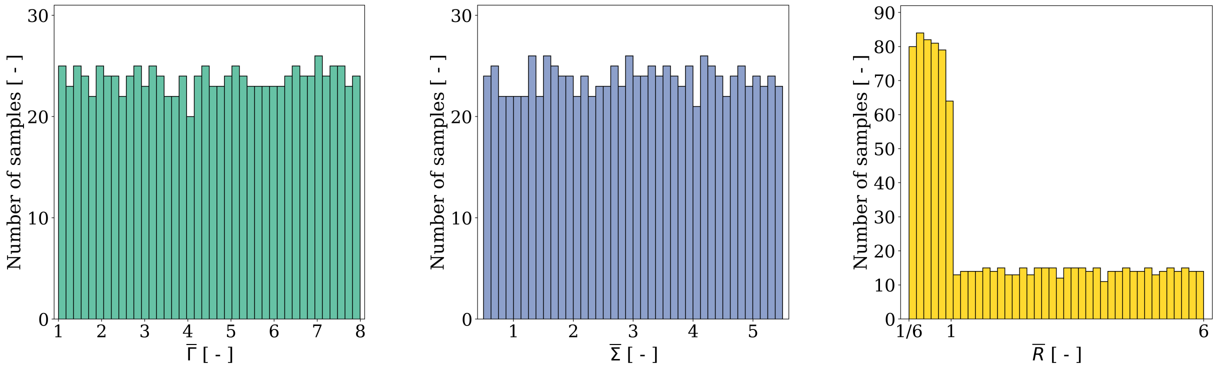

(a) Distribution of $\overline{\Gamma}$.
(b) Distribution of $\overline{\Sigma}$.
(c) Distribution of $\overline{R}$.

Figure 3.11: Histogram of the input variables (a) $\overline{\Gamma}$, (b) $\overline{\Sigma}$ and (c) $\overline{R}$, for 10^3 samples.

4.2.3 Data representativeness

The variables $\overline{\Gamma}$, $\overline{\Sigma}$ and $\overline{R}$ are sampled using the qMC technique based on the Sobol's sequence. To observe the behavior of the random variable $\tilde{F}$ and determine the number of samples needed to form a representative dataset, $2^{12} = 4096$ realizations have initially been built. In case of low representativeness, more samples could have been generated.

The corresponding values of $\tilde{F}$ for each realization are then calculated in about 2 hours, by executing the code in parallel using the aforementioned machine. Still, even if this computation time is relatively small, especially compared to those that are necessary to generate values of Ψ_3, it is not possible to know in advance the number of samples needed for the Sobol indices to converge. For this reason, the surrogate model is built even in this case, in order to ensure that the convergence will be reached. Figure 3.12 illustrates the distribution of $\tilde{F}$ in the dataset. This distribution is bimodal, *i.e.* it has two modes, being $\tilde{f} = 0.03$ and $\tilde{f} = 0.37$.

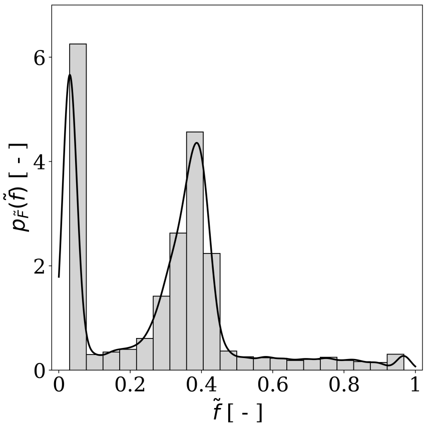

Figure 3.12: Histogram of the distribution of $\tilde{F}$, along with a kernel density estimation of its PDF.

Figure 3.13 depicts the convergence of the average and the standard deviation of the random wrapping degree at equilibrium $\tilde{F}$, in terms of the number of samples, along with their respective standard deviation (shaded gray zones) via bootstrapping with a resampling size of 200 in order to remove noise coming from the random nature of the problem. To determine the convergence, which is not trivial from the values of the mean and standard deviation of $\tilde{F}$, the absolute value of the normalized gradient is computed. It is worth recalling that this error estimator is not suitable when the QoI converge to small (in absolute value) values, as introduced in Section 2.2.2, which is not the case for $\tilde{F}$. Figure 3.14 shows the absolute normalized gradients of the average and the standard deviation of $\tilde{F}$, in terms of the number of samples. The red dashed lines are used to highlight the threshold defining the convergence, which was set to 10^{-2}, *i.e.* a variation smaller than 1 %, when adding a single sample to the set.

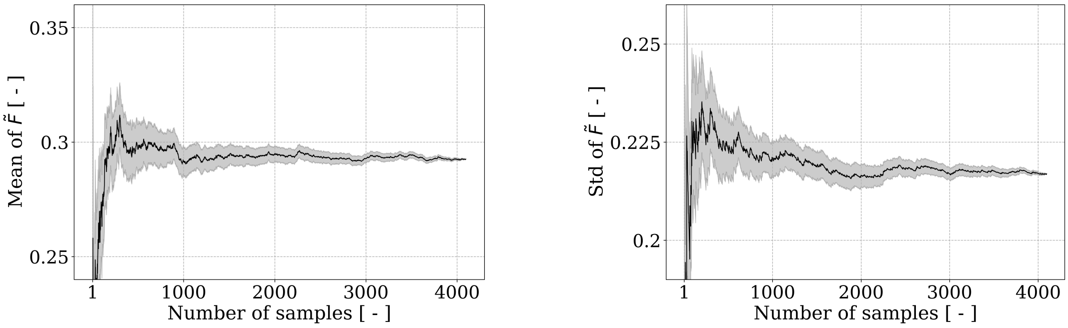

(a) (b)

Figure 3.13: Convergence of the (a) mean and (b) standard deviation of the random wrapping degree at equilibrium $\tilde{F}$, in terms of the number of samples (thick solid lines), along with their respective standard deviation, denoted by the gray regions.

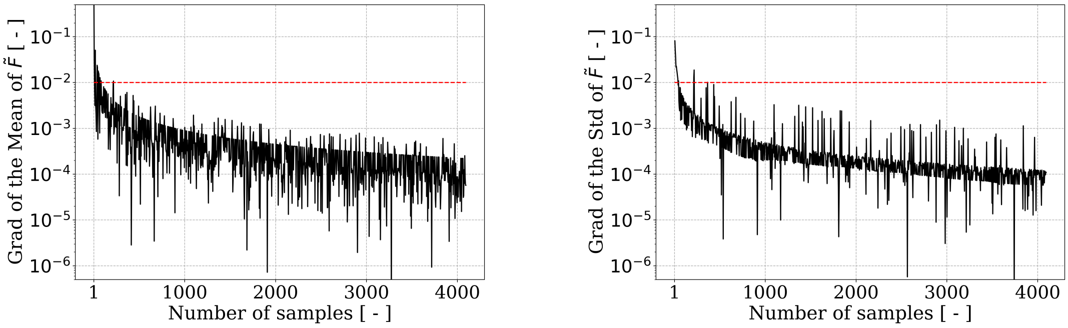

(a) (b)

Figure 3.14: Normalized gradient of the (a) mean and (b) standard deviation of $\tilde{F}$, with respect to the number of samples. The dashed lines correspond to the threshold of 1 %. Only one out of four points have been represented for the clarity of the plots.

According to this plot, the dataset needs to contain at least 217 estimations of $\tilde{F}$ to be representative of its mean. Similarly, 382 evaluations of the QoI are necessary for its standard deviation to converge. To ensure convergence of both of these first and second-order statistics, the size of the dataset necessary for it to be statistically representative of the behavior of $\tilde{F}$ is 382, which represents 9 % of the size of the dataset.

4.2.4 Surrogate modeling

In this section, Kriging and PCE surrogate models are employed to model the random wrapping degree at equilibrium $\tilde{F}$ using OpenTURNS. To proceed the final validation of the metamodels, 10 % of the dataset, *i.e.* 410 samples, will be taken in order to have enough data to properly calculate the value of the predictivity factor Q_2, while making sure that the validation dataset is representative of the data by containing more than 324 samples. Hence, the remaining 90 %, *i.e.* 3686 samples, is used to train the metamodels.

Kriging First, a Kriging metamodel is implemented using OpenTURNS default trend and correlation functions that may be modified in case of poor performance. As such, the trend function is constant and the correlation function is defined with a squared exponential (Gaussian) model. This choice will be discussed in Section 5. After optimization, a predictivity factor $Q_2^{KRI} = 0.97$ was obtained. The true vs predicted plot, depicted in Figure 3.15, shows that most of the predictions are close to the true values.

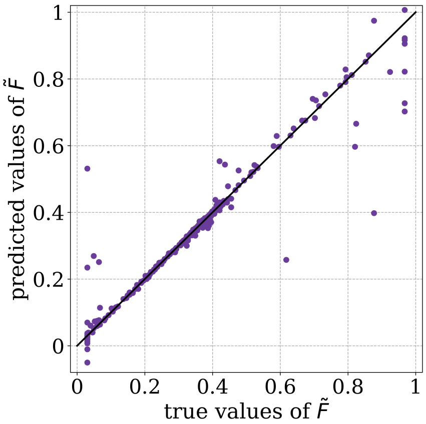

Figure 3.15: Comparison of the Kriging predictions of $\tilde{F}$ with the true values from the dataset.

In addition, the kernel density estimation for the PDF of $\tilde{F}$, based on the response of the metamodel to an input dataset containing 10^5 samples, generated using the MC sampling method, is compared to that of the original dataset in Figure 3.18 and shows that the distribution of the predictions (dashed purple line) is similar to that of the original data.

PCE Based on the mathematical definition of the PCE provided in Section 3.2.2, the following steps need to be performed to build the metamodel:

1. Normalization of the input variables to reduce their domain of definition to $[-1, 1]$ in order to apply common orthogonal polynomials;
2. Definition of the family of orthogonal polynomials with respect to the distribution of the input parameters;

3. Determination of a truncation degree p for the orthogonal basis;
4. Estimation of the vector of expansion coefficients $\boldsymbol{a}$.

The implementation of these steps is presented in the following. Figure 3.16 shows the distribution of the input variables after mapping into the interval $[-1, 1]$. The standardized input parameters are thus three independent random variables $\bar{\Gamma}^* \sim \mathcal{U}(-1, 1)$, $\bar{\Sigma}^* \sim \mathcal{U}(-1, 1)$ and $\bar{R}^* \sim \mathcal{U}^P(-1, -0.7; -0.7, 1)$.

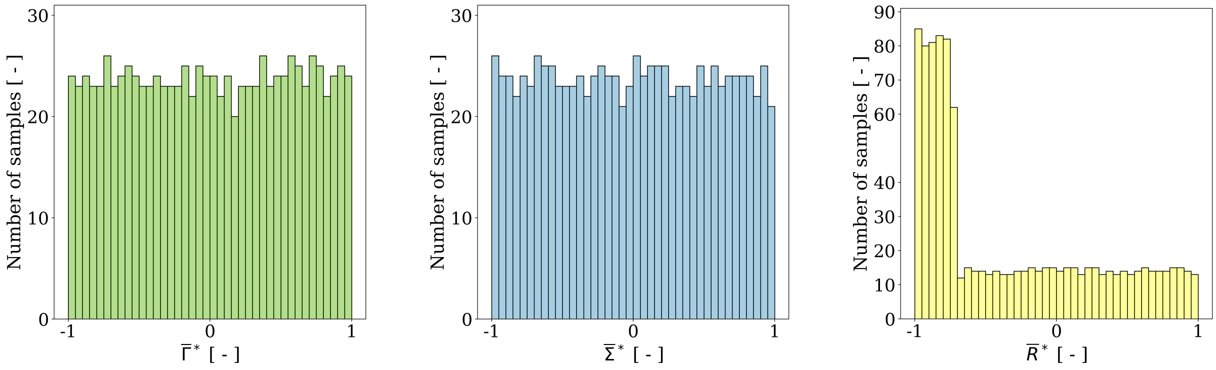

(a) (b) (c)

Figure 3.16: Histograms of the standardized random input variables (a) $\overline{\Gamma}^*$, (b) $\overline{\Sigma}^*$ and (c) $\overline{R}^*$ for 10^3 samples.

The orthogonal polynomial associated to the uniform distribution is Legendre's. For the piecewise uniform distribution, there is no existing associated family of orthogonal polynomial. We henceforth used a built-in function of OpenTURNS to approximate the distribution of $\bar{R}$ based on the input dataset, and thus to infer the corresponding polynomial for the orthogonal basis using the adaptive Stieltjes algorithm [204].

Then, the polynomial degree p is chosen such that the predictivity factor Q_2 is the closest to 1. For this purpose, the latter is calculated for different values of p ranging from 1 to 20, which is the maximum degree, according to the rule of thumb introduced in Section 3.2.2 (Equation 3.7). Figure 3.17a shows that the predictivity factor is maximized for a degree $p = 17$ ($Q_2^{PCE} = 0.79$). Furthermore, Figure 3.18 compares the PDF of the predictions of $\tilde{F}$ to that based on the original dataset.

The bimodal distribution of the data is not well represented by the estimations of PCE, which shows a peak at $\tilde{f} \approx 0.4$, but a small peak lies at $\tilde{f} \approx 0.03$. The errors in the predictions of PCE are also observable in Figure 3.17b, which shows that most of the mispredictions are concentrated around $\tilde{f} = 0.03$.

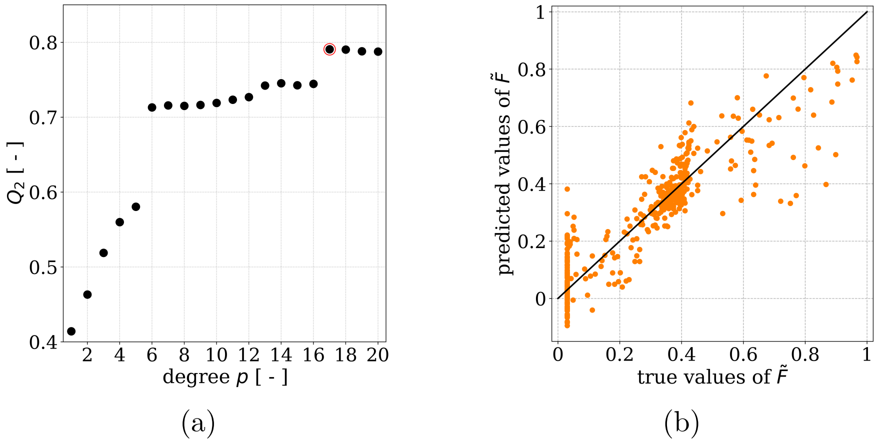

(a) (b)

Figure 3.17: (a) Predictivity factor Q_2 in terms of the degree p of the PCE and (b) validation plot of the estimations of the model with the PCE truncated at a degree $p = 17$.

Comparison of the performances of Kriging and PCE metamodels Kriging and PCE metamodels provided the predictivity factors $Q_2^{KRI} = 0.97$ and $Q_2^{PCE} = 0.79$. The predictions from PCE are consequently less accurate than those of Kriging when comparing them to the original dataset with 324 samples, that have been used for the validation of the metamodels. In addition, the PDF of $\tilde{F}$, estimated based on the metamodels, are compared to that of the model (estimated with 3686 samples). The kernel density estimation of these PDFs, represented in Figure 3.18, revealed that the distribution of the predictions of Kriging is more similar to that of the dataset than according to PCE, which does present a slight bimodal distribution.

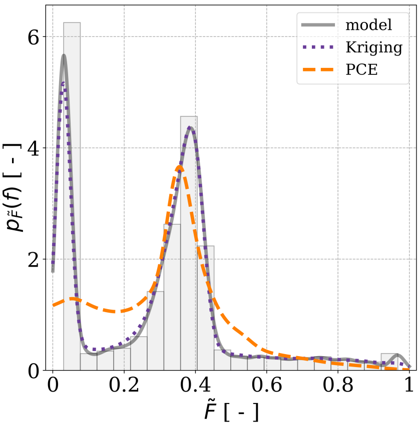

Figure 3.18: Comparison of the PDFs of $\tilde{F}$ from the metamodels' predictions and from the model.

However, despite the good predictivity factors of these metamodels, one can still observe absurd predictions, as they are not included within the domain of definition of the QoI, being $[0.03, 0.97]$. As such, applying a clip to those predictions would reduce their distance to the expected estimations. This postprocessing could be a way to artificially increase the accuracy of the metamodels by restraining the domain of definition of the estimations. An example for the formulation of this postprocessing function is:

$$\hat{Y} = \begin{cases} 0.97 & \text{if } \hat{Y} > 0.97 \\ 0.03 & \text{if } \hat{Y} < 0.03 \\ \hat{Y} & \text{otherwise.} \end{cases}$$

4.2.5 Sensitivity analysis: Sobol indices

Since estimations of Kriging properly depict the behavior of the original model, with $Q_2^{KRI} = 0.97$ and almost the same PDF estimation, this metamodel will be used to approximate the Sobol sensitivity indices. First, the sampling of the input parameters is discussed. Then, results from different algorithms used to compute the indices are compared.

Sampling of the input parameters

Distribution The distributions used to sample the input parameters $\overline{\gamma}$, $\overline{\sigma}$ and $\overline{r}$ are the same as those used to build the metamodels. Hence, $\bar{\Gamma} \sim \mathcal{U}(1, 8)$, $\bar{\Sigma} \sim \mathcal{U}(0.5, 5.5)$ and $\bar{R} \sim \mathcal{U}^P(1/6, 1; 1, 6)$.

Size of the dataset The influence of the number of realizations used to compute the Sobol indices is investigated. For this purpose, the first and total Sobol indices, computed with the Mauntz-Kucherenko algorithm, are represented in Figure 3.19, with respect to the number of samples, along with their 95 % CIs. The latter are computed using the bootstrap method [164], with a resampling size of 100, implemented in OpenTURNS. Then, the evolution of the normalized absolute gradient, in terms of the number of samples, is provided in Figure 3.20, where the dashed lines represent the same threshold as that used for the data representativeness, *i.e.* 1 %.

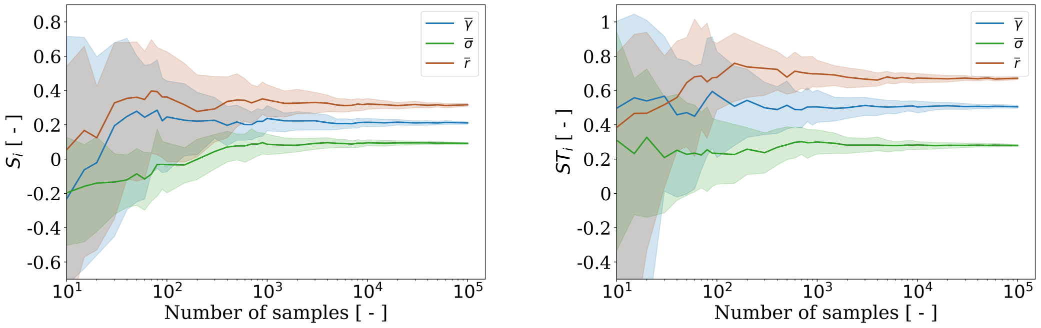

(a) (b)

Figure 3.19: Convergence of the (a) first and (b) total Sobol indices, computed with the Mauntz-Kucherenko algorithm. The shaded regions correspond to the 95 % confidence intervals.

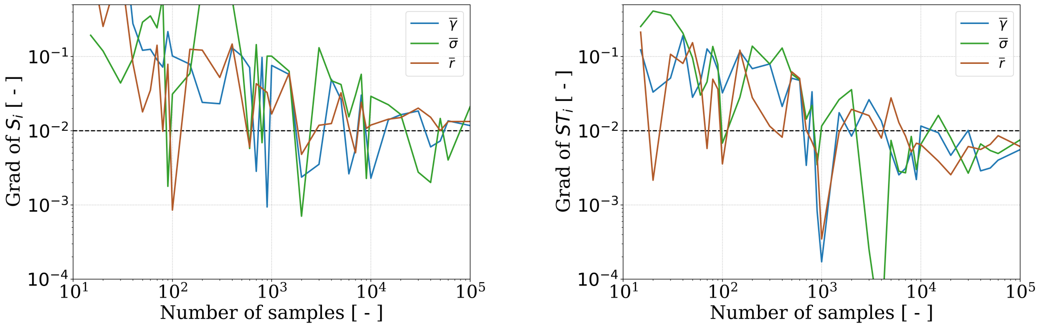

(a) (b)

Figure 3.20: Normalized absolute gradient of the (a) first and (b) total Sobol indices depending on the number of estimations of the metamodel, computed with the Mauntz-Kucherenko algorithm. The black dashed lines correspond to the threshold of 1 %.

According to this figure, the convergence of S_i is not reached, even for 10^5 samples. This conclusion does not match observations from Figure 3.19, where the mean curves of S_i seem stabilized for 10^3 samples. This contradiction shows that the use of the normalized gradient does not suit for investigating the convergence of Sobol indices because of small converged values. This observation validates the necessity of using another convergence criterion based on the range of the CIs, as mentioned in Section 2. Then, following the criterion proposed by Sarrazin *et. al* [164], S_i and ST_i converge when the range of the CIs is smaller than 0.05 (dashed lines in Figure 3.21). Hence, both first and total indices converge for 2×10^4 samples.

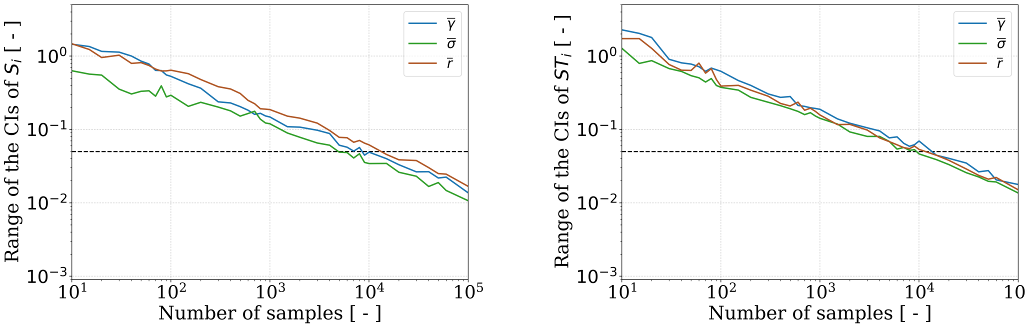

(a) (b)

Figure 3.21: Ranges of the 95 % confidence intervals (CI) of the (a) first and (b) total Sobol indices in terms of the number of estimations of the metamodel, computed using the Mauntz-Kucherenko algorithm. The black dashed lines correspond to a threshold of 0.05.

Influence of the algorithm The convergence study presented in the previous paragraph was conducted using the Sobol indices computed with the Mauntz-Kucherenko algorithm. The aim of the present paragraph is therefore to compare the results obtained using different algorithms (Saltelli, Jansen and Martinez). The number of samples necessary for the convergence of S_i and ST_i, following the criterion relative to the range of the CIs, is compared for these algorithms in Table 3.1.

Table 3.1: Number of samples necessary for the convergence of the Sobol indices following the criterion on the range of the confidence intervals of S_i and ST_i estimated using different algorithms.

Index	Mauntz-Kucherenko	Saltelli	Jansen	Martinez
S_i	2×10^4	2×10^4	3×10^4	2×10^4
ST_i	2×10^4	3×10^4	10^4	4×10^4

The plots representing the variation of the Sobol indices, their normalized absolute gradient, along with the range of their 95 % CIs, for these algorithms, are contained in Section 2 of Appendix D. Disparities in the convergence of the indices depending on the algorithm are highlighted in Table 3.1. Indeed, indices computed with Martinez require the most samples to converge (4×10^4 for ST_i) and Mauntz-Kucherenko enables convergence with less samples (2×10^4 for both S_i and ST_i). The indices obtained after convergence (calculated with 10^5 samples), are compared with those analytically evaluated from the coefficients of PCE in Table 3.2.

Table 3.2: Comparison of the first and total Sobol indices, calculated analytically based on the coefficients of PCE, with those computed using 10^5 estimations of the Kriging metamodel.

Index	**Parameter**	**PCE**	**Kriging**
S_i	$\overline{\gamma}$	0.26	0.21
	$\overline{\sigma}$	0.11	0.09
	$\overline{r}$	0.38	0.32
ST_i	$\overline{\gamma}$	0.42	0.51
	$\overline{\sigma}$	0.21	0.28
	$\overline{r}$	0.60	0.67

Once the convergence is ensured (10^5 samples), there is no notable difference between the indices computed with different algorithms using estimations from Kriging. Nonetheless, despite similar trends, one can note differences between the Sobol values, computed using Kriging and PCE metamodels. It is not surprising, since the PCE model does not represent the true values as reliably as Kriging. Therefore, we are going to use the values obtained for Kriging to draw our conclusions.

Interpretation of the Sobol indices The first order indices are the following: 0.21 for the adhesion $\bar{\Gamma}$, 0.09 for the membrane tension $\bar{\Sigma}$ and 0.32 for the aspect ratio $\bar{R}$ of the NP, which reveals that if we consider the individual effects of these variables on the random wrapping degree at equilibrium $\tilde{F}$, the aspect ratio of the NP is the most influential. Then the adhesion $\bar{\Gamma}$ contributes twice as much as the membrane tension $\bar{\Sigma}$. The total sensitivity indices for $\bar{\Gamma}$, $\bar{\Sigma}$ and $\bar{R}$ are 0.51, 0.28 and 0.67, respectively. The difference $ST_i - S_i$ shows the influence of the interactions of different orders on the variance of $\tilde{F}$ for a given variable i. These interactions contribute by 59 %, 68 % and 52 % to the total indices of $\bar{\Gamma}$, $\bar{\Sigma}$ and $\bar{R}$ respectively, showing that the interactions have a significant influence on $\tilde{F}$.

5 Discussion

The results presented in this chapter match previous conclusions from the literature, to some extent, as it is covered in detail in the next paragraphs. Then, the hypotheses and the methods that have been implemented to obtain these results are also challenged.

Comparison with previous results from the literature

The conclusions, presented in this chapter, regarding the influence of $\overline{r}$ on the uptake of the NP, agree with the results from experimental and numerical studies. Indeed, our results showed that highly elongated NPs are less likely to be uptaken by a cell than circular ones. These results match those obtained experimentally by Champion *et al.* [19, 29], who manufactured and tested NPs with various aspect ratios and shapes and observed that the circular and vertical NPs are engulfed faster by macrophages than those with other shapes. Their results also show that highly elongated vertical NPs could not be engulfed. An experimental study made on the uptake of gold NPs by macrophages led to similar results [205]. Additional experimental studies conducted on NPs with various shapes, such as disks [206, 207] or cubes [208], tend to demonstrate that the shape of the particle is a prominent factor on its uptake [16].

To the best of our knowledge, no experimental investigation was performed to compare the influence of the mechanical properties of the NP-cell interaction (adhesion and membrane tension) and of the roundness of the NP. This is due to several reasons, such as the lack of focus of medical and biological experimenters on the mechanical aspect of the interaction. Furthermore, experimental techniques to measure the mechanical properties of cells, without damaging it, are not well developed and require expertise that may not be shared in medical or biological research fields. Last, these mechanical properties vary along the cell membrane [20, 57, 209, 210] and may not be the same close and far from the contact region with the membrane, leading to actual difficulties to evaluate them locally. Finally, the lack of comparative experimental investigations on the influence of both geometrical and mechanical properties does not enable to directly compare the results from the sensitivity analyses with experimental results available in the literature. Nonetheless, all the aforementioned references tend to highlight the role of the aspect ratio of the NP, even though their conclusions derive from observations performed on several cell types. Hence, the aspect ratio of the NP is an important parameter regardless of the cell itself and all its intrinsic mechanical properties. This result actually matches the conclusion of the sensitivity analysis conducted in this chapter, which is that the aspect ratio of the NP is the most important parameter among those investigated, given that it has the highest Sobol indices.

It was also found experimentally [211] and numerically [105, 212, 213] that if an elliptic particle touches the membrane by its flat side, it will tend to rotate in order to be engulfed by its tip. However, this phenomenon appears to depend on the membrane tension, as demonstrated in [85]: the NP is wrapped in its vertical configuration if the tension is lower than a threshold value of $\bar{\sigma}$ and in its horizontal configuration otherwise. This phenomenon could not be considered in this approach, but is a perspective of future work.

Furthermore, this chapter only considers constant values of $\bar{\sigma}$ and $\bar{\gamma}$ during endocytosis, while they could be variable with respect to f, as explained in [32, 106, 112, 134–140]. Indeed, the cell tends to adapt to the contact with the NP by simultaneously increasing the amount of interactions at the contact region (and consequently increasing the adhesion) and reorganizing its actin network, limiting the increase in the membrane tension. It may explain why the *in vivo* observations [19, 29] concluded that vertical elliptic NPs are more likely to enter the cell than horizontal ones in almost all cases, while our model did not show differences in the wrapping of horizontal and vertical highly elongated NPs, since both do not reach full wrapping. Indeed, the variation of the mechanical properties leads the energy barrier to vanish in most cases. The rearrangement in the microstructure of the cell membrane and its influence on the model predictions is the subject of Chapter 4.

Quantity of interest

The sensitivity analysis, conducted in this chapter, aimed at quantifying the influence of the input parameters $\overline{\gamma}$, $\overline{\sigma}$ and $\overline{r}$ on the wrapping degree at equilibrium $\tilde{f}$. However, as shown in the previous chapters, knowing $\tilde{f}$ does not directly provide information on the uptake of the NP. Indeed, the NP is considered to be engulfed by the cell when the membrane trapped it by merging after the wrapping of the NP. Conducting a study whose QoI is the distance between the two sides of the free membrane ($\max r_{2l}(s_{2l}) - \min r_{2r}(s_{2r})$) could therefore enable to investigate the entry of the NP into the cell more accurately. Furthermore, this fusion of the membrane depends on the membrane tension $\overline{\sigma}$. Hence, it is even more important to evaluate $\overline{\sigma}$ more accurately, as this parameter plays a role in both $\tilde{f}$, and in determining if the NP will remain in the cell.

Approaches for the post-processing of the model

In order to post-process the results of the model, surrogates have been constructed to further conduct global sensitivity analyses. The techniques that have been implemented are among the most commonly used in the literature, which also enables easier comparison based on similar works. Furthermore, the Kriging metamodel was built based on common initial settings for the trend and the covariance functions, which are necessary for the optimization of the algorithm. Still, the performance of the subsequent metamodel are very satisfying ($Q_2^{KRI} = 0.97$). Nonetheless, providing appropriate settings could enable the algorithm to compute faster. However, the metamodel was constructed in approximately 2 minutes with a machine with the same configuration as that presented previously in this chapter. This computation time is reasonable and do not justify to spend efforts for its reduction by providing the lengthscale parameter of the correlation function, determined after prior investigations, for instance.

In addition, the predictions of the metamodels included values out of the domain of definition of the QoI. The application of a clip to the predictions would consequently reduce the distance between the final predictions and the true values.

Distribution of the input parameters

The distributions used to model the input parameters have been set based on the maximum entropy principle, which led to the implementation of uniform distributions for $\overline{\gamma}$ and $\overline{\sigma}$. Still, the same could not be made with the aspect ratio $\overline{r}$ of the NP, defined in $[1/6, 6]$, since a uniform distribution for its entire domain of definition would lead to an under representation of the vertical NPs ($\overline{r} < 1$). As such, a piecewise distribution was used, being a linear combination (with weight coefficients being 1/2) of two uniform distribution in $[1/6, 1[$ and in $]1, 6]$. The probability of having a horizontal NP is therefore the same as that of having a vertical one. However, this distribution does not provide an equivalent probability of having highly elongated vertical NPs as that of having slightly elongated ones. Indeed, with this distribution, $\mathsf{P}(1/6 < \overline{R} < 1/5) < \mathsf{P}(1/5 < \overline{R} < 1/4) < \mathsf{P}(1/4 < \overline{R} < 1/3) < \mathsf{P}(1/2 < \overline{R} < 1)$. In order to have equality between these probabilities, the distribution of $\overline{R}$ for $\overline{R} < 1$ should be the inverse of the uniform distribution for the horizontal NPs, leading to the following

PDF:

$$f_{\bar{R}}(x) = \begin{cases} \frac{1}{2}\frac{1}{6-1}\frac{1}{x^2} = \frac{1}{10}\frac{1}{x^2} & \text{for } x \in [\frac{1}{6}, 1[\\ \frac{1}{2}\frac{1}{6-1} = \frac{1}{10} & \text{for } x \in]1, 6] \\ 0 & \text{otherwise.} \end{cases}$$

The distribution used to build the random input parameters has an influence on the outcome of the sensitivity analyses [214]. In this case, since the very elongated vertical NPs are less represented in the dataset that we have used, and considering that for these values the full wrapping is impossible, one can suppose that a sensitivity analysis, conducted with a more accurate distribution of $\overline{R}$, would emphasize the influence of this parameter, which has been underestimated in this chapter. As such, building a more accurate knowledge on the domain of definition of the input parameters, thanks to experimental measurements for instance, is consequently an interesting perspective for future works. It is nonetheless worth noting that such information is complex to collect, because of the challenges related to the characterization of living cells, as introduced in Chapter 1. It should also be noted that we investigated the sensitivity of the results of the screening methods (Morris indices) to the bounds of the domain of definition of $\overline{\gamma}$ in a proceeding presented at the French Colloquium on Structure Modeling (CSMA) in 2022 [215].

6 Conclusions of Chapter 3

The current chapter presented an investigation of the influence of the aspect ratio of the NP on its wrapping degree at equilibrium. For this purpose, the wrapping of an elliptic NP was modeled and a sensitivity analysis was conducted to compare the influence of the mechanical and geometrical parameters of the system on the final wrapping degree. Preliminary observations of the model predictions have first been presented. The following conclusions have been drawn:

- **Preliminary observations of the model** enabled to observe the effect of the aspect ratio of the NP on the evolution of the variation of the total potential energy, with respect to the wrapping degree of the NP. The difference of curvature of elliptic NPs alongside their circumference causes barriers in the bending energy and thus in the total energy. Large adhesion and low membrane tension tend to reduce the amplitude of these barriers, but it is usually not sufficient for the barrier to vanish, leading to an equilibrium position often placed slightly before it. Circular to slightly elongated NPs (aspect ratios between 1/3 and 2) are consequently the most likely to be fully wrapped by the cell.

- **Surrogate models** have been presented and compared. Kriging metamodel was preferred over PCE based on to accuracy of the predictions, with $Q_2^{KRI} = 0.97$ and $Q_2^{PCE} = 0.79$.
- **A sensitivity analysis** was conducted to quantitatively compare the influence of the mechanical and geometrical properties of the system formed by the cell membrane and the NP. For this purpose, Sobol indices were computed as they account for the individual effect of each variable as well as their interactions with the others. The Sobol indices have been estimated using several algorithms and a comparison of these algorithms, along with a convergence study on the size of the dataset used to compute them, led to estimate them using the Mauntz-Kucherenko algorithm, applied to a dataset containing 10^5 samples. The aspect ratio of the NP is the most influential parameter on its cellular uptake, followed by the adhesion between the NP and the membrane and then by the membrane tension. The adhesion influences the variability of the model predictions twice as much as the membrane tension, and the aspect ratio of the NP influences them three times as much as the membrane tension. The difference between the first and total Sobol indices yielded non negligible interactions between the parameters, as they account for more than 50 % of the effect of each variable.
- **Comparisons with the literature,** although difficult to interpret accurately, tend to confirm the conclusions from our sensitivity analysis as most related papers also showed the importance of the aspect ratio of the NPs on their cellular uptake, regardless of the mechanical properties. However, as mentioned in the discussion, the model used in this chapter does not reproduce faithfully the behavior of a living cell, since it does not represent most of its faculties, such as mechano-adaptation of the membrane during wrapping. The objective of the next chapter is thus to address this issue by proposing a model for this phenomenon.

Chapter 4

MECHANICAL ADAPTATION OF THE MEMBRANE DURING ENDOCYTOSIS

1 Introduction

This chapter presents the enrichment of the model introduced in Chapter 2 and used to conduct investigations on the influence of the aspect ratio of the NP in Chapter 3. The model is indeed enriched by accounting for the mechanical adaptation (or mechano-adaptation) of the cell membrane during the wrapping of the NP. This phenomenon is introduced in Section 2. The parameters, used to model the evolution of the membrane properties, are presented and justified in Section 3. The effects of this new approach on the predictions of wrapping of a circular NP are investigated in Section 4, in which preliminary observations of the contribution of these parameters on the variation of the total potential energy and the phase diagrams are made. Then, these influences are quantified thanks to sensitivity analyses. Last, in Section 4.3, the contributions of the new parameters are compared to those of the initial properties of the system, in order to understand the contribution of the mechano-adaptation on the predictions of uptake of the NP. The same investigation will be extended to the case of elliptic NPs in Chapter 5, to understand the role of their aspect ratio when the mechano-adaptation is taken into account. The content of this chapter is the exhaustive version of an article that will soon be submitted to the International Journal for Numerical Methods in Biomedical Engineering [216]. Part of this work was also presented at the 18th European Mechanics of Materials Conference (EMMC18) in 2022 [217] and to the Western French Congress on Cancer (Journées du Cancéropôle Grand Ouest) in 2021 [218].

2 Membrane mechano-adaptation

This section aims at presenting the observations, reported in the literature, that led us to face the need for taking into account the mechanical adaptation of the membrane in our model. Hence, the way the membrane tension and the adhesion between the NP and the membrane change, as a response to the wrapping of the NP, are presented in the following.

2.1 Membrane tension

During the wrapping process, a tension occurs along the membrane, since the wrapping of the NP requires to stretch the former. However, mechanisms take place in the cell membrane in order to reduce the variations of the membrane tension. Indeed, the cell is not a flat contour, even though in our numerical model it is considered as smooth. It is instead constituted of several invaginations and protuberances, that form membrane reservoirs, as illustrated in Figure 4.1 [120, 134, 138, 219, 220]. These membrane reservoirs are additional membrane material that can be unfolded, in order to prevent the membrane tension from increasing too much. Furthermore, actin filaments also contribute to the unfolding of the membrane reservoirs, as a response to membrane tension. In light of these elements, the membrane tension is considered constant during the wrapping process, leading to $\overline{\sigma}(f) := \overline{\sigma}_0$, that will hereinafter simply be denoted as $\overline{\sigma}$.

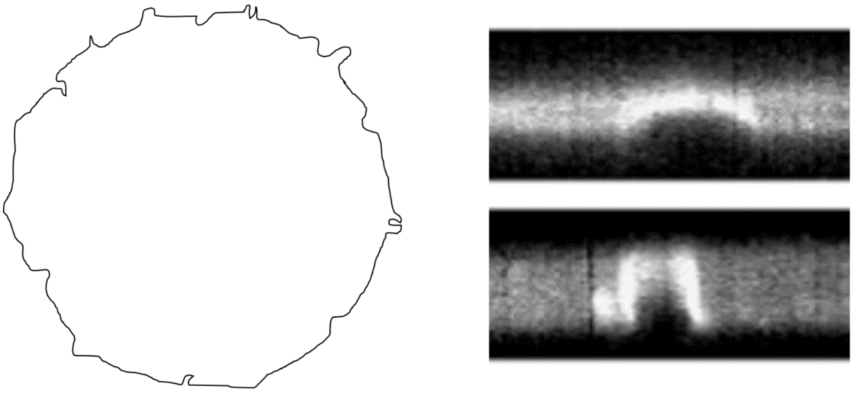

(a) (b)

Figure 4.1: (a) Simplified illustration of the nonsmooth shape of a cell. (b) Observation of a reservoir on a stretched membrane, (top) during and (bottom) after unfolding, reproduced from [138].

2.2 NP-membrane adhesion

The forces of adhesion between the NP and the membrane can be classified into two kinds: the non-specific and the specific ones. The latter are related to bonds between a receptor and a ligand, while the non-specific ones are due to attraction or repulsion between molecules from the NP and the membrane, caused by interactions such as van der Waals, electrostatic bonds or hydrophobic interactions [30, 221]. Regarding the specific adhesion, the movement of membrane receptors has been observed and studied in the case of the interaction with a NP [106, 135] and also for the adhesion of a cell to a substrate [135, 139, 222]. A schematic illustration of this phenomenon is provided in Figure 4.2. Furthermore, the constituents of the membrane are able to reorganize laterally. Thus, the proteins and lipids, that are susceptible to contribute to non-specific adhesion, may reach the contact zone during wrapping and increase the adhesion with the NP, as the wrapping degree increases [20, 222–224]. Consequently, $\overline{\gamma}$ needs to be modeled as a function of the wrapping degree. The nature of this function is discussed in Section 3.

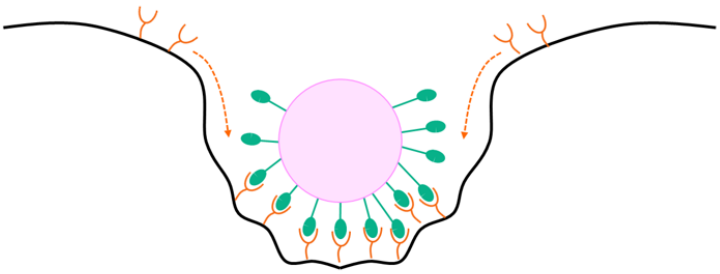

Figure 4.2: Illustration of the lateral reorganization of receptors to the contact region during the wrapping of the NP.

3 Modeling of the mechanical adaptation of the membrane during endocytosis

From now on, the NP-membrane adhesion, denoted as $\overline{\gamma}$, is considered as a function of the wrapping degree f, leading to $\overline{\gamma} := \overline{\gamma}(f)$. The nature of the function, that will be proposed in this work, is determined according to conclusions from the experimental studies, reported in the literature, that have been presented in Section 2.2. Based on that information, one can infer that the adhesion tends to increase during the wrapping process until reaching a final value, which corresponds to the stage when all the possible bonds between constituents from the NP and the membrane are formed [135, 139, 225]. It is however unclear if the constituents responsible for adhesion (specific receptors or ligands, proteins and lipids) start moving to the contact region as soon as the NP approaches the membrane, or if there is a delay, that would correspond to the information transmission to the rest of the membrane. We assume that this process contributes to an increase in adhesion and therefore we expect the adhesion to monotonically increase with respect to the wrapping degree f, starting from an initial minimum value and reaching to a maximum final value.

Among possible candidate functions to model $\overline{\gamma}(f)$ that respect the desired characteristics, *e.g.* hyperbolic tangent, logistic or smoothstep function, a three parameter sigmoidal evolution was chosen. Indeed, these functions depict variations from one plateau to another and enable to tune when the inflection point takes place, which represents different delays before the values of the function start changing significantly. Moreover, sigmoids have already been used in biology for the modeling of measures of nerve activity in terms of the arterial pressure [226–228]. They are also commonly used in other fields of mechanics to model the diffusion phenomenon [229], which may be similar to the behavior of the constituents of the membrane along its circumference. The function $\overline{\gamma}(f)$, used to model the evolution of adhesion during the wrapping process, reads:

$$\overline{\gamma}(f) = \frac{\overline{\gamma}_0(\overline{\gamma}_A - 1)}{1 + \exp\left[-2\overline{\gamma}_S(f - f_{\text{inf}})\right]} + \overline{\gamma}_0, \tag{4.1}$$

where f_{inf} is the inflection point, defined in terms of the delay $\overline{\gamma}_D$ as $f_{\text{inf}} = 0.5 + \overline{\gamma}_D$, while $\overline{\gamma}_A$ represents the amplitude of the transition and $\overline{\gamma}_S$ is the curvature parameter, which is independent of the aforementioned parameters and is used to control the slope of $\overline{\gamma}$ at the inflection point. The initial value of adhesion, *i.e.* $\overline{\gamma}(f \to 0)$, is denoted by $\overline{\gamma}_0$. These parameters are detailed in Table 4.1 and their contributions to $\overline{\gamma}(f)$ are schematically illustrated in Figure 4.3.

Table 4.1: Parameters of the sigmoid functions

Parameter	**Definition**	**Range**
$\overline{\gamma}_A$	Ratio between $\overline{\gamma}(f = 1)$ and $\overline{\gamma}_0$	$[1\ ,\ 6]$
$\overline{\gamma}_D$	Delay of the transition, compared to $f = 0.5$	$[-0.2\ ,\ 0.2]$
$\overline{\gamma}_S$	Curvature parameter	$[10\ ,\ 100]$

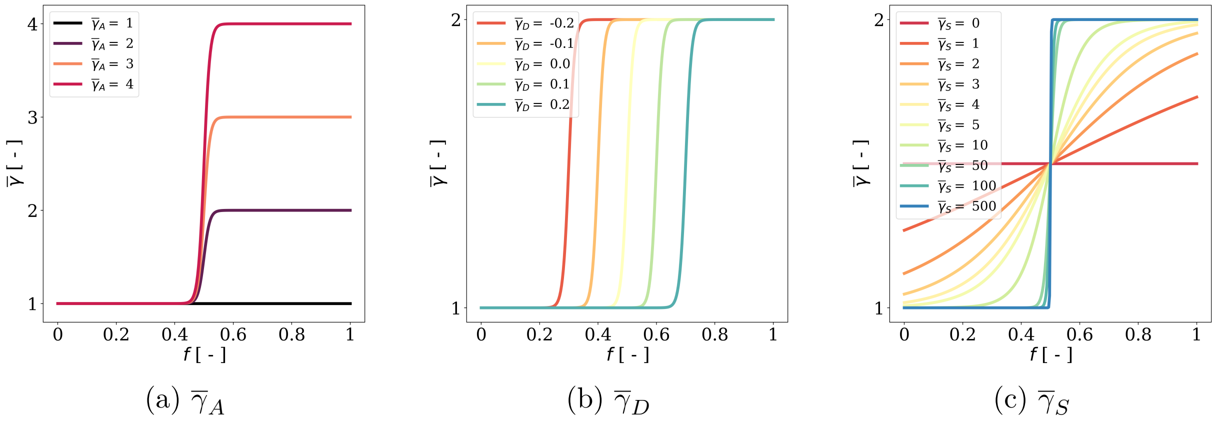

(a) $\overline{\gamma}_A$ (b) $\overline{\gamma}_D$ (c) $\overline{\gamma}_S$

Figure 4.3: Illustration of the effect of the parameters of an increasing sigmoid function: (a) evolution of $\overline{\gamma}(f)$ for (a) $\overline{\gamma}_A \in \{1, 2, 3, 4\}$, (b) $\overline{\gamma}_D \in \{-0.2, -0.1, 0, 0.1, 0.2\}$ and (c) $\overline{\gamma}_S \in [0, 500]$. The parameters $\overline{\gamma}_A$, $\overline{\gamma}_D$ and $\overline{\gamma}_S$, $\overline{\gamma}_0$ and $\overline{\sigma}$ were set to 2, 0, 50, 1 and 2 respectively for all cases, except when stated otherwise in the graphs. Note that for the particular case, where $\overline{\gamma}_S = 0$, $\overline{\gamma}$ is independent of f and equals $\overline{\gamma}_0(\overline{\gamma}_A + 1)/2 = 1.5$.

It is worth noting that the particular configuration where $\overline{\gamma}_A = 1$ corresponds to a passive membrane, in which case the parameters $\overline{\gamma}_D$ and $\overline{\gamma}_S$ have no influence, since the first term of the right-hand side of Equation 4.1 vanishes, yielding $\overline{\gamma}(f) = \overline{\gamma}_0$. The domain of definition of $\overline{\gamma}_D$ is determined using mathematical constraints. Indeed, as the mid value of the transition from $\overline{\gamma}_0$ to $\overline{\gamma}(f \to 1)$ is reached at $f_{\text{inf}} = 0.5 + \overline{\gamma}_D$, $\overline{\gamma}_D$ should vary in $[-0.5, 0.5]$. To avoid numerical singularities and a too early or late transition, we chose to set a smaller interval, *i.e.* $\overline{\gamma}_D \in [-0.2, 0.2]$. Then, the domain of $\overline{\gamma}_S$ was set to represent a reasonable range of values of curvatures, while ensuring that the boundary conditions $\overline{\gamma}(0) = \overline{\gamma}_0$ and $\overline{\gamma}(1) = \overline{\gamma}_0\overline{\gamma}_A$ are respected. Note that the curvature parameter $\overline{\gamma}_S$ is used to evaluate the slope of $\overline{\gamma}(f)$ at the inflection point f_{inf} that is a function of $\overline{\gamma}_S$, $\overline{\gamma}_0$ and $\overline{\gamma}_A$, as described by the expression of the derivative of $\overline{\gamma}(f)$, with respect to f, denoted as $\dot{\overline{\gamma}}$, in Equation 4.2.

$$\dot{\overline{\gamma}}(f) = \frac{2\overline{\gamma}_0(\overline{\gamma}_A - 1)\overline{\gamma}_S \exp\left[-2\overline{\gamma}_S(f - f_{\text{inf}})\right]}{\left(1 + \exp\left[-2\overline{\gamma}_S(f - f_{\text{inf}})\right]\right)^2}, \tag{4.2}$$

which implies that the slope at the inflection point ($f = f_{\text{inf}}$) is $\overline{\gamma}_0(\overline{\gamma}_A - 1)\overline{\gamma}_S/4$. Furthermore, one can also check that the derivative tends to 0 when $f \to 0^+$ and $f \to 1^-$, if $\overline{\gamma}_S$ is large enough. The expressions for the derivative at these boundary points are given in the following:

$$\dot{\overline{\gamma}}(0) = \frac{\overline{\gamma}_0(\overline{\gamma}_A - 1)\overline{\gamma}_S \exp\left[\overline{\gamma}_S(2\overline{\gamma}_D + 1)\right]}{\left(1 + \exp\left[\overline{\gamma}_S(2\overline{\gamma}_D + 1)\right]\right)^2}, \tag{4.3a}$$

$$\dot{\overline{\gamma}}(1) = \frac{\overline{\gamma}_0(\overline{\gamma}_A - 1)\overline{\gamma}_S \exp\left[\overline{\gamma}_S(2\overline{\gamma}_D - 1)\right]}{\left(1 + \exp\left[\overline{\gamma}_S(2\overline{\gamma}_D - 1)\right]\right)^2}. \tag{4.3b}$$

Based on the domain of definition of $\overline{\gamma}_D$, we have $2\overline{\gamma}_D + 1 > 0$ and that $2\overline{\gamma}_D - 1 < 0$. Thus, since

$$\lim_{\overline{\gamma}_S \to \infty} e^{\overline{\gamma}_S(2\overline{\gamma}_D+1)} = \lim_{\overline{\gamma}_S \to \infty} e^{\overline{\gamma}_S(2\overline{\gamma}_D-1)} = 0,$$

one can show that

$$\lim_{\overline{\gamma}_S \to \infty} \dot{\overline{\gamma}}(0) = \lim_{\overline{\gamma}_S \to \infty} \dot{\overline{\gamma}}(1) = 0.$$

When $\overline{\gamma}_0$ and $\overline{\gamma}_A$ are fixed, $\overline{\gamma}_S$ alone enables to control the slope of $\overline{\gamma}$ at $f = f_{\text{inf}}$. Indeed, a positive (resp. negative) value of $\overline{\gamma}_S$ corresponds to an increasing (resp. decreasing) function. The smaller $\overline{\gamma}_S$, the smoother the transition, until the transition degenerates to no transition at all as $\overline{\gamma}_S$ approaches zero. This asymptotic case corresponds to the constant evolution $\overline{\gamma}(f) = \overline{\gamma}_0(1 + \overline{\gamma}_A)/2$, that does not respect the boundary conditions. On the contrary, a large $\overline{\gamma}_S$, in absolute value, leads to a sharp transition, as illustrated in Figure 4.3c. It is possible to show that $\overline{\gamma}(f)$ tends to a step function for large values of $\overline{\gamma}_S$. In addition, this figure also shows, that the boundary conditions, *i.e.* $\overline{\gamma}(0) = \overline{\gamma}_0$ and $\overline{\gamma}(1) = \overline{\gamma}_0\overline{\gamma}_A$, are not reached for small values of $\overline{\gamma}_S$. Thus, the boundaries of the domain of definition of $\overline{\gamma}_S$ are defined so that the boundary conditions are fulfilled even for the extreme values of $\overline{\gamma}_D$. The variation of $\overline{\gamma}(f)$ for several values of $\overline{\gamma}_S$ with $\overline{\gamma}_D = -0.2$ and $\overline{\gamma}_D = 0.2$ is represented in Figure 4.4.

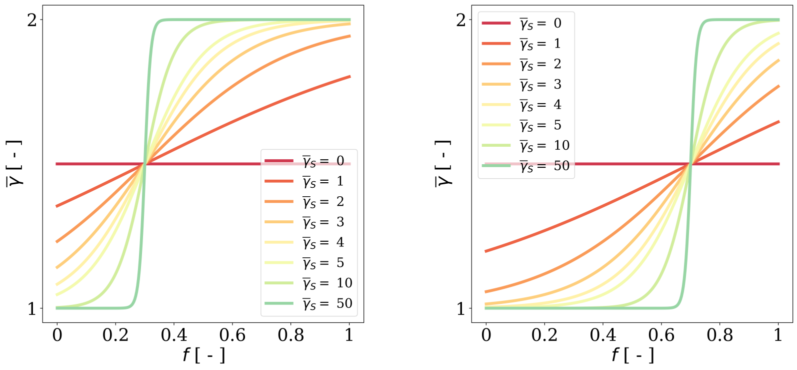

(a) $\overline{\gamma}_D = -0.2$

(b) $\overline{\gamma}_D = 0.2$

Figure 4.4: Illustration of the effect of $\overline{\gamma}_D$ for (a) $\overline{\gamma}_D = -0.2$ and (b) $\overline{\gamma}_D = 0.2$, both with $(\overline{\gamma}_A, \overline{\gamma}_0, \overline{\sigma}) = (2, 1, 2)$.

Based on this figure, the boundary conditions tend to be respected for $\overline{\gamma}_S \geq 10$, which thereby defines the lower bound of the domain of definition of $\overline{\gamma}_S$. Still, because of the asymptotic behavior of the sigmoid function, it only tends to the target bounds, *i.e.* $(\overline{\gamma}_0, \overline{\gamma}_0 \overline{\gamma}_A)$, without reaching them. The upper bound of $\overline{\gamma}_S$ is set to 100, since there is no notable change in $\overline{\gamma}(f)$ when increasing $\overline{\gamma}_S$ above this value. Furthermore, for $\overline{\gamma}_S > 100$, numerical issues are encountered because $\overline{\gamma}(f)$ gets close to a step function, which implies discretization problems around the transition point f_{inf}.

Last, the domain of definition of $\overline{\gamma}_A$ is more complicated to determine. The lower bound of $\overline{\gamma}_A$ is equal to 1 as $\overline{\gamma}$ is an increasing function of f. The upper bound of $\overline{\gamma}_A$ could not be set based on mathematical considerations and was thus arbitrarily set to 6, as it is close to the ratio between the upper and lower bounds of the domain of definition of $\overline{\gamma}_0$, which has been defined in Section 4 of Chapter 2, as the interval $[1, 8]$. However, since the sampling is a crucial step in sensitivity analyses [230], this hypothesis will be discussed later in Section 6.

4 Influence of the mechanical adaptation of the membrane on the predictions of endocytosis of a circular nanoparticle

It is not known yet whether accounting for the mechanical adaptation of the membrane has an effect on the model predictions. To determine if it is the case, a sensitivity analysis will be conducted in order to evaluate the influence of the newly introduced parameters on the model outputs. Hence, preliminary observations of the model will be made in Section 4.1. This enables us to have a general picture of the effect of the mechano-adaptation on the model. A sensitivity analysis will then be conducted afterwards, in Section 4.2, in order to rank the parameters based on their respective influence. Last, another sensitivity analysis will be performed in Section 4.3, in order to compare the influence of the parameters used to describe the initial properties of the system with those used to model the membrane mechanical adaptation. The Python script developed to build the metamodels and to conduct the sensitivity analyses is available in the Github repository[1] associated to this thesis.

---

[1] `https://github.com/SarahIaquinta/PhDthesis`

4.1 Preliminary observations

To get an insight into the effect of the membrane mechano-adaptation on the predictions of endocytosis, some results obtained from the model can be compared between the cases of an active (*i.e.* adaptive) and a passive membrane. As explained in Chapter 2, the first step of the model is to compute the evolution of the variation of the potential energy $\overline{\Delta E}(f)$. Figure 4.5 illustrates the influence of $\overline{\gamma}_A$, $\overline{\gamma}_D$ and $\overline{\gamma}_S$ on $\overline{\Delta E}(f)$ and thus on $\tilde{f}$ for two values for the tuple $(\overline{\gamma}_0, \overline{\sigma})$, in order to compare the cases where $\overline{\Delta E}$ increases and decreases.

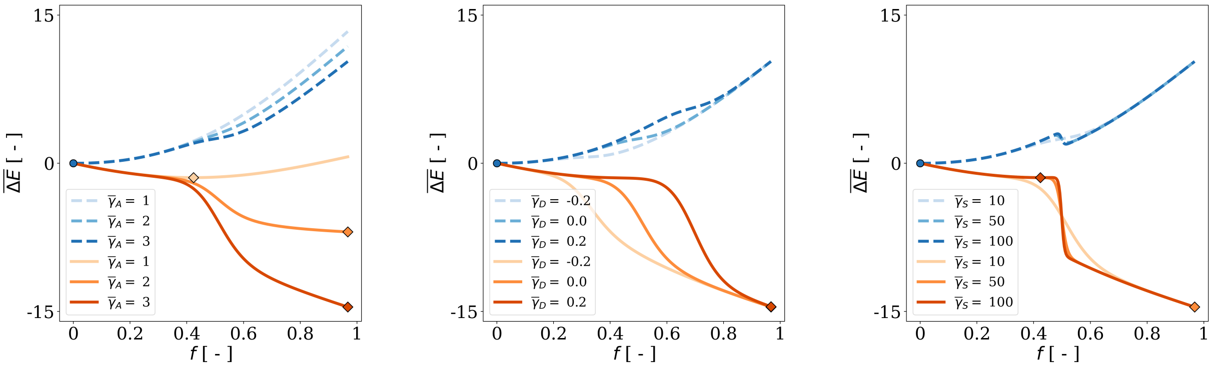

(a) $\overline{\gamma}_A$ (b) $\overline{\gamma}_D$ (c) $\overline{\gamma}_S$

Figure 4.5: Illustration of the effect of the parameters of the sigmoid for $(\overline{\gamma}_0, \overline{\sigma}) = (1, 1)$ (dashed blue lines) and $(\overline{\gamma}_0, \overline{\sigma}) = (10, 2)$ (solid orange lines) on $\overline{\Delta E}(f)$. The position of the equilibrium is showed by a circular marker for increasing $\overline{\Delta E}(f)$ and by a diamond otherwise. The parameter values are $(\overline{\gamma}_A, \overline{\gamma}_D, \overline{\gamma}_S) = (3, 0, 10)$ for all cases, except when stated otherwise in the graphs.

These results show that for $(\overline{\gamma}_0, \overline{\sigma}) = (1, 1)$, *i.e.* increasing $\overline{\Delta E}$, $\tilde{f}$ is not altered when the parameters of the sigmoid are modified. When $\overline{\Delta E}$ decreases, *i.e.* when $(\overline{\gamma}_0, \overline{\sigma}) = (10, 2)$, the location of the first local minimum is altered when $\overline{\gamma}_A$ and $\overline{\gamma}_S$ vary, while $\overline{\gamma}_D$ does not influence $\tilde{f}$ in this case. Furthermore, the initial properties $(\overline{\gamma}_0, \overline{\sigma})$ also have an influence on the way $\tilde{f}$ is altered by the parameters of the sigmoid. Hence, one can already conclude that most likely all parameters are influential on the values of $\tilde{f}$, and that they have coupled effects. To generalize the inferences resulting from these observations of $\overline{\Delta E}$ for a given tuple of $(\overline{\gamma}_0, \overline{\sigma})$ to their entire domain of definition, phase diagrams are compared for different values of $\overline{\gamma}_A$, $\overline{\gamma}_D$ and $\overline{\gamma}_S$ in Figures 4.6, 4.7 and 4.8, where the dotted lines in the background correspond to the contours of the phase diagram in the case of a passive membrane, which was already depicted in Figure 3.10.

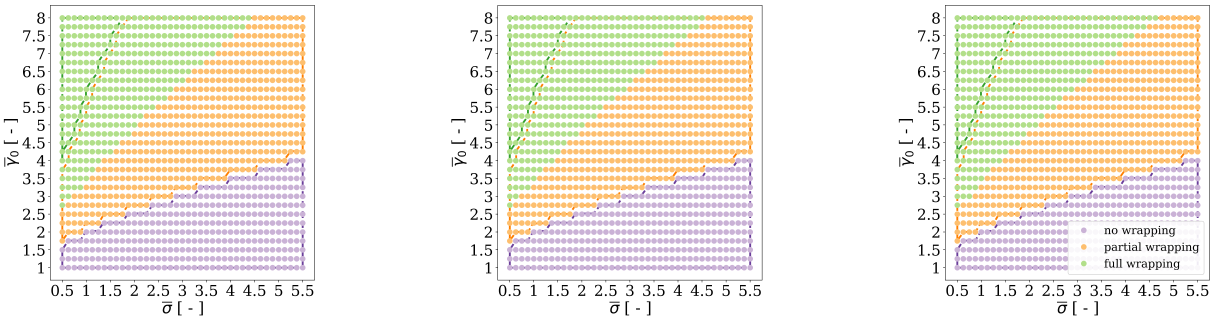

(a) $\overline{\gamma}_A = 2$ (b) $\overline{\gamma}_A = 3$ (c) $\overline{\gamma}_A = 4$

Figure 4.6: Effect of $\overline{\gamma}_A$ on the phase diagram, when $\overline{\gamma}_D = 0$ and $\overline{\gamma}_S = 50$. The dotted lines in the background correspond to the contours of the phase diagram in the case of a passive membrane, which was already depicted in Figure 3.10.

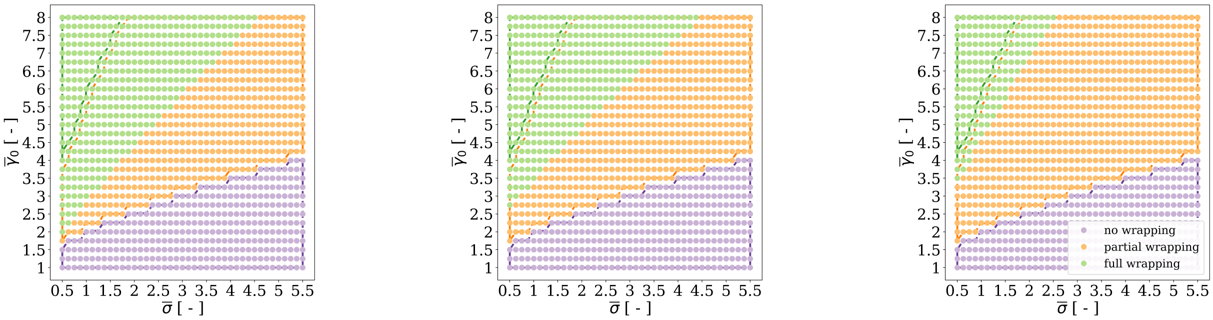

(a) $\overline{\gamma}_D = -0.2$ (b) $\overline{\gamma}_D = 0$ (c) $\overline{\gamma}_D = 0.2$

Figure 4.7: Effect of $\overline{\gamma}_D$ on the phase diagram, when $\overline{\gamma}_A = 2$ and $\overline{\gamma}_S = 50$. The dotted lines in the background correspond to the contours of the phase diagram in the case of a passive membrane, which was already depicted in Figure 3.10.

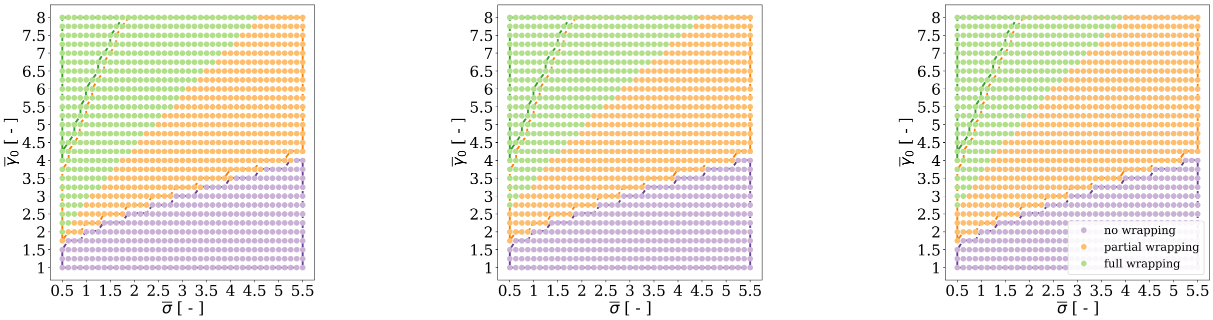

(a) $\overline{\gamma}_S = 10$ (b) $\overline{\gamma}_S = 50$ (c) $\overline{\gamma}_S = 100$

Figure 4.8: Effect of $\overline{\gamma}_S$ on the phase diagram, when $\overline{\gamma}_A = 2$ and $\overline{\gamma}_D = 0$. The dotted lines in the background correspond to the contours of the phase diagram in the case of a passive membrane, which was already depicted in Figure 3.10.

These diagrams enable us to generalize the previous observations, since the distribution of the regions corresponding to partial and full wrapping is noticeably different between the diagrams. In addition, Figure 4.6 shows that the value of $\overline{\gamma}_A$, as long as it is different from 1 (passive membrane), does not significantly change the phase diagram. Also, increasing $\overline{\gamma}_D$ leads to a reduction of the proportion of full wrapping (green dots in the phase diagrams). The same observation, in a smaller scale for this range of values, is made for $\overline{\gamma}_S$. Nonetheless, the proportion of no wrapping does not seem to be altered by the mechanical adaptation of the membrane, as it remains the same, regardless of the values taken by $\overline{\gamma}_A$, $\overline{\gamma}_D$ and $\overline{\gamma}_S$.

From these observations, one can already conclude that accounting for the mechanical adaptation of the membrane in the model leads to different predictions. However, these first results only yield qualitative interpretations and do not provide accurate information on the influence of the parameters of the sigmoid function used to describe the variation of the adhesion during the wrapping of the NP (Equation 4.1). Sensitivity analyses will consequently be conducted in Section 4.2 in order to quantify the influence of the mechanical adaptation of the membrane on the full wrapping predictions based on the model.

4.2 Quantification of the influence of the parameters of the sigmoid

The model, presented in Equation 4.1, has three input parameters: $\overline{\gamma}_A$, $\overline{\gamma}_D$ and $\overline{\gamma}_S$. The output is the proportion of cases which led to a full wrapping state at equilibrium, denoted by ψ_3. Similar to the approach used in Chapter 3 to perform the sensitivity analysis on $\tilde{f}$, a surrogate model will first be built in Section 4.2.1, in order to generate the estimations necessary to evaluate the Sobol indices. The results of the subsequent sensitivity analysis are presented in Section 4.2.2.

4.2.1 Surrogate model

Sampling A dataset containing $2^{10} = 1024$ realizations, built using qMC sampling method, is generated for the three independent random variables $\overline{\Gamma}_A$, $\overline{\Gamma}_D$ and $\overline{\Gamma}_S$. As introduced above, only the bounds of the domain of definition of these variables are known. Thus, following the maximum entropy principle [203], a uniform distribution is used to model them. Hence, $\overline{\Gamma}_A \sim \mathcal{U}(1, 6)$, $\overline{\Gamma}_D \sim \mathcal{U}(-0.2, 0.2)$ and $\overline{\Gamma}_S \sim \mathcal{U}(10, 100)$.

The corresponding values of the proportion of phase 3, Ψ_3, are then calculated for each realization. The histogram of Ψ_3, based on the dataset, along with a kernel density estimation of its PDF, are depicted in Figure 4.9.

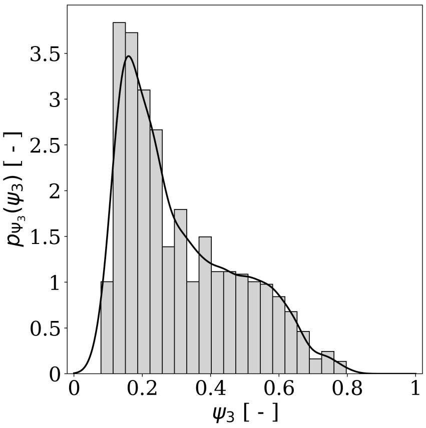

Figure 4.9: Histogram of Ψ_3 based on the dataset, along with its PDF.

Figure 4.10 depicts the convergence of the mean and the standard deviation of the random variable describing the proportion of phase 3, Ψ_3, in terms of the number of samples along with the corresponding standard deviation (shaded gray zones). To determine the convergence, the absolute normalized gradient is computed, similar to the study presented in Chapter 3.

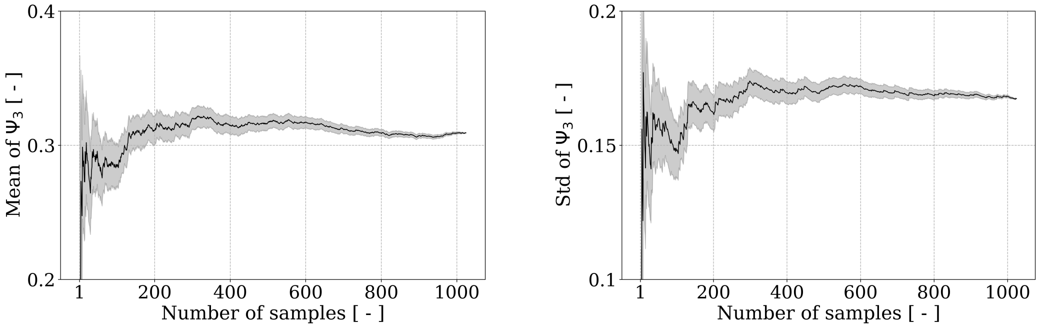

(a) (b)

Figure 4.10: (a) Mean and (b) standard deviation of Ψ_3, with respect to the number of simulations, along with their respective standard deviation denoted by the gray regions.

Figure 4.11 shows the absolute normalized gradients of the average and the standard deviation of Ψ_3, in terms of the number of samples. According to these graphs, the dataset needs to contain respectively at least 117 and 144 estimations of the QoI for its mean and standard deviation to converge. Hence, to ensure the convergence of both of these statistics, at least 144 model estimations are needed.

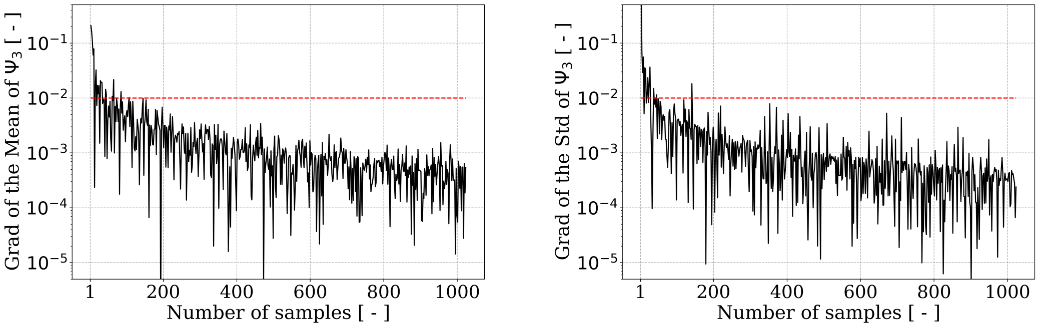

(a) (b)

Figure 4.11: Absolute normalized gradient of the (a) mean and (b) standard deviation of Ψ_3, with respect to the number of simulations. The dashed lines correspond to the threshold of 1 %. Only one out of two points have been represented for the clarity of the plots.

Implementation of the metamodels As in the previous chapter, a surrogate model was built to generate approximations of the model using OpenTURNS. According to the study on the data representativeness above, 144 samples are necessary to properly capture the behavior of the model. This is thus the minimal size of the test dataset. The whole dataset being of size 1024, the portion of the dataset used for final validation is therefore set to 20 %, which corresponds to 204 samples. The remaining 820 samples are used for the training of the metamodels. Both Kriging and PCE metamodels have been constructed. The former has been implemented using the same configuration as in Chapter 3. The truncation degree of the PCE has been determined by comparing the predictivity factor Q_2 obtained with different degrees. It is worth noting that the maximum truncation degree for which singularities are avoided, when using a dataset of 820 samples with three input parameters, should respect the following rule of thumb: $2\binom{p+3}{3} < 820$, leading to is $p \leq 11$ (see Section 3.2.2). Figure 4.12 represents the accuracy of the PCE predictions in terms of the truncation degree, and shows that Q_2 is the closest to 1 for a truncation degree of 10, with $Q_2^{PCE} = 0.98$.

Figure 4.13 compares the predictions obtained using Kriging and PCE models with the predicted vs true plots along with their PDFs, estimated with 10^5 MC responses of the metamodels. Both metamodels yield satisfying results, with predictivity factors almost equal to 1, being $Q_2^{KRI} = 0.99$ and $Q_2^{PCE} = 0.98$. In conclusion, both metamodels can be used to perform the sensitivity analysis, that will be presented in the following section.

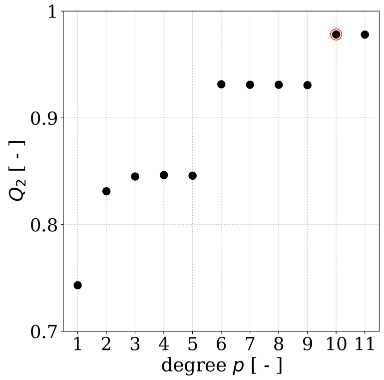

Figure 4.12: Accuracy of PCE predictions in terms of the truncation degree.

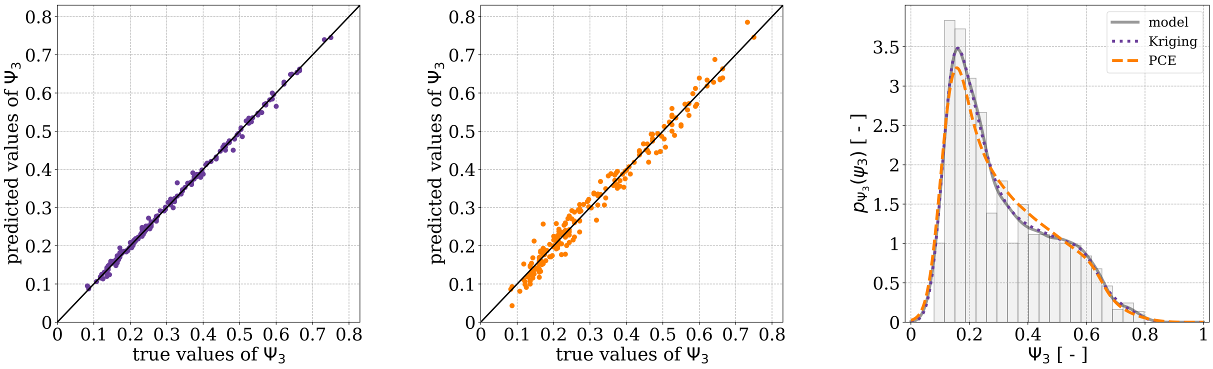

(a) Kriging (b) PCE (c) PDFs

Figure 4.13: Predicted vs true values obtained with (a) Kriging and (b) PCE metamodels after optimization of their hyperparameters, along with a comparison of the PDFs obtained for these metamodels.

4.2.2 Variance based sensitivity analysis: Sobol indices

Similar to the metamodel construction, sensitivity indices are also computed using the OpenTURNS library and the associated script is available in the aforementioned Github repository. As introduced in Chapter 3, the Sobol sensitivity indices can be analytically calculated directly from the coefficients of the PCE metamodel [178], or they can be approximated based on evaluations of the different terms related to the variance of the output. In this case, based on the rule of thumb introduced in Section 2 of Chapter 3, which estimates the amount of data points necessary to compute the Sobol indices, according to the behavior of the model and to the number of input parameters, we assume that 10^4 samples are necessary to estimate the influence of the inputs on the output of our model, which is a function of three inputs and is nonlinear and nonmonotonous.

In order to generate these samples, both Kriging and PCE metamodels, constructed in the previous section, can be used. However, recalling that the Sobol indices can be calculated analytically from the coefficients of PCE, it is not necessary to generate 10^4 estimations of the model to approximate the Sobol indices with this metamodel. As such, these estimations will be generated only for Kriging, and the indices calculated with both methods will be compared.

Sampling of the input parameters

Distribution The only available information regarding the input parameters, is their lower and upper bounds, as introduced in Table 4.1. Thus, based on a non-parametric probabilistic approach, a uniform distribution is the only candidate that maximizes the entropy measure [203]. As such, the input parameters are modeled as independent random variables following uniform PDFs, similar to the construction of the metamodels.

Number of estimations The influence of the number of realizations used to compute the Sobol indices based on the Kriging metamodel was investigated. The first and total Sobol indices, computed with the Mauntz-Kucherenko algorithm, are represented in Figure 4.14, with respect to the number of samples that have been used to estimate them.

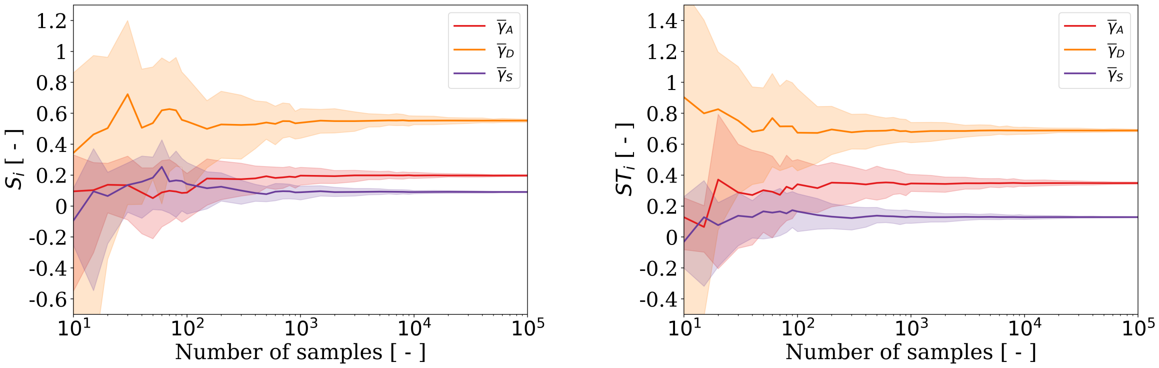

(a) (b)

Figure 4.14: Convergence of the (a) first and (b) total Sobol indices, computed with the Mauntz-Kucherenko algorithm. The shaded regions correspond to the 95 % confidence intervals.

Their 95 % CIs are depicted in Figure 4.15. Adopting the convergence criterion introduced in Chapter 3, the Sobol indices converge when the range of the CIs is smaller than 0.05. Hence, first and total indices converge with 1.2×10^4 and 8×10^3 samples, respectively.

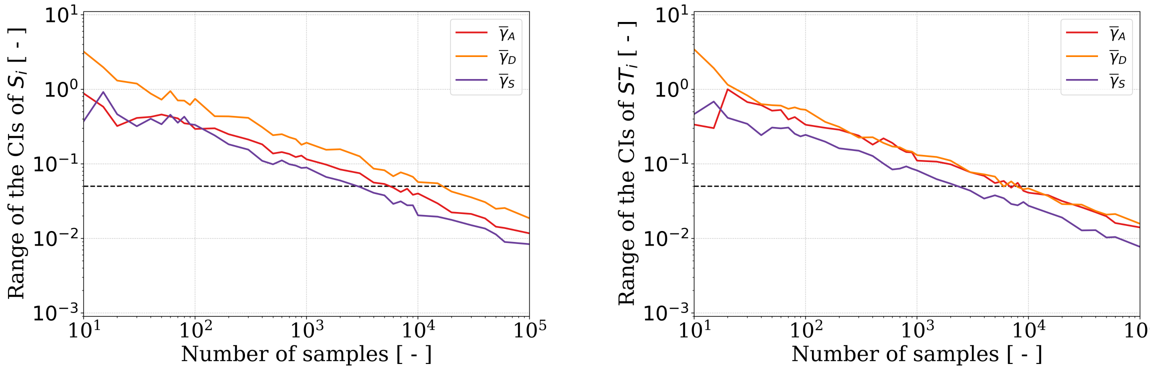

(a) (b)

Figure 4.15: Ranges of the 95 % confidence intervals for the (a) first and (b) total Sobol indices, in terms of the number of estimations of the metamodel, computed using the Mauntz-Kucherenko algorithm. The black dashed lines correspond to a threshold of 0.05.

Influence of the algorithm The investigation of the convergence of the Sobol indices, with respect to the number of samples, conducted for the Mauntz-Kucherenko, Saltelli, Jansen, and Martinez algorithms, did not reveal differences in the mean values nor in the CIs, when more than 3×10^4 samples are used. The number of samples necessary for the Sobol indices to converge with these algorithms are compared in Table 4.2. More details are provided in Section 3.1 of Appendix D.

Table 4.2: Number of samples necessary for the convergence of the Sobol indices following the criterion on the range of the 95 % confidence intervals of S_i and ST_i, estimated with several algorithms.

Index	**Mauntz-Kucherenko**	**Saltelli**	**Jansen**	**Martinez**
S_i	2×10^4	10^4	10^4	10^4
ST_i	9×10^4	3×10^4	9×10^4	3×10^4

The Sobol indices obtained with the entire dataset, *i.e.* 10^5 samples, are presented in Table 4.3, where they are compared to those obtained directly from the coefficients of PCE. The indices computed with estimations from the Kriging metamodel yielded equal indices for all the algorithms. They are also equal to those computed with PCE. In this case study, the algorithm used to compute the Sobol indices has no influence on the results.

Table 4.3: Comparison of the first and total Sobol indices, calculated analytically, based on the coefficients of PCE, with those computed using 10^5 estimations of the Kriging metamodel.

Index	Parameter	PCE	Kriging
S_i	$\overline{\gamma}_A$	0.20	0.20
	$\overline{\gamma}_D$	0.56	0.56
	$\overline{\gamma}_S$	0.09	0.09
ST_i	$\overline{\gamma}_A$	0.35	0.35
	$\overline{\gamma}_D$	0.68	0.68
	$\overline{\gamma}_S$	0.13	0.13

Interpretation of the Sobol indices According to the Sobol indices, the curvature parameter, $\overline{\gamma}_S$, is the least significant variable, with a total index of 0.13. Its first order index $S_{\overline{\gamma}_S}$ is close to the total one, meaning that the interactions of $\overline{\gamma}_S$ with the other parameters are negligible. The most important variable is the delay of the transition, $\overline{\gamma}_D$, with a total index of 0.68. Its first order index is 0.56, implying that the Sobol index relative to the interactions of $\overline{\gamma}_D$ with $\overline{\gamma}_A$ and $\overline{\gamma}_S$ are $0.68-0.56 = 0.12$. Furthermore, since the interactions of $\overline{\gamma}_S$ are negligible, $\overline{\gamma}_D$ solely interacts with $\overline{\gamma}_A$, hence $S_{\overline{\gamma}_A,\overline{\gamma}_D} \approx 0.12$. The amplitude of the transition, $\overline{\gamma}_A$, is the second most influential parameter on the variance of Ψ_3 ($ST_{\overline{\gamma}_A} = 0.35$) and the interactions of $\overline{\gamma}_D$ with $\overline{\gamma}_A$ contribute by $100 \times 0.12/0.35 = 34\,\%$ to the effect of $\overline{\gamma}_A$ on Ψ_3.

These results lead to the conclusion that $\overline{\gamma}_D$ is the most important parameter, followed by $\overline{\gamma}_A$, which contributes to the output almost twice as little as $\overline{\gamma}_D$. The interactions between these two variables also contribute to the variance of the output. Last, $ST_{\overline{\gamma}_S} = 0.13$, which, even if it is small, is not negligible compared to the order of magnitude of the contribution of the other parameters.

This section helped to observe first qualitatively and then quantitatively the influence of different parameters used to model the membrane mechano-adaptation during the wrapping of a circular NP. However, it was also shown that the initial properties of the system, $\overline{\gamma}_0$ and $\overline{\sigma}$, remain influential on the predictions of the model, since the phase diagrams still present different regions depending on the values of these parameters (see Section 4.1). Hence, Section 4.3 aims at comparing the influence of the initial parameters with those relative to the membrane mechano-adaptation.

4.3 Comparison of the effects of the mechanical adaptation with respect to the initial parameters

The results presented in the previous section showed that the mechanical adaptation of the membrane, as well as the initial parameters $(\overline{\gamma}_0, \sigma)$, have an effect on the predictions of the model. For instance, Figure 4.6a shows that the phases are indeed altered, when accounting for the mechanical adaptation. In addition, this diagram shows that the predictions also depend on both $\overline{\gamma}_0$ and $\overline{\sigma}$, otherwise the diagram would be filled with a single phase only. The objective of this section is consequently to determine how each parameter, among the initial ones and those relative to the mechanical adaptation, *i.e.* $\overline{\gamma}_0$, $\overline{\sigma}$, $\overline{\gamma}_A$, $\overline{\gamma}_D$ and $\overline{\gamma}_S$, influences the model predictions of the cellular uptake of a circular NP. For this purpose, a sensitivity analysis will be performed in Section 4.3.2 once a surrogate model is built, as presented in Section 4.3.1. Contrary to the previous sensitivity analyses, no additional result will be displayed for preliminary observations, since the effect of the involved parameters was already discussed in the introduction of this section, based on the graphs presented in Section 4.1.

In this case, the study does not involve ψ_3, since the influence of the initial parameters $\overline{\gamma}_0$ and $\overline{\sigma}$ is also investigated. Hence, the QoI, *i.e.* the output of the model, is the wrapping degree at equilibrium $\tilde{F}$ and the inputs variable are $\overline{\Gamma}_0$, $\overline{\Sigma}$, $\overline{\Gamma}_A$, $\overline{\Gamma}_D$ and $\overline{\Gamma}_S$, whose domains of definitions have been introduced earlier in Section 3.

4.3.1 Surrogate model

Data representativeness Analogously to the construction of the previous surrogate models, the data representativeness is first investigated. Since the QoI is $\tilde{F}$, the computation time, necessary to obtain each point, is only around 1 second. Hence, a dataset of size $2^{12} = 4096$ realizations of input parameters and the corresponding values of $\tilde{F}$, has been generated in about 2 hours, with our available computational resources. Still, even if this computation time is reasonable, especially compared to those necessary to generate the values of Ψ_3, one does not *a priori* know the number of samples that will be necessary for the Sobol indices to converge. For this reason, a surrogate model is constructed even in this case, in order to ensure that enough samples are available to verify the convergence of the Sobol indices. The histogram of the random variable of the wrapping degree at equilibrium, $\tilde{F}$, based on the dataset, along with a kernel density estimation of its PDF, are depicted in Figure 4.16.

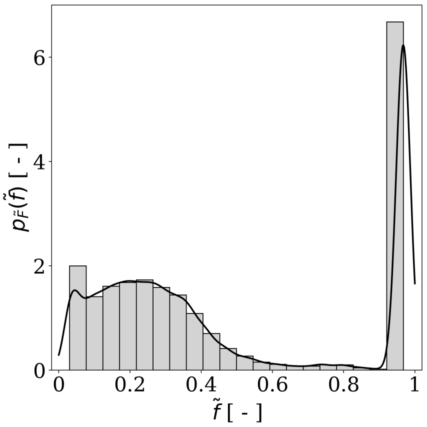

Figure 4.16: Histogram of $\tilde{F}$, based on the dataset, along with an estimation for its PDF.

The data representativeness is investigated in order to determine the minimum number of samples the dataset needs to contain to be representative of the behavior of the model. For this purpose, the cumulative mean and standard deviation of $\tilde{F}$, along with their absolute gradient, in terms of the number of samples, are displayed in Figures 4.17 and 4.18.

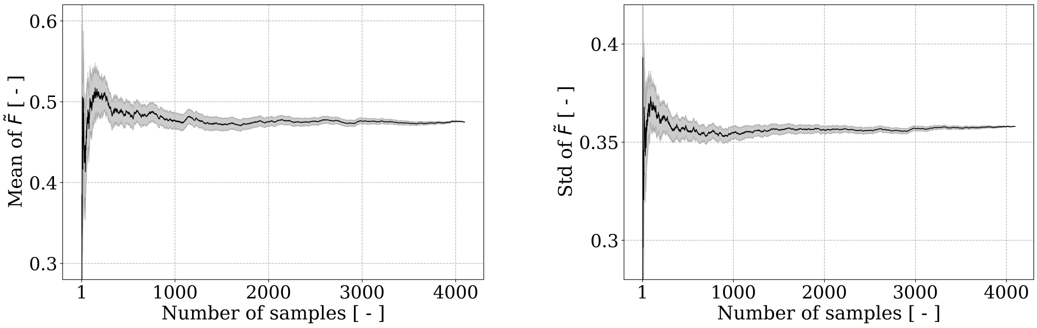

(a)

(b)

Figure 4.17: (a) Mean and (b) standard deviation of $\tilde{F}$, with respect to the number of simulations.

According to these figures, one can deduce that 91 and 73 samples are necessary for the mean and standard deviation to converge, respectively. The minimum number of samples for both to converge is thus 91. This number is very small compared to the size of the dataset as it only represents 2 % of it.

Implementation of the metamodels To proceed to the final validation of the metamodels, 20 % of the dataset, *i.e.* 820 samples, will be taken in order to have enough data to calculate properly the value of the predictivity factor Q_2. Hence, the remaining 80 %

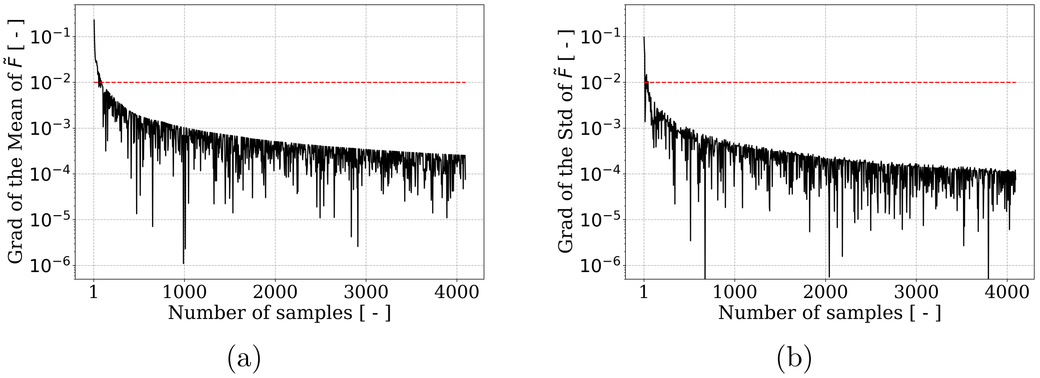

Figure 4.18: Absolute normalized gradient of the (a) mean and (b) standard deviation of $\tilde{F}$, with respect to the number of simulations. The dashed lines correspond to the threshold of 1 %. Only one out of four points have been represented for the clarity of the plots.

of the data, *i.e.* 3276 samples, is used to build the metamodels.

PCE and Kriging metamodels have been constructed. The latter was built using the same settings as in the previous investigations conducted in this thesis. Concerning the former, the truncation degree p, that provided the most accurate predictions, has been determined by comparing the accuracy of the predictions for truncation degrees between 1 and 7, which is the maximum degree that prevents singularities issues for a model with five input parameters and a dataset containing 3276 samples, following the rule of thumb introduced in Chapter 3. The performance of PCE in terms of the truncation degree is illustrated in Figure 4.19, showing that Q_2 is the closest to 1 for $p = 7$, with $Q_2^{PCE} = 0.80$.

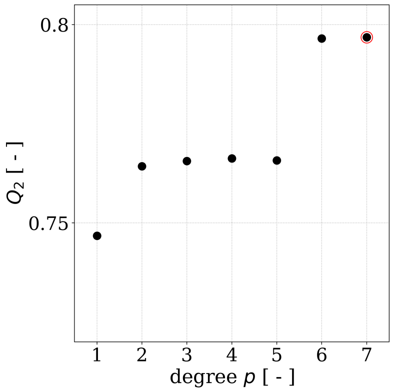

Figure 4.19: Accuracy of PCE predictions in terms of the truncation degree.

Figure 4.20 compares the predictions obtained via Kriging and PCE algorithms with the predicted vs true plots as well as the kernel density estimation of their PDFs using an input dataset of 10^5 samples generated using the MC technique. Both metamodels yield mediocre results, with a predictive square correlation coefficient equal to $Q_2^{KRI} = 0.86$ and $Q_2^{PCE} = 0.80$.

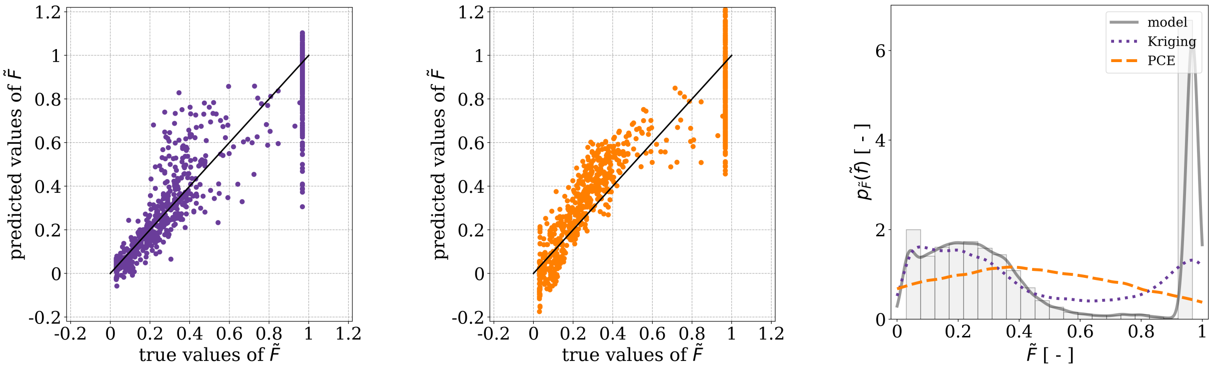

(a) Kriging (b) PCE (c) PDFs

Figure 4.20: Predicted vs true values obtained with (a) Kriging and (b) PCE algorithms, after optimization of the hyperparameters, along with a comparison of the PDFs obtained for these metamodels and the histogram of the data from the model.

In addition, one can observe that the accuracy of the metamodels is lower in this case, compared to the previous one, which involved ψ_3. This can be explained by the distribution of the data, represented in Figure 4.16. Indeed, from the data, it seems that the variable $\tilde{F}$ has a bimodal distribution, as the data is mostly clustered in two regions: on the interval $\tilde{f} \in [0, 0.4]$ and around $\tilde{f} = 0.97$. In Figure 4.20, one can distinguish a large amount of points corresponding to true values close to $\tilde{f} = 0.97$. These points, that gather vertically, are due to misapproximations of the metamodel for such values, which corresponds to the maximal wrapping degree at equilibrium. As such, there is a bound effect which causes a large amount of input data that yield a response equal to that bound. Furthermore, the bound effect tends to mislead the metamodel. Indeed, when the first local minimum of the total potential energy is outside the interval domain $[0.03, 0.97]$, the wrapping degree is clipped to the extreme values of the interval ($\tilde{f} = 0.03$ or $\tilde{f} = 0.97$), which the metamodel struggles to reproduce. The application of a clip to the predictions of the metamodels, as introduced in the previous studies, would consequently lead to the improvement of the accuracy of the estimations.

In this case, the approximation of the model using PCE yielded a value of Q_2 similar to that obtained for Kriging, mostly due to the difficulty to properly predict the data around $\tilde{f} = 0.97$, as showed by the dispersion of the associated predictions. Based on the approximation of the PDFs of the metamodels estimations, one can see that Kriging represents a bimodal distribution of $\tilde{F}$, with the same location for the peaks (modes) as that of the model, even though the value of the peaks of the PDFs at the modes are not equal to those of the model. In contrast, PCE yields a close-to-uniform distribution, with a weak peak around $\tilde{f} = 0.4$.

4.3.2 Sensitivty analysis

Sampling of the input parameters

Distribution Similar to the previous studies, because of the lack of experimental data, the input parameters $\overline{\gamma}_0$, $\overline{\sigma}$, $\overline{\gamma}_A$, $\overline{\gamma}_D$ and $\overline{\gamma}_S$ are modeled as independent random variables following uniform PDFs, in order to maximize the entropy measure [203].

Number of estimations The first and total Sobol indices, along with their respective 95 % CIs, in terms of the number of samples, estimated with the Mauntz-Kucherenko algorithm, are depicted in Figure 4.21. The range of their CIs are represented in Figure 4.22.

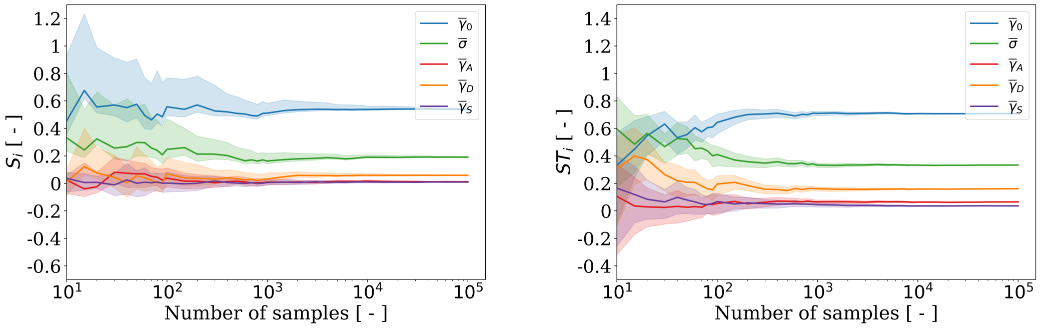

(a) (b)

Figure 4.21: Convergence of the (a) first and (b) total Sobol indices, computed with the Mauntz-Kucherenko algorithm. The shaded regions correspond to the 95 % confidence intervals.

The range of the CIs of the first (resp. total) Sobol indices is smaller than 0.05 when using more than 5×10^3 (resp. 9×10^3) samples. As such, to ensure convergence with respect to all Sobol indices, at least 9×10^3 samples need to be used.

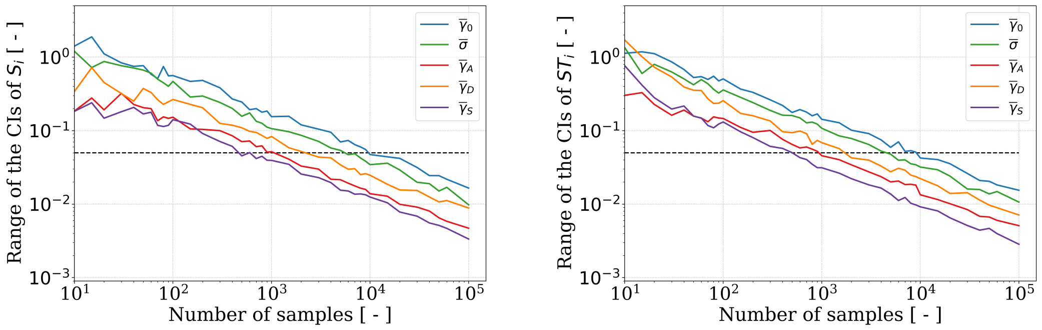

(a) (b)

Figure 4.22: Range of the 95 % confidence interval of the (a) first and (b) total Sobol indices in terms of the number of samples, computed with the Mauntz-Kucherenko algorithm. Dashed lines correspond to the numerical convergence threshold of 0.05.

Influence of the algorithm The four algorithms reach convergence, considering the criterion of the range of the CIs, with 9×10^4 samples for the Mauntz-Kucherenko and Saltelli algorithms, while 10^4 and 2×10^4 samples are necessary for the Jansen and Matinez algorithms, respectively, as summarized in Table 4.4. Hence, at least 9×10^4 samples are necessary to ensure the convergence of the four algorithms. The convergence plots for the remaining algorithms are provided in Section 3.2 of Appendix D.

Table 4.4: Number of samples necessary for the convergence of the Sobol indices following the criterion on the range of the 95 % confidence intervals of S_i and ST_i, estimated with several algorithms.

Index	**Mauntz-Kucherenko**	**Saltelli**	**Jansen**	**Martinez**
S_i	10^4	9×10^4	10^4	10^4
ST_i	9×10^4	2×10^4	10^4	2×10^4

Regardless of the algorithm, the convergence criterion is fulfilled when using 10^5 samples. These indices will then be used to compare their converged values with those obtained using PCE in Table 4.5.

Table 4.5: Comparison of the first and total Sobol indices, calculated analytically based on the coefficient of PCE, with those computed using 10^5 estimations of the Kriging metamodel.

Index	**Parameter**	PCE	Kriging
S_i	$\overline{\gamma}_0$	0.63	0.54
	$\overline{\sigma}$	0.25	0.20
	$\overline{\gamma}_A$	0.01	0.01
	$\overline{\gamma}_D$	0.07	0.05
	$\overline{\gamma}_S$	0.02	0.01
ST_i	$\overline{\gamma}_0$	0.66	0.71
	$\overline{\sigma}$	0.25	0.34
	$\overline{\gamma}_A$	0.02	0.06
	$\overline{\gamma}_D$	0.09	0.15
	$\overline{\gamma}_S$	0.02	0.03

Different algorithms, used to compute the Sobol indices, based on Kriging estimations, provided similar results. However, these results differ from those obtained via PCE. This is likely due to the poor accuracy of the metamodels. Indeed, they yielded $Q_2^{KRI} = 0.86$ and $Q_2^{PCE} = 0.80$ and did not lead to similar predictions, as illustrated in Figure 4.20 and also in the comparison of the PDFs of their predictions. However, despite these differences, it is still possible to draw, at least qualitatively, conclusions on the influence of the input parameters on the model, as the ranking of the indices is not altered. Their interpretation is provided below.

Interpration of the Sobol indices The numerical values used for the interpretation of the Sobol indices come from those computed using Kriging metamodel, since its accuracy is higher than that of PCE. Furthermore, noting that the four Sobol algorithms, applied to the estimations from Kriging, provided similar results, only those obtained with Mauntz-Kucherenko will be used here. It should also be noted that the predictions of the metamodel do not always match the original model ($Q_2^{KRI} = 0.86$) and therefore all the estimations are to be taken as if they had as main goal to quantify the order of magnitude of importance between the different parameters. Their values have been presented in Table 4.5.

The most influential parameter on the model is the initial adhesion, $\overline{\gamma}_0$, since its total Sobol index is the largest, with $ST_{\overline{\gamma}_0} = 0.71$. Second is the membrane tension, $\overline{\sigma}$, with

$ST_{\overline{\sigma}} = 0.34$, being 2.1 times smaller than $ST_{\overline{\gamma}_0}$. The third most important parameter is the delay of the transition, $\overline{\gamma}_D$, whose total Sobol index is 0.15. The remaining parameters, the amplitude and curvature parameter, $\overline{\gamma}_A$ and $\overline{\gamma}_S$, do not have significant influence, with respective total Sobol indices of 0.06 and 0.03. The difference between the total and first order Sobol indices of $\overline{\gamma}_0$, *i.e.* the influence of the interactions of $\overline{\gamma}_0$ with the other parameters, is 0.17, which corresponds to 24 % of its total effect. Analogously, the interactions represent 41 % and 67 % of the total influence of $\overline{\sigma}$ and $\overline{\gamma}_D$, respectively.

These results match the other results that have been obtained in this thesis. Indeed, the sensitivity analyses conducted in Chapter 3 and whose Sobol indices are displayed in Table 3.2 also showed that $\overline{\gamma}_0$ has more influence on $\tilde{f}$ than $\overline{\sigma}$. Furthermore, the ranking of the Sobol indices, regarding the parameters related to the membrane mechanical adaptation, *i.e.* $\overline{\gamma}_A$, $\overline{\gamma}_D$ and $\overline{\gamma}_S$, is the same as the one calculated in Section 4.2. The total Sobol indices obtained in these two studies are compared in Figure 4.23, which shows that the influence of $\overline{\gamma}_0$ is approximately twice as large as that of $\overline{\sigma}$ in both cases.

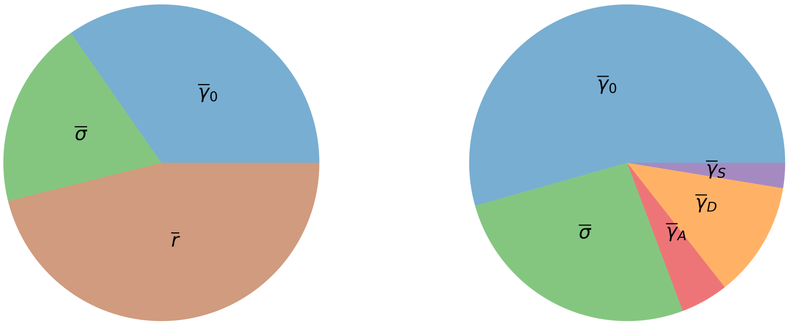

(a) (b)

Figure 4.23: Distribution of the total Sobol indices obtained in (a) Chapter 3, concerning the investigation of the influence of $\overline{\gamma}_0$, $\overline{\sigma}$ and $\overline{r}$ in the case of a passive membrane on $\tilde{f}$ and (b) in this chapter.

The Sobol indices computed in this section aim at quantifying the influence of $\overline{\gamma}_0$, $\overline{\sigma}$, $\overline{\gamma}_A$, $\overline{\gamma}_D$ and $\overline{\gamma}_S$ on the variability of the wrapping degree at equilibrium $\tilde{f}$. It was shown that the initial parameters, *i.e.* $\overline{\gamma}_0$ and $\overline{\sigma}$, are the most influential, while the influence of the parameters used to model the membrane mechanical adaptation are less important. Effectively, the amplitude of the transition, as well as its curvature parameter, respectively denoted as $\overline{\gamma}_A$ and $\overline{\gamma}_S$, have low Sobol indices and therefore have a negligible influence on $\tilde{f}$. Lastly, the delay of the transition, $\overline{\gamma}_D$, influences $\tilde{f}$. This leads to the conclusion that accounting for the delay of the transition alters the predictions of the model, even if it is not the most important factor.

5 Discussion

Several elements can be highlighted in order to discuss the methods and results presented in this thesis. They are presented in the following.

- **Two studies have been presented** in this chapter, one involving the proportion of full wrapping ψ_3 and another involving the wrapping degree at equilibrium $\tilde{f}$. Similar to the previous chapter, it is worth recalling that $\tilde{f}$ alone does not provide sufficient information to characterize the uptake of the NP, which requires the fusion of the two sides of free membrane. As such, using the distance between them as a QoI instead of $\tilde{f}$ would enable to overcome this issue.
- **Some of the sensitivity indices have been calculated using inaccurate predictions**. Indeed, in the study of the influence of the five input parameters on $\tilde{f}$, the predictions of both metamodels were not precise ($Q_2^{KRI} = 0.86$ and $Q_2^{PCE} = 0.80$), which yielded important uncertainties in the estimations of the samples necessary to compute the Sobol indices and also to the analytical calculation of the Sobol indices based on the coefficients of PCE, which could not be possible either. The consequence of these uncertainties on the CIs of the Sobol indices was not investigated, but techniques to account for them, when estimating the uncertainty of the Sobol indices, have been presented in the literature [231].
- **Additional surrogate modeling approaches**, among which those that have been introduced in Chapter 3 (*e.g.* PCE-Kriging and machine learning), may provide different and potentially better predictions. Hence, it would be of great interest to investigate these methods in order to improve the accuracy of the Sobol indices. Furthermore, the probabilistic content of the dataset used to construct the metamodel for the approximation of $\tilde{f}$ shows a concentration of samples for $\tilde{f} = 0.97$. It thus tends to create a bias in the metamodel, which can yield inaccurate conclusions. That also means that less information on the behavior is provided to the metamodel for certain values that are less represented in the dataset. As such, it increases the difficulty for the metamodel to accurately predict such values of which

not enough samples are contained in the dataset. For these reasons, using a dataset from which the distribution of the output is close to a uniform distribution could help avoiding such effect. In addition, the metamodels could be post processed in order to clip the predictions within the domain of definition of the QoI. As such, each estimation larger (resp. smaller) than the upper (resp. lower) bound would be replaced by the bound that has not been respected, which would compensate the over- (resp. under-) estimations.

- **Few information is known about the input parameters**, especially those of the sigmoid used to describe the variation of the adhesion between the NP and the cell membrane during the wrapping process. Hence, the domain of definition of these parameters were set following inferences based on observations reported in the literature, along with mathematical considerations. Given that the domain of definition of a variable has an effect on the sensitivity analyses [214], conducting a study in which the bounds vary could consequently enable us to quantify the dependence of the results of the sensitivity analyses on the domains of definition of the parameters. A similar remark can be made concerning the influence of the statistical distribution of these parameters on the sensitivity analysis, as it is also likely to alter their results.
- **The results presented in this section were obtained after investigating the cellular uptake of a circular NP**. Indeed, although we demonstrated previously in Chapter 3 that the aspect ratio of the NP plays an important role in the predictions of the model, the present chapter focused on isolating the contributions of the other parameters. The reason for such approach is to enrich the model step-by-step and keep track of the contribution of each individual parameter. As such, Chapter 5 will aim at studying the model with all the parameters together, by investigating the influence of the mechano-adaptation on the uptake of an elliptic NP.

6 Conclusions of Chapter 4

In this chapter, we introduced some further interactions that happen alongside the membrane during the wrapping of the NP and we proposed a way to account for them in our numerical model, by describing the adhesion between the NP and the membrane as a function of the wrapping degree of the NP. Then, sensitivity analyses have been conducted on the enriched model in order to quantify the influence of the newly introduced parameters on the predictions of the model. Metamodels have been built in order to provide enough data for the sensitivity analyses in affordable time. The following conclusions have been drawn:

- **The phenomenon of membrane mechano-adaptation** as a response to the wrapping of the NP has been observed based on the literature. A wrapping-degree-dependant adhesion has consequently been introduced in order to depict this phenomenon. The evolution of $\overline{\gamma}$ is modeled with a sigmoid, in order to represent a variation between two finite values with tunable parameters. As such, the adhesion $\overline{\gamma}$ is depicted as a function of the initial adhesion $\overline{\gamma}_0$, the amplitude of the transition between the initial and the final adhesion, $\overline{\gamma}_A$, the wrapping degree at which the transition begins, $\overline{\gamma}_D$, and the curvature parameter $\overline{\gamma}_S$.

- **Preliminary observations of the model**, especially the evolution of $\overline{\Delta E}(f)$ and the phase diagrams, revealed that accounting for the evolution of $\overline{\gamma}$ with respect to f yields different predictions than when the adhesion is considered constant (passive membrane).

- **Metamodels have been built for the sensitivity analyses** to be performed. Kriging and PCE metamodels have been used for the analyses on ψ_3 and $\tilde{f}$. For the first analysis, both metamodels, built using a dataset of 2^{10} samples, provided very accurate predictions of ψ_3 ($Q_2^{KRI} = 0.99$ and $Q_2^{PCE} = 0.98$), that have been used to calculate the Sobol indices. In the second analysis, the metamodels, built with a dataset of size 2^{12}, provided less accurate predictions of $\tilde{f}$ ($Q_2^{KRI} = 0.86$ and $Q_2^{PCE} = 0.80$), yielding slightly different Sobol indices. Nonetheless, the same qualitative conclusions on the influence of the input parameters could be drawn regardless of the type of the metamodel. The convergence of the Sobol indices was verified by evaluating the variation of the range of their 95 % CIs.

- **Sensitivity analyses enabled to confirm** the preliminary observations. First, the roles of the three parameters used to describe $\overline{\gamma}(f)$ have been quantified by performing a sensitivity analysis of their influence on ψ_3. From the Sobol indices being different from zero, this study showed that all the parameters are influential, and the delay of the transition $\overline{\gamma}_D$ is the most important parameter, followed by the amplitude $\overline{\gamma}_A$ and the curvature parameter $\overline{\gamma}_S$. That is to say that among the 280 cells (*i.e.* tuples of $(\overline{\sigma}, \overline{\gamma}_0)$) that are investigated, the proportion of cells that would internalize the circular NP depends on the way the cell membrane adapts during the wrapping. Second, when considering a single cell with random properties, it was shown that the effects of the amplitude of the transition and the curvature parameter on the wrapping degree at equilibrium are negligible, compared to those of the initial properties of the cell $\overline{\sigma}$ and $\overline{\gamma}_0$. When considering the mechano-adaptation of the membrane, the influence of $\overline{\gamma}_0$ remains around 2 times larger than that of $\overline{\sigma}$, similar to the results from Chapter 3.

- **Investigations on the cellular uptake of a circular NP** require the knowledge of several input parameters. In this chapter, we showed that, even accounting for the mechanical adaptation of the membrane, efforts for the characterization of the cells need to be focused on $\overline{\gamma}_0$, then on $\overline{\sigma}$ and finally on $\overline{\gamma}_D$, by order of influence on the model.

Chapter 5

EFFECT OF THE MECHANO-ADAPTATION OF THE MEMBRANE ON THE CELLULAR UPTAKE OF ELLIPTIC NPS

---

1 Introduction

The results presented in the previous chapter showed that accounting for the mechano-adaptation of the membrane during the wrapping of the NP alters the engulfment predictions. The investigations were carried out for the case of circular NPs. In Chapter 3, we showed that the aspect ratio of the NP also affects these predictions, and even more than the mechanical properties, in the case of a passive membrane. Hence, it is interesting to explore whether it is still the case while accounting for the mechano-adaptation of the membrane. A sensitivity analysis will thus be conducted, in order determine the influence of the shape parameters describing the evolution of $\overline{\gamma}$ during wrapping and to compare it with that of the aspect ratio of the NP. For this purpose, a first observation of the model is made, then a metamodel is built and the Sobol sensitivity indices are finally calculated. The code used to build the metamodels and to conduct the sensitivity analyses is available in the Github repository[1] associated to this thesis.

2 Preliminary observations

In order to build the intuition on the influence of the parameters characterizing an adaptive membrane, *i.e.* $\overline{\gamma}_A$, $\overline{\gamma}_D$ and $\overline{\gamma}_S$, on the uptake of an elliptic NP, the variation of the potential energy $\overline{\Delta E}$ is compared, similar to Figure 3.8, for different values of these parameters, in Figures 5.1, 5.2 and 5.3.

---

[1] `https://github.com/SarahIaquinta/PhDthesis`

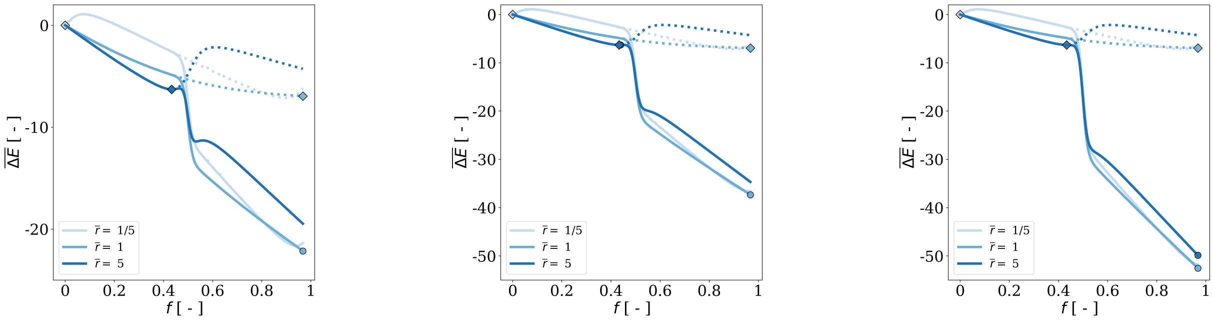

(a) $\overline{\gamma}_A = 2$ (b) $\overline{\gamma}_A = 3$ (c) $\overline{\gamma}_A = 4$

Figure 5.1: Effect of $\overline{\gamma}_A$ on the influence of $\overline{r}$ on $\overline{\Delta E}(f)$, for $\overline{\gamma}_D = 0$ (inflection point at $f = 0.5$) and $\overline{\gamma}_S = 50$ (sharp transition). The dotted lines correspond to the passive case ($\overline{\gamma}_A = 1$). The dots (resp. diamonds) represent the equilibrium position ($f = \tilde{f}$) in the adaptive (resp. passive) case.

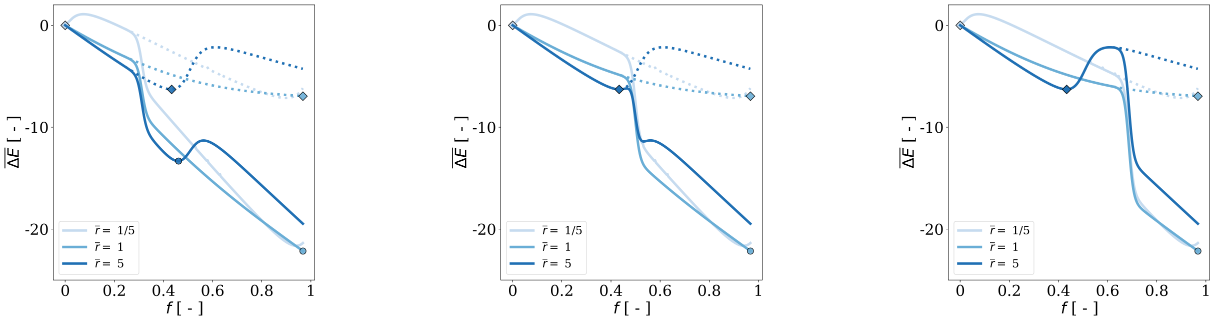

(a) $\overline{\gamma}_D = -0.2$ (b) $\overline{\gamma}_D = 0$ (c) $\overline{\gamma}_D = 0.2$

Figure 5.2: Effect of $\overline{\gamma}_D$ on the influence of $\overline{r}$ on $\overline{\Delta E}(f)$, for $\overline{\gamma}_A = 2$ (*i.e.* $\overline{\gamma}(f \to 1^-) = 2\overline{\gamma}_0$) and $\overline{\gamma}_S = 50$ (sharp transition). The dotted lines correspond to the passive case ($\overline{\gamma}_A = 1$). The dots (resp. diamonds) represent the equilibrium position ($f = \tilde{f}$) in the adaptive (resp. passive) case.

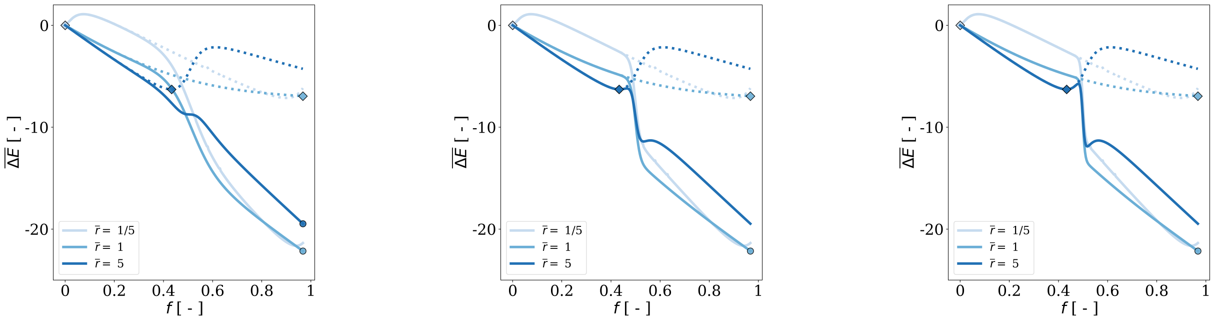

(a) $\overline{\gamma}_S = 10$ (b) $\overline{\gamma}_S = 50$ (c) $\overline{\gamma}_S = 100$

Figure 5.3: Effect of $\overline{\gamma}_S$ on the influence of $\overline{r}$ on $\overline{\Delta E}(f)$, for $\overline{\gamma}_A = 2$ (*i.e.* $\overline{\gamma}(f \to 1^-) = 2\overline{\gamma}_0$) and $\overline{\gamma}_D = 0$ (inflection point at $f = 0.5$). The dotted lines correspond to the passive case ($\overline{\gamma}_A = 1$). The dots (resp. diamonds) represent the equilibrium position ($f = \tilde{f}$) in the adaptive (resp. passive) case.

From Figure 5.1, one can see that $\overline{\gamma}_A$ influences the evolution of $\overline{\Delta E}$, but it does not alter the position of the first local minimum of energy. Indeed, it is located before the wrapping degree at which the mechano-adaptation starts, that does not change with $\overline{\gamma}_A$ ($\tilde{f}$ is the same in Figures (a), (b) and (c)). Then, Figure 5.2 shows that the position of $\tilde{f}$, *i.e.* the x-coordinate of the first local minimum of the potential energy, is altered by $\overline{\gamma}_D$. This is similar to what was observed in Figure 4.5 for a circular NP. Furthermore, Figure 5.3 shows that the energy barrier, that appears after the first local minimum, created due to the variation of $\overline{\gamma}$, vanishes if the transition is sufficiently smooth (*i.e.* small values of $\overline{\gamma}_S$). One can also note the presence of energy barriers in the passive case (dotted lines), which is due to $\overline{r}$. This first observation consequently highlighted that the transition delay $\overline{\gamma}_D$ seems to have a concurrent effect to that of $\overline{r}$ on $\overline{\Delta E}$, since both influence $\tilde{f}$ in this case.

Observing how these parameters influence $\overline{\Delta E}$ provides qualitative information on how $\tilde{f}$ may be affected by them. However, as highlighted in the previous chapters, we are more interested in the phase at equilibrium than in $\tilde{f}$. For this reason, the proportion of phases at equilibrium is plotted with a model where the mechano-adaptation is considered. Figure 5.4 shows the evolution of the proportion of each phase, as a function of $\overline{r}$, with $(\overline{\gamma}_A, \overline{\gamma}_D, \overline{\gamma}_S) = (2, 0, 50)$.

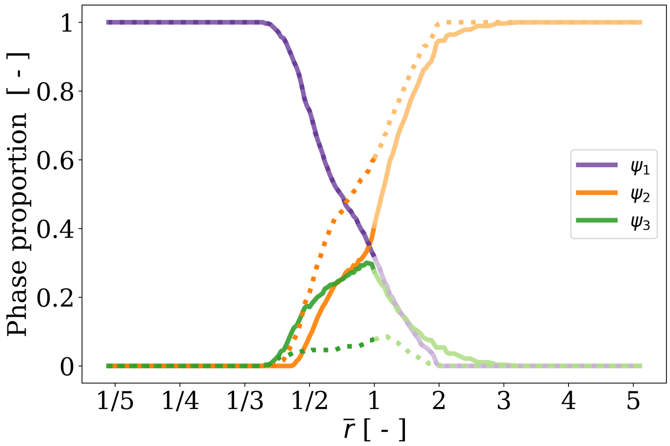

Figure 5.4: Phase proportions in terms of the aspect ratio $\overline{r}$ of the NP, accounting for the mechano-adaptation of the membrane for $(\overline{\gamma}_A, \overline{\gamma}_D, \overline{\gamma}_S) = (2, 0, 50)$. The dark (resp. light) lines stand for vertical (resp. horizontal) NPs. The dotted lines correspond to the passive case (Figure 3.10 of Chapter 3).

By comparing the solid and dotted lines, *i.e.* the phase proportions in the case of adaptive and passive membranes, one can deduce that the way the phase proportion evolves with $\overline{r}$ can be highly altered by the introduction of the adaptive model. Note that the point $\overline{r} = 1$ corresponds to the particular case of a circular NP, and reproduces the proportions from the phase diagram in Figure 4.6a. The latter showed an increase in the proportion of phase 3 and a decrease in that of phase 2, while the proportion of phase 1 did not change, when accounting for the membrane mechano-adaptation. This conclusion can be extended to the entire domain of definition of $\overline{r}$, as illustrated in Figure 5.4. The fact that the phase 1 (purple curves) is not affected by the membrane mechano-adaptation is due to the definition of the phases. Indeed, the minimal inflection point $f_{\text{inf}} = 0.5 + \overline{\gamma}_D$ is 0.3, meaning that $\overline{\gamma}$ changes for $\tilde{f} > 0.2$, which is the threshold wrapping degree after which the phase is defined to be 2. The phase diagrams obtained for $\overline{r} \in [1/3, 3]$ for adaptive and passive cells, with the aforementioned properties, are compared in Appendix C.

Moreover, some of the NPs that could not reach the phase 3 with a passive membrane ($\psi_3 = 0$) are able to do so when the mechano-adaptation of the membrane is modeled. For instance, NPs whose aspect ratio is in the interval $[2, 3]$ are able to be fully wrapped by an adaptive membrane, while they are not by a passive membrane. In addition, the values of ψ_3 are larger than in the passive case, meaning that more cells, represented by tuples of initial cellular properties $(\overline{\gamma}_0, \overline{\sigma})$, are able to engulf them than in the case of passive membranes. These results show the obvious effect of the membrane mechanical adaptation on the model predictions, but only for the specific configuration where the parameters are set as $(\overline{\gamma}_A, \overline{\gamma}_D, \overline{\gamma}_S) = (2, 0, 50)$. To clarify the influence of these parameters on the model, sensitivity analyses are conducted in Section 3.

3 Quantification of the influence of the parameters related to the mechano-adaptation

The model presented in this study has four input parameters: $\overline{\gamma}_A$, $\overline{\gamma}_D$, $\overline{\gamma}_S$ and $\overline{r}$, while the output parameter is ψ_3. Following an analogous approach to that used in Chapters 3 and 4 to perform the sensitivity analysis, a surrogate model will first be built in Section 3.1 in order to generate the estimations necessary to evaluate the Sobol indices. The results of the subsequent sensitivity analysis are presented in Section 3.2.

3.1 Surrogate model

Sampling A dataset containing 2^{10} realizations of the input random variables along with the estimations of the random variable Ψ_3 is generated. The input parameters follow the same distributions as those presented in the previous chapters, *i.e.* $\overline{\Gamma}_A \sim \mathcal{U}(1,6)$, $\overline{\Gamma}_D \sim \mathcal{U}(-0.2,0.2)$, $\overline{\Gamma}_S \sim \mathcal{U}(10,100)$ and $\bar{R} \sim \mathcal{U}^P(1/6,1;1,6)$. The probability distribution of Ψ_3, based on these values, is represented in Figure 5.5.

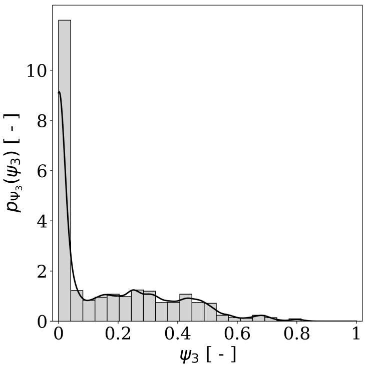

Figure 5.5: Histogram of Ψ_3, along with a kernel density estimation of its PDF.

In order to determine the minimum size of the dataset for it to be representative of the behavior of the data, the cumulative mean and standard deviation of Ψ_3, along with their gradient, are plotted in Figures 5.6 and 5.7.

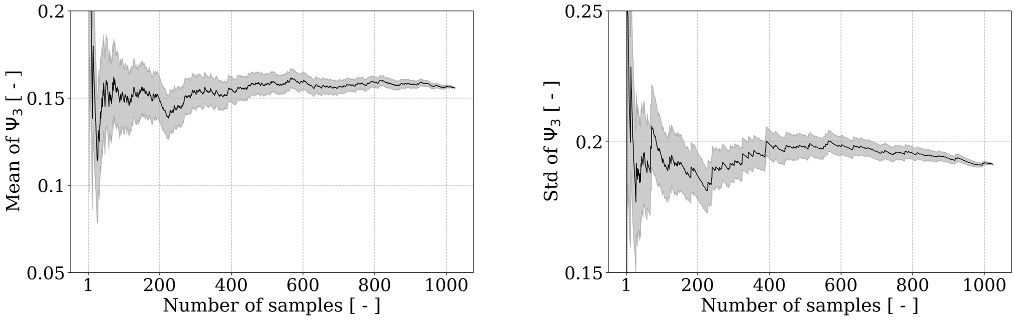

(a) (b)

Figure 5.6: (a) Mean and (b) standard deviation of Ψ_3, with respect to the number of samples.

According to these figures, 365 samples are necessary for the gradients of both statistics to converge. Hence, 365 samples, which represents about 35 % of the dataset, will be used for the validation of the metamodels, and the remaining 659 samples will be used for its training. The results of the metamodels are presented afterwards.

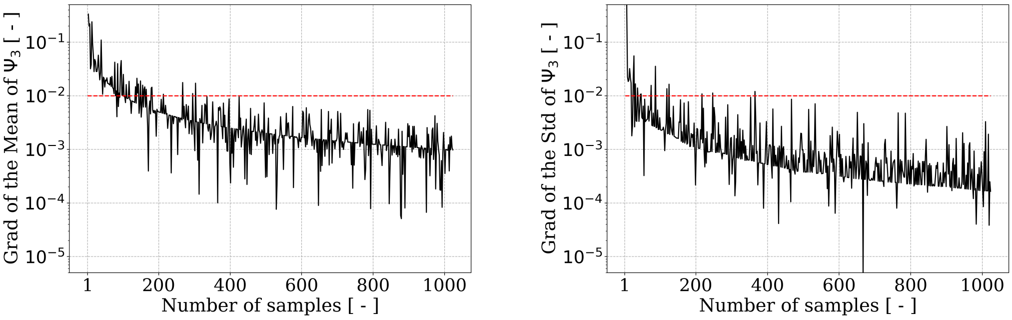

(a) (b)

Figure 5.7: Absolute normalized gradient of the (a) mean and (b) standard deviation of Ψ_3, with respect to the number of samples. Only one out of two points have been represented for the clarity of the plots.

Implementation of the metamodels In order to avoid singularities, the truncation degree p of the PCE has to verify $3\binom{p+4}{4} < 659$ (rule of thumb introduced in Equation 3.7), yielding $p \leq 6$. The predictivity factor Q_2 of the metamodels for $p \in \{1, 2, 3, 4, 5, 6\}$ is represented in Figure 5.8, from which one can conclude that Q_2 is maximized for $p = 5$, with $Q_2^{PCE} = 0.68$. Kriging metamodel has been build using the same initial configurations as in the previous chapters and yielded $Q_2^{KRI} = 0.92$.

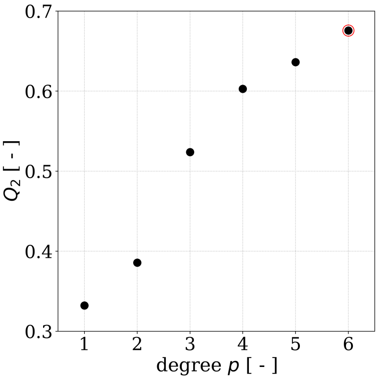

Figure 5.8: Accuracy of PCE predictions in terms of the truncation degree.

Figure 5.9 compares the predictions of the metamodels with the data from the model, using the validation dataset of size 365, along with estimations of the PDF of Ψ_3 obtained by evaluating each metamodel with 10^5 samples of input parameters generated by the MC method.

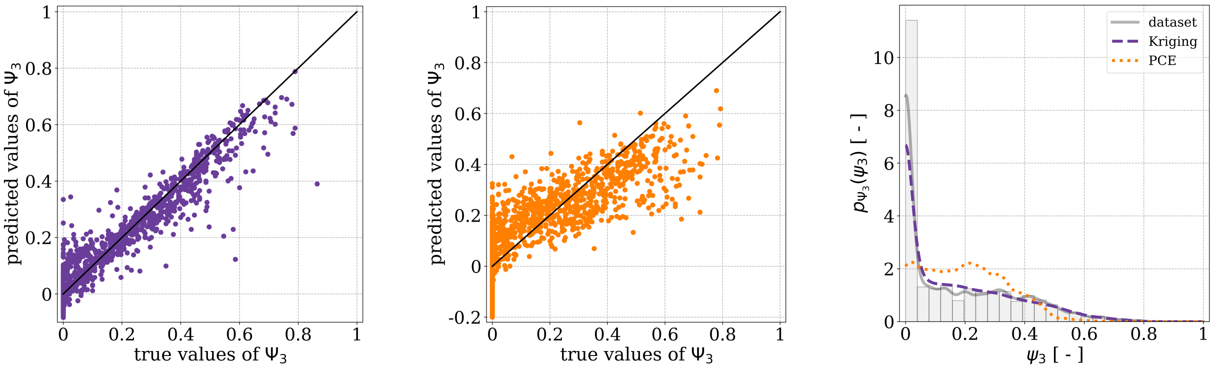

(a) Kriging (b) PCE (c) PDFs

Figure 5.9: Predicted vs true values obtained with (a) Kriging and (b) PCE algorithms, along with a comparison of the PDFs, estimated via these metamodels.

The true vs predicted plots highlight the presence of predictions out of the domain of definition of Ψ_3, *i.e.* the interval $[0, 1]$. As such, a clip, as introduced previously in Chapter 3 for the study of $\tilde{F}$, could be applied to the metamodel to ensure that the predictions belong to the interval of definition of the QoI. The estimation of the PDFs based on Kriging predictions shows a closer distribution to that of the original data than that of PCE. This difference is due to the fact that PCE is based on fitting polynomial functions of a small degree ($p = 6$), which is not large enough to represent the behavior of the model, based on the dataset.

3.2 Sensitivity analysis

3.2.1 Computation of the Sobol indices

Number of samples The influence of the parameters used to model the mechano-adaptation of the membrane, *i.e.* $\overline{\gamma}_A$, $\overline{\gamma}_D$ and $\overline{\gamma}_S$, along with the aspect ratio $\overline{r}$ of the NP, is investigated in order to determine if the way the former parameters influence ψ_3 differs depending on $\overline{r}$. These results will be compared with those obtained in Section 4.2 of Chapter 4, in which their influence was investigated in the case of the uptake of a circular NP, *i.e.* $\overline{r} = 1$. The Sobol sensitivity indices will be computed using the estimations of the Kriging metamodel. Recalling that no additional computational cost is necessary, they will also be calculated based on the PCE coefficients. First, the convergence of the Sobol indices, with respect to the number of samples used to estimate them, is investigated using the four aforementioned algorithms available in OpenTURNS. Solely the results obtained with the Mauntz-Kucherenko algorithm will be shown in this section. The convergence studies using Saltelli, Jansen and Martinez algorithms are provided in Section 4.1 of Appendix A. The evolution of the first and total Sobol indices, in terms of the number of samples, is depicted in Figure 5.10, along with their 95 % CIs, for which the variation of the range is represented in Figure 5.11.

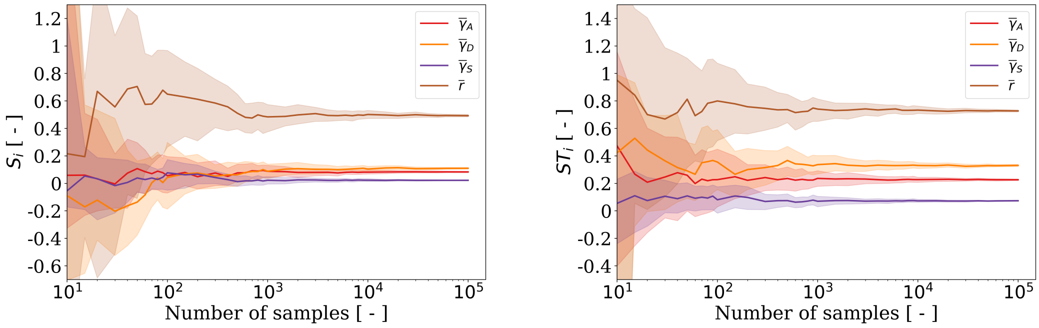

(a) (b)

Figure 5.10: Convergence of the (a) first and (b) total Sobol indices, computed with the Mauntz-Kucherenko algorithm. The shaded regions correspond to the 95 % confidence intervals.

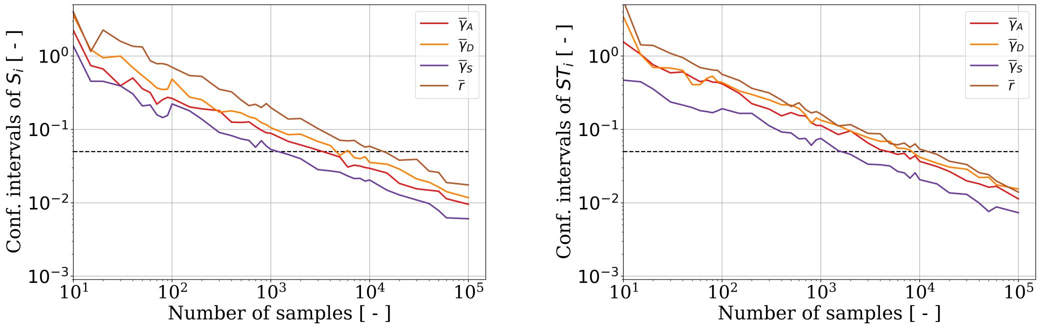

(a) (b)

Figure 5.11: Range of the 95 % confidence intervals of the (a) first and (b) total Sobol indices, in terms of the number of estimations of the metamodel, computed with the Mauntz-Kucherenko algorithm. The dashed lines correspond to the threshold of 0.05.

According to Figure 5.11, at least 1.5×10^4 samples are necessary for the CIs of the S_i and ST_i to be smaller than 0.05, ensuring the convergence of the Sobol indices. The absolute gradients of the indices are given in appendix.

Influence of the algorithm Differences in the convergence of the indices depending on the algorithm are highlighted in Table 5.1. Indeed, indices computed using the Martinez algorithm require the most samples to converge (5×10^4 for ST_i), while Mauntz-Kucherenko enables convergence with less samples (1.5×10^4 for both indices). The plots representing the variation of the Sobol indices, their normalized absolute gradient, along with the range of their 95 % CIs, for the aforementioned algorithms, are contained in appendix.

Table 5.1: Number of samples necessary for the convergence of the Sobol indices following the criterion on the range of the 95 % confidence intervals of S_i and ST_i, estimated with several algorithms.

Index	Mauntz-Kucherenko	Saltelli	Jansen	Martinez
S_i	1.5×10^4	10^4	2×10^4	10^4
ST_i	1.5×10^4	4×10^4	1.5×10^4	5×10^4

The estimations, based on these four algorithms, using 10^5 samples, are compared to those obtained from the PCE coefficients in Table 5.2.

Table 5.2: Comparison of the first and total Sobol indices, calculated analytically using PCE, with those computed using 10^5 estimations of the Kriging metamodel.

Index	Parameter	PCE	Kriging
S_i	$\overline{\gamma}_A$	0.14	0.09
	$\overline{\gamma}_D$	0.17	0.11
	$\overline{\gamma}_S$	0.04	0.02
	$\overline{r}$	0.65	0.49
ST_i	$\overline{\gamma}_A$	0.14	0.23
	$\overline{\gamma}_D$	0.17	0.33
	$\overline{\gamma}_S$	0.04	0.07
	$\overline{r}$	0.65	0.72

PCE and Kriging yielded different indices, which is due to the accuracy of their respective predictions. Indeed, the indices evaluated with PCE ($Q_2^{PCE} = 0.68$) cannot be used for the sensitivity analysis since the inaccuracy of the PCE coefficients would yield inaccurate sensitivity indices. As such, only the indices estimated via Kriging will be used to proceed to the sensitivity analysis, since $Q_2^{KRI} = 0.92$ is closer to 1.

3.2.2 Intrepretation of the Sobol indices

This study highlights that $\overline{r}$ is the most influential parameter, with the largest total Sobol index, $ST_{\overline{r}} = 0.72$, while the curvature parameter $\overline{\gamma}_S$ is the less influential parameter with the lowest total Sobol index: $ST_{\overline{\gamma}_S} = 0.07$. Its first order index is almost zero ($S_{\overline{\gamma}_S} = 0.02$), meaning that its influence on Ψ_3, is primarily due to interactions with other parameters $\overline{\gamma}_A$, $\overline{\gamma}_D$ and $\overline{r}$. A similar observation is made for the amplitude of the transition, $\overline{\gamma}_A$, whose first order Sobol index is small ($S_{\overline{\gamma}_A} = 0.09$). The parameter with the largest total Sobol index, after $\overline{r}$, is the transition delay $\overline{\gamma}_D$, with $ST_{\overline{\gamma}_D} = 0.33$. It is thus the second most influential parameter. Still, its first order index ($S_{\overline{\gamma}_D} = 0.11$) is small compared to the total index, meaning that the effect of $\overline{\gamma}_D$ is mainly due to its interactions with the remaining parameters. The curvature parameter and the amplitude of the transition, $\overline{\gamma}_S$ and $\overline{\gamma}_A$ being of small importance, one can infer that the influence of $\overline{\gamma}_D$ on Ψ_3 is mostly due to interactions with the aspect ratio $\overline{r}$ of the NP. One can also note that the ranking of importance between the parameters $\overline{\gamma}_A$, $\overline{\gamma}_D$ and $\overline{\gamma}_S$ is the same as the one obtained for circular NPs ($\overline{r} = 1$), as illustrated in Figure 5.12.

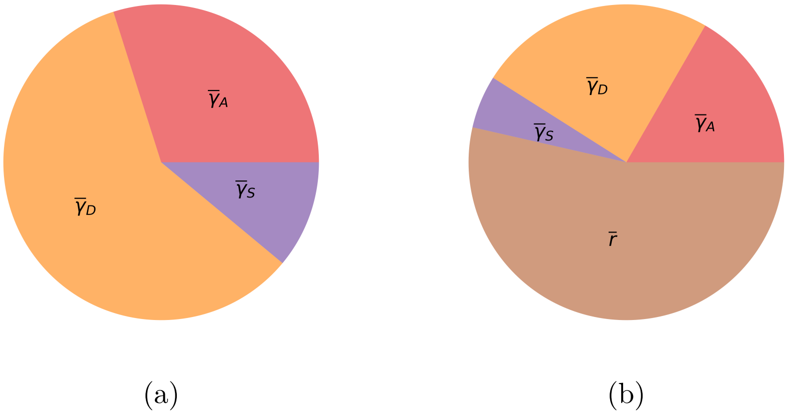

(a) (b)

Figure 5.12: Distribution of the total Sobol indices obtained in (a) Chapter 4, concerning the investigation of the influence of $\overline{\gamma}_A$, $\overline{\gamma}_D$ and $\overline{\gamma}_S$ on the uptake of a circular NP and in (b) in this chapter, which compares the influence of $\overline{\gamma}_A$, $\overline{\gamma}_D$ and $\overline{\gamma}_S$ to that of the aspect ratio $\overline{r}$ of an elliptic NP.

Furthermore, the fact that the aspect ratio of the NP influences more ψ_3 than the mechanical properties matches the results from Chapter 3, where we concluded that $\overline{r}$ is a prominent parameter, as it influenced the most the proportion of full wrapping of an elliptic NP by a passive membrane.

4 Comparison of the effects of the initial and mechano-adaptation-related parameters on the uptake of an elliptical NP

As in Section 4.3 of Chapter 4, the influence of the mechano-adaptation, investigated with the shape parameters $\overline{\gamma}_A$, $\overline{\gamma}_D$ and $\overline{\gamma}_S$, is compared to that of the initial cell parameters $\overline{\gamma}_0$ and $\overline{\sigma}$. In this chapter, we conduct the same study in the case of the uptake of an elliptic NP, meaning that $\overline{r}$ is an input parameter instead of being set to 1 (circular NP). To do so, we create a metamodel in Section 4.1 and compute the Sobol indices in Section 4.2, using the metamodel predictions.

4.1 Surrogate model

Sampling Both PCE and Kriging metamodels are built and compared in this section. Similar to the previous cases, the representativeness of the dataset is first observed, in order to determine the minimum number of samples necessary to be representative of the behavior of the dataset, which, similar to the previous studies where the QoI was $\tilde{F}$, contains $2^{12} = 4096$ samples. The histogram of the random variable $\tilde{F}$, based on this dataset, is represented in Figure 5.13.

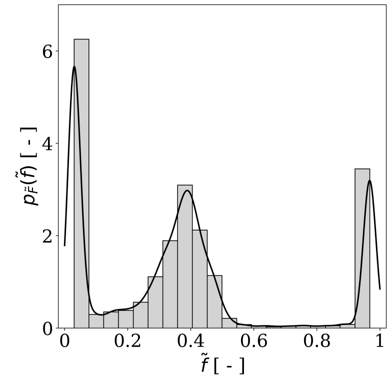

Figure 5.13: Histogram of $\tilde{F}$, based on the dataset along with a kernel density estimation of its PDF.

To investigate the representativeness of the dataset, the mean and standard deviation of $\tilde{F}$, along with their gradient, in terms of the number of samples, are depicted in Figures 5.14 and 5.15, respectively.

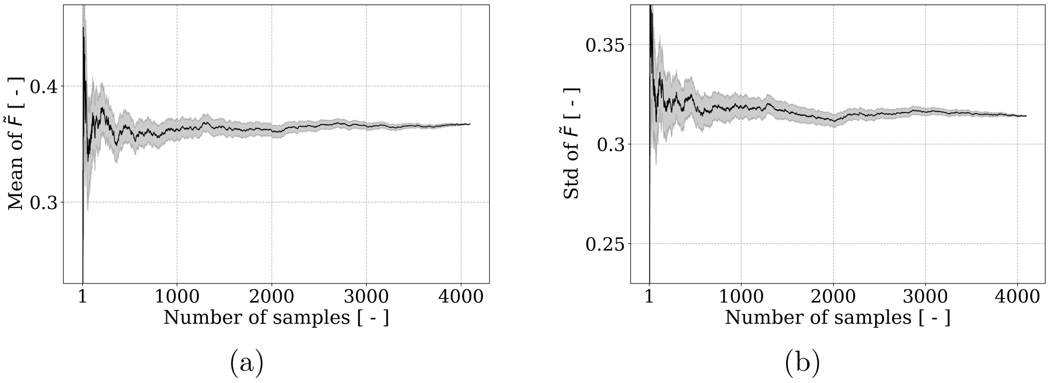

(a) (b)

Figure 5.14: (a) Mean and (b) standard deviation of $\tilde{F}$, with respect to the number of simulations. The shaded regions correspond to the standard deviation, obtained with 200 shuffled samples.

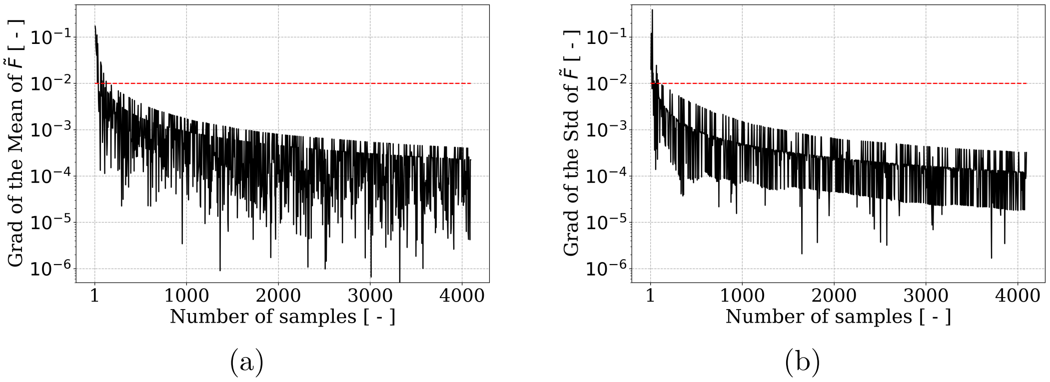

(a) (b)

Figure 5.15: Absolute normalized gradient of the (a) mean and (b) standard deviation of $\tilde{F}$, with respect to the number of simulations. The dashed lines correspond to the 1 % threshold. Only one out of four points have been represented for the clarity of the plots.

They show that in order for $\tilde{F}$ to have convergent first and second order statistics, datasets of size 134 and 127 should be used, respectively. Based on this result, 10 % of the dataset, which represents 409 samples, will be used for the validation of the metamodels, and the remaining 90 %, *i.e.* 3687 samples, will be employed for their training.

Implementation of the metamodels In order to avoid singularities, the truncation degree p of the PCE has to verify $5\binom{p+6}{6} < 3687$ that yields $p \leq 5$. The predictivity factor Q_2 of the metamodels for $p \in \{1, 2, 3, 4, 5\}$ is represented in Figure 5.16, from which one can conclude that Q_2 is maximized for $p = 5$, with $Q_2^{PCE} = 0.55$.

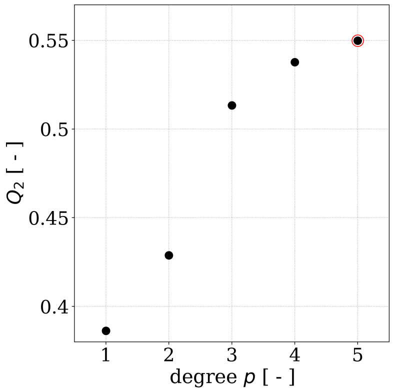

Figure 5.16: Accuracy of PCE predictions in terms of the truncation degree.

The predicted vs true values plots obtained with PCE and Kriging, which have been built with settings that are similar to those used in the previous studies, are depicted in Figures 5.17a and 5.17b. The predictivity factor associated to Kriging estimations is $Q_2^{KRI} = 0.42$. Estimations for the PDF of $\tilde{F}$, using a MC dataset of size 10^5, with Kriging and PCE along with the one based on the original data, are shown in Figure 5.17c.

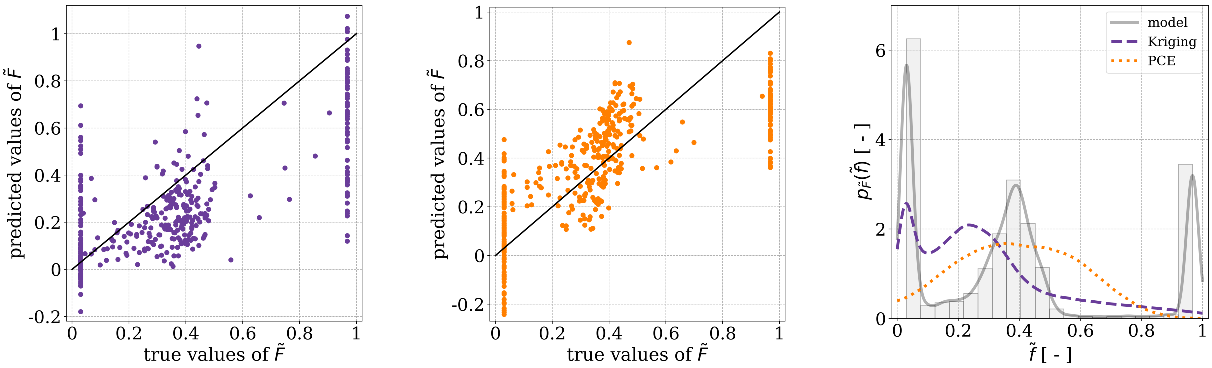

(a) Kriging (b) PCE (c) PDFs

Figure 5.17: Predicted vs true values obtained using (a) Kriging and (b) PCE surrogate models, along with (c) a comparison of the kernel density estimations of the PDFs estimated via these metamodels with 10^5 MC-based samples, and the histogram of the initial data.

The comparison of the estimation of the PDFs based on the metamodels predictions to that of the initial data shows that the surrogate models were not able to reproduce a distribution similar to that of the data. Indeed, while the data has a multimodal distribution represented by three peaks at $\tilde{f} \approx 0.03$, $\tilde{f} \approx 0.4$ and $\tilde{f} \approx 0.97$, PCE predictions have a unimodal distribution with a large peak of low value at $\tilde{f} \approx 0.4$. Kriging yields a bimodal distribution whose peaks are located at $\tilde{f} \approx 0.03$ and $\tilde{f} \approx 0.25$. Furthermore, the predictivity factors obtained for these metamodels are not satisfying either. The former are $Q_2^{KRI} = 0.42$ and $Q_2^{PCE} = 0.55$, which are too far from 1 to consider the predictions accurate. This result shows that none of these metamodels is able to provide accurate predictions of the model. In this case, we can suppose that Kriging was not able to build accurate estimations based on the interpolation of the points of the dataset because of the dispersion of the data, combined to a large amount of input parameters that yielded equal values of $\tilde{F}$ in the training dataset.

4.2 Sensitivity analysis

Number of samples Analogously to the previous section, the influence of the initial parameters $\overline{\gamma}_0$ and $\overline{\sigma}$, as well as those used to model the membrane mechano-adaptation, *i.e.* $\overline{\gamma}_A$, $\overline{\gamma}_D$ and $\overline{\gamma}_S$, along with the aspect ratio $\overline{r}$ of the NP, are investigated. The objective is to determine whether the way the influence of the former parameters $\tilde{F}$ differs depending on the value of $\overline{r}$. These results will be compared with those obtained in Section 4.3.2 of Chapter 4, where their influence was investigated in the case of the uptake of a circular NP. The sensitivity indices will be computed using the estimations of the Kriging metamodel and also based on the PCE coefficients, even though their predictions were poor, as we do not possess any alternative in this study. This point will be discussed at the end of this chapter. First, the convergence of the Sobol indices, in terms of the number of samples used to estimate them, is investigated using all aforementioned algorithms. However, only the results obtained with the Mauntz-Kucherenko algorithm will be displayed in this section. The estimations based on Saltelli, Jansen and Martinez algorithms are provided in Section 4.2 of Appendix D. The evolution of the first and total Sobol indices in terms of the number of sample along with their 95 % CIs are depicted in Figure 5.18. The variation of their range, shown in Figure 5.19, implies that at least 1.5×10^4 and 2×10^4 samples are necessary for the range of the CIs of S_i and ST_i to be smaller than 0.05. Based on this criterion, one can conclude that more than 2×10^4 samples are required to ensure the convergence of the Sobol indices.

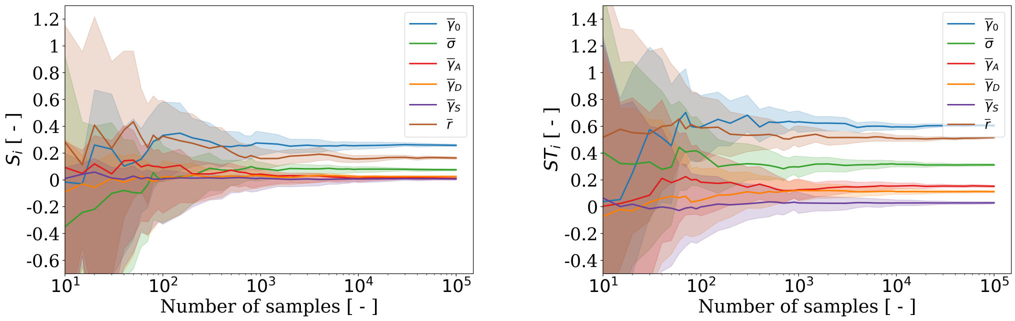

(a) (b)

Figure 5.18: Convergence of the (a) first and (b) total Sobol indices, computed with the Mauntz-Kucherenko algorithm. The shaded regions correspond to the 95 % confidence intervals.

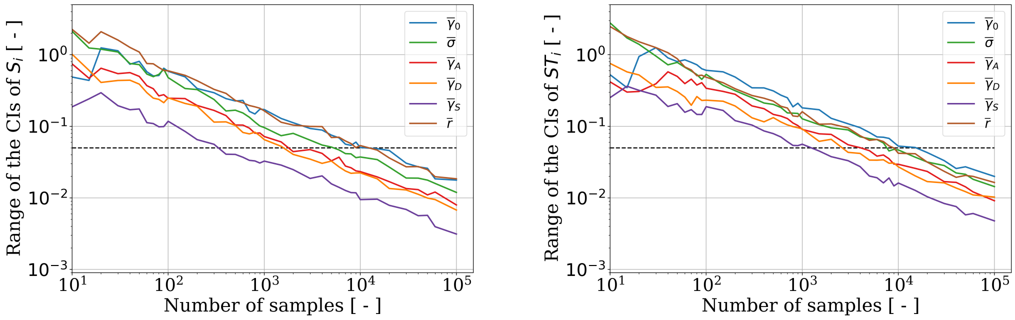

(a) (b)

Figure 5.19: Range of the 95 % confidence intervals the (a) first and (b) total Sobol indices in terms of estimations of the metamodel, computed with the Mauntz-Kucherenko algorithm. The black dashed lines correspond to the threshold of 0.05.

Influence of the algorithm Discrepancies in the convergence of the indices depending on the algorithm are highlighted in Table 5.3.

Table 5.3: Number of samples necessary for the convergence of the Sobol indices following the criterion of the range of the 95 % confidence intervals of S_i and ST_i evaluated with several algorithms.

Index	**Mauntz-Kucherenko**	**Saltelli**	**Jansen**	**Martinez**
S_i	1.5×10^4	1.5×10^4	1.5×10^4	10^4
ST_i	2×10^4	5×10^4	2×10^4	4×10^4

Indeed, indices computed with Saltelli require the largest number of samples to converge (5×10^4 for ST_i) while Mauntz-Kucherenko and Jansen enable convergence with less samples (1.5×10^4 and 2×10^4 for S_i and ST_i). The plots representing the variation of the

Sobol indices, their normalized absolute gradient, along with the range of their 95 % CIs, in terms of the number of samples, are contained in appendix. The indices obtained after convergence (calculated with 10^5 samples) are compared with those analytically evaluated from the PCE coefficients in Table 5.4, that shows notable difference in the Sobol indices computed using both methods.

Table 5.4: Comparison of the first and total Sobol indices, calculated analytically using PCE, with those computed using 10^5 estimations of the Kriging metamodel.

Index	**Parameter**	**PCE**	**Kriging**
S_i	$\overline{\gamma}_0$	0.25	0.26
	$\overline{\sigma}$	0.07	0.08
	$\overline{\gamma}_A$	0.03	0.01
	$\overline{\gamma}_D$	0.09	0.03
	$\overline{\gamma}_S$	0.02	0.01
	$\overline{r}$	0.17	0.16
ST_i	$\overline{\gamma}_0$	0.48	0.61
	$\overline{\sigma}$	0.17	0.31
	$\overline{\gamma}_A$	0.05	0.15
	$\overline{\gamma}_D$	0.17	0.11
	$\overline{\gamma}_S$	0.04	0.03
	$\overline{r}$	0.45	0.52

Indeed, Sobol indices computed using Kriging estimations are organized as follows:

$$ST_{\overline{\gamma}_0} > ST_{\overline{r}} > ST_{\overline{\sigma}} > ST_{\overline{\gamma}_A} > ST_{\overline{\gamma}_D} > ST_{\overline{\gamma}_S},$$

$$S_{\overline{\gamma}_0} > S_{\overline{r}} > S_{\overline{\sigma}} > S_{\overline{\gamma}_D} > S_{\overline{\gamma}_A} = S_{\overline{\gamma}_S}.$$

On the other hand, those computed using PCE give the following ordering:

$$ST_{\overline{\gamma}_0} > ST_{\overline{r}} > ST_{\overline{\gamma}_D} = ST_{\overline{\sigma}} > ST_{\overline{\gamma}_A} \approx ST_{\overline{\gamma}_S},$$

$$S_{\overline{\gamma}_0} > S_{\overline{r}} > S_{\overline{\gamma}_D} > S_{\overline{\sigma}} = S_{\overline{\gamma}_A}.$$

The ordering of the total indices obtained with Kriging and PCE are compared in a pie-chart in Figure 5.20.

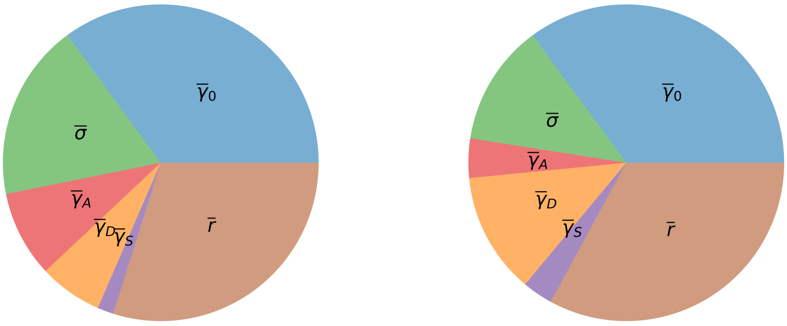

(a) (b)

Figure 5.20: Distribution of the total Sobol indices obtained with (a) Kriging and (b) PCE.

Consequently, both approaches lead to different conclusions on the influence of the input parameters on $\tilde{F}$. However, results from PCE show tendencies similar to those that have been observed in Chapter 4. Indeed, the analogous analysis, performed on a circular NP, provided the same ranking of the first and total Sobol indices as that obtained with PCE. Nonetheless, the results from Chapter 3 showed that $ST_{\overline{r}} > ST_{\overline{\gamma}_0}$ and $S_{\overline{r}} > S_{\overline{\gamma}_0}$, when the membrane mechano-adaptation is not considered. None of the methods provided here shows similar results concerning these variables. Supposing that PCE-estimated Sobol indices are correct, that would mean that the influence of the aspect ratio of the NP on $\tilde{F}$ is inhibited by the initial parameters for an adaptive membrane. However, recalling that the accuracy of the metamodels prediction is poor ($Q_2^{KRI} = 0.42$ and $Q_2^{PCE} = 0.55$), the precision of the Sobol indices obtained using such models is non ensured. For this reason, no conclusion could be drawn from this study.

5 Discussion

The methods and results presented in this chapter are similar to those introduced in Chapter 4. As such, most of the discussion points have already been addressed previously. Nonetheless, the investigations conducted in this chapter on elliptic NPs involved additional challenges that yielded difficulties in the construction of the metamodels. These elements are discussed in the following.

Difficulties in the predictions of the dataset have been encountered, especially in the comparative study between the passive and active cases, where the predictivity factors of the metamodels were $Q_2^{KRI} = 0.42$ and $Q_2^{PCE} = 0.55$. These predictions are less accurate compared to those in the previous chapter ($Q_2^{KRI} = 0.99$ and $Q_2^{PCE} = 0.98$ for the study on Ψ_3 and $Q_2^{KRI} = 0.86$ and $Q_2^{PCE} = 0.80$ for the study on $\tilde{F}$), which highlights the limitations of both Kriging and PCE when having $\overline{r}$ as an input parameter. Indeed, both Chapters 4 and 5 aimed at investigating the role of the mechano-adaptation of the membrane, with the only difference being the consideration of $\overline{r}$ as input parameter. Thus, one can infer that $\overline{r}$ has possibly a nonlinear effect on the model, with interactions with other input parameters. Furthermore, one can note that the effect of $\overline{r}$ on $\overline{\Delta E}$, and consequently on the predictions, changes drastically when $\overline{r} > 1$ or $\overline{r} < 1$. As such, using different types of metamodels for these two cases could lead to better predictions, since each of them would be in charge of approximating two distinct behaviors separately.

Furthermore, the predictions of the model could also be improved by increasing the size of the training dataset, which was set to $2^{12} = 4096$ in this study. However, considering that the objective of building a metamodel is to simulate the initial model in order to avoid time-consuming model calculations, it does not seem appropriate to increase the number of samples in this case. Another possibility is to explore other meta-modeling approaches, like those that have been introduced in Chapter 3, *e.g.* PCE-Kriging and artificial neural networks, or to use training dataset with a similar-to-uniform distribution in order to avoid the limitations due to multi modal distributions. Last, the application of a clip to the metamodel predictions, as introduced in the previous chapters, could improve the accuracy of the samples used for the estimations of the Sobol indices.

These errors in the predictions of the metamodels yielded inaccurate Sobol indices, from which no conclusion regarding the sensitivity analysis could be drawn for the study of $\tilde{F}$. Moreover, even if the predictivity factors of the metamodels constructed for the study of Ψ_3 are closer to 1 ($Q_2^{KRI} = 0.92$ and $Q_2^{PCE} = 0.68$), they were not satisfying either, especially PCE, as they are not close to 1. As such, the recommendations for improving the predictions of metamodels, that have been presented in the previous paragraphs, should be applied to this study as well.

6 Conclusions of Chapter 5

In this chapter, the cellular uptake of an elliptic NP was investigated when considering the mechanical adaptation of the membrane during the wrapping of the NP. The steps that have been followed, along with the results, are presented below.

- **The influence of the aspect ratio of the NP** has first been highlighted in the case of a passive membrane (constant mechanical properties) in Chapter 3. The study conducted in the present chapter confirmed that its influence on the model is maintained when accounting for the mechanical adaptation of the membrane.

- **The proportion of full wrapping** is indeed mostly influenced by the aspect ratio of the NP, then by the delay in the membrane mechanical response, for the range of values adopted in this study. The amplitude and curvature parameter of the transition have less significant influences. This conclusion was drawn based on a sensitivity analysis conducted using predictions from Kriging and PCE metamodels, generated with a dataset of size 2^{10}. The convergence of the Sobol indices was verified, as well as the accuracy of the metamodel predictions ($Q_2^{KRI} = 0.92$).

- **The influence of the aspect ratio of a NP on its uptake by a cell with random properties** was also investigated. Indeed, a dataset of size 2^{12} of the six input parameters was built and the corresponding values of the wrapping degree at equilibrium have been computed. Then, metamodels have been constructed in order to have estimations of the model based on this dataset, to finally compute the sensitivity indices. However, the metamodels, used to generate these predictions, did not provide satisfying accuracies, with predictivity factors $Q_2^{KRI} = 0.42$ and $Q_2^{PCE} = 0.55$. As a consequence, the sensitivity indices, that have been obtained using these metamodels, are not exploitable. It was thus impossible to conclude on the influence of the investigated parameters. One can note that this study is the one conducted with most input parameters, among which two of them have been shown to influence significantly the outputs of the model, when involved in the studies that have been presented previously in this thesis. These difficulties for predicting the data may be due to the domain of definition and/or the PDF of the QoI. Indeed, this investigation aimed at determining the influence of the input parameters on the wrapping degree at equilibrium, $\tilde{F}$. Studies that have been conducted in previous chapters, which also involved $\tilde{F}$, showed that this variable is more difficult to be estimated by the metamodels, as they often struggle to estimate the extreme values of its domain of definition, *i.e.* $\tilde{f} \to 0.03$ and $\tilde{f} \to 0.97$.

Chapter 6

APPLICATION OF THE MODEL TO A GIVEN CANCER BASED ON REAL DATA

1 Introduction

The ultimate objective of the present thesis is to provide a model able to determine the optimal mechanical and geometrical properties of a NP, in order to maximize its uptake by cancer cells, while avoiding healthy ones. In this context, this chapter aims at applying our model to a concrete case. Hence, a literature review is conducted in order to identify the mechanical properties of both healthy and cancer cells. Then, the model is used, with these input mechanical parameters, in order to estimate the aspect ratios of the NPs that would enable them to be internalized solely by cancer cells. Among the wide variety of existing cancers, this application will focus on breast cancer (which touches mammary cells), being the most frequent (see Table 6.1) and documented cancer [3, 232, 233], as illustrated in Figure 6.1.

Table 6.1: Seven most frequent cancer types worldwide, based on data from 2020, adapted from [233].

Rank	Cancer	New cases in 2020	% of all cancers
	All cancers	18 094 716	
1	Breast	2 261 419	12.5
2	Lung	2 206 771	12.2
3	Colon	1 931 590	10.7
4	Prostate	1 414 259	7.8
5	Stomach	1 089 103	6
6	Liver	905 677	5
7	Cervix uteri	604 127	3.3

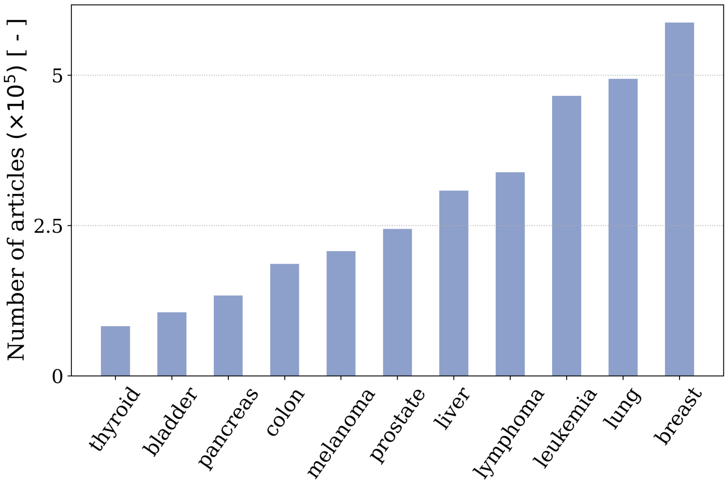

Figure 6.1: Number of existing research articles on different types of cancers, obtained using the Scopus[1] data basis with the keywords "[type of cancer]" + "cancer".

Section 2 presents the data from the literature that have been used to provide numerical values for the mechanical parameters of our model, while Section 3 details and applies the methodology to determine the optimal aspect ratio for the NP. Last, the results are discussed in Section 4.

2 Mechanical properties of healthy and cancer breast cells

2.1 Bending rigidity

The bending rigidity κ of the membrane, introduced in Chapter 2, is used to calculate the values of adimensional variables $\overline{\gamma}$ and $\overline{\sigma}$. As such, this section aims at providing a review of the studies that have been conducted in order to measure κ or to approximate the ratio between the bending rigidity of healthy and cancer cells. Händel *et al.* [234] computed κ based on a Fourier decomposition of the variation of the cell membrane shape, determined with mass spectroscopy, as a response to thermal fluctuations. Using this technique, the bending rigidity of healthy and cancer cells were estimated as $\kappa^H = 4.5 \times 10^{-19}$ Nm and $\kappa^C = 1.3 \times 10^{-19}$ Nm, respectively. This notation will be used in the sequel.

To the best of our knowledge, this is the only experimental study on the bending

---

[1] Scopus is a data basis that gathers the research articles published by the scientific editor Elsevier. Available at `https://scopus.com`.

rigidity of healthy and cancer breast cells conducted so far. Nonetheless, more data could be found about the Young modulus E since it is an easier parameter to be characterized, and which is currently being investigated as a tool for cancer diagnosis [235–238]. The Young modulus does not belong to the set of parameters required to feed the numerical model introduced in this thesis. However, it is related to the bending stiffness via $\kappa = Eh^3(1-\nu^2)^{-1}/12$ [40], where h is the thickness of the membrane and ν its Poisson's ratio. In this chapter, even though discrepancies in the structure of the cell membrane of healthy and cancer cells suggest the contrary, we suppose that h and ν are the same for all the cells that are investigated. This hypothesis, that will be discussed in Section 4, enables us to use the studies conducted on the Young modulus E in order to estimate the ratio between κ^C and κ^H. The following sections introduce different methods that have been used to determine the Young modulus of breast cancer cells, along with their possible limitations. The results that have been obtained with such methods are also presented.

2.1.1 AFM measurements of the Young modulus

Overview Atomic Force Microscopy (AFM) consists in sweeping a sharp tip, attached to a flexible cantilever, over the surface of a sample. Variations in depth consequently lead to changes in the bending of the cantilever, which is detected by an optical device [239]. This technique aims at reproducing the vertical profile of the sample. In addition, AFM also reproduces the principle of indentation as it is possible to apply a vertical force, usually between 100 and 1000 pN, to the cantilever. The vertical displacement, induced by this force, can be measured following techniques similar to those used in indentation. Then, the evolution of the loading force, in terms of the vertical displacement, enables to determine the stiffness of the sample at the location of the indent [70, 240].

Limitations and important considerations It is worth noting that the AFM measurements highly depend on several parameters: (i) the substrate in which the cell is placed alters the measurements. For this reason, it is not possible to compare results from different AFM studies. As such, only the ratios between values of E^H and E^C, measured in the same study, will be used in this chapter. (ii) Furthermore, the indentation depth of the AFM measurements plays a key role in the result. Indeed, when applying a small indentation depth, only a measure of the local rigidity of the actin filaments is obtained, while only a larger indentation depth enables to measure the Young modulus of the cell. It is consequently of great interest to ensure that the indentation depth is in the same order of magnitude, and large enough, in two studies used to compare values of E. (iii) Then, the load velocity of the AFM measurement also alters significantly the measurements (up to 173 % for healthy bladder cells [64]). Note that this highlights a viscoelastic behavior of the cell. (iv) Moreover, a long load duration may lead to a reorganization of the actin filaments and hence to a different measure of the Young modulus. For all the aforementioned reasons, it is indispensable to make sure that the AFM measurements have been performed in similar conditions before comparing the Young moduli. Last, AFM measurements are not trivial to perform, as they require complex electronics and optics, which do not work properly in opaque liquids [72].

Evaluation Young modulus of breast cancer cells Lekka *et al.* [64, 241] conducted AFM measurements on breast healthy and cancer cells and obtained $E^H = 2.5$ kPa and $E^C = 1.25$ kPa, leading to $E^C = 0.5\, E^H$. These are averaged values obtained with 20 cells. Lin *et al.* [65] compared the Young modulus of breast cancer cells with that of healthy breast cells and showed that $E^C \in [0.2, 0.4] \times E^H$, while Li *et al.* [69] measured $E^C \in [0.56, 0.71] \times E^H$. Note that the intervals obtained in these different studies have no intersection, which illustrates the variability of the measures and enforces the conclusion that no direct comparison between the results obtained from different articles is possible.

2.1.2 Optical deformability

Overview The optical deformability technique enables to observe the deformation of an isolated cell, *i.e.* independent of a tissue or a substrate, after the application of a stretching to deduce the cell stiffness. An illustration of optically deformed cells is provided in Figure 6.2.

As presented in [67, 73], the cell stiffness is approximated by the optical deformability index OD, defined as:

$$OD = \left(\frac{ab^0}{a^0 b} - 1 \right) \frac{F_a^0}{F_b^0} \frac{F_b}{F_a}, \tag{6.1}$$

in which exponent 0 refers to the initial configuration, F_a and F_b refer to the stretching forces along the semi major and minor axes of the elliptic cell, while a and b refer to their length.

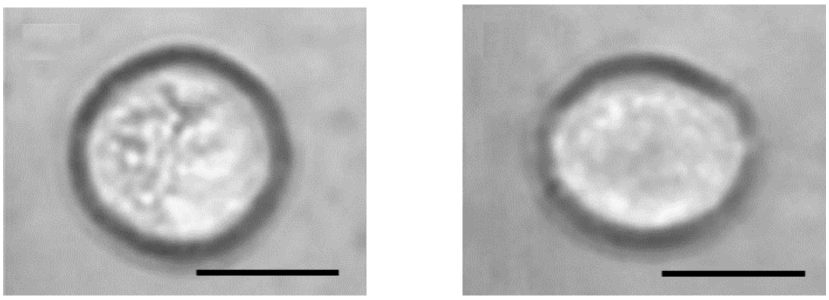

(a) (b)

Figure 6.2: Illustration of the stretching of breast (a) healthy and (b) cancer cells, applied to deduce their optical deformability and hence their stiffness. The black lines represent a scale of 10 μm. Adapted from [73].

Limitations and important considerations If the strain level that is applied to the cells is important, a reorganization of the actin filaments may take place, which could alter the measure of stiffness. Furthermore, the force that is applied to the cells by the optical tweezers may not be large enough to trigger and observe all the phenomena that can happen in the cell. In addition, the cells are exposed to laser during this experiment, which may alter their mechanical properties. Hence, like in the previous measurement techniques, it is necessary to use results that have been obtained in similar experimental conditions, in order to have accurate ratios of E^H/E^C. Moreover, this model approximates the shape of the cell as elliptic, which can be discussed since the cells have mostly not perfectly elliptic shapes, as illustrated in Figure 6.2b.

Measurements Investigations of the optical deformability of healthy and cancer breast cells, conducted by Guck *et al.* [73], determined that healthy cells are, in average, twice as stiff as cancer cells.

2.2 Membrane tension

No article comparing the membrane tension in healthy and cancer mammary cells was found. For this reason, the remaining is dedicated to non-comparative studies of the membrane tension. On the one hand, Händel *et al.* [234] assessed both the membrane tension σ and the bending rigidity κ of cancer mammary cells, obtaining $\sigma^C = 8.69 \pm 1.76 \times 10^{-2}\,\mathrm{mN/m}$. On the other hand, Zhang *et al.* [30] introduced $\sigma = 0.05\,\mathrm{mN/m}$ regardless of the cell type or healthiness. Based on such findings, it will be difficult to compare σ^C and σ^H.

2.3 Cellular adhesion

The adhesion does not solely depend on the cell, it is rather a measure which considers two objects, *e.g.* the cell membrane and a NP. For this reason, it is necessary to consider the two bodies that are involved, when characterizing adhesion. In this thesis, we are interested in retrieving data relative to the adhesion between the membrane of a breast cell and a NP. Unfortunately, such data could not be found, as the studies on cellular adhesion are often rather focused on the cell-cell adhesion, or on the adhesion between the cell and the extra-cellular medium (ECM), as it enables to investigate the propagation behavior of cancer cells, that takes place during the metastasis for instance. To obtain an estimation of the order of magnitude of the ratios of the adhesion between healthy or cancer cells and a NP, we will suppose that this ratio is the same as the ratio between the cell-cell adhesion of healthy and cancer cells, or as that of cell-ECM adhesion.

Measurements The cell-cell adhesion can be assessed by micro-pipette aspiration [67], which consists in coating two cells with a substrate (often dextran), that is used as a glue, and then to put the two coated cells in contact, as illustrated in Figure 6.3.

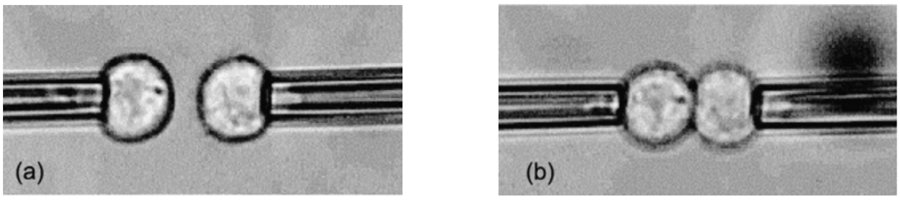

(a) (b)

Figure 6.3: Illustration of the micro-pipette aspiration experiment used to measure the adhesion energy between two murine sarcoma cells. The cells are (a) first maintained in position thanks to the pipettes, before (b) being brought into contact, and then separated again (not represented). Adapted from [67, 82].

Then, the force necessary to separate the cells is measured and used to evaluate the adhesion energy with the Johnson-Kendall-Roberts theory [242]. It is worth noting that the adhesion energy obtained with this experimental technique depends on the dextran volume fraction [67, 82, 243]. Therefore, the values of adhesion need to be determined in experiments involving the same dextran volume fraction. Unfortunately, no comparative studies on the adhesion of healthy and cancer cells could be found, neither any measure of the adhesion of breast cells.

Nonetheless, measurements of adhesion between objects different from those introduced above could help to find at least an order of magnitude for the adhesion between healthy and cancer breast cells. For instance, Evans *et al.* [243] reported a measure of the adhesion energy between two artificial lipid vesicles, being the interval $\gamma \in [0.01, 0.1]$ mN/m. Chu *et al.* [82] measured $\gamma \in [0.1, 1]$ mN/m for the adhesion between two murine sarcoma cells. Furthermore, Colbert [244] performed a micro-pipette aspiration experiment to measure the adhesion between a lipid vesicle and a gold substrate and found $\gamma \in [0.03, 0.07]$mN/m. In addition, Dietrich *et al.* [110], in their analytical investigation of the adhesion of a latex sphere to a giant phospholipid vesicle, used the range of values of adhesion $\gamma \in [0.1, 5]$ mN/m. Last, a review on the endocytosis of NPs introduced $\gamma = 0.1\,\text{mN/m}$ [30].

Limitations and important considerations The cellular adhesion is actually mostly due to the glycocalix (see Chapter 1 for more details). However, these micro-pipette aspiration measurements are conducted on single cells and therefore it is possible that part of the cell coat was lost before the measurement. For this reason, the adhesion that is measured with such technique may underestimate the real adhesion between the cells, and more importantly, they do not account for the influence of the glycocalix on the cellular adhesion. In addition, several studies [76, 245] showed discrepancies in the composition of glycocalix in healthy and cancer cells, and more specifically in the distribution of adhesion molecules [246, 247]. Thus, even though micro-pipette aspiration experiments provided similar adhesion in the case of healthy and cancer cells, their adhesion may actually differ because of the glycocalix difference. Jones *et al.* [248] explain that the proportion of different types of adhesion molecules varies between healthy and cancer cells. A review on the adhesion molecules in breast healthy and cancer cells highlighted the fact that the glycocalix of breast cancer cells contains less integrins than their healthy counterparts [246]. Integrins is the major protein family present in glycocalix [249]. The other protein families in glycocalix are cadherins, integrins, selectins or immunoglobulins [250]. The cell-cell and cell-ECM adhesion is mostly due to integrins. Unfortunately, the variations in the protein composition of the glycocalix are too biology-oriented for us to understand them properly. Thus, we will assume that integrins compose 3/4 of the proteins and that their amount is reduced by 50 % in cancer cells. Hence,

$$\gamma^C = \left(\frac{1}{2}\frac{3}{4} + \frac{1}{4}\right)\gamma^H = 0.625\gamma^H \tag{6.2}$$

Furthermore, some studies showed that the thickness of the glycocalix of cancer cells is smaller than that of healthy cells [61, 75, 251, 252]. However, no relevant measure of the difference in these thicknesses could be found and thus it is not taken into account in this chapter.

2.4 Evolution of the adhesion

The adaptation of the adhesion is a complex phenomenon that has been observed but not characterized experimentally, *i.e.* to the best of our knowledge, there is no measure of the variation of adhesion during the wrapping of a NP, which we defined in Chapter 4 in terms of an amplitude γ_A, a delay γ_D and a curvature parameter γ_S. Still, based on studies on the kinetic segregation of receptors in the glycocalix [76, 253], which is the dynamics that take place in the glycocalix in order to ease the formation of receptor-ligand bonds, one can conclude that there is an increase of the proportion of integrin close to the region in contact with an extra-cellular penetrant. This phenomenon seems to be more important in cancer cells. However, no precise data could be used to quantify the discrepancies of the adhesive properties between healthy and cancer cells.

2.5 Synthesis of the measured data

The values that have been found in literature for the bending rigidity κ, the membrane tension σ, and the cellular adhesion γ, presented in the previous sections, are summarized in Table 6.2.

Table 6.2: Synthesis of the measured values of the input parameters of the model for healthy and cancer breast cells, according to the literature.

Parameter	**Technique**	**Value**	**Reference**
κ	Mass spectroscopy to observe the response of healthy and cancer breast cells to thermal fluctuation	$\kappa^H = 4.5 \times 10^{-19}\,\mathrm{Nm}$ $\kappa^C = 1.3 \times 10^{-19}\,\mathrm{Nm}$	Händel *et al.* [234]
E	AFM of healthy and cancer breast cell	$E^C = 0.5\,E^H$	Lekka *et al.* [64, 241]
		$E^C \in [0.2, 0.4] \times E^H$	Lin *et al.* [65]
		$E^C \in [0.56, 0.71] \times E^H$	Li *et al.* [69]
	Optical deformability	$E^C = 0.5\,E^H$	Guck *et al.* [73]
σ	Mass spectroscopy to observe the response of healthy and cancer breast cells to thermal fluctuation	$\sigma^C = (8.69 \pm 1.76) \times 10^{-2}\,\mathrm{mN/m}$	Händel *et al.* [234]
	Review on the endocytosis of NPs	$\sigma = 0.05\,\mathrm{mN/m}$	Zhang *et al.* [30]
γ_0	Micro-pipette aspiration between two artificial lipid vesicles	$\gamma \in [0.01, 0.1]\,\mathrm{mN/m}$	Evans *et al.* [243]
	Micro-pipette aspiration between two murine sarcoma cells	$\gamma \in [0.1, 1]\,\mathrm{mN/m}$	Chu *et al.* [82]
	Micro-pipette aspiration between a lipid vesicle and a gold substrate	$\gamma \in [0.03, 0.07]\,\mathrm{mN/m}$	Colbert [244]
	Analytical investigation of the adhesion of a latex sphere to a giant vesicle	$\gamma \in [0.1, 5]\,\mathrm{mN/m}$	Dietrich *et al.* [110]
	Review on the endocytosis of NPs	$\gamma = 0.1\,\mathrm{mN/m}$	Zhang *et al.* [30]

3 Optimization of the aspect ratio of the NP

The objective of this section is to apply the model developed in this thesis to a concrete case of breast cancer. To do so, the mechanical properties that are necessary to describe the behavior of healthy and cancer breast cells have been investigated in the previous section. These values will be used in order to determine the aspect ratio of a NP enabling it to be engulfed only by cancer cells, while being unable to enter healthy cells. An illustration of the application of the model is provided in Figure 6.4. The values, used as input parameters for the model, are introduced in Section 3.1 and the aspect ratios that enable the NPs to enter cancer cells only are presented afterwards in Section 3.2.

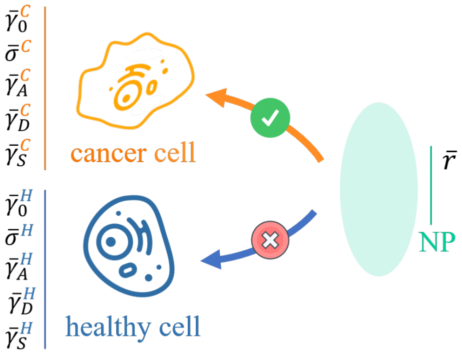

Figure 6.4: Illustration of the application of the model.

3.1 Input parameters

First, we used the values for bending stiffness estimated in [234], *i.e.* $\kappa^H = 4.5\times10^{-19}$ N/m and $\kappa^C = 4.5 \times 10^{-19}$ N/m. Second, we took an intermediate value for the membrane tension of both healthy and cancer cells, being $\sigma^H = \sigma^C = 0.01$ mN/m. This value is equal for both cell types as we could not find precise quantitative information to distinguish them. Then, the adhesion of healthy breast cells was set to $\gamma^H = 0.1$ mN/m, as it is an average value between those that have been gathered from the literature. Since no data could be found for γ^C, we use Equation 6.2, based on the reduction of the proportion of integrins in the glycocalix, leading to $\gamma^C = 0.0625$ mN/m. Thus, the values of the adimensional parameters $\overline{\sigma}$ and $\overline{\gamma}$ can be determined via $\overline{\sigma} = 2\sigma a^2/\kappa$ and $\overline{\gamma} = 2\gamma a^2/\kappa$, in which a is the relative radius of the NP, set to 100 nm. Hence, $\overline{\sigma}^H = 0.44$, $\overline{\sigma}^C = 1.54$, $\overline{\gamma}^H = 4.44$ and $\overline{\gamma}^C = 9.62$. Last, we could not find any data describing the membrane adaptation. However, we will suppose that the reactivity of the cancer cell membrane is more important than that of the healthy cell, since the former has in general a more adaptive behavior to ensure their proliferation for instance. In order to emphasize this, extreme values of the domains of definition of γ_A, γ_D and γ_S are chosen. As such, $\gamma_A^H = 1.5$, $\gamma_A^C = 4$, $\gamma_D^H = 0.2$, $\gamma_D^C = -0.2$ and γ_S is set equal to 50 for both cases, as we showed in the previous chapters that this parameter has no influence on the cellular uptake predictions. The values taken for these input parameters are summarized in Table 6.3.

Table 6.3: Synthesis of the values used as input parameters for the model.

Parameter	**Healthy cell**	**Cancer cell**
a	100 nm	
κ	4.5×10^-19 Nm	1.3×10^-19 Nm
σ	0.01 mN/m	
γ	0.1 mN/m	0.0625 mN/m
$\overline{\sigma}$	0.44	1.54
$\overline{\gamma}$	4.44	9.62
$\overline{\gamma}_A$	1.5	4
$\overline{\gamma}_D$	0.2	-0.2
$\overline{\gamma}_S$	50	

3.2 Results

In order to determine if the NP is fully wrapped, depending on its aspect ratio, the wrapping phase is evaluated in terms of $\overline{r}$. The results, concerning the uptake of the NP by cancer and healthy breast cells, are provided in Figure 6.5. It is possible to distinguish several regions in this graph. For $\overline{r} < 0.32$, there is no distinction between healthy and cancer cells, both do not wrap the NP (phase 1). For $\overline{r} \in [0.32, 0.48]$, the NP stays in phase 1 with the healthy cell and is fully wrapped by the cancer cell (phase 3). Then, for $\overline{r} \in [0.48, 1.47]$, the NP is fully wrapped regardless of the cell state. Next, for $\overline{r} \in [1.47, 4.96]$, NPs are fully wrapped by cancer cells and partially wrapped by healthy cells. Last, for $\overline{r} \in [4.96, 6]$, the NPs are partially wrapped by both healthy and cancer cells. The variation of the total potential energy during the wrapping of NPs for $\overline{r} \in \{0.25, 0.4, 4\}$ by healthy and cancer cells is illustrated in Figure 6.6.

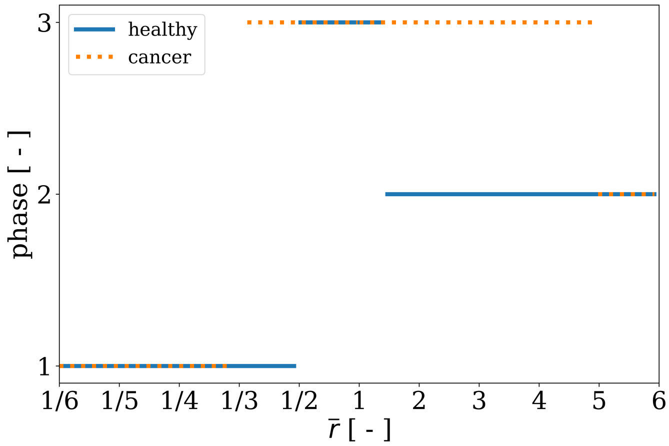

Figure 6.5: Evolution of the wrapping phase of the NP in terms of its aspect ratio $\overline{r}$, for both healthy (solid blue line) and cancer (dotted orange line) breast cells.

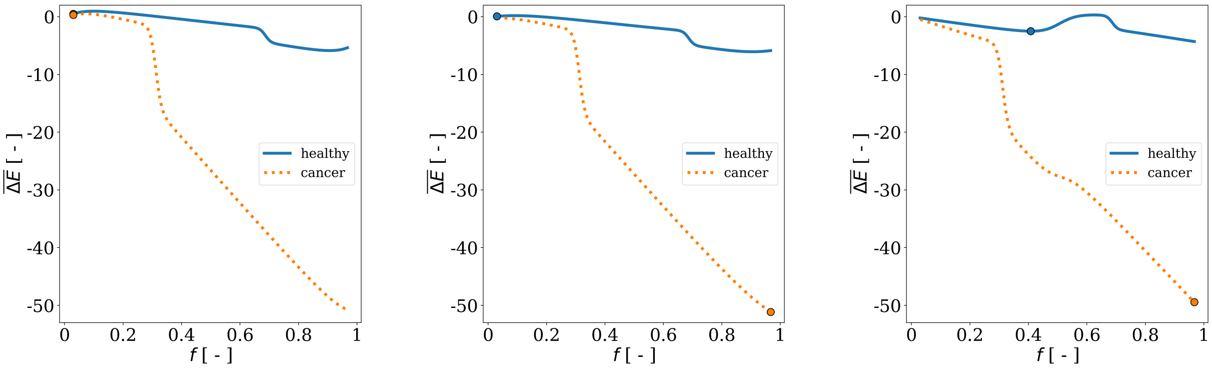

(a) $\overline{r} = 0.25$

(b) $\overline{r} = 0.4$

(c) $\overline{r} = 4$

Figure 6.6: Variation of $\overline{\Delta E}$ during the wrapping of NPs with (a) $\overline{r} = 0.25$ (the NP is wrapped nor by healthy neither cancer cells), (b) $\overline{r} = 0.4$ (the NP is fully wrapped by the cancer cell and not wrapped by the healthy cell) and (c) $\overline{r} = 4$ (the NP is fully wrapped by the cancer cell and only partially wrapped by the healthy cell). Solid blue (resp. dotted orange) lines represent healthy (resp. cancer) breast cells. The colored markers correspond the equilibrium positions.

One can then conclude from these results that using NPs with $\overline{r} \in [0.32, 0.48]$ enhances the chances for them to be internalized only by cancer cells.

4 Discussion

As already introduced earlier in this chapter, this application is based on the evaluation of the mechanical properties of the cell. The method, used to set them for our model, along with the conclusions that could be drawn from the model output, are discussed in the following.

- **Few studies have been used to evaluate the input parameters**, and the ones we found were conducted in different conditions, making difficult the comparisons between the values that have been measured in these different studies. In addition, some of these studies, especially the AFM, which is the most commonly used characterization technique in this context, usually investigate the mechanical behavior of tumors, *i.e.* an ensemble of cancer cells that compose a cancerous tissue, and not that of a single cell. It is consequently crucial to verify the settings of the experiments and only data obtained during a same study should be compared. Furthermore, in order to be able to use the interpretations from the measurements of the Young modulus E in this study, we consider that it was proportional to the bending rigidity κ. Although, the relation between E and κ also involves the thickness and the Poisson's ratio of the membrane, that was supposed to be the same between healthy and cancer breast cells, even if the differences in the composition of the lipid membrane and in the glycocalix of these cells challenge this hypothesis. As such, the ratios between E^C and E^H can be used to infer that of κ^C and κ^H only if those involving the thickness of the membrane h and its Poisson's ratio ν are known as well. Note that we actually used the values of κ, instead of E, since they were available for breast cells.

- **Some variables could not be determined,** such as the parameters relative to the evolution of the adhesion during wrapping. Indeed, to determine them accurately, it would have been necessary to have a better understanding of the mechanics that involve the adhesion molecules in the glycocalix. Unfortunately, these phenomena are complex and could not be interpreted with our background, as they require a wide knowledge in histology and chemistry.

- **The results are highly sensitive to the input parameters,** which are not known with precision. Hence, a study of the propagation of uncertainties would provide more accurate results and would enable us to define a smaller interval of values of $\overline{r}$ that ensure the uptake of the NP by cancer cells only, with the smallest uncertainty possible.

5 Conclusions of Chapter 6

In this chapter, we applied our numerical model to the concrete case of breast cancer, which aimed at optimizing the aspect ratio of NPs so that they will only enter cancer cells. The steps and the results of this application are summarized in the following.

- **The values for the input parameters of the model** have been determined, based on an extensive literature review focused on experimental studies. Different techniques have been introduced, *e.g.* AFM for assessing the Young modulus of the cell or micro-pipette aspirations for the cellular adhesion. Still, only little data were available for that particular cancer, even though we chose it for being the most documented according to Scopus statistics. Indeed, such measurements are not common in the literature, given that knowing the mechanical properties of the cell does not present much interest for physicians or biologists. Furthermore, these measurements are usually difficult to conduct due to the scale of the objects, and consequently the precision of the instruments that are necessary. AFM measurements of the Young modulus are more frequent, since E is a promising indicator for cancer diagnosis, for being relatively easy to perform with standardized methods. Thus, the values that have been chosen for determining the input parameters of the model come from few studies, which only enable us to collect information about the order of magnitude of the variables. Nonetheless, it is worth noting that the results, obtained in different studies, are close, which suggests the relevance of the data we used.

- **According to the model**, we could find a range of aspect ratios of the NP, being $[0.32, 0.48]$, for which the NPs are fully wrapped by cancer cells, while they are not wrapped by healthy cells. These are therefore the aspect ratios that need to be used to deliver cancer treatments so that they cannot be internalized by the healthy cells. On the contrary, NPs with $\overline{r} \in [0.48, 1.47]$ should be avoided, as they can be engulfed by both healthy and cancer cells, with no discrimination.

- **These results are promising,** as they show that it is possible to control and optimize the internalization of NPs by breast cancer cells, based on the aspect ratio of the former.

CONCLUSION

1 Summary of the thesis

The work presented in this thesis is part of the METCIN project, which aims at identifying the influence of the mechanical properties of NPs on their internalization by cells of different biological phenotypes. In order to achieve this goal, we focused here on the development of a mechanical model of the cellular uptake of rigid NPs with variable aspect ratio. The objective was to provide a better understanding of the phenomenon by identifying the most influential parameters on the wrapping of a NP.

Hence, a general presentation of the investigated objects, *i.e.* the NPs and the cell membranes, as well as the existing methods developed to study the cellular uptake of NPs, has been provided in Chapter 1. The comparison of such methods enabled us to identify the most suitable approach in the context of this thesis.

Thus, an energetic investigation of the phenomenon at the scale of the NP, considered rigid and elliptical in this study, was preferred for being a good compromise between representativeness and computational costs. The henceforth developed model is presented in details, along with the different hypotheses, in Chapter 2.

This approach was then used to identify the influence of the input parameters, *i.e.* the membrane tension, the NP-cell adhesion and the aspect ratio of the NP, on the cellular internalization of a NP. For this purpose, sensitivity analyses have been conducted. In order to overcome the limitations relative to an extensive computation time, necessary to generate the samples needed for the sensitivity analyses, surrogate models have been developed. The aforementioned techniques, along with their application to the model, have been presented in Chapter 3.

Furthermore, in order to enforce the ability of the model to depict the phenomena that take place in the cell membrane, a law describing the evolution of the NP-membrane adhesion in terms of the cellular wrapping of the NP as a mechanical response of the membrane to the interaction with an extra-cellular object, has been proposed. The influence of this new feature of the model has then been investigated in Chapter 4, in the case of the wrapping of a circular NP. A similar study, conducted on elliptical NPs, has been presented in Chapter 5. These studies enabled to identify the aspect ratio of the NP and the initial NP-membrane adhesion as the two most important parameters.

Finally, in Chapter 6, the model has been applied to mammary healthy and cancer cells, in order to identify the aspect ratios of the NP that would enable it to enter only the cancer cells, while being unable to penetrate healthy cells, which would limit the side effects of the treatment and improve its efficiency. For this purpose, the mechanical properties of such cells have been identified based on existing characterization results from the literature. This study demonstrated the existence of aspect ratios (between 1/3 and 1/2) that fulfill this criterion. Still, the conclusions of this application remain questionable, based on several hypotheses and uncertainties that exist concerning the identification of the input parameters. Nonetheless, they can be used as an guidance for the NP manufacturers to drive their efforts on NPs with such ratios in order to ensure that the contact with the membrane takes place by the tip of the ellipse (vertical NP). In the meantime, oncologists can use these results to focus their experimental studies on breast cancer as it seems to display more noticeable differences between healthy and cancer cells for the NP internalization to be differentiated.

Our contribution

In this thesis, we used an existing model from the literature to investigate the cellular uptake of elliptic NPs. As a novelty, we conducted sensitivity analyses in order to quantify the influence of the input parameters of this model, which had solely been investigated qualitatively in the previous studies. Then, based on the literature, we enriched this model by accounting for the mechano-adaptation of the membrane. The interest of this new feature of the model was demonstrated through a sensitivity analysis. Last, an incremental technique, enabling to apply such model to a concrete case of cancer has been introduced for the first time in this thesis.

2 Perspective for future work

Some of the hypotheses that have been considered can be discussed and hence be investigated deeper in future work, in order to contribute to resolve the challenges of the METCIN project. As such, perspectives at short, mid and long term are presented in the following.

2.1 Short-term perspectives

Multiphysics approach

In this study, the bending stiffness of the membrane is considered constant during the wrapping of the NP. However, based on the phenomena that have been introduced in this thesis, it would be interesting to discuss the hypothesis of a constant bending rigidity in future work in order to strengthen our approach by implementing this biological phenomenon more accurately. However, similar to the variation of adhesion, the lack of existing data relative to the variation of κ would challenge the implementation of a variable bending stiffness.

Multiscale approach

Furthermore, a strong hypothesis was made on the homogeneity of the membrane composition. This supposes that the bending rigidity of the membrane does not vary with respect to the position on the membrane. Thus, the model could be enriched by accounting for a bending stiffness that is a function of the arclength, such as $\kappa_2 = \kappa_2(s_2)$ and $\kappa_3 = \kappa_3(s_3)$, as introduced by Zhang [108], in a recent study.

Moreover, we considered the NPs as homogeneous, while their mechanical properties (more especially their surface properties) vary along their circumference. The variation of the distribution of ligands on rigid elliptic NPs has for instance been investigated in [254]. As such, we could implement this non uniform distribution in a non uniform adhesion γ to our model as a perspective of short-term future work. This would enable to account for the challenges related to the manufacturing of NPs, which is one of the objective of the METCIN project.

Post-processing

Quantities of interest In addition, part of the studies conducted in this thesis focused on the influence of input parameters on the wrapping degree at equilibrium, $\tilde{f}$. However, despite being a good indicator, this quantity is not sufficient by itself to define the full wrapping of the NP. Indeed, it is also necessary to make sure that the two sides of free membrane merge above the NP, so that a vesicle can be formed inside the cell and its spontaneous releasing to the extra cellular medium (exocytosis) is made more difficult. For this reason, it would be pertinent to evaluate the influence of the different parameters of the model on the distance between the two sides of the membrane, the objective being to have it minimized.

Surrogate modeling The surrogate models, that have been constructed in this thesis, provide different accuracies depending both on the dimensionality of the problem and on the distribution of the QoI. The metamodels provided some predictions out of the domain of definition of the QoIs. As such, applying a clip to these predictions would reduce their distance to the expected estimations. This post-processing could be a way to artificially increase the accuracy of the metamodels by restraining the domain of definition of the estimations. Furthermore, the accuracy of the Kriging predictions could also be improved with different settings for the optimization algorithm (*e.g.* trend and covariance functions), as the influence of which has not been investigated in this thesis.

Sensitivity analysis As introduced above, there is little knowledge on the actual statistical distribution and domains of definition of the input parameters of the model. However, the sampling of the input parameters being of most importance in the evaluation of the sensitivity indices [214], it should be investigated in more details in future work, as it is possible that using different bounds of the input parameters would lead to different results. Furthermore, the identification of more accurate domains of definition than those used in this study is introduced as a long-term perspective.

2.2 Mid-term perspectives

Post-processing

Part of the analyses conducted in this work were focused on the proportion of phase 3 *i.e.* of full wrapping. Indeed, it was the quantity that represented most interest in the scope of this study, as we aimed at predicting the engulfment of the NP. In this case, knowing in details the evolution of the amount of NPs that remained in phases 1 and 2 would not directly contribute to our objective. Nonetheless, the study of the proportion of cases that yielded no and partial wrapping may be of great interest to investigate the initial steps of wrapping, and more especially the initiation of adhesion, which would therefore contribute to the objectives of the METCIN project.

Experimental validation

In order to validate the results presented in this work, a study on the correlation between the model and experiments should be performed. Nonetheless, we introduced in this work some of the limitations to conduct this validation. For instance, it is challenging to control or to measure the mechanical properties of cells into which the internalization of NPs is investigated, which induces barriers for the comparison between experiments and numerical models. However, the use of artificial vesicles could help to overcome these difficulties. Indeed, they are artificial cellular membranes, for which the mechanical properties are known, reproducible and constant along the circumference [255]. As such, they are a more stable tool for experimental validation than living cells, which could be used for validation as a long-term perspective.

2.3 Long-term perspectives

Hypotheses on the mechanical behavior of the membrane

Another simplification that was used in this model concerns the elastic behavior of the cell membrane. Indeed, even though this hypothesis is commonly made in the study of membrane deformation (following the Helfrich [59] model), viscoelastic and hyperelastic behaviors of the membrane have been highlighted through several studies [256]. The influence of the constitutive law of the membrane could consequently be investigated in future work. However, this requires experimental validation. It is therefore necessary to design an experimental setting in order to observe the membrane deformation during the wrapping of the NP, to compare it to the kinetics that are modeled. Therefore, this study needs to be performed in collaboration with an interdisciplinary research team.

Identification of the model input parameters

Moreover, the bounds of the mechanical parameters used in this model, especially $\overline{\gamma}_A$, $\overline{\gamma}_D$ and $\overline{\gamma}_S$, were not set based on accurate values from the literature, since they are mathematical parameters that have been introduced for the first time in this work. However, since the bounds of the variables are of great importance in sensitivity analyses, the results may be altered. For this reason, an accurate study on the influence of the bounds of the domain of definition of these variables on the results of the sensitivity analyses is necessary to have a critical vision of the results that have been provided in this thesis.

This point was already mentioned as a short-term perspective. Once the influence of the uncertainty on the domains of definition are quantified and if they change the conclusions of the sensitivity analyses conducted in this thesis, it will be necessary to determine them with more accuracy. This can be done by performing experimental studies in order to measure the parameters relative to the adaptation of the cell membrane introduced in this thesis. Still, since such techniques have not been developed yet, their application is a perspective for long-term.

Alteration of the mechanical properties of the cell

Then, Lam *et al.* [257] showed that chemotherapy agents (daunorubicin, applied to leukemia) may have an effect on the architecture of the cytoskeleton, that can lead to an alteration of their mechanical properties, such as an increase by up to 30 % of their Young modulus, for instance. Hence, a model accounting for the cell mechanical properties during the treatment of the patients could improve the accuracy of the predictions. This is a relevant perspective in the scope of the METCIN project, whose objectives include the identification of the effect of the NPs on the cellular phenotype. However, little is known on this topic, meaning that an extensive literature review, along with experimental investigations, should be conducted before implementing this feature to the model.

Hypotheses on the modeling of endocytosis

In addition, the model presented in this work is able to account for discrepancies in the mechanical properties of healthy and cancer cells for a NP entering a cell through a similar endocytic process. However, these cells tend to prefer different endocytic pathways. This point was addressed by Sahay *et al.* [258]. Thus, perspective for future work could be to account for these different possibilities, by, for instance, considering a probability for healthy and cancer cells to engulf NPs through a given endocyctic pathway. Furthermore, even though this work is focused on the wrapping of a NP, it is important not to neglect the steps of the NP following its engulfment by the cell [23, 86], as it is not certain that the NP will be able to reach its final intracellular target. For instance, Vácha *et. al* [90] have modeled the steps in which the NP escapes from the endosome (*i.e.* the coat composed of the part of the membrane through which the NP entered the cell, see Figure 1.15).

Cellular tissue

Furthermore, this study investigated the entry of a NP in a cell, that was supposed free, such as blood cells. However, 90 % of cancers are located in epithelial tissues [65]. Hence, it would be interesting to identify if the model still applies in this case. However, the perspective of modeling a group of cells requires to account for additional mechanical constaints, such as contacts. It is consequently possible that the model developed in this thesis does not apply. As such, a long-term perspective would consist is conducting a literature review on the existing model of epithelial tissues and their dynamics, identifying the approach for the model and the key parameters, implementing the model and finally proceed to an experimental validation.

Appendices

Appendix A

COMPUTATION OF THE SOBOL INDICES

In this thesis, several sensitivity analyses have been conducted, using the open-source Python library OpenTURNS, which provides useful tools for computing the Sobol sensitivity indices using different algorithms. The objective of this appendix is to present these algorithms (Section 2), along with additional methods implemented in other tools, such as UQlab or SALib, which are introduced in Section 3. Before presenting the computation method, general information on the Sobol indices are reminded in Section 1.

1 Reminder on the Sobol indices

The Sobol indices are used in order to quantify the influence of a model input on the variability of its output. A complete definition of the Sobol indices is provided in Section 2.2.2 from Chapter 3. Still, here we remind the main equations for the first and total Sobol indices, denoted as S_i and ST_i:

$$S_i = \frac{\mathrm{Var}[\mathbb{E}[Y|X_i]]}{\mathrm{Var}[Y]}, \tag{A.1a}$$

$$ST_i = 1 - \frac{\mathrm{Var}[\mathbb{E}[Y|X_1, ..., X_i, X_{i+1}, ...X_M]]}{\mathrm{Var}[Y]}, \tag{A.1b}$$

wherein, $X_i, i \in \{1, 2, ..., M\}$ is the set of M input variables and Y is an output quantity of interest. The first order index S_i estimates the part of the variance of Y due to X_i only. Moreover, the total index ST_i also accounts for the effect of the interactions with other variables $X_{j,j\neq i}$. These equations can also be written as a function of V_i and $V_{\sim i}$, in which $V_i = \mathrm{Var}[\mathbb{E}[Y|X_i]]$ and $V_{\sim i} = \mathrm{Var}[\mathbb{E}[Y|X_1, ..., X_i, X_{i+1}, ...X_M]]$.

Hence, Equations A.1 become:

$$S_i = \frac{V_i}{\mathrm{Var}[Y]}, \tag{A.2a}$$

$$ST_i = 1 - \frac{V_{\sim i}}{\mathrm{Var}[Y]}. \tag{A.2b}$$

Thus, in order to compute the Sobol indices, it is necessary to evaluate different components of these equations that are relative to the conditional variance of Y, *i.e.* V_i and $V_{\sim i}$. Solutions have been developed in the literature, *e.g.* by Saltelli *et al.* [149], Jansen [157], Sobol *et al.* [155] (Mauntz-Kucherenko algorithm) and Martinez [156], which are the most commonly used approaches [259]. These methods are implemented in OpenTURNS and have been used in this thesis to compute the Sobol indices. They are presented in details in the following section.

2 Built-in algorithms in OpenTURNS

The information provided in this section is based on the documentation of OpenTURNS, available in [158]. OpenTURNS is a tool that also enables to build surrogate models and perform sensitivity analysis in a user-friendly manner, thanks to several built-in methods. In this section, four of the most commonly used algorithms to compute the Sobol sensitivity indices, implemented in OpenTURNS, are presented. These approaches consist in generating two independent input datasets, containing N samples, using on a Monte Carlo (*i.e.* random) sampling. Based on these datasets, two matrices of size $N \times M$, denoted as $\mathbf{A}$ and $\mathbf{B}$ are created as follows:

$$\mathbf{A} = \begin{pmatrix} a_{1,1} & a_{1,2} & \cdots & a_{1,M} \\ a_{2,1} & a_{2,2} & \cdots & a_{2,M} \\ \vdots & \vdots & \ddots & \vdots \\ a_{N,1} & a_{N,2} & \cdots & a_{N,M} \end{pmatrix}, \mathbf{B} = \begin{pmatrix} b_{1,1} & b_{1,2} & \cdots & b_{1,M} \\ b_{2,1} & b_{2,2} & \cdots & b_{2,M} \\ \vdots & \vdots & \ddots & \vdots \\ b_{N,1} & b_{N,2} & \cdots & b_{N,M} \end{pmatrix}.$$

In these matrices, each line corresponds to a set of realizations of the input parameters according to their PDF. Based on these matrices, two additional matrices, denoted as $\mathbf{E}^i$ and $\mathbf{C}^i$ are defined. The matrix $\mathbf{E}^i$ (resp. $\mathbf{C}^i$) is the matrix $\mathbf{A}$ (resp. $\mathbf{B}$) in with the i^{th} column in replaced by the i^{th} column of the matrix $\mathbf{B}$ (resp. $\mathbf{A}$).

Then, g is introduced such as $Y = g(X)$. The empirically centered function, denoted as $\tilde{g}$, is defined for any $x \in \mathbb{R}^M$ as $\tilde{g}(x) = g(x) - \overline{g}$, where $\overline{g}$ is the mean of $g(\mathbf{A})$. The total variance of Y is thus computed as the variance of $\tilde{g}(\mathbf{A})$.

The Sobol indices relative to the influence of the interactions between two variables X_i and X_j, denoted as $V_{i,j}$ can henceforth be estimated by $\hat{V}_{i,j}$ using the following formula, regardless of the algorithm:

$$\hat{V}_{i,j} = \frac{1}{N-1}\sum_{k=1}^{N} \tilde{g}(\mathbf{E}_k^i)\tilde{g}(\mathbf{C}_k^j) - \frac{1}{N}\sum_{k=1}^{N} \tilde{g}(\mathbf{A}_k)\tilde{g}(\mathbf{B}_k) - \hat{V}_i - \hat{V}_j. \tag{A.3}$$

The estimation of V_i, denoted as $\hat{V}_i$, along with that of $V_{\sim i}$, differ between the algorithms and the formulas used to approximate them are presented in the following.

2.1 Saltelli

The Saltelli method was developed in 2004 by Saltelli *et al.* [149]. It consists in estimating the values of V_i and $V_{\sim i}$ as:

$$\hat{V}_i = \frac{1}{N-1}\sum_{k=1}^{N} \tilde{g}(\mathbf{B}_k)\tilde{g}(\mathbf{E}_k^i) - \left(\frac{1}{N}\sum_{k=1}^{N} \tilde{g}(\mathbf{A}_k)\right)\left(\frac{1}{N}\sum_{k=1}^{N} \tilde{g}(\mathbf{B}_k)\right), \tag{A.4a}$$

$$\hat{V}_{\sim i} = \frac{1}{N-1}\sum_{k=1}^{N} \tilde{g}(\mathbf{A}_k)\tilde{g}(\mathbf{E}_k^i) - \left(\frac{1}{N}\sum_{k=1}^{N} \tilde{g}(\mathbf{A}_k)\right)\left(\frac{1}{N}\sum_{k=1}^{N} \tilde{g}(\mathbf{B}_k)\right). \tag{A.4b}$$

2.2 Jansen

In the Jansen method, published in 1999 by Jansen [157], V_i and VT_i are approximated. The variable VT_i, which was not introduced before, is defined as $\text{Var}[Y] - V_{\sim i}$ and can be used to calculate the total Sobol indices as $ST_i = VT_i/\text{Var}[Y]$. Jansen provides the following estimators for V_i and VT_i:

$$\hat{V}_i = \frac{1}{N-1}\sum_{k=1}^{N} \tilde{g}(\mathbf{A}_k)^2 - \frac{1}{2N-1}\sum_{k=1}^{N} (\tilde{g}(\mathbf{E}_k^i) - \tilde{g}(\mathbf{B}_k))^2, \tag{A.5a}$$

$$\hat{VT}_i = \frac{1}{2N-1}\sum_{k=1}^{N} (\tilde{g}(\mathbf{E}_k^i) - \tilde{g}(\mathbf{A}_k))^2. \tag{A.5b}$$

2.3 Mauntz-Kucherenko

The Mauntz-Kucherenko approach, developed in 2007 by Sobol *et. al.*[155], consists in estimating V_i and VT_i as:

$$\hat{V}_i = \frac{1}{N-1}\sum_{k=1}^{N}\tilde{g}(\mathbf{B}_k)(\tilde{g}(\mathbf{E}^i_k) - \tilde{g}(\mathbf{A}_k)), \tag{A.6a}$$

$$\hat{VT}_i = \frac{1}{N-1}\sum_{k=1}^{N}\tilde{g}(\mathbf{A}_k)(\tilde{g}(\mathbf{A}_k) - \tilde{g}(\mathbf{E}^i_k)). \tag{A.6b}$$

2.4 Martinez

The Martinez technique, presented in 2011 by Martinez [156], provides a method to directly estimate the first and total Sobol indices, without using intermediate variables such as V_i for instance. This approximation involves the empirical correlation ρ_n between two vectors of size N, say $\mathbf{Z}$ and $\mathbf{Z}'$, defined as:

$$\rho_n(\mathbf{Z}, \mathbf{Z}') = \frac{\sum_{k=1}^{N}\mathbf{Z}_k\mathbf{Z'}_k}{\sqrt{\sum_{k=1}^{N}\mathbf{Z}^2_k}\sqrt{\sum_{k=1}^{N}\mathbf{Z'}^2_k}}. \tag{A.7}$$

The Sobol indices are then estimated as:

$$\hat{S}_i = \rho_n(\tilde{g}(\mathbf{B}), \tilde{g}(\mathbf{E}^i)), \tag{A.8a}$$

$$\hat{ST}_i = 1 - \rho_n(\tilde{g}(\mathbf{A}), \tilde{g}(\mathbf{E}^i)). \tag{A.8b}$$

This section aimed at introducing the built-in algorithms frequently used in the literature and implemented in OpenTURNS that have been used in this thesis to compute the Sobol indices. The convergence of these indices with respect to the algorithm is discussed in the different chapters of the thesis, as well as in the following appendix. Still, other numerical tools could have been used to investigate the sensitivity of the model. They are briefly introduced in Section 3 below.

3 Other tools

UQlab [260] is an open-source toolbox on Matlab, that can be used for general stochastic approaches on models, such as surrogate modeling, sensitivity analyses or uncertainty quantification. As such, this library enables to compute the Sobol sensitivity indices with the Saltelli estimator, but also with the Janon estimator [261], which leads to:

$$\hat{V}_i = \frac{1}{N}\sum_{k=1}^{N} g(\mathbf{A}_k)g(\mathbf{E}^i_k) - \frac{1}{N^2}\sum_{k=1}^{N} g(\mathbf{A}_k)\sum_{k=1}^{N} g(\mathbf{E}^i_k). \tag{A.9}$$

Jansen, Mauntz-Kucherenko and Martinez estimators are not implemented in UQlab [152]. A cloud version of this tool, available with Python, called UQ[py]lab [262], is currently in development.

Other libraries are available in Python, such as SALib [159], which is an open-source library for Python that only provides tools for sensitivity analyses. Alternative options also exist for different programing languages, such as the sensitivity library in R, developed in 2020 by Iooss *et. al.* [263], or the one developed for Julia [264]. Additional information on the existing packages for performing sensitivity analyses are provided in [265].

Appendix B

PHASE DIAGRAMS FOR A PASSIVE CELL, DEPENDING ON THE ASPECT RATIO OF THE NP

The following presents the phase diagrams, obtained in the case of passive cells, for various aspect ratios. These diagrams refer to the study presented in Chapter 3.

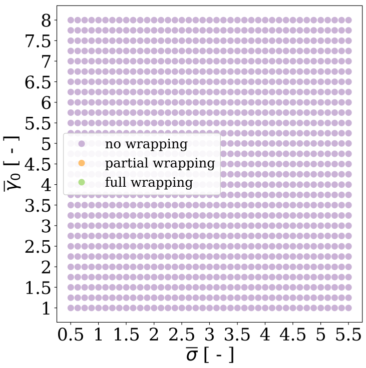

$\bar{r} \leq 1/3$

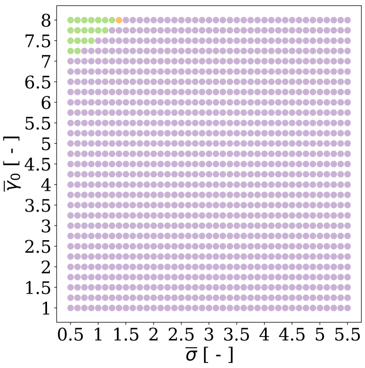

$\bar{r} = 1/2.4$

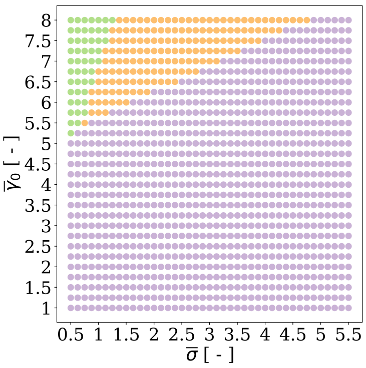

$\bar{r} = 1/2.2$

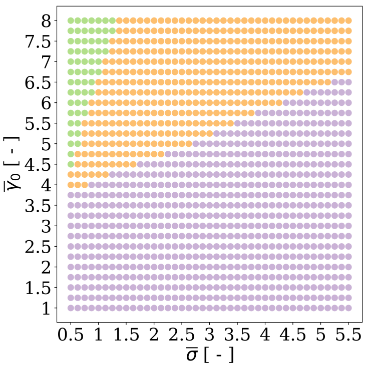

$\bar{r} = 1/1.8$

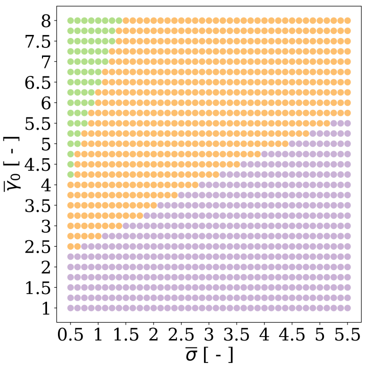

$\bar{r} = 1/1.4$

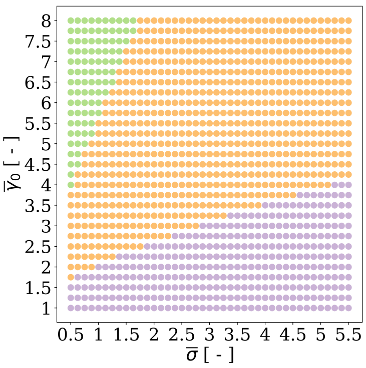

$\bar{r} = 1$

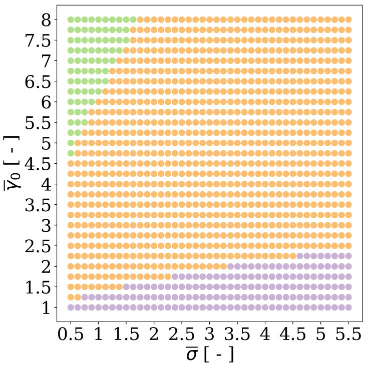

$\bar{r} = 1.4$

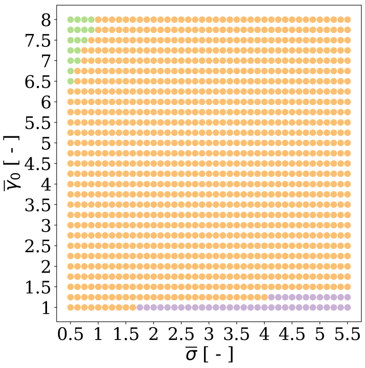

$\bar{r} = 1.8$

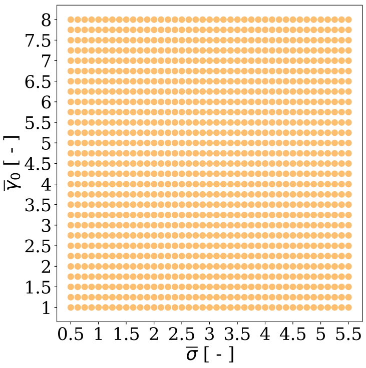

$\bar{r} \geq 2.2$

Appendix C

PHASE DIAGRAMS FOR AN ADAPTIVE CELL, DEPENDING ON THE ASPECT RATIO OF THE NP

The following compares the phase diagrams obtained in the case of adaptive cells $(\overline{\gamma}_A, \overline{\gamma}_D, \overline{\gamma}_S) = (2, 0, 50)$ to those obtained for passive cells, for various aspect ratios. These diagrams refer to the study presented in Chapter 5.

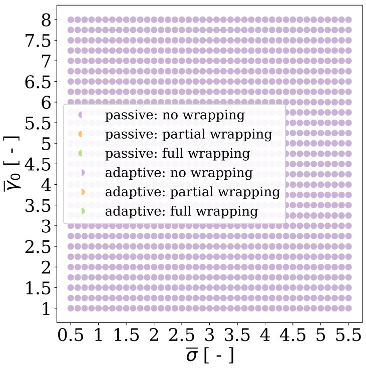

$\overline{r} \leq 1/3$

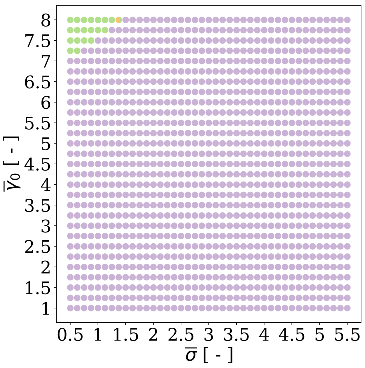

$\overline{r} = 1/2.4$

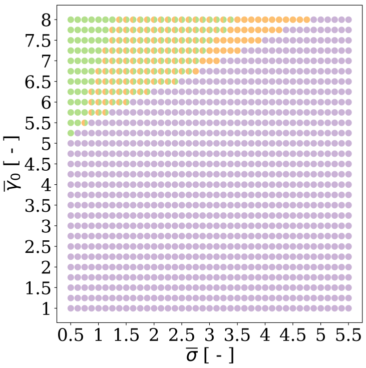

$\overline{r} = 1/2.2$

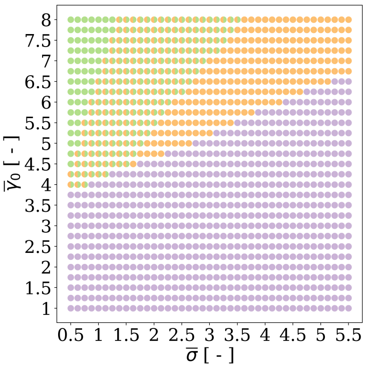

$\overline{r} = 1/1.8$

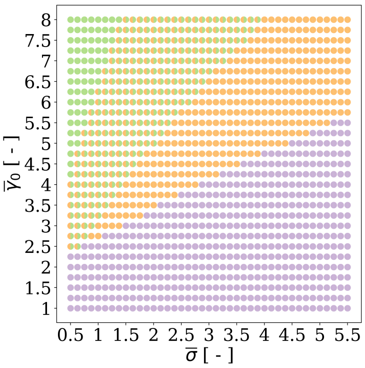

$\overline{r} = 1/1.4$

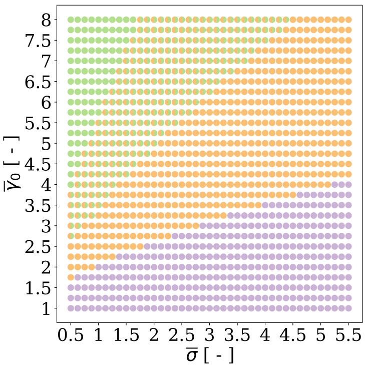

$\overline{r} = 1$

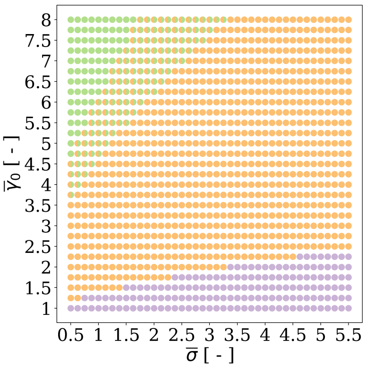

$\overline{r} = 1.4$

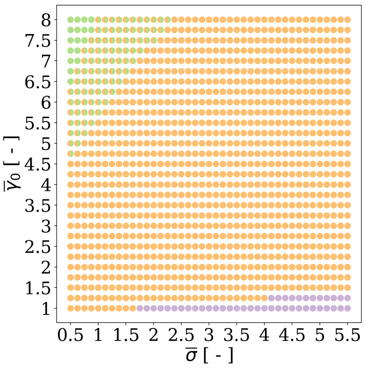

$\overline{r} = 1.8$

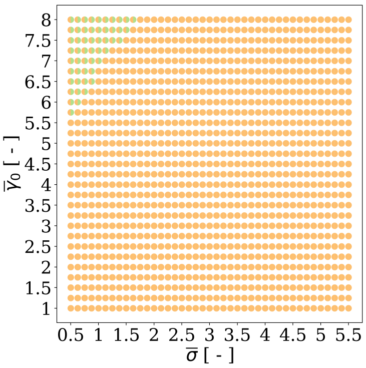

$\overline{r} = 2.2$

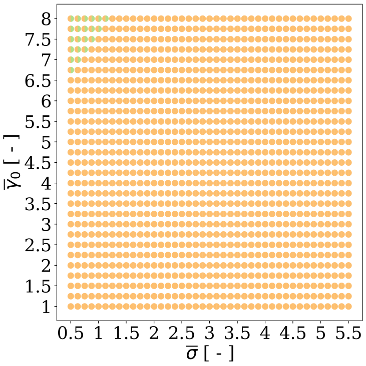

$\overline{r} = 2.6$

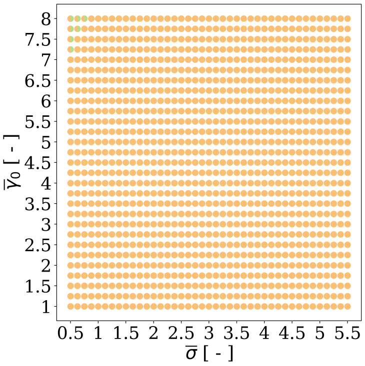

$\overline{r} = 3$

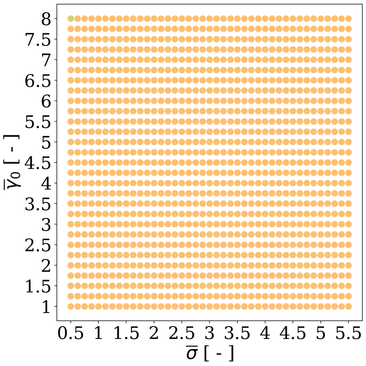

$\overline{r} \geq 3.4$

Appendix D

CONVERGENCE OF THE SOBOL SENSITIVITY INDICES

1 Introduction

Chapters 3, 4 and 5 investigated the influence of the models input parameters on the uptake of a NP under different conditions. Chapter 3 aimed at determining the influence of $\overline{\gamma}_0$, $\overline{\sigma}$ and $\overline{r}$, which respectively stand for the (initial) NP-membrane adhesion, the membrane tension, and the aspect ratio of the NPs. In this Chapter, the behavior of the membrane is supposed passive, *i.e.* there is no variation of the properties of the membrane in response to the wrapping of the NP. Then, in Chapter 4 we presented a model of the membrane mechano-adaptation of the membrane, in which the NP-membrane adhesion variates with the degree of wrapping of the NP. As such, three additional parameters are introduced: $\overline{\gamma}_A$, $\overline{\gamma}_D$ and $\overline{\gamma}_S$, which stand for the amplitude, the delay and the curvature parameter of the variation of $\overline{\gamma}$, respectively. The initial adhesion is then denoted by $\overline{\gamma}_0$. The study conducted in Chapter 4 aimed at determining the influence of this variation on the uptake of a circular NP ($\overline{r} = 1$) which was then extended on an elliptical NP (variable $\overline{r}$) in Chapter 5. These studies involve sensitivity analyses, and more especially the evaluation of the Sobol indices, in order to quantify the influence of different parameters on the uptake of the NPs. The accuracy of the approximation of the Sobol indices depends on the number of estimations that have been used. As such, a convergence study has been carried out in order to ensure that enough estimations of the model have been used for the calculation of these indices.

As such, this appendix is organized in three sections, one for each Chapter (Chapter 3, Chapter 4 and Chapter 5). Then, for each study, the convergence of the Sobol indices is depicted for the four algorithms (Mauntz-Kucherenko, Saltelli, Jansen, Martinez). Then, a conclusion is drawn on the main aspect of the convergence studies conducted for the Sobol indices in this work.

2 Uptake of an elliptic NP by a passive membrane (Chapter 3)

This section presents the results of the convergence study conducted in Chapter 3 in the case of the sensitivity analysis conducted on the influence of $\overline{\gamma}_0$, $\overline{\sigma}$ and $\overline{r}$ on the wrapping degree at equilibrium $\tilde{f}$. Each subsection contains figures which depict the variation, in terms of the number of samples, of (i) the first and total Sobol indices (S_i and ST_i), (ii) the range of the 95 % confidence intervals (CIs) and (iii) the normalized absolute gradients. Note that the caption of the figures mentions $\overline{\gamma}$ instead of $\overline{\gamma}_0$, since the mechano-adaptation of the membrane had not yet been introduced in Chapter 3.

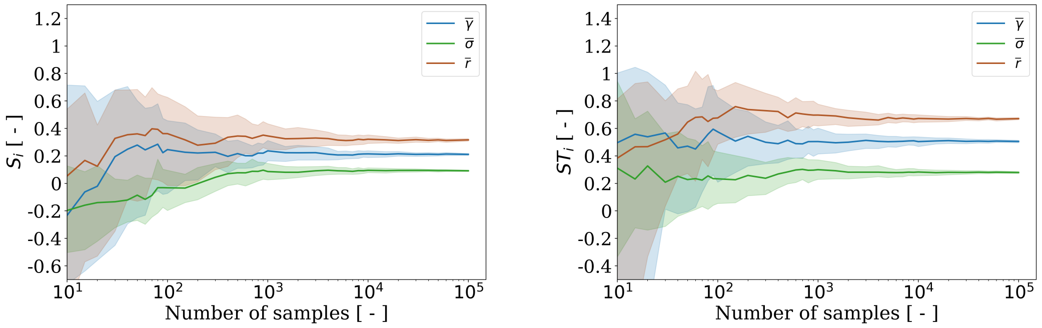

(a) (b)

Figure D.1: (a) First and (b) total Sobol indices depending on the number of estimations of the metamodel, computed with the Mauntz-Kucherenko algorithm. The shaded regions correspond to the 95 % confidence intervals.

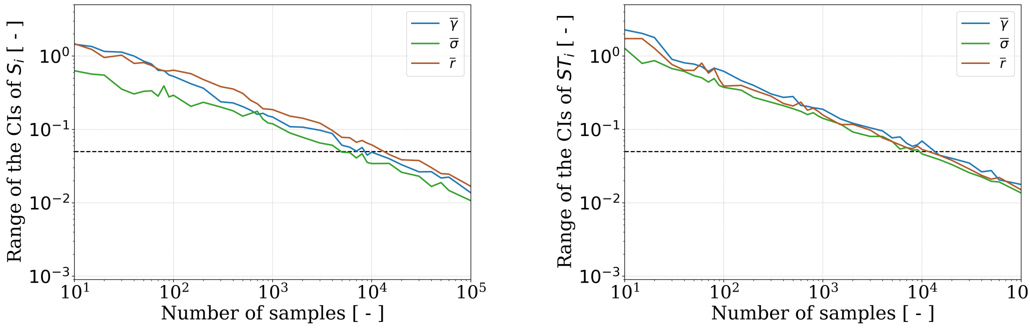

(a) (b)

Figure D.2: Range of the 95 % confidence intervals the (a) first and (b) total Sobol indices depending on the number of estimations of the metamodel, computed with the Mauntz-Kucherenko algorithm. The black dashed lines correspond to the threshold of 0.05.

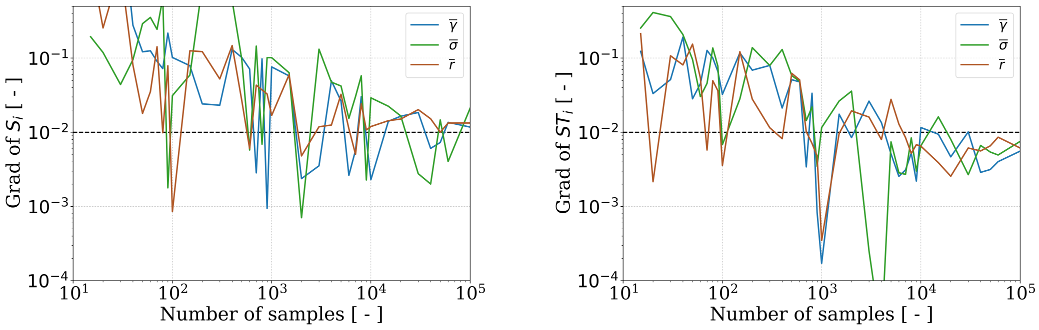

(a) (b)

Figure D.3: Absolute gradient of the (a) first and (b) total Sobol indices depending on the number of estimations of the metamodel, computed with the Mauntz-Kucherenko algorithm. The black dashed lines correspond to the threshold of 0.05.

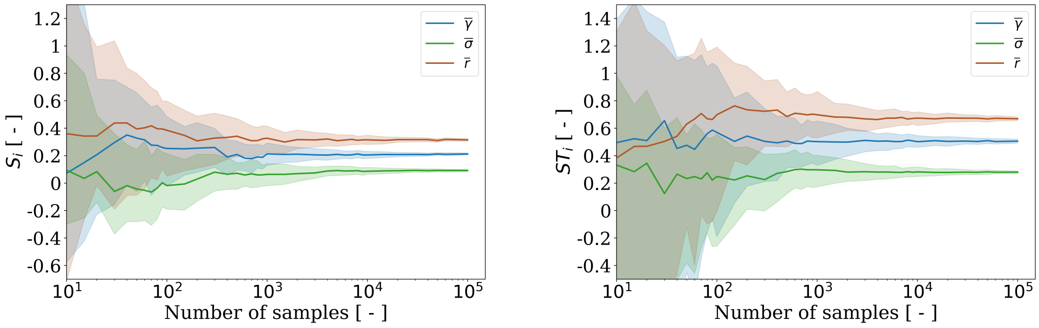

(a) (b)

Figure D.4: (a) First and (b) total Sobol indices depending on the number of estimations of the metamodel, computed with the Saltelli algorithm. The shaded regions correspond to the 95 % confidence intervals.

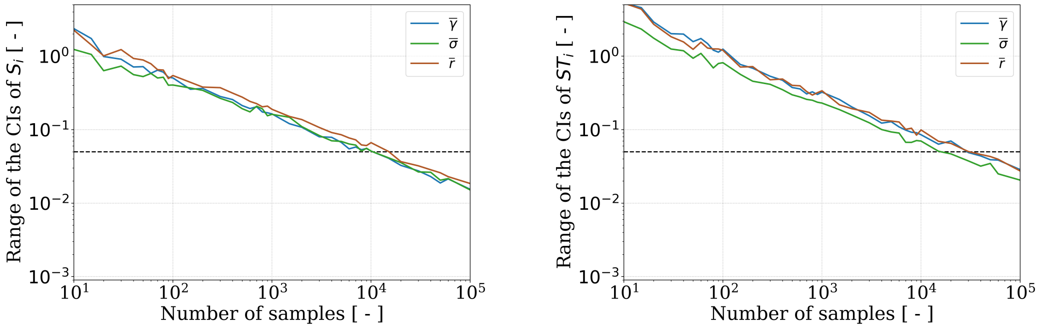

(a) (b)

Figure D.5: Range of the 95 % confidence intervals the (a) first and (b) total Sobol indices depending on the number of estimations of the metamodel, computed with the Saltelli algorithm. The black dashed lines correspond to the threshold of 0.05.

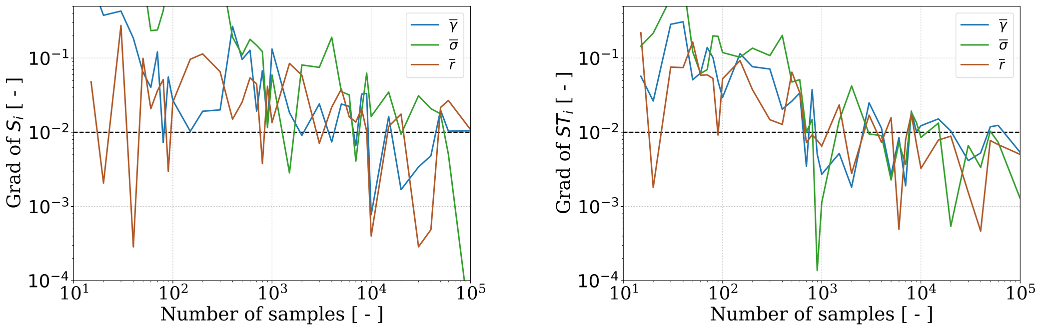

(a) (b)

Figure D.6: Absolute gradient of the (a) first and (b) total Sobol indices depending on the number of estimations of the metamodel, computed with the Saltelli algorithm. The black dashed lines correspond to the threshold of 0.05.

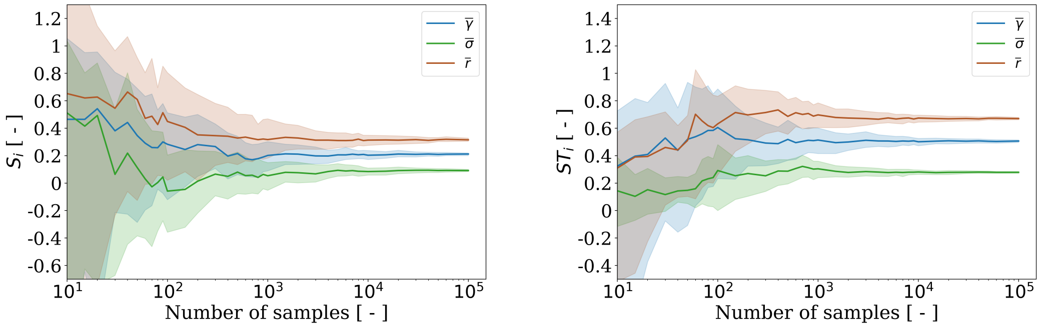

(a) (b)

Figure D.7: (a) First and (b) total Sobol indices depending on the number of estimations of the metamodel, computed with the Jansen algorithm. The shaded regions correspond to the 95 % confidence intervals.

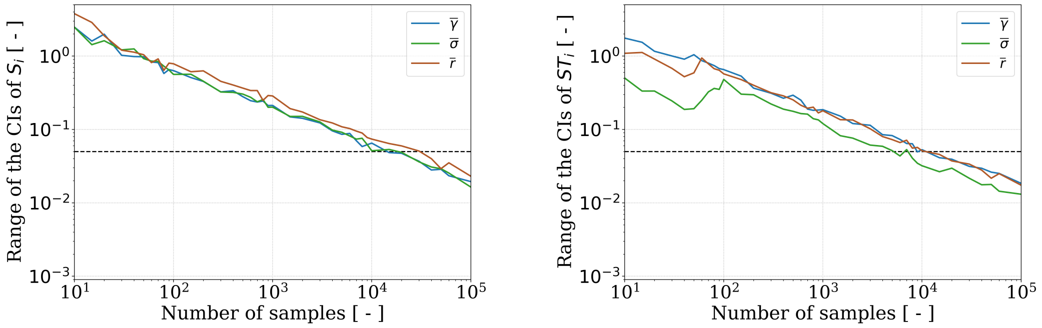

(a) (b)

Figure D.8: Range of the 95 % confidence intervals the (a) first and (b) total Sobol indices depending on the number of estimations of the metamodel, computed with the Jansen algorithm. The black dashed lines correspond to the threshold of 0.05.

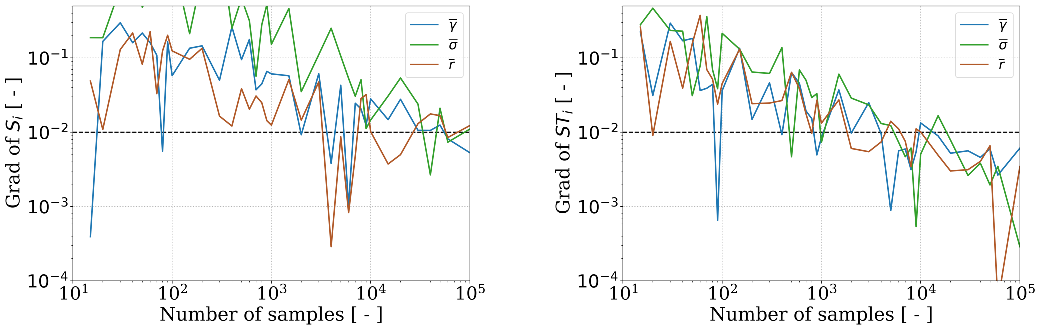

(a) (b)

Figure D.9: Absolute gradient of the (a) first and (b) total Sobol indices depending on the number of estimations of the metamodel, computed with the Jansen algorithm. The black dashed lines correspond to the threshold of 0.05.

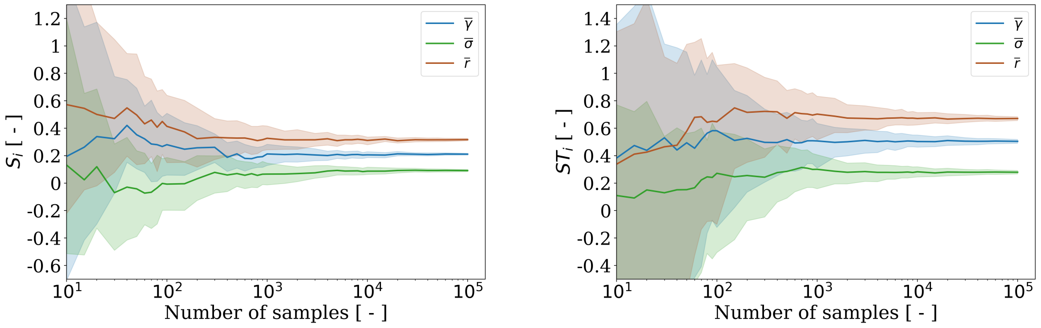

(a) (b)

Figure D.10: (a) First and (b) total Sobol indices depending on the number of estimations of the metamodel, computed with the Martinez algorithm. The shaded regions correspond to the 95 % confidence intervals.

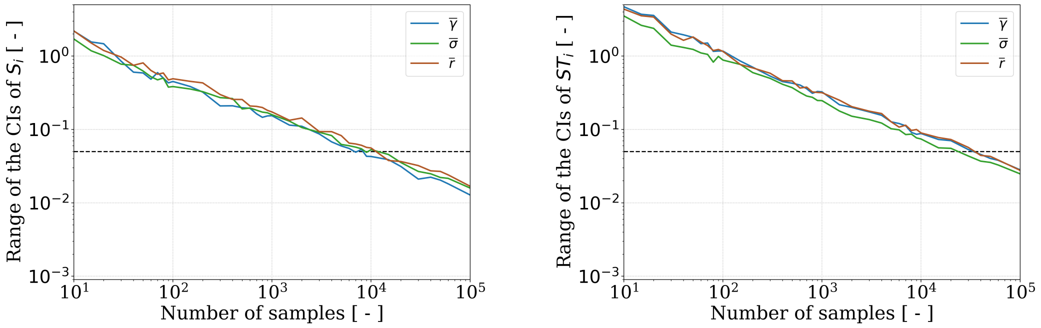

(a) (b)

Figure D.11: Range of the 95 % confidence intervals the (a) first and (b) total Sobol indices depending on the number of estimations of the metamodel, computed with the Martinez algorithm. The black dashed lines correspond to the threshold of 0.05.

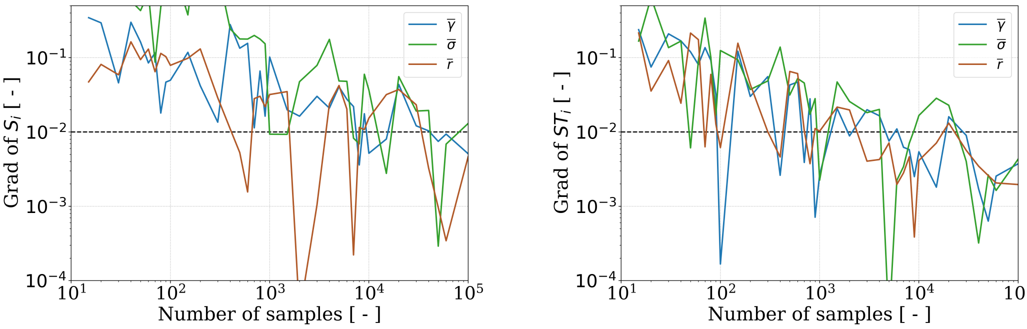

(a) (b)

Figure D.12: Absolute gradient of the (a) first and (b) total Sobol indices depending on the number of estimations of the metamodel, computed with the Martinez algorithm. The black dashed lines correspond to the threshold of 0.05.

3 Uptake of a circular NP by an adaptive membrane (Chapter 4)

3.1 Influence of the mechano-adaptation-related parameters on the proportion of full wrapping

This section presents the results of the convergence study conducted in Chapter 4 in the case of the sensitivity analysis conducted on the influence of $\overline{\gamma}_A$, $\overline{\gamma}_D$ and $\overline{\gamma}_S$ on the wrapping degree at equilibrium $\tilde{f}$. Each subsection contains figures which depict the variation, in terms of the number of samples, of (i) the first and total Sobol indices (S_i and ST_i), (ii) the range of the 95 % confidence intervals (CIs) and (iii) the normalized absolute gradients.

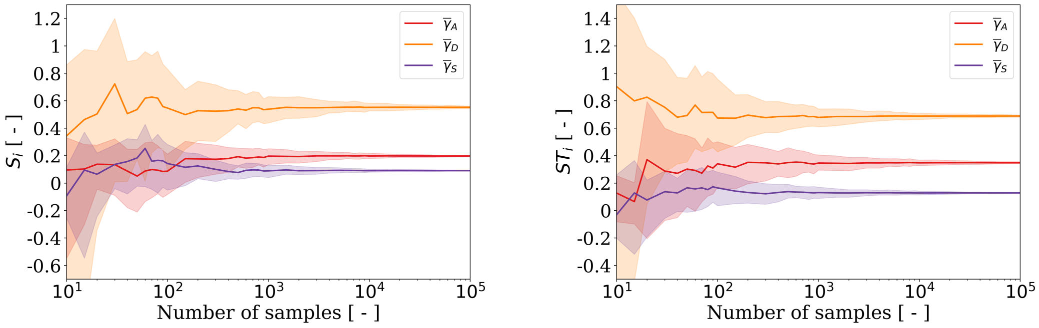

(a) (b)

Figure D.13: (a) First and (b) total Sobol indices depending on the number of estimations of the metamodel, computed with the Mauntz-Kucherenko algorithm. The shaded regions correspond to the 95 % confidence intervals.

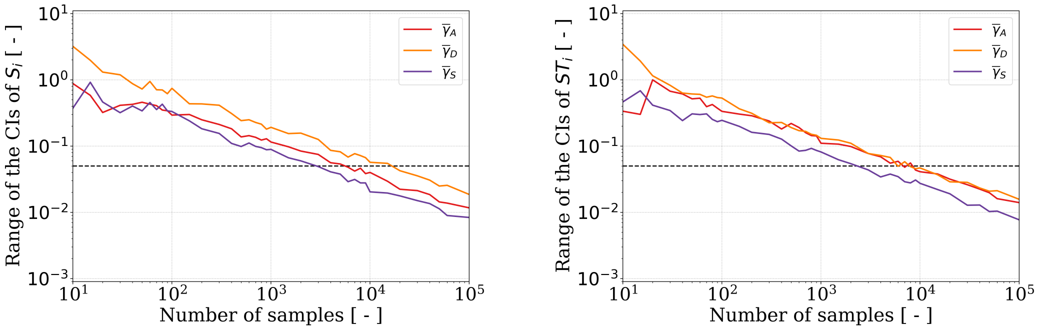

(a) (b)

Figure D.14: Range of the 95 % confidence intervals the (a) first and (b) total Sobol indices depending on the number of estimations of the metamodel, computed with the Mauntz-Kucherenko algorithm. The black dashed lines correspond to the threshold of 0.05.

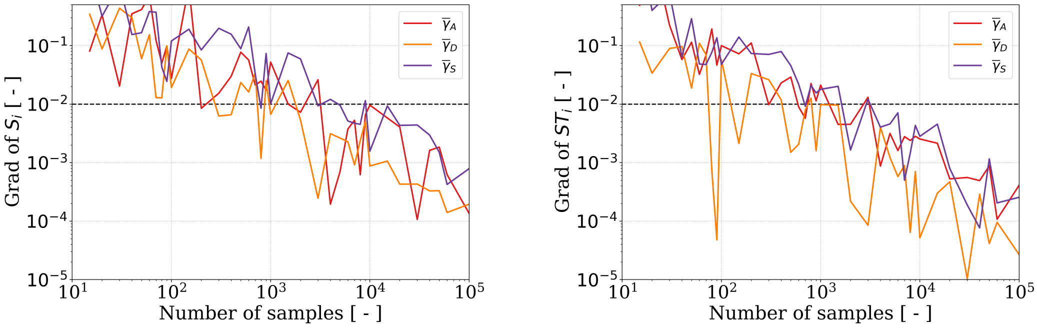

(a) (b)

Figure D.15: Absolute gradient of the (a) first and (b) total Sobol indices depending on the number of estimations of the metamodel, computed with the Mauntz-Kucherenko algorithm. The black dashed lines correspond to the threshold of 0.05.

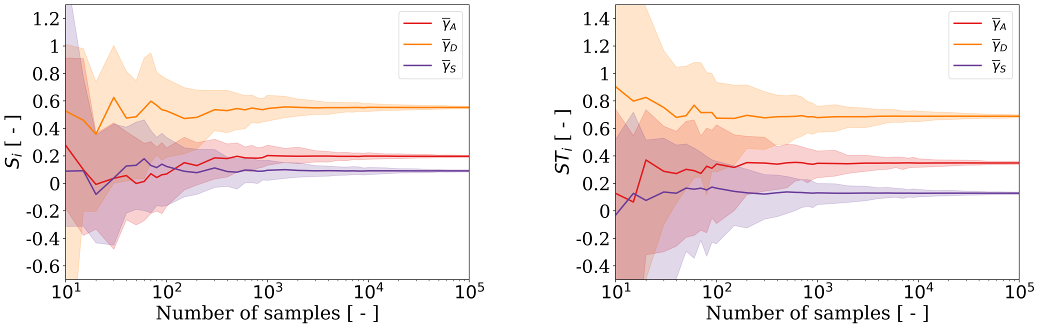

(a) (b)

Figure D.16: (a) First and (b) total Sobol indices depending on the number of estimations of the metamodel, computed with the Saltelli algorithm. The shaded regions correspond to the 95 % confidence intervals.

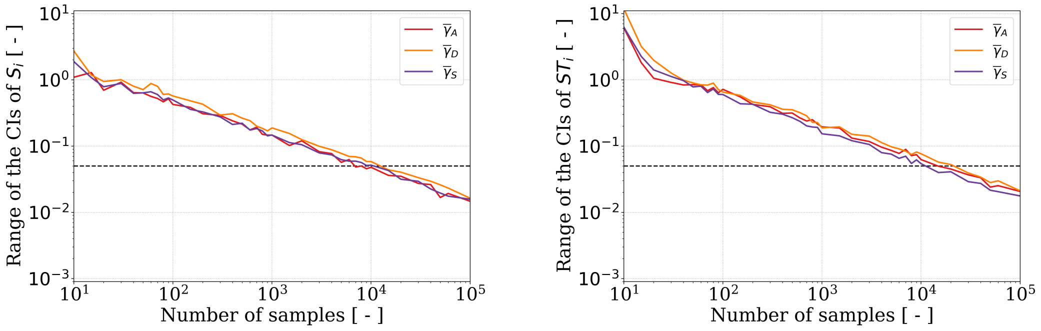

(a) (b)

Figure D.17: Range of the 95 % confidence intervals the (a) first and (b) total Sobol indices depending on the number of estimations of the metamodel, computed with the Saltelli algorithm. The black dashed lines correspond to the threshold of 0.05.

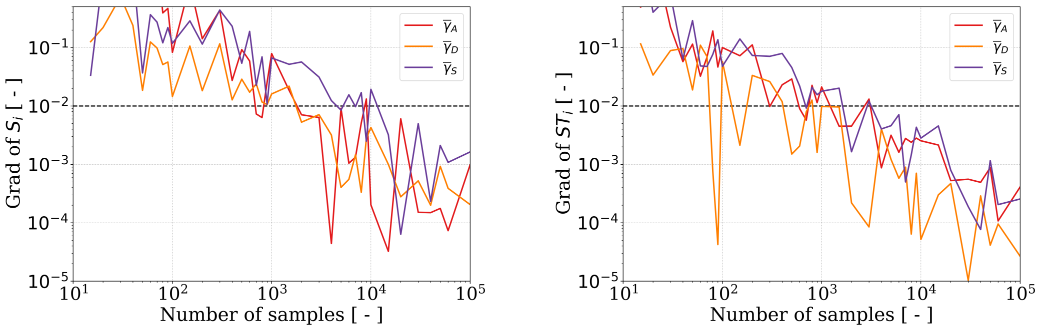

(a) (b)

Figure D.18: Absolute gradient of the (a) first and (b) total Sobol indices depending on the number of estimations of the metamodel, computed with the Saltelli algorithm. The black dashed lines correspond to the threshold of 0.05.

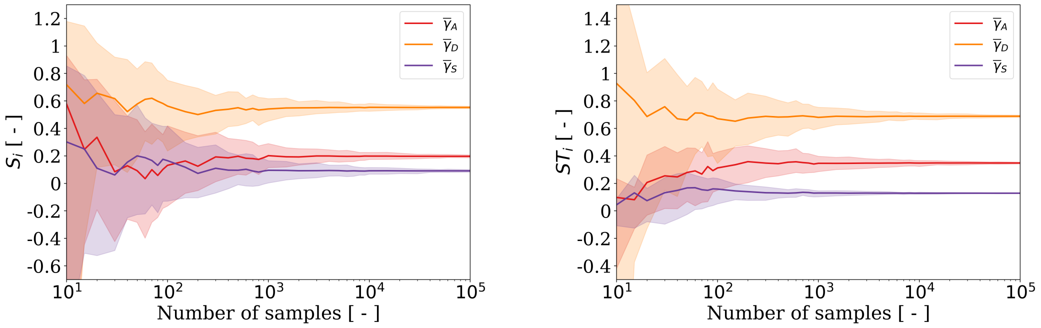

(a) (b)

Figure D.19: (a) First and (b) total Sobol indices depending on the number of estimations of the metamodel, computed with the Jansen algorithm. The shaded regions correspond to the 95 % confidence intervals.

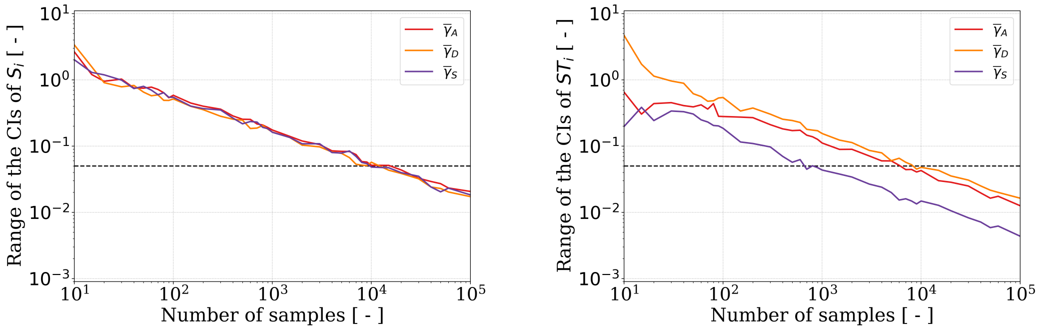

(a) (b)

Figure D.20: Range of the 95 % confidence intervals the (a) first and (b) total Sobol indices depending on the number of estimations of the metamodel, computed with the Jansen algorithm. The black dashed lines correspond to the threshold of 0.05.

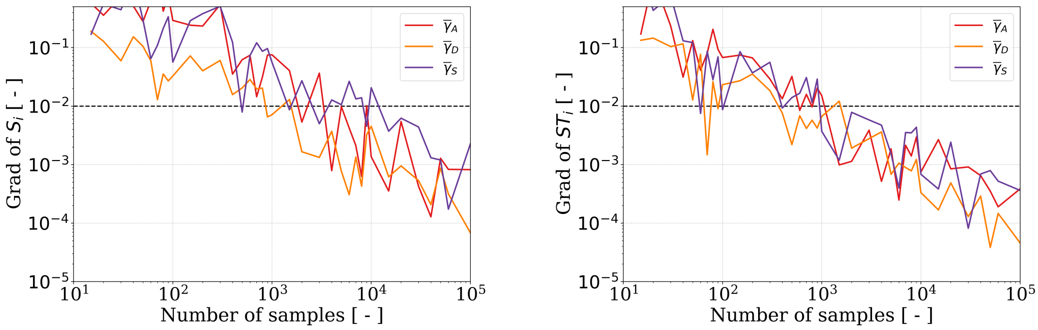

(a) (b)

Figure D.21: Absolute gradient of the (a) first and (b) total Sobol indices depending on the number of estimations of the metamodel, computed with the Jansen algorithm. The black dashed lines correspond to the threshold of 0.05.

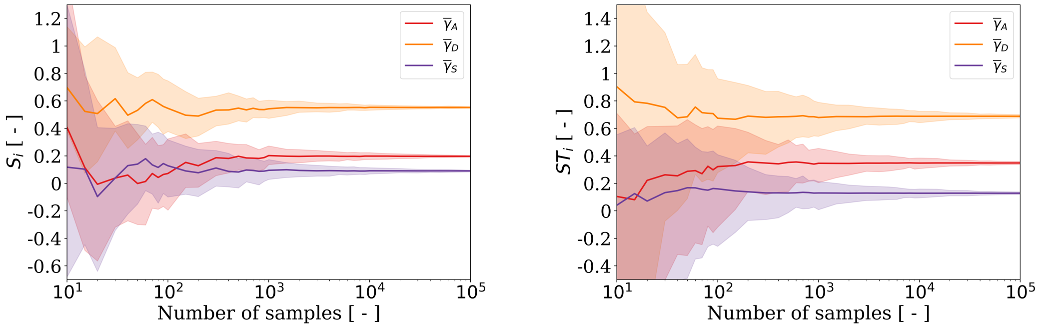

(a) (b)

Figure D.22: (a) First and (b) total Sobol indices depending on the number of estimations of the metamodel, computed with the Martinez algorithm. The shaded regions correspond to the 95 % confidence intervals.

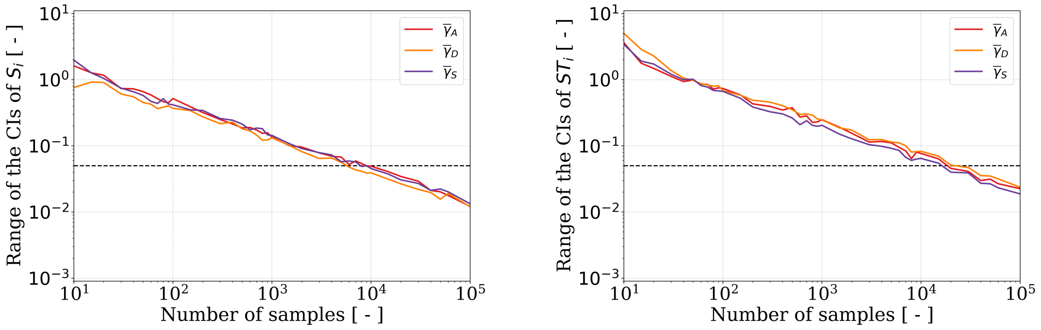

(a) (b)

Figure D.23: Range of the 95 % confidence intervals the (a) first and (b) total Sobol indices depending on the number of estimations of the metamodel, computed with the Martinez algorithm. The black dashed lines correspond to the threshold of 0.05.

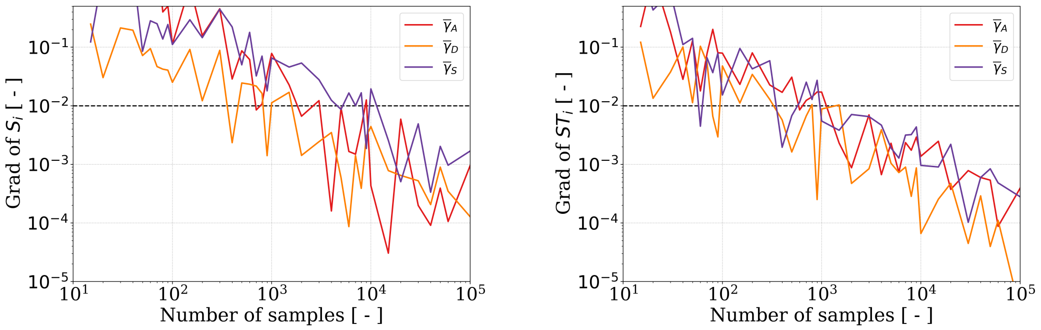

(a) (b)

Figure D.24: Absolute gradient of the (a) first and (b) total Sobol indices depending on the number of estimations of the metamodel, computed with the Martinez algorithm. The black dashed lines correspond to the threshold of 0.05.

3.2 Comparison of the effect of the initial and mechano-adaptation-related parameters on the wrapping degree at equilibrium

This section presents the results of the convergence study conducted in Chapter 4 in the case of the sensitivity analysis conducted on the influence of $\overline{\gamma}_0$, $\overline{\sigma}$, $\overline{\gamma}_A$, $\overline{\gamma}_D$ and $\overline{\gamma}_S$ on the proportion of full wrapping ψ_3. Each subsection contains figures which depict the variation, in terms of the number of samples, of (i) the first and total Sobol indices (S_i and ST_i), (ii) the range of the 95 % confidence intervals (CIs) and (iii) the normalized absolute gradients.

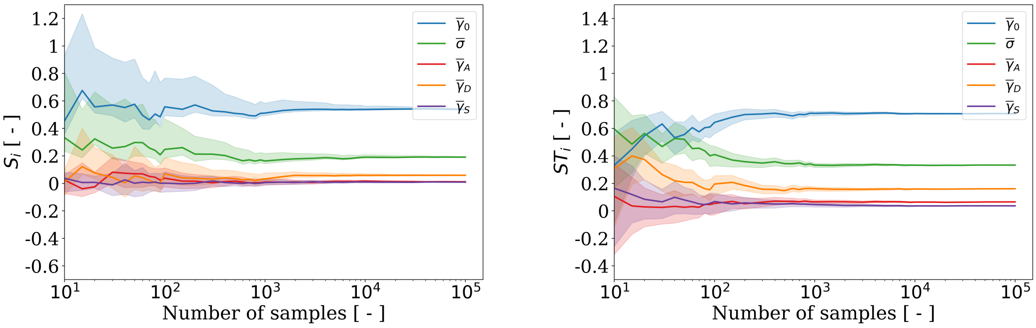

(a) (b)

Figure D.25: (a) First and (b) total Sobol indices depending on the number of estimations of the metamodel, computed with the Mauntz-Kucherenko algorithm. The shaded regions correspond to the 95 % confidence intervals.

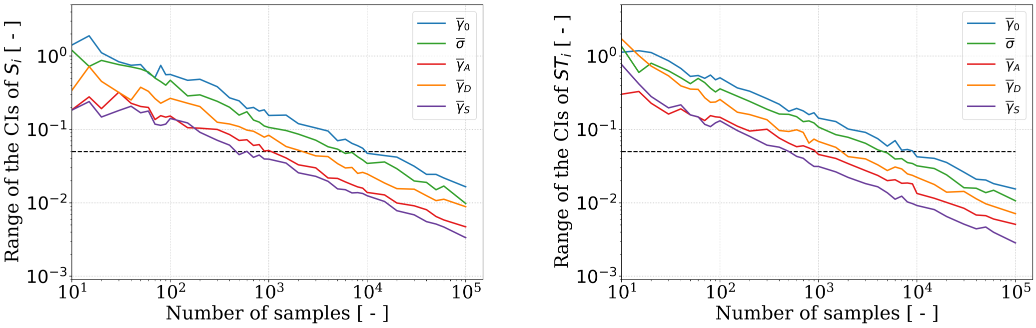

(a) (b)

Figure D.26: Range of the 95 % confidence intervals the (a) first and (b) total Sobol indices depending on the number of estimations of the metamodel, computed with the Mauntz-Kucherenko algorithm. The black dashed lines correspond to the threshold of 0.05.

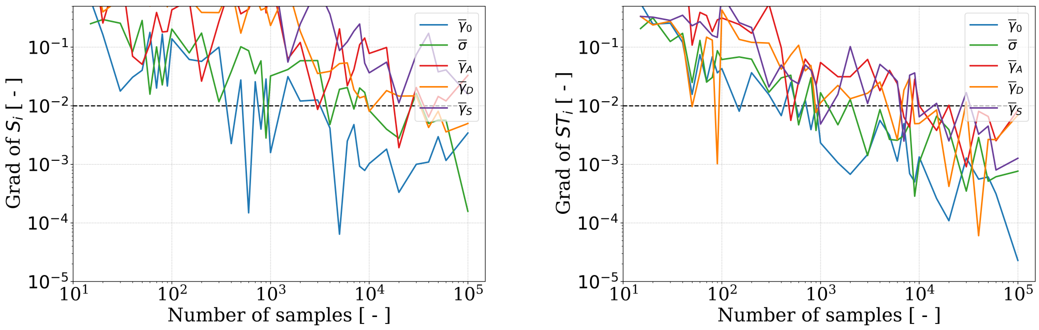

(a) (b)

Figure D.27: Absolute gradient of the (a) first and (b) total Sobol indices depending on the number of estimations of the metamodel, computed with the Mauntz-Kucherenko algorithm. The black dashed lines correspond to the threshold of 0.05.

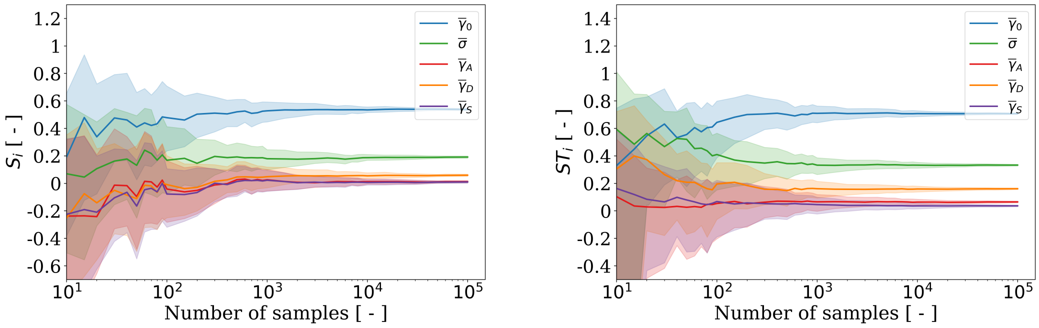

(a) (b)

Figure D.28: (a) First and (b) total Sobol indices depending on the number of estimations of the metamodel, computed with the Saltelli algorithm. The shaded regions correspond to the 95 % confidence intervals.

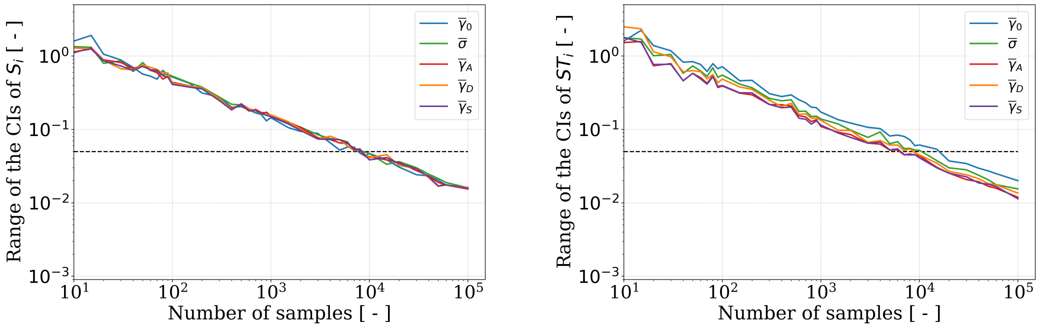

(a) (b)

Figure D.29: Range of the 95 % confidence intervals the (a) first and (b) total Sobol indices depending on the number of estimations of the metamodel, computed with the Saltelli algorithm. The black dashed lines correspond to the threshold of 0.05.

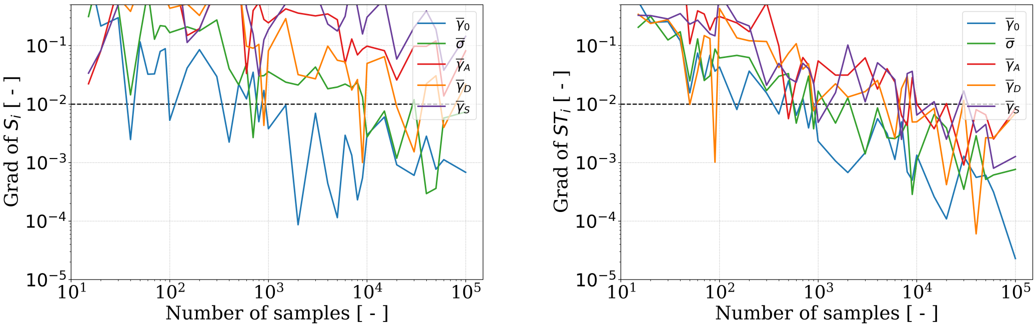

(a) (b)

Figure D.30: Absolute gradient of the (a) first and (b) total Sobol indices depending on the number of estimations of the metamodel, computed with the Saltelli algorithm. The black dashed lines correspond to the threshold of 0.05.

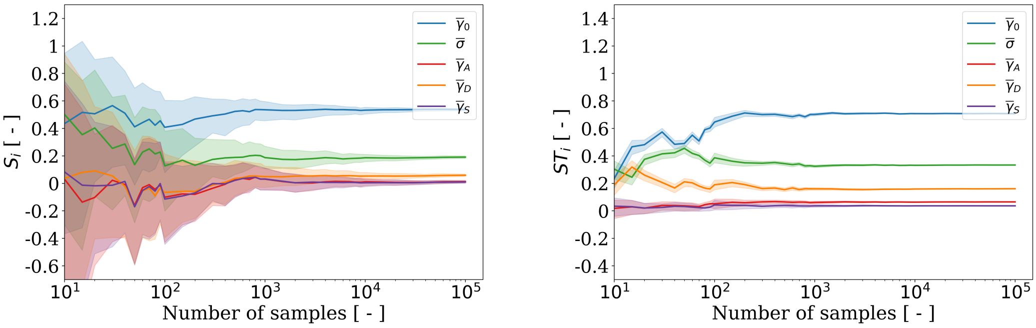

(a) (b)

Figure D.31: (a) First and (b) total Sobol indices depending on the number of estimations of the metamodel, computed with the Jansen algorithm. The shaded regions correspond to the 95 % confidence intervals.

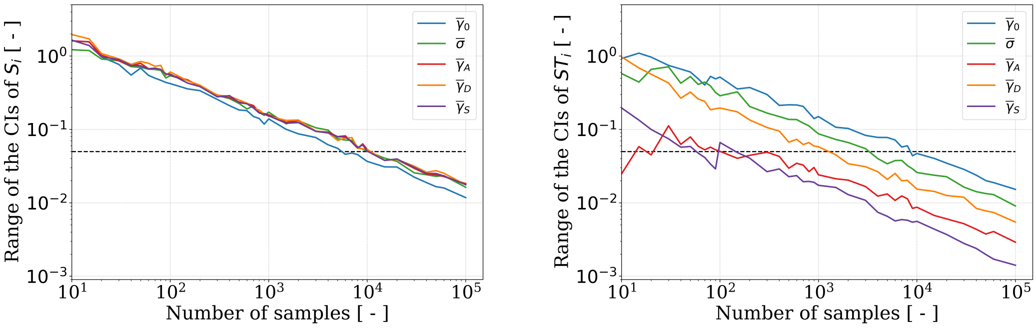

(a) (b)

Figure D.32: Range of the 95 % confidence intervals the (a) first and (b) total Sobol indices depending on the number of estimations of the metamodel, computed with the Jansen algorithm. The black dashed lines correspond to the threshold of 0.05.

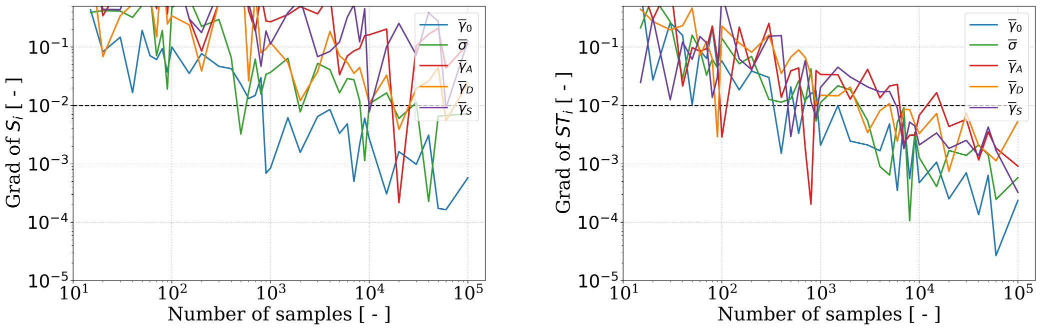

(a) (b)

Figure D.33: Absolute gradient of the (a) first and (b) total Sobol indices depending on the number of estimations of the metamodel, computed with the Jansen algorithm. The black dashed lines correspond to the threshold of 0.05.

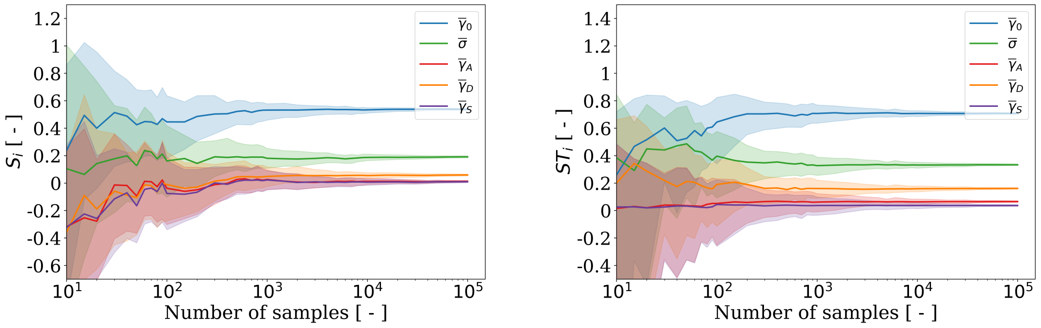

(a) (b)

Figure D.34: (a) First and (b) total Sobol indices depending on the number of estimations of the metamodel, computed with the Martinez algorithm. The shaded regions correspond to the 95 % confidence intervals.

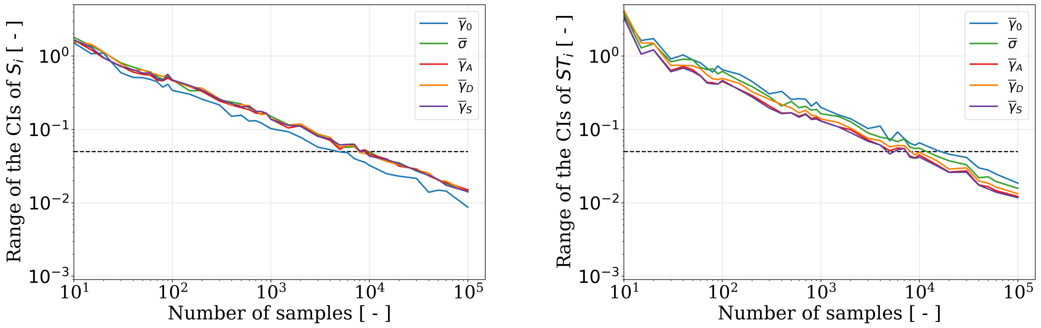

(a) (b)

Figure D.35: Range of the 95 % confidence intervals the (a) first and (b) total Sobol indices depending on the number of estimations of the metamodel, computed with the Martinez algorithm. The black dashed lines correspond to the threshold of 0.05.

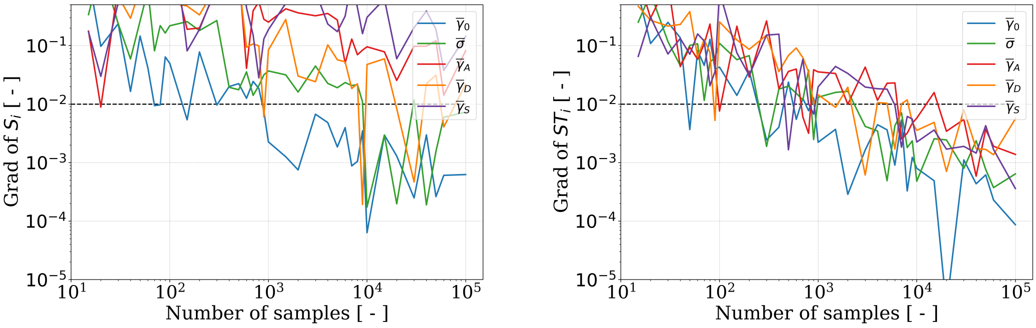

(a) (b)

Figure D.36: Absolute gradient of the (a) first and (b) total Sobol indices depending on the number of estimations of the metamodel, computed with the Martinez algorithm. The black dashed lines correspond to the threshold of 0.05.

4 Uptake of an elliptic NP by an adaptive membrane (Chapter 5)

4.1 Influence of the mechano-adaptation-related parameters on the proportion of full wrapping

This section presents the results of the convergence study conducted in Chapter 5 in the case of the sensitivity analysis conducted on the influence of $\overline{\gamma}_A$, $\overline{\gamma}_D$, $\overline{\gamma}_S$ and $\overline{r}$ on the wrapping degree at equilibrium $\tilde{f}$. Each subsection contains figures which depict the variation, in terms of the number of samples, of (i) the first and total Sobol indices (S_i and ST_i), (ii) the range of the 95 % confidence intervals (CIs) and (iii) the normalized absolute gradients.

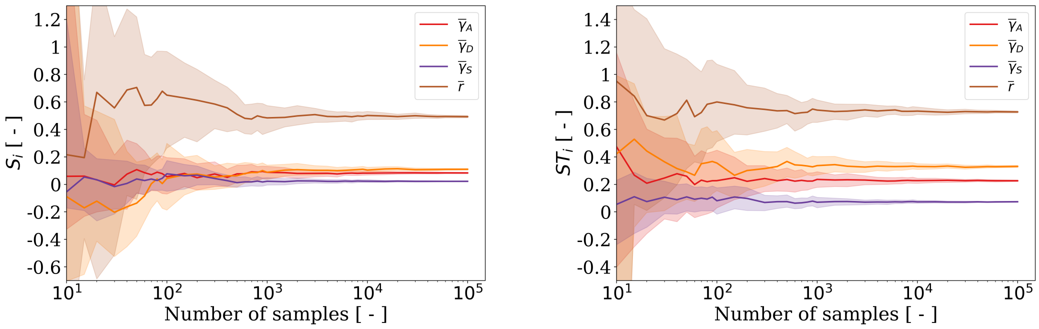

(a) (b)

Figure D.37: (a) First and (b) total Sobol indices depending on the number of estimations of the metamodel, computed with the Mauntz-Kucherenko algorithm. The shaded regions correspond to the 95 % confidence intervals.

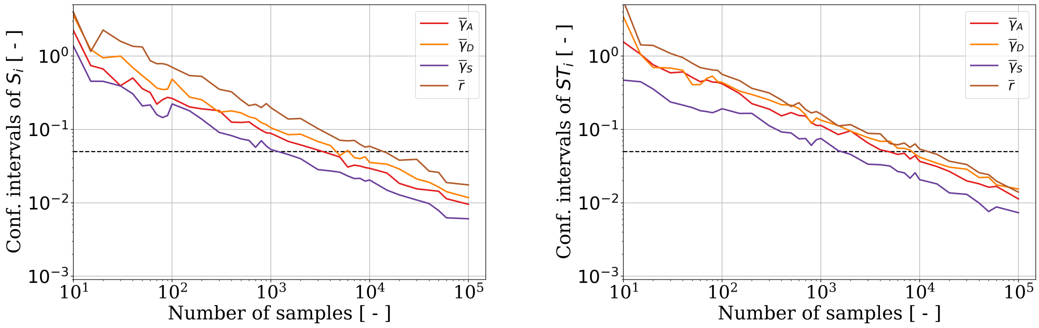

(a) (b)

Figure D.38: Range of the 95 % confidence intervals the (a) first and (b) total Sobol indices depending on the number of estimations of the metamodel, computed with the Mauntz-Kucherenko algorithm. The black dashed lines correspond to the threshold of 0.05.

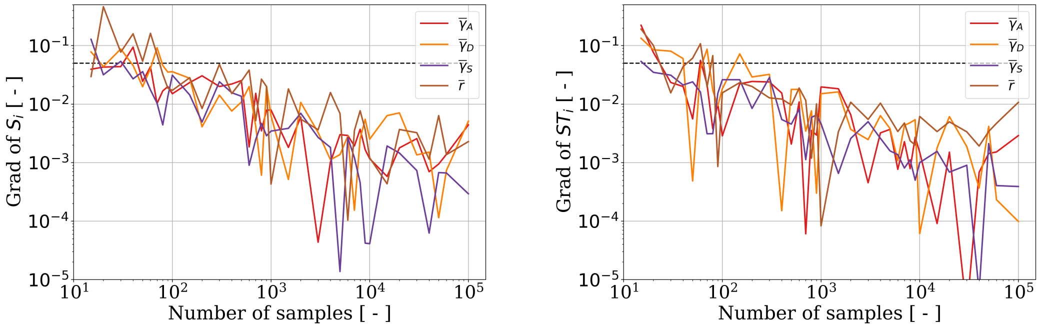

(a) (b)

Figure D.39: Absolute gradient of the (a) first and (b) total Sobol indices depending on the number of estimations of the metamodel, computed with the Mauntz-Kucherenko algorithm. The black dashed lines correspond to the threshold of 0.05.

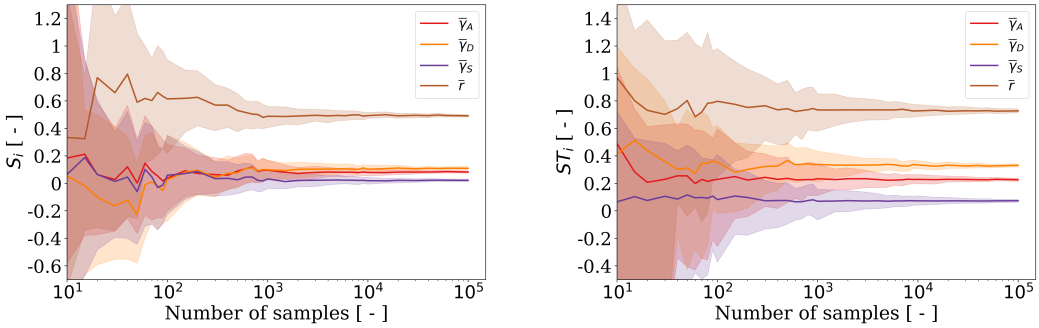

(a) (b)

Figure D.40: (a) First and (b) total Sobol indices depending on the number of estimations of the metamodel, computed with the Saltelli algorithm. The shaded regions correspond to the 95 % confidence intervals.

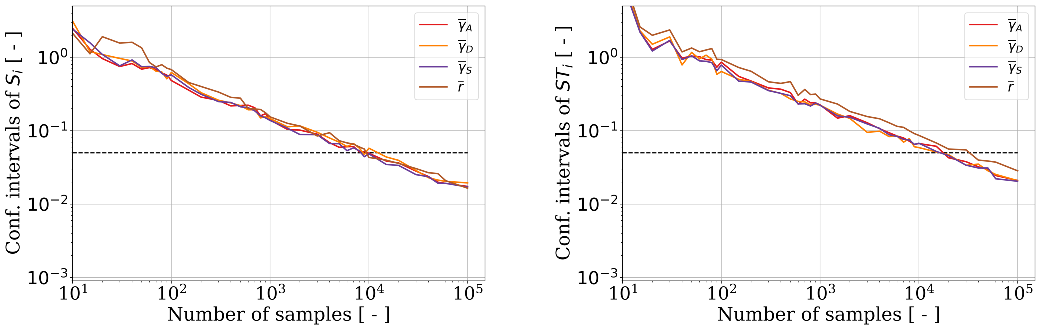

(a) (b)

Figure D.41: Range of the 95 % confidence intervals the (a) first and (b) total Sobol indices depending on the number of estimations of the metamodel, computed with the Saltelli algorithm. The black dashed lines correspond to the threshold of 0.05.

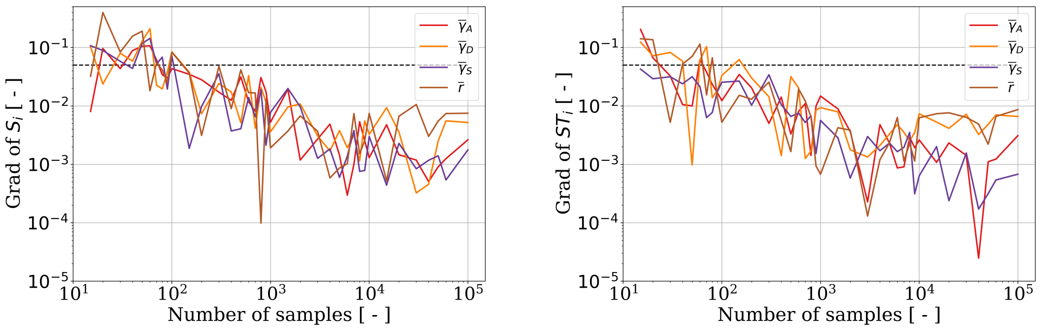

(a) (b)

Figure D.42: Absolute gradient of the (a) first and (b) total Sobol indices depending on the number of estimations of the metamodel, computed with the Saltelli algorithm. The black dashed lines correspond to the threshold of 0.05.

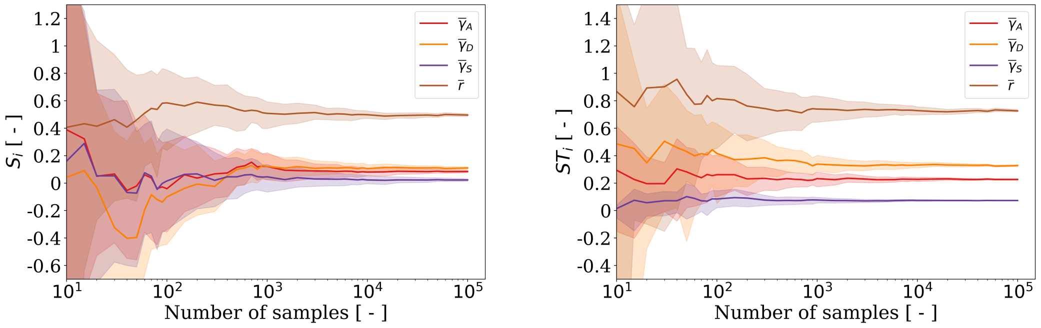

(a) (b)

Figure D.43: (a) First and (b) total Sobol indices depending on the number of estimations of the metamodel, computed with the Jansen algorithm. The shaded regions correspond to the 95 % confidence intervals.

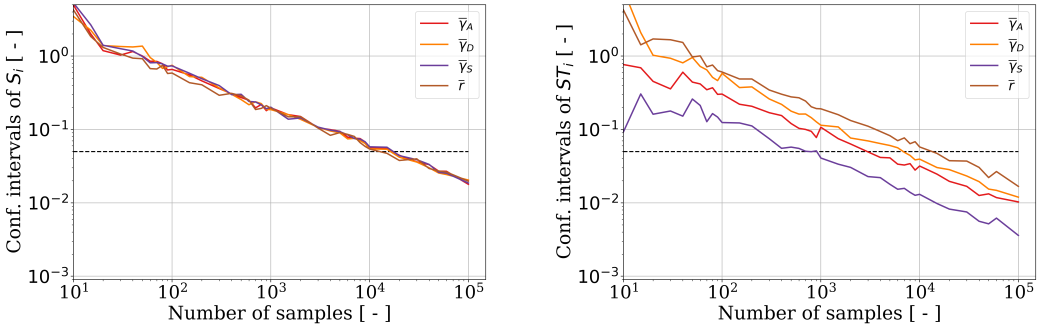

(a) (b)

Figure D.44: Range of the 95 % confidence intervals the (a) first and (b) total Sobol indices depending on the number of estimations of the metamodel, computed with the Jansen algorithm. The black dashed lines correspond to the threshold of 0.05.

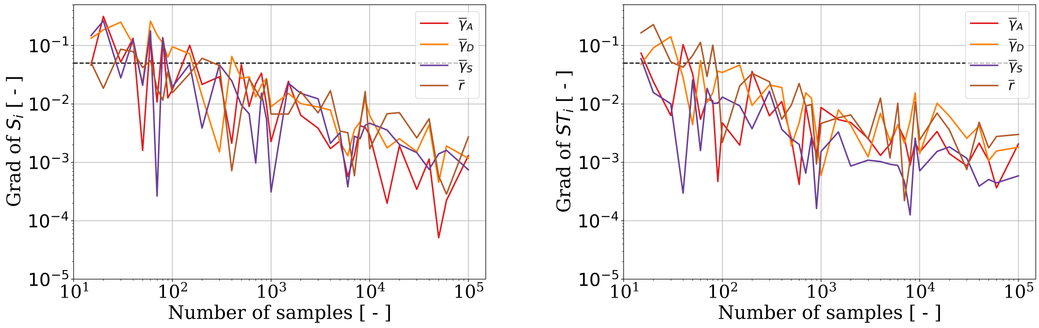

(a) (b)

Figure D.45: Absolute gradient of the (a) first and (b) total Sobol indices depending on the number of estimations of the metamodel, computed with the Jansen algorithm. The black dashed lines correspond to the threshold of 0.05.

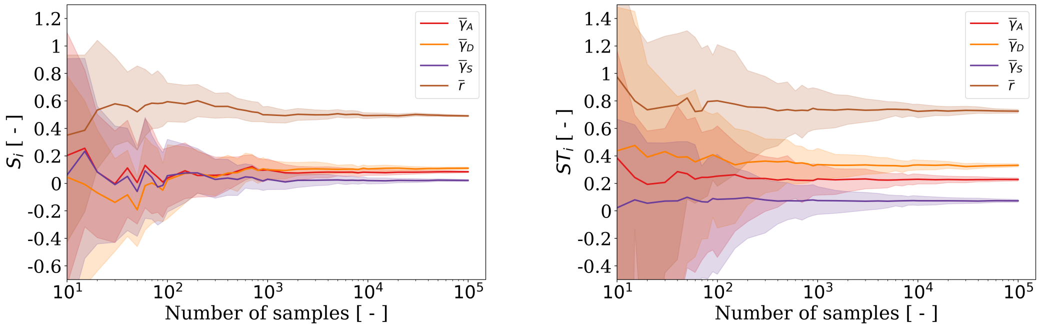

(a) (b)

Figure D.46: (a) First and (b) total Sobol indices depending on the number of estimations of the metamodel, computed with the Martinez algorithm. The shaded regions correspond to the 95 % confidence intervals.

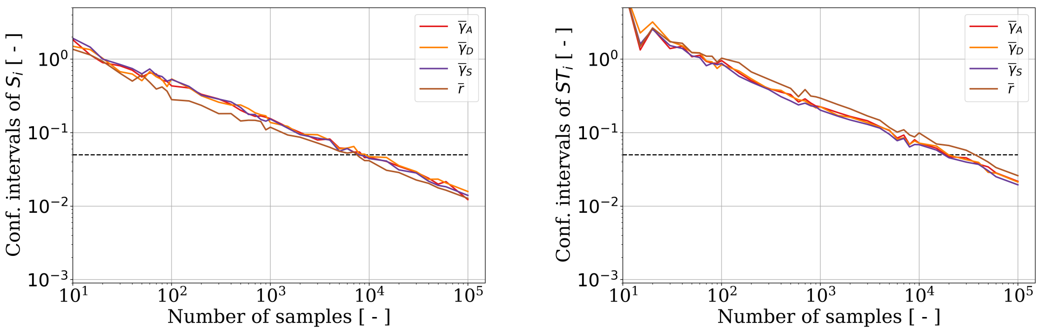

(a) (b)

Figure D.47: Range of the 95 % confidence intervals the (a) first and (b) total Sobol indices depending on the number of estimations of the metamodel, computed with the Martinez algorithm. The black dashed lines correspond to the threshold of 0.05.

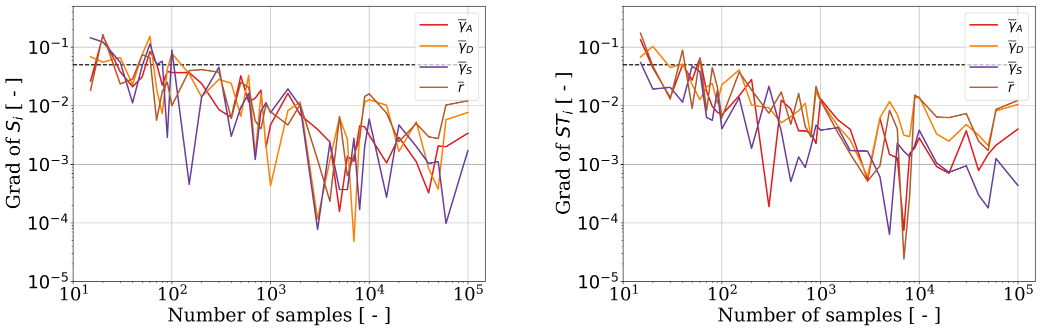

(a) (b)

Figure D.48: Absolute gradient of the (a) first and (b) total Sobol indices depending on the number of estimations of the metamodel, computed with the Martinez algorithm. The black dashed lines correspond to the threshold of 0.05.

4.2 Comparison of the effect of the initial and mechano-adaptation-related parameters on the initial ones on the wrapping degree at equilibrium

This section presents the results of the convergence study conducted in Chapter 5 in the case of the sensitivity analysis conducted on the influence of $\overline{\gamma}_0$, $\overline{\sigma}$, $\overline{\gamma}_A$, $\overline{\gamma}_D$ and $\overline{\gamma}_S$ on the proportion of full wrapping ψ_3. Each subsection contains figures which depict the variation, in terms of the number of samples, of (i) the first and total Sobol indices (S_i and ST_i), (ii) the range of the 95 % confidence intervals (CIs) and (iii) the normalized absolute gradients.

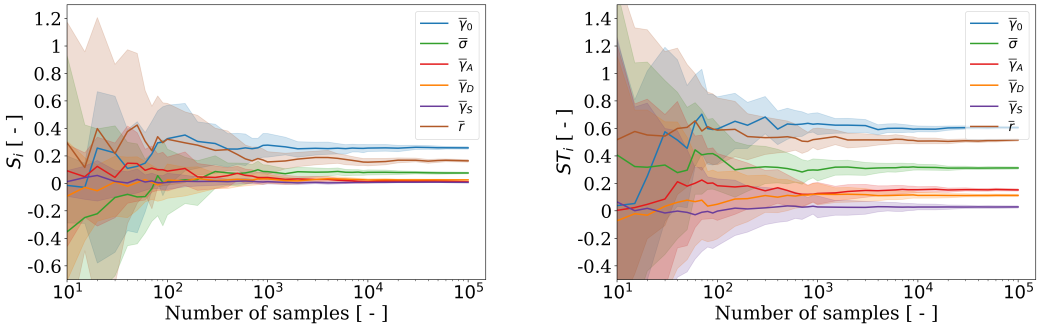

(a) (b)

Figure D.49: (a) First and (b) total Sobol indices depending on the number of estimations of the metamodel, computed with the Mauntz-Kucherenko algorithm. The shaded regions correspond to the 95 % confidence intervals.

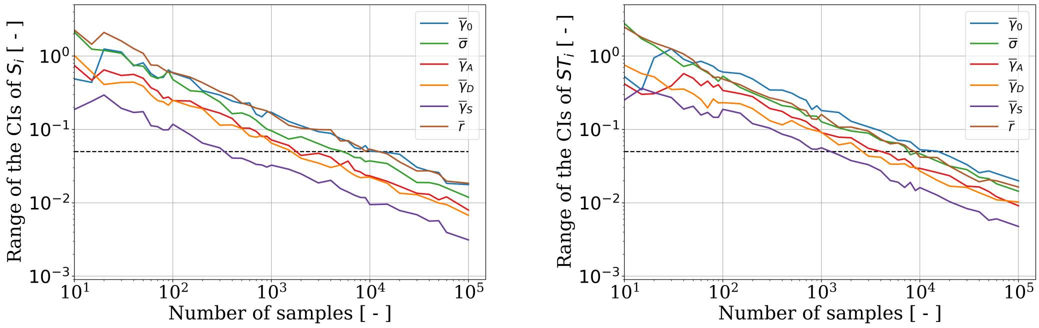

(a) (b)

Figure D.50: Range of the 95 % confidence intervals the (a) first and (b) total Sobol indices depending on the number of estimations of the metamodel, computed with the Mauntz-Kucherenko algorithm. The black dashed lines correspond to the threshold of 0.05.

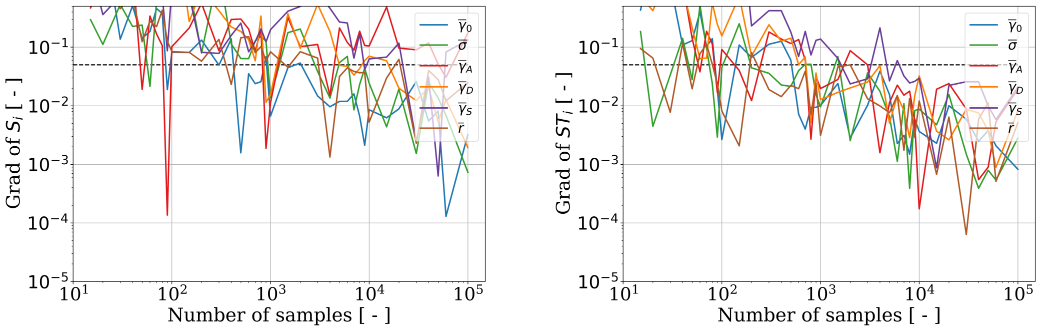

(a) (b)

Figure D.51: Absolute gradient of the (a) first and (b) total Sobol indices depending on the number of estimations of the metamodel, computed with the Mauntz-Kucherenko algorithm. The black dashed lines correspond to the threshold of 0.05.

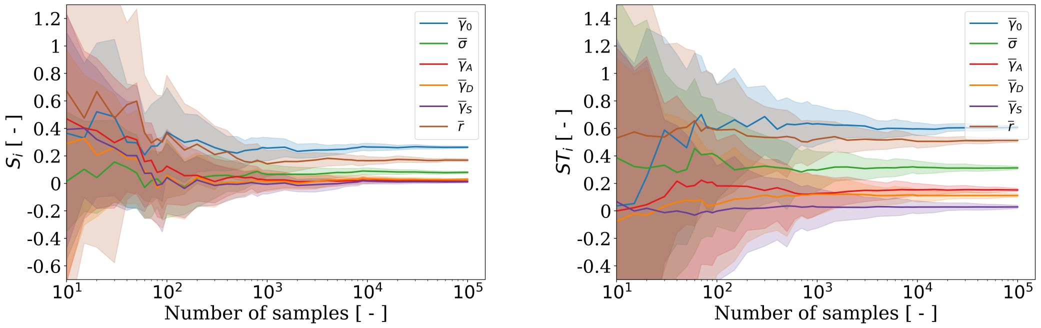

(a) (b)

Figure D.52: (a) First and (b) total Sobol indices depending on the number of estimations of the metamodel, computed with the Saltelli algorithm. The shaded regions correspond to the 95 % confidence intervals.

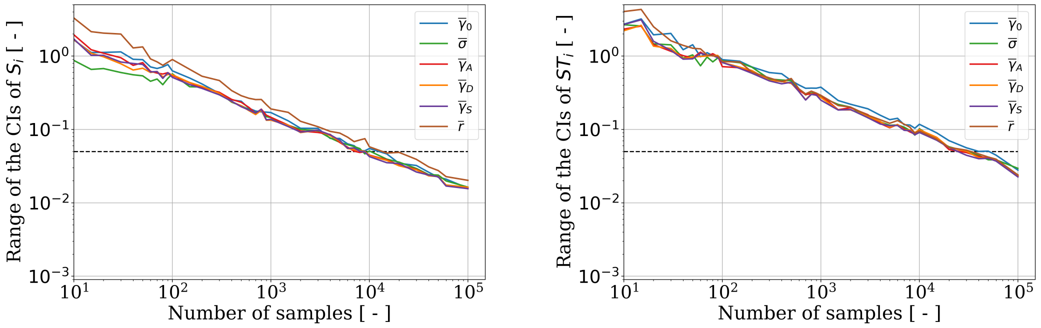

(a) (b)

Figure D.53: Range of the 95 % confidence intervals the (a) first and (b) total Sobol indices depending on the number of estimations of the metamodel, computed with the Saltelli algorithm. The black dashed lines correspond to the threshold of 0.05.

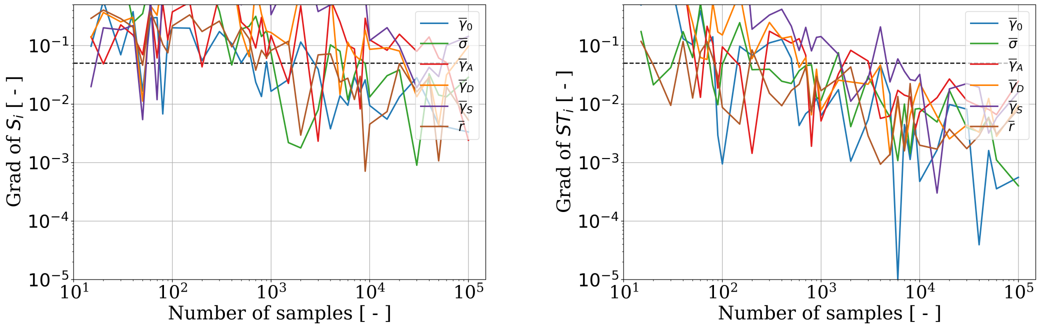

(a) (b)

Figure D.54: Absolute gradient of the (a) first and (b) total Sobol indices depending on the number of estimations of the metamodel, computed with the Saltelli algorithm. The black dashed lines correspond to the threshold of 0.05.

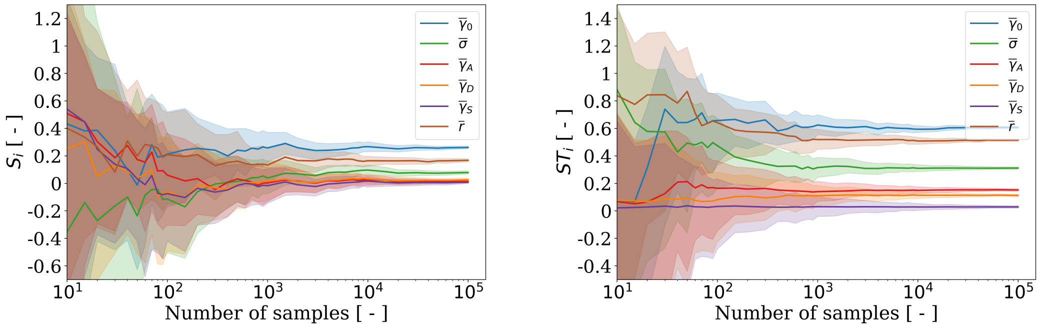

(a) (b)

Figure D.55: (a) First and (b) total Sobol indices depending on the number of estimations of the metamodel, computed with the Jansen algorithm. The shaded regions correspond to the 95 % confidence intervals.

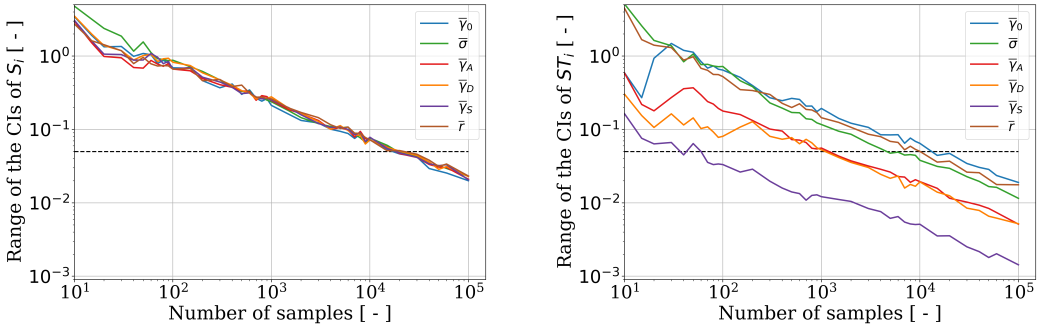

(a) (b)

Figure D.56: Range of the 95 % confidence intervals the (a) first and (b) total Sobol indices depending on the number of estimations of the metamodel, computed with the Jansen algorithm. The black dashed lines correspond to the threshold of 0.05.

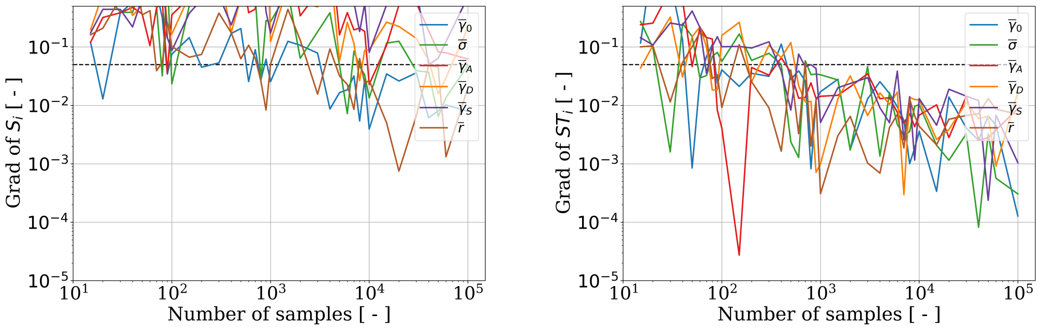

(a) (b)

Figure D.57: Absolute gradient of the (a) first and (b) total Sobol indices depending on the number of estimations of the metamodel, computed with the Jansen algorithm. The black dashed lines correspond to the threshold of 0.05.

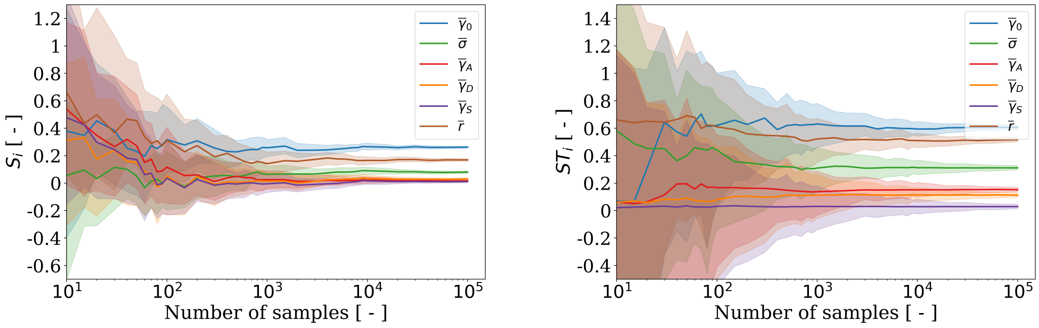

(a) (b)

Figure D.58: (a) First and (b) total Sobol indices depending on the number of estimations of the metamodel, computed with the Martinez algorithm. The shaded regions correspond to the 95 % confidence intervals.

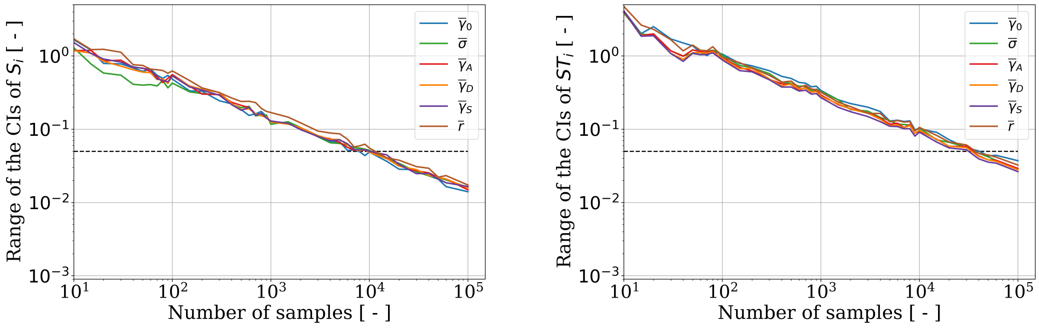

(a) (b)

Figure D.59: Range of the 95 % confidence intervals the (a) first and (b) total Sobol indices depending on the number of estimations of the metamodel, computed with the Martinez algorithm. The black dashed lines correspond to the threshold of 0.05.

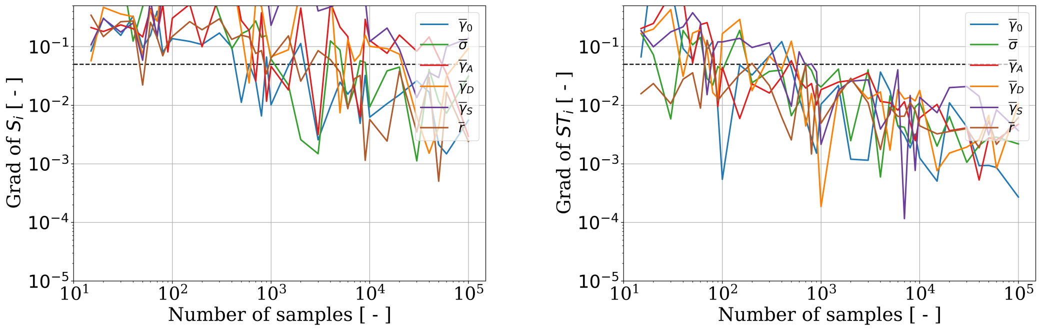

(a) (b)

Figure D.60: Absolute gradient of the (a) first and (b) total Sobol indices depending on the number of estimations of the metamodel, computed with the Martinez algorithm. The black dashed lines correspond to the threshold of 0.05.

5 Conclusions

The results presented in this appendix show that:

- **Investigating the convergence of the Sobol indices** is of great importance. Indeed, the indices, regardless of the algorithm used to approximate them, present a large variation in term of the number of estimations.

- **The normalized gradient is not relevant to establish convergence**. Indeed, as already introduced and demonstrated in Chapter 3, the use of the normalized absolute gradient does not apply to the convergence of the Sobol indices, of which the values can be close to 0, in the case of a non-influential parameter, which is for instance the case with S_σ for a passive membrane. For this variable, the convergence criterion of 1 % is not reached, even using 10^5 estimations. This result do not match direct observations of the variation of the sobol indices in terms of the number of estimations, which are stabilized much faster.

- **The CIs need to be investigated** since they require most estimations to vanish than the number that is necessary for the indices to stabilize. In addition, their range is important, as it can be larger than 1, which is the upper bound of the Sobol indices, when little estimations are used. This element has been pointed out by Sarrazin *et. al* [164], who determined that the Sobol indices converge when the range of their CIs is smaller than 0.05.

- **The number of parameters does not alter the convergence,** which in our study is always reached for a number of samples between 10^4 and 5×10^4 (that varies depending on the algorithm, as explained in the next point). Indeed, the number of variables does not appear in the approximation of the indices (see Appendix A for more details). It does nonetheless influence the computational cost. However, considering the negligible computation times that have been measured (≈ 5 seconds), the latter have not been represented in the graphs of this appendix and the change due to the number of variables is not relevant to be discussed.

- **Independently of the algorithm** used to compute the Sobol indices, convergence is reached for 10^5 samples, which is the maximum number of samples that was tested. Note that the computation time is small. As such, it is irrelevant to minimize the number of estimations needed for convergence. Hence, the indices obtained for 10^5 estimations are used for the sensitivity analysis. Consequently, no algorithm suits better than the others for the approximation of the Sobol indices in this study.

Appendix E

FRENCH ABSTRACT

1 Introduction

1.1 Contexte

Les travaux présentés dans ce manuscrit s'inscrivent au sein du projet METCIN[1] (Mechanical Exploration for Tackling Cellular Interactions of Nanoparticules at the Nanoscale), impliquant trois laboratoires : L'Institut de Recherche en Génie Civil et Mécanique UMR CNRS 6183 (GeM), le Centre de Recherche en Cancérologie et Immunologie de Nantes-Angers Unité Inserm U1232 (CRCI2NA) et le laboratoire Chimie Et Interdisciplinarité, Synthèse, Analyse, Modélisation UMR CNRS 6230 (CEISAM). Leurs contributions respectives au projet METCIN sont illustrées Figure 1. Ce projet a été financé par l'initiative NExT[2] (Nantes Excellence Trajectory), portée par Nantes Université.

1.2 Présentation du sujet de thèse

En France, deux femmes sur trois et un homme sur deux sont atteints d'un cancer avant l'âge de 85 ans et 40 % d'entre eux ne se rétablissent pas [1] Les traitements existants causent des effets secondaires qui sont principalement dûs à des erreurs de ciblage des cellules cancéreuses par les principes actifs des médicaments [2]. Ce ciblage est basé sur les hétérogénéités de propriétés biochimiques entre les cellules saines et cancéreuses. Par ailleurs, des études ont récemment mis en lumière l'existence de différences d'ordre mécanique entre ces cellules. L'objectif de ce travail est donc d'explorer la possibilité d'améliorer la précision du ciblage des traitements anti-cancer basés sur l'utilisation de NanoParticules (NPs), en tenant compte des hétérogénéités de comportement mécanique entre les cellules saines et cancéreuses. Pour cela, un modèle numérique (présenté en Section 2) de l'ingestion de NPs a été développé. Ensuite, des analyses de sensiblité ont

---

[1] Pour plus d'informations, consulter `https://next-isite.fr/metcin`.

[2] Pour plus d'informations, consulter `https://next-isite.fr`.

été conduites à partir du modèle afin de quantifier l'influence des paramètres d'entrée qui ont été introduits dans le modèle afin de représenter le comportement mécanique des cellules saines et cancéreuses. Cette étude est présentée en Section 3. Enfin, une revue de la littérature portant sur les méthodes de caractérisation des cellules touchées par le cancer du sein a été menée afin d'identifier les valeurs numériques des paramètres d'entrée du modèle, dans le but final d'optimiser la forme des NPs pour faciliter leur internalisation par les cellules cancéreuses uniquement. Cette application du modèle est réalisée en Section 4.

2 Modèle de l'internalisation de nanoparticules

2.1 Présentation du modèle de l'enveloppement membranaire de la NP

Dans le cadre de cette thèse, l'étude du phénomène d'internalisaton de NPs sera restreint à l'étape préliminaire qui consiste en l'enveloppement de la NP par la membrane cellulaire. Plusieurs approches numérique du phénomène d'enveloppement d'objets du milieu extra-cellulaire par la membrane sont utilisées dans la littérature, en fonction de l'échelle préférée pour étudier le phénomène. Par exemple, les modèles utilisant la dynamique moléculaire [30, 84–89] consistent à représenter l'ensemble des éléments de la micro-structure de la membrane cellulaire et de la NP, avec un niveau de discrétisation pouvant aller jusqu'au niveau de l'atome. Ces méthodes consistent à modéliser les interactions chimiques entre ces différents constituants. Un exemple de modélisation de l'enveloppement d'une NP par une membrane cellulaire, réalisé en dynamique moléculaire, est représenté Figure E.1.

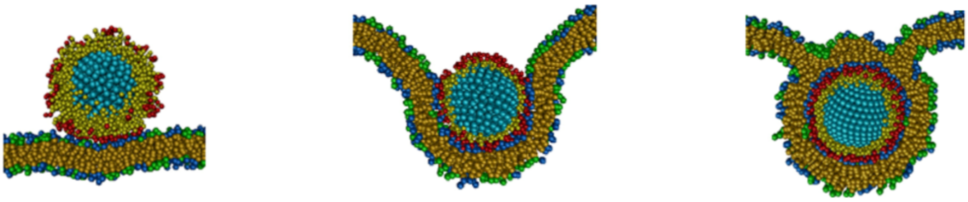

Figure E.1: Exemple de modèle en dynamique moléculaire de l'enveloppement cellulaire d'une NP avec un modèle à gros grains, reproduit à partir de [94].

Un autre type d'approche consiste à étudier le phénomène à l'échelle de la NP, en faisant l'hypothèse que l'épaisseur de la membrane (de l'ordre de quelques nanomètres [20]) est négligeable devant le diamètre de la NP. Lorsque cette hypothèse est vérifiée, la membrane est modélisée comme une ligne homogène. Cette approche a été utilisée pour la première fois en 2011 par Yi *et al.* [40]. L'étude du phénomène est réalisée à partir d'un suivi de la variation d'énergie potentielle au cours de l'enveloppement de la NP, afin d'en identifier l'état d'équilibre à partir de la minimisation de l'énergie. Cette variation est décrite par le Halmitonien de Canham-Helfrich [59, 95–98]. Le système NP-membrane étudié est représenté sur la Figure E.2, où la région 3 représente la partie de la NP en contact avec la membrane, les régions $2r$ et $2l$ les parties droite et gauche de la membrane libre et la région 1 représente la partie libre de la NP. La longueur d'arc de ces régions est suivie par la variable $s_i \in [0, \hat{s}_i]$, où $\hat{s}_i$ est la longueur de chaque région i. L'angle $\psi_i(s_i)$ est l'angle entre la tangente et l'horizontale au point s_i. Le taux d'enveloppement de la NP, noté f est défini tel que $f = \hat{s}_3/p$, où p est le périmètre de la NP. Ainsi, $p = \hat{s}_1 + \hat{s}_3$.

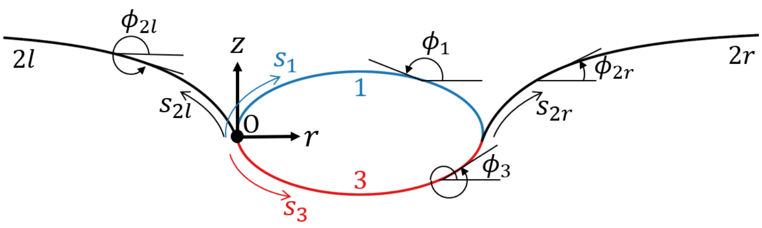

Figure E.2: Illustration de la paramétrisation de l'interaction NP-membrane.

La variation d'énergie potentielle, entre l'état initial et un taux d'enveloppement f donné, est notée $\Delta E(f)$, et est due à (i) la flexion membranaire $\Delta E_b(f)$, (ii) à l'adhésion entre la NP et la membrane $\Delta E_\gamma(f)$ et (iii) à la tension de la membrane $\Delta E_\sigma(f)$. Ainsi :

$$\Delta E(f) = \Delta E_b(f) + \Delta E_\gamma(f) + \Delta E_\sigma(f).$$

Afin d'alléger les prochaines équations, la dépendance à la variable f sera omise. L'énergie de flexion ΔE_b est définie ci-dessous [59]:

$$\Delta E_b = \underbrace{\frac{1}{2}\int_0^{\infty} \kappa_{2r}(s_{2r})[\dot{\phi}_{2r}(s_{2r}) - \widetilde{c}_{2r}(s_{2r})]^2 ds_{2r}}_{\text{région 2r}} + \underbrace{\frac{1}{2}\int_0^{\hat{s}_3} \kappa_3(s_3)[\dot{\phi}_3(s_3) - \widetilde{c}_3(s_3)]^2 ds_3}_{\text{région 3}},$$

où la notation $\dot{}$ représente la dérivée par rapport à la longueur d'arc s_i. Dans l'équation précédente, la rigidité de flexion et la courbure initiale des régions $i \in \{2r, 3\}$ sont notées κ_i et $\widetilde{c}_i$, respectivement. L'énergie d'adhésion ΔE_γ est définie telle que :

$$\Delta E_\gamma = -\int_0^{\hat{s}_3} \gamma(s_3) ds_3,$$

où l'adhésion γ est supposée constante, *i.e.* $\gamma(s_3) := \gamma$. Enfin, l'énergie liée à la tension membranaire ΔE_σ s'écrit :

$$\Delta E_\sigma = \sigma \Delta l,$$

Après la prise en compte de simplifications liées à des hypothèses de membrane homogène et symétrique : $\kappa_{2r} = \kappa_{2l}$, simplifiée en κ. Par ailleurs, l'étude est restreinte aux NPs indéformables. Ainsi, ΔE devient :

$$\begin{aligned}\Delta E(s_{2r}, \phi_{2r}, \dot{\phi}_{2r}, s_3, \phi_3, \dot{\phi}_3) = \int_0^\infty \left(\frac{\kappa}{2}\dot{\phi}_{2r}^2 + \sigma[1 - \cos\phi_{2r}]\right) ds_{2r} \\ + \int_0^{\hat{s}_3} \left(\frac{\kappa}{2}\dot{\phi}_3^2 + \sigma[1 - \cos\phi_3] - \gamma\right) ds_3.\end{aligned}$$

Afin de comparer nos résultats avec ceux présentés dans la littérature, ΔE, γ et σ sont adimensionnalisés en $\overline{\Delta E}$, $\overline{\gamma}$, et $\overline{\sigma}$: $\overline{\Delta E} = \Delta E \frac{2a}{\kappa}$, $\bar{\gamma} = \gamma \frac{2a^2}{\kappa}$ et $\bar{\sigma} = \sigma \frac{2a^2}{\kappa}$, où a est le rayon relatif de la NP, défini en fonction de son périmètre tel que $a = p/(2\pi)$.

2.2 Post-traitement du modèle

Des études paramétriques sont conduites afin d'identifier, de manière qualitative puis quantitative, l'effet des différents paramètres d'entrée du modèle. Ces études seront détaillés en Section 3. Deux quantités d'intérêts (QoIs) ont été utilisées : le taux d'enveloppement à l'équilibre $\tilde{f}$ et la proportion d'enveloppement complet ψ_3. Le taux d'enveloppement à l'équilibre $\tilde{f}$ est le taux d'enveloppement pour lequel le système est à l'équilibre (minimisation de l'énergie). Une fois l'état d'équilibre déterminé, on considère que la NP est complètement enveloppée si les deux parties libres de la membrane se rejoignent au dessus de la NP, l'empêchant ainsi de s'échapper. Ainsi, $\tilde{f}$ est calculé et l'état final du système est déterminé pour un ensemble de valeurs de paramètres d'entrée $\overline{\gamma}$ et $\overline{\sigma}$ et la proportion de cas ayant mené à un enveloppement complet de la NP ψ_3 est calculée.

2.3 Réaction de la membrane

Afin de faciliter l'ingestion des objets extérieurs qui entrent en contact avec la membrane, les récepteurs présents dans celle-ci tendent à se déplacer vers la zone d'interaction [135, 139, 222]. Ce phénomène de réponse de la membrane n'est pas pris en compte dans les modèles qui étudient l'enveloppement à l'échelle de la NP. Dans cette thèse, une modélisation de l'adaptation des propriétés mécaniques au cours de l'enveloppement de la NP a été proposée. Ainsi, la variation de l'adhésion $\overline{\gamma}$ en fonction du taux d'enveloppement f est décrite par la fonction sigmoïdale suivante :

$$\overline{\gamma}(f) = \frac{\overline{\gamma}_0(\overline{\gamma}_A - 1)}{1 + \exp\left[-2\overline{\gamma}_S(f - f_{\text{inf}})\right]} + \overline{\gamma}_0,$$

où f_{inf} est le point d'inflexion, défini en fonction du délai de la transition $\overline{\gamma}_D$ tel que $f_{\text{inf}} = 0.5 + \overline{\gamma}_D$, alors que $\overline{\gamma}_A$ représente l'amplitude de la transition et $\overline{\gamma}_S$ le paramètre de courbure, qui est indépendant des paramètres précédents et qui permet de controler la pente de $\overline{\gamma}$ au point d'inflexion. L'adhésion initiale, *i.e.* $\overline{\gamma}(f \to 0)$, est notée $\overline{\gamma}_0$. L'effet de ces différents paramètres sur $\overline{\gamma}(f)$ est illustré Figure E.3.

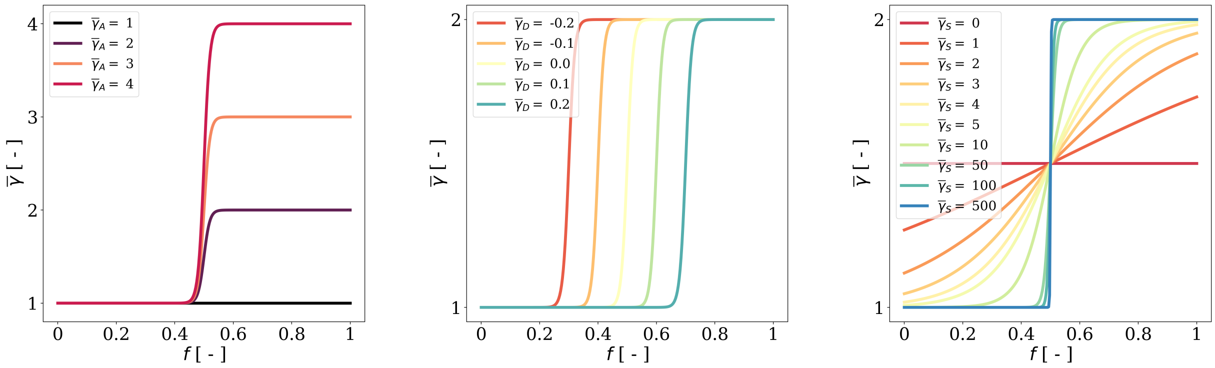

(a) $\overline{\gamma}_A$ (b) $\overline{\gamma}_D$ (c) $\overline{\gamma}_S$

Figure E.3: Illustration de l'effet des paramètres d'une fonction sigmoïdale croissante : évolution de $\overline{\gamma}(f)$ pour (a) $\overline{\gamma}_A \in \{1, 2, 3, 4\}$, (b) $\overline{\gamma}_D \in \{-0.2, -0.1, 0, 0.1, 0.2\}$ et (c) $\overline{\gamma}_S \in [0, 500]$. Les paramètres $\overline{\gamma}_A$, $\overline{\gamma}_D$, $\overline{\gamma}_S$, $\overline{\gamma}_0$ et $\overline{\sigma}$ sont fixés à 2, 0, 50, 1 et 2 respectivement pour tous les cas, sauf si spécifié différemment dans la légende des graphes. Notons que dans le cas particulier où $\overline{\gamma}_S = 0$, $\overline{\gamma}$ est de f et vaut $\overline{\gamma}_0(\overline{\gamma}_A + 1)/2 = 1.5$.

Avec la prise en compte de la réaction de la membrane, le modèle contient 6 paramètres d'entrée : $\overline{\gamma}_0$, $\overline{\sigma}$, $\overline{\gamma}_A$, $\overline{\gamma}_D$, $\overline{\gamma}_S$, $\overline{r}$.

3 Analyse de sensibilité

3.1 Introduction

Afin de quantifier l'effet d'un paramètre d'entrée sur un paramètre de sortie Y d'un modèle, des analyses de sensibilité peuvent être conduites [142]. Parmi ces méthodes, le calcul des indices de Sobol du premier ordre S_i permet de quantifier les effets d'un paramètres d'entrée X_i seul et les indices totaux ST_i permettent de quantifier l'effet des différentes interactions de X_i avec les autres paramètres $X_{j\neq i}$. Le calcul de ces indices est détaillé ci-dessous.

$$\begin{aligned} S_i &= \frac{\mathrm{Var}[\mathbb{E}[Y|X_i]]}{\mathrm{Var}[Y]}, \\ ST_i &= 1 - \frac{\mathrm{Var}[\mathbb{E}[Y|X_1, ..., X_{i-1}, X_{i+1}, ...X_M]]}{\mathrm{Var}[Y]}, \end{aligned}$$

où $\mathbb{E}$ et Var représentent respectivement l'espérance et la variance d'une variable aléatoire.

Le calcul des indices de Sobol pouvant nécessiter un grand nombre de données du modèle, c'est à dire de réalisations de Y, leur calcul à partir d'appels directs au modèle représenterait un coût de calcul trop important, pouvant aller jusqu'à plusieurs semaines. Des métamodèles de Kriging et Chaos Polynomial (PCE) ont donc été développés afin de parer à cette problématique. Ces métamodèles sont parvenus à plus ou moins bien à approcher le comportement du modèle original, en fonction du cas d'étude choisi. Les différents résultats ainsi obtenus sont présentés en Section 3.2.

3.2 Résultats

Afin de simplifier le développement des métamodèles à partir d'une progression par étape, des cas d'études simplifiés ont été utilisés. Ces cas sont décrits dans le Tableau E.1 et les valeurs des coefficients de prédictibilité Q_2 obtenus pour chacun de ces cas sont présentés dans le Tableau E.2. Les métamodèles sont parvenus à reproduire le comportement du modèle avec justesse dans les cas 1, 2a, 2b et 3a, mais pas pour le cas 3b. Dans ce dernier cas, les approximations du métamodèle ne peuvent pas être utilisées pour réaliser les estimations nécessaires au calcul des indices de Sobol. Dans les autres cas, les indices obtenus, dont les valeurs numériques sont données dans le manuscrit, ont mis en évidence l'importance du rapport de forme de la NP $\overline{r}$, de l'adhésion initiale $\overline{\gamma}_0$, de la tension membranaire $\overline{\sigma}$ et du délai de la transition $\overline{\gamma}_D$.

Table E.1: Cas d'étude utilisés pour le développement des métamodèles et les analyses de sensibilité.

Description	Paramètres d'entrée	Paramètre de sortie
1 - NP elliptique et membrane passive	$\overline{\gamma}_0$, $\overline{\sigma}$, $\overline{r}$	$\tilde{f}$
2a - NP circulaire et membrane adaptative	$\overline{\gamma}_A$, $\overline{\gamma}_D$, $\overline{\gamma}_S$	ψ_3
2b - NP circulaire, comparaison entre les membrane passive et adaptative	$\overline{\gamma}_0$, $\overline{\sigma}$, $\overline{\gamma}_A$, $\overline{\gamma}_D$, $\overline{\gamma}_S$	$\tilde{f}$
3a - NP elliptique et membrane adaptative	$\overline{\gamma}_A$, $\overline{\gamma}_D$, $\overline{\gamma}_S$, $\overline{r}$	ψ_3
3b - NP elliptique, comparaison entre les membrane passive et adaptative	$\overline{\gamma}_0$, $\overline{\sigma}$, $\overline{\gamma}_A$, $\overline{\gamma}_D$, $\overline{\gamma}_S$, $\overline{r}$	$\tilde{f}$

Table E.2: Valeurs des facteurs de prédictibilité Q_2 obtenus avec Kriging et PCE dans les différents cas.

Cas	Q_2^{KRI}	Q_2^{PCE}
1	0.97	0.79
2a	0.99	0.98
2b	0.86	0.80
3a	0.92	0.68
3b	0.42	0.55

4 Application du modèle au cancer du sein

Les résultats présentés dans la section précédente ont mis en évidence l'influence des propriétés mécaniques des cellules sur le taux d'enveloppement à l'équilibre et donc sur l'internalisation des NPs. Ainsi, il pourrait être possible de prendre en compte les hétérogénéités de propriétés mécaniques entre les cellules saines et cancéreuses. Afin de vérifier la possibilité de différencier l'internalisation de NPs par les cellules saines et cancéreuses, une étude appliquée au cancer du sein a été réalisée. Pour cela, une revue de la littérature portant sur la caractérisation mécanique des cellules mammaires saines et cancéreuse a d'abord été menée afin d'identifier les valeurs des paramètres d'entrée du modèle $\overline{\gamma}_0$, $\overline{\sigma}$, $\overline{\gamma}_A$, $\overline{\gamma}_D$, $\overline{\gamma}_S$. Ensuite, les différents rapports de forme $\overline{r}$ des NPs ont été testés pour les cellules saines et cancéreuses et une gamme de valeurs de $\overline{r}$ pour lesquelles celles-ci ne sont internalisées uniquement par les cellules cancéreuses a pu être identifiée. La méthode retenue pour l'application du modèle est illustrée en Figure E.4. Ces résultats permettent d'envisager la possibilité d'améliorer le ciblage des traitements anti-cancer pour le cancer du sein à partir d'une différenciation mécanique.

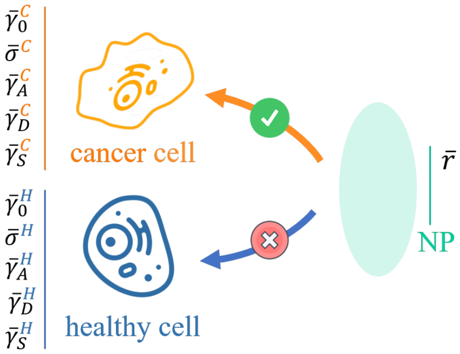

Figure E.4: Illustration de la méthode d'application du modèle.

5 Conclusions

L'objectif de cette thèse est de caractériser l'influence des propriétés mécaniques des cellules et des NPs sur l'internalisation de NPs dans le but d'améliorer le ciblage des cellules cancéreuses par les nanovecteurs d'agents anti-cancer. Pour cela, un modèle de l'ingestion cellulaire de NPs a été développé puis des analyses de sensbilité ont été conduites afin de quantifier l'effet des paramètres d'entrée du modèle (adhésion initiale entre la NP et la membrane, amplitude, délai, paramètre de courbure de la variation de l'adhésion, tension membranaire et rapport de forme de la NP). Enfin, une revue de la littérature a été réalisée afin d'identifier les valeurs numériques des paramètres d'entrée du modèle dans le cas du cancer du sein ainsi que les rapports de forme permettant d'optimiser le ciblage des traitements anti-cancer.

BIBLIOGRAPHY

[1] Catherine Hill and Françoise Doyon, “Frequency of cancer in France”, *in*: *Bulletin du cancer* 90.*3* (2003), pp. 207–213 (cit. on pp. 3, 193).

[2] Twan Lammers, Fabian Kiessling, Marianne Ashford, Wim Hennink, Daan Crommelin, and Gert Storm, “Cancer nanomedicine: is targeting our target?”, *in*: *Nature Reviews Materials* 1.*9* (2016), pp. 1–2 (cit. on pp. 3, 193).

[3] Ahmedin Jemal, Taylor Murray, Elizabeth Ward, Alicia Samuels, Ram C Tiwari, Asma Ghafoor, Eric J Feuer, and Michael J Thun, “Cancer statistics, 2005 (vol 55, pg 10, 2005)”, *in*: *Ca-a Cancer Journal for Clinicians* 55.*4* (2005), pp. 259–259 (cit. on pp. 7, 8, 133).

[4] Akulapalli Sudhakar, “History of cancer, ancient and modern treatment methods”, *in*: *Journal of cancer science & therapy* 1.*2* (2009), p. 1 (cit. on p. 7).

[5] Samuel R. Denmeade and John T. Isaacs, “A history of prostate cancer treatment”, *in*: *Nature Reviews Cancer* 2.*5* (2002), pp. 389–396 (cit. on p. 7).

[6] Dörthe Schaue and William H. McBride, “Opportunities and challenges of radiotherapy for treating cancer”, *in*: *Nature reviews Clinical oncology* 12.*9* (2015), pp. 527–540 (cit. on p. 7).

[7] Peter Nygren, “What is cancer chemotherapy?”, *in*: *Acta Oncologica* 40.*2-3* (2001), pp. 166–174 (cit. on p. 8).

[8] Edward Chu and A. C. Sartorelli, “Cancer chemotherapy”, *in*: *Lange’s Basic and Clinical Pharmacology,* (2018), pp. 948–976 (cit. on p. 8).

[9] Beth A. Hellerstedt and Kenneth J. Pienta, “The current state of hormonal therapy for prostate cancer”, *in*: *CA: a cancer journal for clinicians* 52.*3* (2002), pp. 154–179 (cit. on p. 8).

[10] Caitlin C. Murphy, L. Kay Bartholomew, Melissa Y. Carpentier, Shirley M. Bluethmann, and Sally W. Vernon, “Adherence to adjuvant hormonal therapy among breast cancer survivors in clinical practice: a systematic review”, *in*: *Breast cancer research and treatment* 134.*2* (2012), pp. 459–478 (cit. on p. 8).

[11] Manfred Schuster, Andreas Nechansky, and Ralf Kircheis, “Cancer immunotherapy”, *in*: *Biotechnology Journal: Healthcare Nutrition Technology* 1.*2* (2006), pp. 138–147 (cit. on p. 8).

[12] David E. Gerber, “Targeted therapies: a new generation of cancer treatments”, *in*: *American family physician* 77.*3* (2008), pp. 311–319 (cit. on p. 8).

[13] Tina Briolay, Tacien Petithomme, Morgane Fouet, Nelly Nguyen-Pham, Christophe Blanquart, and Nicolas Boisgerault, “Delivery of cancer therapies by synthetic and bio-inspired nanovectors”, *in*: *Molecular cancer* 20.*1* (2021), pp. 1–24 (cit. on pp. 8, 9).

[14] Krzysztof Sztandera, Michał Gorzkiewicz, and Barbara Klajnert-Maculewicz, “Gold nanoparticles in cancer treatment”, *in*: *Molecular pharmaceutics* 16.*1* (2018), pp. 1–23 (cit. on p. 8).

[15] Huang-Chiao Huang, Sutapa Barua, Gaurav Sharma, Sandwip K. Dey, and Kaushal Rege, “Inorganic nanoparticles for cancer imaging and therapy”, *in*: *Journal of controlled Release* 155.*3* (2011), pp. 344–357 (cit. on p. 9).

[16] Herve Hillaireau and Patrick Couvreur, “Nanocarriers’ entry into the cell: relevance to drug delivery”, *in*: *Cellular and molecular life sciences* 66.*17* (2009), pp. 2873–2896 (cit. on pp. 9, 11, 46, 80).

[17] Lionel Derue, Simon Olivier, Denis Tondelier, Tony Maindron, Bernard Geffroy, and Eléna Ishow, “All-solution-processed organic light-emitting diodes based on photostable photo-cross-linkable fluorescent small molecules”, *in*: *ACS Applied Materials & Interfaces* 8.*25* (2016), pp. 16207–16217 (cit. on p. 9).

[18] Yue Hui, Xin Yi, Fei Hou, David Wibowo, Fan Zhang, Dongyuan Zhao, Huajian Gao, and Chun-Xia Zhao, “Role of nanoparticle mechanical properties in cancer drug delivery”, *in*: *ACS nano* 13.*7* (2019), pp. 7410–7424 (cit. on pp. 9, 25).

[19] Julie A. Champion, Yogesh K. Katare, and Samir Mitragotri, “Making polymeric micro-and nanoparticles of complex shapes”, *in*: *Proceedings of the National Academy of Sciences* 104.*29* (2007), pp. 11901–11904 (cit. on pp. 9, 11, 19, 28, 80, 81).

[20] Geoffrey M. Cooper and Robert E. Hausman, *The cell: a molecular approach*, vol. 4, ASM press Washington, DC, USA: 2007 (cit. on pp. 9, 11–16, 25, 80, 87, 195).

[21] Elie Metchnikoff, “Untersuchungen über die mesodermalen Phagocyten einiger Wirbeltiere”, *in*: *Biol Zentralbl* 3 (1883), pp. 560–5 (cit. on p. 9).

[22] Sandra L. Schmid, Alexander Sorkin, and Marino Zerial, “Endocytosis: past, present, and future”, *in*: *Cold Spring Harbor perspectives in biology* 6.*12* (2014), a022509 (cit. on pp. 9, 19).

[23] Shahed Behzadi, Vahid Serpooshan, Wei Tao, Majd A. Hamaly, Mahmoud Y. Alkawareek, Erik C. Dreaden, Dennis Brown, Alaaldin M. Alkilany, Omid C. Farokhzad, and Morteza Mahmoudi, “Cellular uptake of nanoparticles: journey inside the cell”, *in*: *Chemical Society Reviews* 46.*14* (2017), pp. 4218–4244 (cit. on pp. 10, 47, 152).

[24] Gaurav Sahay, Daria Y. Alakhova, and Alexander V. Kabanov, “Endocytosis of nanomedicines”, *in*: *Journal of controlled release* 145.*3* (2010), pp. 182–195 (cit. on p. 10).

[25] Gary J. Doherty and Harvey T. McMahon, “Mechanisms of endocytosis”, *in*: *Annual review of biochemistry* 78 (2009), pp. 857–902 (cit. on pp. 10, 11, 44, 47).

[26] T. M. Allen, G. A. Austin, A. Chonn, L. Lin, and K. C. Lee, “Uptake of liposomes by cultured mouse bone marrow macrophages: influence of liposome composition and size”, *in*: *Biochimica et Biophysica Acta (BBA)-Biomembranes* 1061.*1* (1991), pp. 56–64 (cit. on p. 11).

[27] Edward D. Korn and Robert A. Weisman, “Phagocytosis of latex beads by acanthamoeba: II. Electron microscopic study of the initial events”, *in*: *The Journal of cell biology* 34.*1* (1967), pp. 219–227 (cit. on p. 11).

[28] Timothy D. Heath, Ninfa G. Lopez, and Demetrios Papahadjopoulos, “The effects of liposome size and surface charge on liposome-mediated delivery of methotrexate-γ-aspartate to cells in vitro”, *in*: *Biochimica et Biophysica Acta (BBA)-Biomembranes* 820.*1* (1985), pp. 74–84 (cit. on p. 11).

[29] Julie A. Champion and Samir Mitragotri, “Role of target geometry in phagocytosis”, *in*: *Proceedings of the National Academy of Sciences* 103.*13* (2006), pp. 4930–4934 (cit. on pp. 11, 80, 81).

[30] Sulin Zhang, Huajian Gao, and Gang Bao, “Physical principles of nanoparticle cellular endocytosis”, *in*: *ACS nano* 9.*9* (2015), pp. 8655–8671 (cit. on pp. 11, 19–21, 41, 87, 137, 139, 141, 194).

[31] Arnaud Vonarbourg, Catherine Passirani, Patrick Saulnier, and Jean-Pierre Benoit, “Parameters influencing the stealthiness of colloidal drug delivery systems”, *in*: *Biomaterials* 27.*24* (2006), pp. 4356–4373 (cit. on p. 11).

[32] A. E. Nel, L. Mädler, D. Velegol, T. Xia, E. MV. Hoek, P. Somasundaran, F. Klaessig, V. Castranova, and M. Thompson, “Understanding biophysicochemical interactions at the nano–bio interface”, *in*: *Nature materials* 8.*7* (2009), pp. 543–557 (cit. on pp. 11, 47, 81).

[33] Yang Li, Xin Chen, and Ning Gu, “Computational investigation of interaction between nanoparticles and membranes: hydrophobic/hydrophilic effect”, *in*: *The Journal of Physical Chemistry B* 112.*51* (2008), pp. 16647–16653 (cit. on p. 11).

[34] Qing Liang, “Penetration of polymer-grafted nanoparticles through a lipid bilayer”, *in*: *Soft Matter* 9.*23* (2013), pp. 5594–5601 (cit. on p. 11).

[35] Robert S. G. D’Rozario, Chze Ling Wee, E. Jayne Wallace, and Mark S. P. Sansom, “The interaction of C60 and its derivatives with a lipid bilayer via molecular dynamics simulations”, *in*: *Nanotechnology* 20.*11* (2009), p. 115102 (cit. on p. 11).

[36] Per M. Claesson, Eva Blomberg, Johan C. Fröberg, Tommy Nylander, and Thomas Arnebrant, “Protein interactions at solid surfaces”, *in*: *Advances in Colloid and Interface Science* 57 (1995), pp. 161–227 (cit. on p. 11).

[37] Dana V. Devine, Kenneth Wong, Katherine Serrano, Arcadio Chonn, and Pieter R Cullis, “Liposome—complement interactions in rat serum: implications for liposome survival studies”, *in*: *Biochimica et Biophysica Acta (BBA)-Biomembranes* 1191.*1* (1994), pp. 43–51 (cit. on p. 11).

[38] Karen A Beningo and Yu-li Wang, “Fc-receptor-mediated phagocytosis is regulated by mechanical properties of the target”, *in*: *Journal of cell science* 115.*4* (2002), pp. 849–856 (cit. on p. 11).

[39] Xavier Banquy, Fernando Suarez, Anteneh Argaw, Jean-Michel Rabanel, Peter Grutter, Jean-François Bouchard, Patrice Hildgen, and Suzanne Giasson, “Effect of mechanical properties of hydrogel nanoparticles on macrophage cell uptake”, *in*: *Soft Matter* 5.*20* (2009), pp. 3984–3991 (cit. on p. 11).

[40] Xin Yi, Xinghua Shi, and Huajian Gao, “Cellular uptake of elastic nanoparticles”, *in*: *Physical review letters* 107.*9* (2011), p. 098101 (cit. on pp. 11, 22, 25, 26, 28, 29, 42, 44–46, 66, 135, 195).

[41] Julio M. Rubio, Alma M. Astudillo, Javier Casas, Marıa A Balboa, and Jesús Balsinde, "Regulation of phagocytosis in macrophages by membrane ethanolamine plasmalogens", *in*: *Frontiers in immunology* 9 (2018), p. 1723 (cit. on p. 11).

[42] Julio M. Rubio, Juan P. Rodrıguez, Luis Gil-de-Gómez, Carlos Guijas, Marıa A. Balboa, and Jesús Balsinde, "Group V secreted phospholipase A2 is upregulated by IL-4 in human macrophages and mediates phagocytosis via hydrolysis of ethanolamine phospholipids", *in*: *The Journal of Immunology* 194.*7* (2015), pp. 3327–3339 (cit. on p. 11).

[43] Gerard Apodaca, "Modulation of membrane traffic by mechanical stimuli", *in*: *American Journal of Physiology-Renal Physiology* 282.*2* (2002), F179–F190 (cit. on pp. 11, 44).

[44] Jianwu Dai, H. Ping Ting-Beall, and Michael P. Sheetz, "The secretion-coupled endocytosis correlates with membrane tension changes in RBL 2H3 cells", *in*: *The Journal of general physiology* 110.*1* (1997), pp. 1–10 (cit. on p. 11).

[45] Antje Kell and Ralf W. Glaser, "On the mechanical and dynamic properties of plant cell membranes: their role in growth, direct gene transfer and protoplast fusion", *in*: *Journal of Theoretical Biology* 160.*1* (1993), pp. 41–62 (cit. on p. 11).

[46] C. E. Morris and Ulrike Homann, "Cell surface area regulation and membrane tension", *in*: *The Journal of membrane biology* 179.*2* (2001), pp. 79–102 (cit. on p. 11).

[47] Drazen Raucher and Michael P. Sheetz, "Membrane expansion increases endocytosis rate during mitosis", *in*: *The Journal of cell biology* 144.*3* (1999), pp. 497–506 (cit. on p. 11).

[48] Michael P. Sheetz, "Cell control by membrane–cytoskeleton adhesion", *in*: *Nature Reviews Molecular Cell Biology* 2.*5* (2001), pp. 392–396 (cit. on p. 11).

[49] Joe Wolfe, Michael F. Dowgert, and Peter L. Steponkus, "Dynamics of membrane exchange of the plasma membrane and the lysis of isolated protoplasts during rapid expansions in area", *in*: *The Journal of Membrane Biology* 86.*2* (1985), pp. 127–138 (cit. on p. 11).

[50] D. N. Tucker, W. C. Hill, and G. E. Gifford, "The effect of pH on phagocytosis by rabbit mononuclear phagocytes", *in*: *The Journal of Infectious Diseases* (1963), pp. 47–52 (cit. on p. 11).

[51] Kieran S. Boochoon, Joseph C. Manarang, Joshua T. Davis, Alison M. McDermott, and William J. Foster, “The influence of substrate elastic modulus on retinal pigment epithelial cell phagocytosis”, *in*: *Journal of biomechanics* 47.*12* (2014), pp. 3237–3240 (cit. on p. 11).

[52] Wolfgang Gross, Franziska Zecherle, Kathrin Weidner-Hertrampf, and Holger Kress, “Macrophages are Sensitive to Substrate Elasticity during Phagocytosis”, *in*: *Biophysical Journal* 112.*3* (2017), 125a (cit. on p. 11).

[53] Anthony Mescher, *Junqueira’s basic histology: text and atlas*, 2013 (cit. on pp. 12, 13).

[54] Open Learning Initiative, *Levels of Organization: Higher Order Structures*, 2022 (cit. on p. 12).

[55] Nuria Lorenzo Brun, Sara Táboas Favorecido, Elisa Inés Sánchez, Raúl Sánchez Álvarez, and Daniel Lens, *Atlas of Plant and Animal Histology*, 2022 (cit. on p. 13).

[56] B. Cornell, *Eukaryotic Cells*, `http://ib.bioninja.com.au`, 2016 (cit. on p. 13).

[57] S. Jonathan Singer and Garth L. Nicolson, “The Fluid Mosaic Model of the Structure of Cell Membranes: Cell membranes are viewed as two-dimensional solutions of oriented globular proteins and lipids.”, *in*: *Science* 175.*4023* (1972), pp. 720–731 (cit. on pp. 13, 44, 47, 80).

[58] Garth L. Nicolson, “Update of the 1972 Singer-Nicolson fluid-mosaic model of membrane structure”, *in*: *Discoveries* 1.*1* (2013) (cit. on pp. 13, 47).

[59] Wolfgang Helfrich, “Elastic properties of lipid bilayers: theory and possible experiments”, *in*: *Zeitschrift für Naturforschung c* 28.*11-12* (1973), pp. 693–703 (cit. on pp. 15, 22, 28, 29, 41, 151, 195).

[60] J. G. Swift and T. M. Mukherjee, “Demonstration of the fuzzy surface coat of rat intestinal microvilli by freeze-etching”, *in*: *The Journal of cell biology* 69.*2* (1976), pp. 491–495 (cit. on p. 16).

[61] Cuixia Yang, Yiwen Liu, Yiqing He, Yan Du, Wenjuan Wang, Xiaoxing Shi, and Feng Gao, “The use of HA oligosaccharide-loaded nanoparticles to breach the endogenous hyaluronan glycocalyx for breast cancer therapy”, *in*: *Biomaterials* 34.*28* (2013), pp. 6829–6838 (cit. on pp. 16, 19, 140).

[62] Douglas Hanahan and Robert A. Weinberg, “The hallmarks of cancer”, *in*: *cell* 100.*1* (2000), pp. 57–70 (cit. on p. 17).

[63] Larry Tait, Herbert D. Soule, and Jose Russo, “Ultrastructural and immunocytochemical characterization of an immortalized human breast epithelial cell line, MCF-10”, *in*: *Cancer research* 50.*18* (1990), pp. 6087–6094 (cit. on p. 18).

[64] Małgorzata Lekka, Katarzyna Pogoda, Justyna Gostek, Olesya Klymenko, Szymon Prauzner-Bechcicki, Joanna Wiltowska-Zuber, Justyna Jaczewska, Janusz Lekki, and Zbigniew Stachura, “Cancer cell recognition: mechanical phenotype”, *in*: *Micron* 43.*12* (2012), pp. 1259–1266 (cit. on pp. 18, 20, 136, 141).

[65] Hsi-Hui Lin, Hsiu-Kuan Lin, I-Hsuan Lin, Yu-Wei Chiou, Horn-Wei Chen, Ching-Yi Liu, Hans I-Chen Harn, Wen-Tai Chiu, Yang-Kao Wang, Meng-Ru Shen, and Ming-Jer Tang, “Mechanical phenotype of cancer cells: cell softening and loss of stiffness sensing”, *in*: *Oncotarget* 6.*25* (2015), p. 20946 (cit. on pp. 18, 136, 141, 153).

[66] Alan Hall, “The cytoskeleton and cancer”, *in*: *Cancer and Metastasis Reviews* 28.*1* (2009), pp. 5–14 (cit. on p. 18).

[67] Subra Suresh, “Biomechanics and biophysics of cancer cells”, *in*: *Acta biomaterialia* 3.*4* (2007), pp. 413–438 (cit. on pp. 18, 20, 136, 138).

[68] Sarah E. Cross, Yu-Sheng Jin, Julianne Tondre, Roger Wong, JianYu Rao, and James K. Gimzewski, “AFM-based analysis of human metastatic cancer cells”, *in*: *Nanotechnology* 19.*38* (2008), p. 384003 (cit. on p. 19).

[69] Qingsen Li, Gabriel Y. H. Lee, Choon Nam Ong, and Chwee T. Lim, “AFM indentation study of breast cancer cells”, *in*: *Biochemical and biophysical research communications* 374.*4* (2008), pp. 609–613 (cit. on pp. 19, 136, 141).

[70] Elsa Correia Faria, Nan Ma, Ehsan Gazi, Peter Gardner, Mick Brown, Noel W. Clarke, and Richard D. Snook, “Measurement of elastic properties of prostate cancer cells using AFM”, *in*: *Analyst* 133.*11* (2008), pp. 1498–1500 (cit. on pp. 19, 135).

[71] Shengyuan Yang and Muhammed Taher A. Saif, “MEMS based force sensors for the study of indentation response of single living cells”, *in*: *Sensors and Actuators A: Physical* 135.*1* (2007), pp. 16–22 (cit. on p. 19).

[72] Hardik J. Pandya, Wenjin Chen, Lauri A. Goodell, David J. Foran, and Jaydev P. Desai, “Mechanical phenotyping of breast cancer using MEMS: a method to demarcate benign and cancerous breast tissues”, *in*: *Lab on a Chip* 14.*23* (2014), pp. 4523–4532 (cit. on pp. 19, 136).

[73] Jochen Guck et al., “Optical deformability as an inherent cell marker for testing malignant transformation and metastatic competence”, *in*: *Biophysical journal* 88.*5* (2005), pp. 3689–3698 (cit. on pp. 19, 136, 137, 141).

[74] Torsten W. Remmerbach, Falk Wottawah, Julia Dietrich, Bryan Lincoln, Christian Wittekind, and Jochen Guck, “Oral cancer diagnosis by mechanical phenotyping”, *in*: *Cancer research* 69.*5* (2009), pp. 1728–1732 (cit. on p. 19).

[75] Barbara Haley and Eugene Frenkel, “Nanoparticles for drug delivery in cancer treatment”, *in*: *Urologic Oncology: Seminars and original investigations*, vol. 26, 1, Elsevier, 2008, pp. 57–64 (cit. on pp. 19, 140).

[76] Joe Chin-Hun Kuo, Jay G. Gandhi, Roseanna N. Zia, and Matthew J. Paszek, “Physical biology of the cancer cell glycocalyx”, *in*: *Nature Physics* 14.*7* (2018), pp. 658–669 (cit. on pp. 19, 139, 140).

[77] Nicolett Kanyo, Kinga Dora Kovacs, Andras Saftics, Inna Szekacs, Beatrix Peter, Ana R. Santa-Maria, Fruzsina R. Walter, András Dér, Mária A. Deli, and Robert Horvath, “Glycocalyx regulates the strength and kinetics of cancer cell adhesion revealed by biophysical models based on high resolution label-free optical data”, *in*: *Scientific reports* 10.*1* (2020), pp. 1–20 (cit. on p. 19).

[78] Irene Canton and Giuseppe Battaglia, “Endocytosis at the nanoscale”, *in*: *Chemical Society Reviews* 41.*7* (2012), pp. 2718–2739 (cit. on p. 19).

[79] Tina Wiegand, Marta Fratini, Felix Frey, Klaus Yserentant, Yang Liu, Eva Weber, Kornelia Galior, Julia Ohmes, Felix Braun, Dirk-Peter Herten, et al., “Forces during cellular uptake of viruses and nanoparticles at the ventral side”, *in*: *Nature communications* 11.*1* (2020), pp. 1–13 (cit. on p. 19).

[80] Anna Francesca Rigato, “Characterization of cell mechanics with atomic force microscopy: Mechanical mapping and high-speed microrheology”, PhD thesis, Aix-Marseille, 2015 (cit. on p. 20).

[81] Jaspreet K. Vasir and Vinod Labhasetwar, “Quantification of the force of nanoparticle-cell membrane interactions and its influence on intracellular trafficking of nanoparticles”, *in*: *Biomaterials* 29.*31* (2008), pp. 4244–4252 (cit. on p. 20).

[82] Yeh-Shiu Chu, Sylvie Dufour, Jean Paul Thiery, Eric Perez, and Frederic Pincet, “Johnson-Kendall-Roberts theory applied to living cells”, *in*: *Physical review letters* 94.*2* (2005), p. 028102 (cit. on pp. 20, 138, 139, 141).

[83] Evan Evans and David Needham, “Physical properties of surfactant bilayer membranes: thermal transitions, elasticity, rigidity, cohesion and colloidal interactions”, *in*: *Journal of Physical Chemistry* 91.*16* (1987), pp. 4219–4228 (cit. on p. 20).

[84] Michael P. Allen, “Introduction to molecular dynamics simulation”, *in*: *Computational soft matter: from synthetic polymers to proteins* 23.*1* (2004), pp. 1–28 (cit. on pp. 20, 194).

[85] Xin Yi, Xinghua Shi, and Huajian Gao, “A universal law for cell uptake of one-dimensional nanomaterials”, *in*: *Nano letters* 14.*2* (2014), pp. 1049–1055 (cit. on pp. 20, 21, 81, 194).

[86] Hong-ming Ding and Yu-Qiang Ma, “Theoretical and computational investigations of nanoparticle–biomembrane interactions in cellular delivery”, *in*: *Small* 11.*9-10* (2015), pp. 1055–1071 (cit. on pp. 20, 152, 194).

[87] Eric J. Spangler, Sudhir Upreti, and Mohamed Laradji, “Partial wrapping and spontaneous endocytosis of spherical nanoparticles by tensionless lipid membranes”, *in*: *The Journal of chemical physics* 144.*4* (2016), p. 044901 (cit. on pp. 20, 194).

[88] Changjin Huang, Yao Zhang, Hongyan Yuan, Huajian Gao, and Sulin Zhang, “Role of nanoparticle geometry in endocytosis: laying down to stand up”, *in*: *Nano letters* 13.*9* (2013), pp. 4546–4550 (cit. on pp. 20, 21, 27, 46, 194).

[89] Sergey Pogodin and Vladimir A. Baulin, “Equilibrium insertion of nanoscale objects into phospholipid bilayers”, *in*: *Current Nanoscience* 7.*5* (2011), pp. 721–726 (cit. on pp. 20, 194).

[90] Robert Vácha, Francisco J. Martinez-Veracoechea, and Daan Frenkel, “Intracellular release of endocytosed nanoparticles upon a change of ligand–receptor interaction”, *in*: *ACS nano* 6.*12* (2012), pp. 10598–10605 (cit. on pp. 20, 152).

[91] Kai Yang and Yu-Qiang Ma, “Computer simulation of the translocation of nanoparticles with different shapes across a lipid bilayer”, *in*: *Nature nanotechnology* 5.*8* (2010), pp. 579–583 (cit. on p. 20).

[92] Robert Vácha, Francisco J. Martinez-Veracoechea, and Daan Frenkel, “Receptor-mediated endocytosis of nanoparticles of various shapes”, *in*: *Nano letters* 11.*12* (2011), pp. 5391–5395 (cit. on p. 21).

[93] Inna Ermilova, “Modeling of biomembranes: from computational toxicology to simulations of neurodegenerative diseases”, PhD thesis, Department of Materials and Environmental Chemistry, Stockholm University, 2019 (cit. on p. 21).

[94] Hong-ming Ding and Yu-Qiang Ma, “Role of physicochemical properties of coating ligands in receptor-mediated endocytosis of nanoparticles”, *in*: *Biomaterials* 33.*23* (2012), pp. 5798–5802 (cit. on pp. 21, 194).

[95] Udo Seifert and Reinhard Lipowsky, “Adhesion of vesicles”, *in*: *Physical Review A* 42.*8* (1990), pp. 4768–4771 (cit. on pp. 22, 25, 26, 195).

[96] Udo Seifert, “Adhesion of vesicles in two dimensions”, *in*: *Physical Review A* 43.*12* (1991), pp. 6803–6814 (cit. on pp. 22, 195).

[97] Markus Deserno and Thomas Bickel, “Wrapping of a spherical colloid by a fluid membrane”, *in*: *EPL (EuroPhysics Letters)* 62.*5* (2003), pp. 767–773 (cit. on pp. 22, 28, 43, 195).

[98] Markus Deserno, “Elastic deformation of a fluid membrane upon colloid binding”, *in*: *Physical Review E* 69.*3* (2004), p. 031903 (cit. on pp. 22, 28, 43, 44, 195).

[99] Xiao-Hua Zhou, Jian-Lin Liu, and Sheng-Li Zhang, “Adhesion of a vesicle on an elastic substrate: 2D analysis”, *in*: *Colloids and Surfaces B: Biointerfaces* 110 (2013), pp. 372–378 (cit. on pp. 22, 28, 42, 44, 45).

[100] Carmel Majidi and Kai-tak Wan, “Adhesion between thin cylindrical shells with parallel axes”, *in*: (2010) (cit. on p. 22).

[101] Ling Miao, Udo Seifert, Michael Wortis, and Hans-Günther Döbereiner, “Budding transitions of fluid-bilayer vesicles: The effect of area-difference elasticity”, *in*: *Physical Review E* 49.*6* (1994), pp. 5389–5410 (cit. on p. 22).

[102] Sovan Das and Qiang Du, “Adhesion of vesicles to curved substrates”, *in*: *Physical Review E* 77.*1* (2008), p. 011907 (cit. on pp. 22, 25, 26).

[103] Wojciech T. Góźdź, “Deformations of lipid vesicles induced by attached spherical particles”, *in*: *Langmuir* 23.*10* (2007), pp. 5665–5669 (cit. on p. 22).

[104] Xin Yi and Huajian Gao, “Cell membrane wrapping of a spherical thin elastic shell”, *in*: *Soft Matter* 11.*6* (2015), pp. 1107–1115 (cit. on pp. 22, 41).

[105] Xi Yi and Huajian Gao, “Phase diagrams and morphological evolution in wrapping of rod-shaped elastic nanoparticles by cell membrane: a two-dimensional study”, *in*: *Physical Review E* 89.*6* (2014), p. 062712 (cit. on pp. 22, 28, 40, 44, 46, 81).

[106] Paolo Decuzzi and Mauro Ferrari, “The receptor-mediated endocytosis of non-spherical particles”, *in*: *Biophysical journal* 94.*10* (2008), pp. 3790–3797 (cit. on pp. 22, 47, 81, 87).

[107] Wendong Shi, Xi Qiao Feng, and Huajian Gao, “Two-dimensional model of vesicle adhesion on curved substrates”, *in*: *Acta Mechanica Sinica* 22.*6* (2006), pp. 529–535 (cit. on p. 22).

[108] Yudie Zhang, Long Li, and Jizeng Wang, “Wrapping of a vesicle nanoparticle with variable bending stiffness by membrane”, *in*: *Journal of the Mechanics and Physics of Solids* (2022), p. 104991 (cit. on pp. 22, 149).

[109] Gaetano Napoli and Alain Goriely, “Elastocytosis”, *in*: *Journal of the Mechanics and Physics of Solids* 145 (2020), p. 104133 (cit. on pp. 22, 28).

[110] Christian Dietrich, Miglena Angelova, and Bernard Pouligny, “Adhesion of latex spheres to giant phospholipid vesicles: statics and dynamics”, *in*: *Journal de Physique II* 7.*11* (1997), pp. 1651–1682 (cit. on pp. 25, 26, 41, 44, 139, 141).

[111] Christine Vauthier and Kawthar Bouchemal, “Methods for the preparation and manufacture of polymeric nanoparticles”, *in*: *Pharmaceutical research* 26.*5* (2009), pp. 1025–1058 (cit. on pp. 27, 65).

[112] Gang Bao and Subra Suresh, “Cell and molecular mechanics of biological materials”, *in*: *Nature materials* 2.*11* (2003), pp. 715–725 (cit. on pp. 27, 47, 81).

[113] Izrail Moiseevitch Gelfand, Richard A Silverman, et al., *Calculus of variations*, Courier Corporation, 2000 (cit. on p. 32).

[114] Markus Deserno, Martin Michael Müller, and Jemal Guven, “Contact lines for fluid surface adhesion”, *in*: *Physical Review E* 76.*1* (2007), p. 011605 (cit. on p. 36).

[115] Pierre-Gilles De Gennes, Françoise Brochard-Wyart, David Quéré, et al., *Capillarity and wetting phenomena: drops, bubbles, pearls, waves*, vol. 315, Springer, 2004 (cit. on p. 36).

[116] Ferdinand Verhulst, *Nonlinear differential equations and dynamical systems*, Springer Science & Business Media, 2006 (cit. on p. 37).

[117] Richard L. Burden, J. Douglas Faires, and Annette M. Burden, *Numerical analysis*, Cengage learning, 2015 (cit. on p. 37).

[118] John C. Strikwerda, *Finite difference schemes and partial differential equations*, SIAM, 2004 (cit. on pp. 37, 38).

[119] Martin Michael Müller, Markus Deserno, and Jemal Guven, "Balancing torques in membrane-mediated interactions: exact results and numerical illustrations", *in*: *Physical Review E* 76.*1* (2007), p. 011921 (cit. on p. 39).

[120] Joachim O. Rädler, Toni J. Feder, Helmut H. Strey, and Erich Sackmann, "Fluctuation analysis of tension-controlled undulation forces between giant vesicles and solid substrates", *in*: *Physical Review E* 51.*5* (1995), pp. 4526–4537 (cit. on pp. 41, 86).

[121] Huajian Gao, Wendong Shi, and Lambert B. Freund, "Mechanics of receptor-mediated endocytosis", *in*: *Proceedings of the National Academy of Sciences* 102.*27* (2005), pp. 9469–9474 (cit. on p. 41).

[122] Pei-Hsun Wu et al., "A comparison of methods to assess cell mechanical properties", *in*: *Nature methods* 15.*7* (2018), pp. 491–498 (cit. on p. 44).

[123] Zhibing Zhang, Mohamed Al-Rubeai, and C. R. Thomas, "Effect of Pluronic F-68 on the mechanical properties of mammalian cells", *in*: *Enzyme and microbial technology* 14.*12* (1992), pp. 980–983 (cit. on p. 44).

[124] Udo Seifert, "Configurations of fluid membranes and vesicles", *in*: *Advances in physics* 46.*1* (1997), pp. 13–137 (cit. on p. 44).

[125] Weidong Zhao, Yongmei Tian, Mingjun Cai, Feng Wang, Jiazhen Wu, Jing Gao, Shuheng Liu, Junguang Jiang, Shibo Jiang, and Hongda Wang, "Studying the nucleated mammalian cell membrane by single molecule approaches", *in*: *PLoS One* 9.*5* (2014), e91595 (cit. on p. 46).

[126] M. Ambrose E. J. Abercrombie, "The surface properties of cancer cells: a review", *in*: *Cancer research* 22.*5 Part 1* (1962), pp. 525–548 (cit. on p. 47).

[127] John A. Allen, Robyn A. Halverson-Tamboli, and Mark M. Rasenick, “Lipid raft microdomains and neurotransmitter signalling”, *in*: *Nature reviews neuroscience* 8.*2* (2007), pp. 128–140 (cit. on p. 47).

[128] Yudie Zhang, Long Li, and Jizeng Wang, “Wrapping of a vesicle nanoparticle with variable bending stiffness by membrane”, *in*: *Journal of the Mechanics and Physics of Solids* (2022), p. 104991 (cit. on p. 47).

[129] James F. Hainfeld, F. Avraham Dilmanian, Daniel N. Slatkin, and Henry M. Smilowitz, “Radiotherapy enhancement with gold nanoparticles”, *in*: *Journal of pharmacy and pharmacology* 60.*8* (2008), pp. 977–985 (cit. on p. 47).

[130] Adrien Faucon, Houda Benhelli-Mokrani, Luis A. Córdova, Bénédicte Brulin, Dominique Heymann, Philippe Hulin, Steven Nedellec, and Eléna Ishow, “Are fluorescent organic nanoparticles relevant tools for tracking cancer cells or macrophages?”, *in*: *Advanced healthcare materials* 4.*17* (2015), pp. 2727–2734 (cit. on p. 47).

[131] Svetlana Gelperina, Kevin Kisich, Michael D. Iseman, and Leonid Heifets, “The potential advantages of nanoparticle drug delivery systems in chemotherapy of tuberculosis”, *in*: *American journal of respiratory and critical care medicine* 172.*12* (2005), pp. 1487–1490 (cit. on p. 47).

[132] Frank Alexis, Eric Pridgen, Linda K. Molnar, and Omid C. Farokhzad, “Factors affecting the clearance and biodistribution of polymeric nanoparticles”, *in*: *Molecular pharmaceutics* 5.*4* (2008), pp. 505–515 (cit. on p. 47).

[133] Weisheng Lin, Yue-wern Huang, Xiao-Dong Zhou, and Yinfa Ma, “In vitro toxicity of silica nanoparticles in human lung cancer cells”, *in*: *Toxicology and applied pharmacology* 217.*3* (2006), pp. 252–259 (cit. on p. 47).

[134] Margarita Staykova, Marino Arroyo, Mohammad Rahimi, and Howard A. Stone, “Confined bilayers passively regulate shape and stress”, *in*: *Physical review letters* 110.*2* (2013), p. 028101 (cit. on pp. 47, 81, 86).

[135] Xin Yi and Huajian Gao, “Kinetics of receptor-mediated endocytosis of elastic nanoparticles”, *in*: *Nanoscale* 9.*1* (2017), pp. 454–463 (cit. on pp. 47, 81, 87, 197).

[136] Hongyan Yuan, Ju Li, Gang Bao, and Sulin Zhang, “Variable nanoparticle-cell adhesion strength regulates cellular uptake”, *in*: *Physical review letters* 105.*13* (2010), p. 138101 (cit. on pp. 47, 81).

[137] Hiroshi Noguchi and Masako Takasu, “Adhesion of nanoparticles to vesicles: a Brownian dynamics simulation”, *in*: *Biophysical journal* 83.*1* (2002), pp. 299–308 (cit. on pp. 47, 81).

[138] Anita Joanna Kosmalska et al., “Physical principles of membrane remodelling during cell mechanoadaptation”, *in*: *Nature communications* 6.*1* (2015), pp. 1–11 (cit. on pp. 47, 81, 86).

[139] Lambert B. Freund and Yuan Lin, “The role of binder mobility in spontaneous adhesive contact and implications for cell adhesion”, *in*: *Journal of the Mechanics and Physics of Solids* 52.*11* (2004), pp. 2455–2472 (cit. on pp. 47, 81, 87, 197).

[140] Bin Chen, “Probing the effect of random adhesion energy on receptor-mediated endocytosis with a semistochastic model”, *in*: *Journal of Applied Mechanics* 81.*8* (2014) (cit. on pp. 47, 81).

[141] Sarah Iaquinta, Shahram Khazaie, Éléna Ishow, Christophe Blanquart, Sylvain Fréour, and Frédéric Jacquemin, “Influence of the mechanical and geometrical parameters on the cellular uptake of nanoparticles: a stochastic approach”, *in*: *International Journal for Numerical Methods in Biomedical Engineering* (2022), e3598 (cit. on p. 51).

[142] Bertrand Iooss and Paul Lemaıtre, “A review on global sensitivity analysis methods”, *in*: *Uncertainty management in simulation-optimization of complex systems*, Springer, 2015, pp. 101–122 (cit. on pp. 52, 53, 198).

[143] H. Christopher Frey and Sumeet R. Patil, “Identification and review of sensitivity analysis methods”, *in*: *Risk analysis* 22.*3* (2002), pp. 553–578 (cit. on p. 52).

[144] M. Fasihul Alam and Andrew Briggs, “Artificial neural network metamodel for sensitivity analysis in a total hip replacement health economic model”, *in*: *Expert Review of Pharmacoeconomics & Outcomes Research* 20.*6* (2020), pp. 629–640 (cit. on p. 52).

[145] Mehdi Ghorbanzadeh, Mohammad H. Fatemi, and Masoumeh Karimpour, “Modeling the cellular uptake of magnetofluorescent nanoparticles in pancreatic cancer cells: a quantitative structure activity relationship study”, *in*: *Industrial & engineering chemistry research* 51.*32* (2012), pp. 10712–10718 (cit. on p. 52).

[146] Jérôme Morio, “Global and local sensitivity analysis methods for a physical system”, *in*: *European journal of physics* 32.*6* (2011), pp. 1577–1588 (cit. on p. 52).

[147] Matthieu Petelet, “Analyse de sensibilité globale de modeles thermomécaniques de simulation numérique du soudage”, PhD thesis, Dijon, 2007 (cit. on p. 52).

[148] Andrea Saltelli, Marco Ratto, Terry Andres, Francesca Campolongo, Jessica Cariboni, Debora Gatelli, Michaela Saisana, and Stefano Tarantola, *Global sensitivity analysis: the primer*, John Wiley & Sons, 2008 (cit. on p. 52).

[149] Andrea Saltelli, Stefano Tarantola, Francesca Campolongo, and Marco Ratto, *Sensitivity analysis in practice: a guide to assessing scientific models*, vol. 1, Wiley Online Library, 2004 (cit. on pp. 52, 157, 158).

[150] Karen Chan, Andrea Saltelli, and Marian Scott, *Sensitivity analysis*, Wiley, 2000 (cit. on p. 52).

[151] Etienne de Rocquigny, Nicolas Devictor, and Stefano Tarantola, *Uncertainty in industrial practice: a guide to quantitative uncertainty management*, John Wiley & Sons, 2008 (cit. on p. 53).

[152] Stefano Marelli, C. Lamas, Katerina Konakli, Charilaos Mylonas, Philippe Wiederkehr, and Bruno Sudret, *UQLab user manual – Sensitivity analysis*, tech. rep., Report # UQLab-V1.4-106, Chair of Risk, Safety and Uncertainty Quantification, ETH Zurich, Switzerland, 2021 (cit. on pp. 54, 55, 58, 159).

[153] Ilya M. Sobol, “Sensitivity analysis for non-linear mathematical models”, *in*: *Mathematical modelling and computational experiment* 1 (1993), pp. 407–414 (cit. on p. 54).

[154] Andrea Saltelli, “Making best use of model evaluations to compute sensitivity indices”, *in*: *Computer physics communications* 145.*2* (2002), pp. 280–297 (cit. on p. 55).

[155] Stefano Tarantola, D. Gatelli, S. S. Kucherenko, Wolfgang Mauntz, et al., “Estimating the approximation error when fixing unessential factors in global sensitivity analysis”, *in*: *Reliability engineering & system safety* 92.*7* (2007), pp. 957–960 (cit. on pp. 55, 157, 158).

[156] Jean-Marc Martinez, “Analyse de sensibilité globale par décomposition de la variance”, *in*: *Presentation in “Journée des GdR Ondes & Mascot* 13 (2011) (cit. on pp. 55, 157, 159).

[157] Michiel J. W. Jansen, “Analysis of variance designs for model output”, *in*: *Computer Physics Communications* 117.*1-2* (1999), pp. 35–43 (cit. on pp. 55, 157, 158).

[158] Michaël Baudin, Anne Dutfoy, Bertrand Iooss, and Anne-Laure Popelin, “OpenTURNS: An Industrial Software for Uncertainty Quantification in Simulation”, *in*: *Handbook of Uncertainty Quantification*, ed. by Roger Ghanem, David Higdon, and Houman Owhadi, Cham: Springer International Publishing, 2016, pp. 1–38, ISBN: 978-3-319-11259-6, DOI: `10.1007/978-3-319-11259-6_64-1` (cit. on pp. 55, 57, 58, 157).

[159] Takuya Iwanaga, William Usher, and Jonathan Herman, “Toward SALib 2.0: Advancing the accessibility and interpretability of global sensitivity analyses”, *in*: *Socio-Environmental Systems Modelling* 4 (May 2022), p. 18155, DOI: `10.18174/sesmo.18155` (cit. on pp. 55, 160).

[160] Jon Herman and Will Usher, “SALib: An open-source Python library for Sensitivity Analysis”, *in*: *The Journal of Open Source Software* 2.*9* (Jan. 2017), DOI: `10.21105/joss.00097` (cit. on p. 55).

[161] Bruno Sudret, “Global sensitivity analysis using polynomial chaos expansions”, *in*: *Reliability engineering & system safety* 93.*7* (2008), pp. 964–979 (cit. on pp. 55, 58).

[162] Peter A. Vanrolleghem, Giorgio Mannina, Alida Cosenza, and Marc B. Neumann, “Global sensitivity analysis for urban water quality modelling: Terminology, convergence and comparison of different methods”, *in*: *Journal of Hydrology* 522 (2015), pp. 339–352 (cit. on p. 55).

[163] J. D. Herman, J. B. Kollat, P. M. Reed, and Thorsten Wagener, “Method of Morris effectively reduces the computational demands of global sensitivity analysis for distributed watershed models”, *in*: *Hydrology and Earth System Sciences* 17.*7* (2013), pp. 2893–2903 (cit. on p. 55).

[164] Fanny Sarrazin, Francesca Pianosi, and Thorsten Wagener, “Global Sensitivity Analysis of environmental models: Convergence and validation”, *in*: *Environmental Modelling & Software* 79 (2016), pp. 135–152 (cit. on pp. 55, 76, 77, 190).

[165] G. Gary Wang and Songqing Shan, “Review of metamodeling techniques in support of engineering design optimization”, *in*: *International Design Engineering Technical Conferences and Computers and Information in Engineering Conference*, vol. 4255, 2006, pp. 415–426 (cit. on p. 56).

[166] Bertrand Iooss, Loıc Boussouf, Vincent Feuillard, and Amandine Marrel, “Numerical studies of the metamodel fitting and validation processes”, *in*: *arXiv preprint arXiv:1001.1049* (2010) (cit. on pp. 56, 62).

[167] Manolis Papadrakakis, Nikos D. Lagaros, and Yiannis Tsompanakis, “Structural optimization using evolution strategies and neural networks”, *in*: *Computer methods in applied mechanics and engineering* 156.*1-4* (1998), pp. 309–333 (cit. on p. 56).

[168] Noel Cressie, “The origins of kriging”, *in*: *Mathematical geology* 22.*3* (1990), pp. 239–252 (cit. on p. 56).

[169] Jerome Sacks, William J. Welch, Toby J. Mitchell, and Henry P. Wynn, “Design and analysis of computer experiments”, *in*: *Statistical science* (1989), pp. 409–423 (cit. on p. 56).

[170] Michael L. Stein, *Interpolation of spatial data: some theory for kriging*, Springer Science & Business Media, 2012 (cit. on p. 56).

[171] Thomas J. Santner, Brian J. Williams, and William I. Notz, *The design and analysis of computer experiments*, Springer Science & Business Media, 2013 (cit. on p. 56).

[172] Carl Edward Rasmussen, “Gaussian processes in machine learning”, *in*: *Advanced lectures on machine learning*, Springer, 2004, pp. 63–71 (cit. on p. 56).

[173] Matthias De Lozzo and Amandine Marrel, “Estimation of the derivative-based global sensitivity measures using a Gaussian process metamodel”, *in*: *SIAM/ASA Journal on Uncertainty Quantification* 4.*1* (2016), pp. 708–738 (cit. on p. 56).

[174] Amandine Marrel, Bertrand Iooss, François Van Dorpe, and Elena Volkova, “An efficient methodology for modeling complex computer codes with Gaussian processes”, *in*: *Computational Statistics & Data Analysis* 52.*10* (2008), pp. 4731–4744 (cit. on p. 56).

[175] Roger G. Ghanem and Pol D. Spanos, *Stochastic finite elements: a spectral approach*, Dover publications, 2003 (cit. on p. 56).

[176] Seung-Kyum Choi, Ramana V. Grandhi, Robert A. Canfield, and Chris L. Pettit, “Polynomial chaos expansion with Latin hypercube sampling for estimating response variability”, *in*: *American Institute of Aeronautics and Astronautics* 42.*6* (2004), pp. 1191–1198 (cit. on p. 56).

[177] Marc Berveiller, Bruno Sudret, and Maurice Lemaire, “Stochastic finite element: a non intrusive approach by regression”, *in*: *European Journal of Computational Mechanics/Revue Européenne de Mécanique Numérique* 15.*1-3* (2006), pp. 81–92 (cit. on p. 56).

[178] Bruno Sudret, “Global sensitivity analysis using polynomial chaos expansions”, *in*: *Reliability Engineering & System Safety* 93.*7* (2008), pp. 964–979 (cit. on pp. 56, 58, 97).

[179] Ruichen Jin, Wei Chen, and Timothy W. Simpson, “Comparative studies of metamodelling techniques under multiple modelling criteria”, *in*: *Structural and multidisciplinary optimization* 23.*1* (2001), pp. 1–13 (cit. on p. 56).

[180] András Sobester, Alexander Forrester, and Andy Keane, *Engineering design via surrogate modelling: a practical guide*, John Wiley & Sons, 2008 (cit. on pp. 56, 62).

[181] Shahram Khazaie, Xun Wang, Dimitri Komatitsch, and Pierre Sagaut, “Uncertainty quantification for acoustic wave propagation in a shallow water environment”, *in*: *Wave Motion* 91 (2019), p. 102390 (cit. on p. 57).

[182] Roger G. Ghanem and Pol D. Spanos, “Stochastic Finite Element Method: Response Statistics”, *in*: *Stochastic finite elements: a spectral approach*, Springer, 1991, pp. 101–119 (cit. on p. 57).

[183] Olivier Le Maitre and Omar M. Knio, *Spectral methods for uncertainty quantification: with applications to computational fluid dynamics*, Springer Science & Business Media, 2010 (cit. on p. 57).

[184] Eric Savin and Beatrice Faverjon, “Computation of higher-order moments of generalized polynomial chaos expansions”, *in*: *International Journal for Numerical Methods in Engineering* 111.*12* (2017), pp. 1192–1200 (cit. on p. 57).

[185] Andrea Saltelli, Paola Annoni, Ivano Azzini, Francesca Campolongo, Marco Ratto, and Stefano Tarantola, "Variance based sensitivity analysis of model output. Design and estimator for the total sensitivity index", *in*: *Computer physics communications* 181.*2* (2010), pp. 259–270 (cit. on p. 58).

[186] Fabian Pedregosa et al., "Scikit-learn: Machine Learning in Python", *in*: *Journal of Machine Learning Research* 12 (2011), pp. 2825–2830 (cit. on pp. 58–60).

[187] V. Gholami, J. Torkaman, and P. Dalir, "Simulation of precipitation time series using tree-rings, earlywood vessel features, and artificial neural network", *in*: *Theoretical and Applied Climatology* 137.*3* (2019), pp. 1939–1948 (cit. on p. 59).

[188] Ron Kohavi, "A study of cross-validation and bootstrap for accuracy estimation and model selection", *in*: *Ijcai*, vol. 14, 2, Montreal, Canada, 1995, pp. 1137–1145 (cit. on p. 60).

[189] Gareth James, Daniela Witten, Trevor Hastie, and Robert Tibshirani, *An introduction to statistical learning*, vol. 112, Springer, 2013 (cit. on p. 60).

[190] Geraud Blatman and Bruno Sudret, "An adaptive algorithm to build up sparse polynomial chaos expansions for stochastic finite element analysis", *in*: *Probabilistic Engineering Mechanics* 25.*2* (2010), pp. 183–197 (cit. on p. 60).

[191] Jessica Franco, "Planification d'expériences numériques en phase exploratoire pour la simulation des phénomènes complexes", PhD thesis, Ecole Nationale Supérieure des Mines de Saint-Etienne, 2008 (cit. on pp. 62, 63).

[192] Michael D. McKay, Richard J. Beckman, and William J. Conover, "A comparison of three methods for selecting values of input variables in the analysis of output from a computer code", *in*: *Technometrics* 42.*1* (2000), pp. 55–61 (cit. on p. 62).

[193] Christiane Lemieux, *Monte Carlo and quasi Monte Carlo sampling*, Springer-Verlag New York, 2009 (cit. on p. 63).

[194] Harald Niederreiter, "Low-discrepancy and low-dispersion sequences", *in*: *Journal of number theory* 30.*1* (1988), pp. 51–70 (cit. on p. 63).

[195] Amith Singhee and Rob A. Rutenbar, "Why quasi-Monte Carlo is better than Monte Carlo or Latin hypercube sampling for statistical circuit analysis", *in*: *IEEE Transactions on Computer-Aided Design of Integrated Circuits and Systems* 29.*11* (2010), pp. 1763–1776 (cit. on pp. 63, 64).

[196] Bruno Tuffin, “On the use of low discrepancy sequences in Monte Carlo methods”, *in*: *Monte Carlo Methods and Appl.* 2.*4* (1996), pp. 195–320 (cit. on p. 63).

[197] Ladislav Kocis and William J. Whiten, “Computational investigations of low-discrepancy sequences”, *in*: *ACM Transactions on Mathematical Software (TOMS)* 23.*2* (1997), pp. 266–294 (cit. on p. 63).

[198] Hongmei Chi, Michael Mascagni, and Tony Warnock, “On the optimal Halton sequence”, *in*: *Mathematics and computers in simulation* 70.*1* (2005), pp. 9–21 (cit. on p. 63).

[199] Sebastian Burhenne, Dirk Jacob, and Gregor P. Henze, “Sampling based on Sobol’sequences for Monte Carlo techniques applied to building simulations”, *in*: *Proc. Int. Conf. Build. Simulat*, 2011, pp. 1816–1823 (cit. on p. 63).

[200] Paul Bratley and Bennett L. Fox, “Algorithm 659: Implementing Sobol’s quasirandom sequence generator”, *in*: *ACM Transactions on Mathematical Software (TOMS)* 14.*1* (1988), pp. 88–100 (cit. on p. 63).

[201] Henri Faure and Christiane Lemieux, “Generalized Halton sequences in 2008: A comparative study”, *in*: *ACM Transactions on Modeling and Computer Simulation (TOMACS)* 19.*4* (2009), pp. 1–31 (cit. on p. 63).

[202] Sergei Kucherenko, Daniel Albrecht, and Andrea Saltelli, “Exploring multi-dimensional spaces: A comparison of Latin hypercube and quasi Monte Carlo sampling techniques”, *in*: *arXiv preprint arXiv:1505.02350* (2015) (cit. on p. 64).

[203] E. T. Jaynes, “Information theory and statistical mechanics”, *in*: *Physical review* 106.*4* (1957), p. 620 (cit. on pp. 69, 94, 98, 105).

[204] Zexin Liu and Akil Narayan, “A Stieltjes algorithm for generating multivariate orthogonal polynomials”, *in*: *arXiv preprint arXiv:2202.04843* (2022) (cit. on p. 74).

[205] Arnida, Margit M. Janát-Amsbury, Abhijit Ray, C. Matthew Peterson, and Hamid Ghandehari, “Geometry and surface characteristics of gold nanoparticles influence their biodistribution and uptake by macrophages”, *in*: *European Journal of Pharmaceutics and Biopharmaceutics* 77.*3* (2011), pp. 417–423 (cit. on p. 80).

[206] Luke S. S. Guo, “Amphotericin B colloidal dispersion: an improved antifungal therapy”, *in*: *Advanced drug delivery reviews* 47.*2-3* (2001), pp. 149–163 (cit. on p. 80).

[207] Malika Larabi, Vanessa Yardley, Philippe M. Loiseau, Martine Appel, Philippe Legrand, Annette Gulik, Christian Bories, Simon L. Croft, and Gillian Barratt, “Toxicity and antileishmanial activity of a new stable lipid suspension of amphotericin B”, *in*: *Antimicrobial agents and chemotherapy* 47.*12* (2003), pp. 3774–3779 (cit. on p. 80).

[208] Calum J. Drummond and Celesta Fong, “Surfactant self-assembly objects as novel drug delivery vehicles”, *in*: *Current opinion in colloid & interface science* 4.*6* (1999), pp. 449–456 (cit. on p. 80).

[209] Kai Simons and Winchil L. C. Vaz, “Model systems, lipid rafts, and cell membranes”, *in*: *Annu. Rev. Biophys. Biomol. Struct.* 33 (2004), pp. 269–295 (cit. on p. 80).

[210] Linda J. Pike, “The challenge of lipid rafts”, *in*: *Journal of lipid research* 50 (2009), S323–S328 (cit. on p. 80).

[211] Xinghua Shi, Annette von Dem Bussche, Robert H Hurt, Agnes B Kane, and Huajian Gao, “Cell entry of one-dimensional nanomaterials occurs by tip recognition and rotation”, *in*: *Nature nanotechnology* 6.*11* (2011), pp. 714–719 (cit. on p. 81).

[212] Amir Houshang Bahrami, “Orientational changes and impaired internalization of ellipsoidal nanoparticles by vesicle membranes”, *in*: *Soft Matter* 9.*36* (2013), pp. 8642–8646 (cit. on p. 81).

[213] Sabyasachi Dasgupta, Thorsten Auth, and Gerhard Gompper, “Shape and orientation matter for the cellular uptake of nonspherical particles”, *in*: *Nano letters* 14.*2* (2014), pp. 687–693 (cit. on p. 81).

[214] Areski Cousin, Alexandre Janon, Véronique Maume-Deschamps, and Ibrahima Niang, “On the consistency of Sobol indices with respect to stochastic ordering of model parameters”, *in*: *ESAIM: Probability and Statistics* 23 (2019), pp. 387–408 (cit. on pp. 83, 110, 150).

[215] Sarah Iaquinta, Shahram Khazaie, Sylvain Fréour, and Frédéric Jacquemin, “Prise en compte de l’adaptation mécanique de la cellule lors de l’enveloppement de nanoparticules”, *in*: *15ème colloque national en calcul des structures*, 2022 (cit. on p. 83).

[216] Sarah Iaquinta, Shahram Khazaie, Sylvain Fréour, and Frédéric Jacquemin, "An enhanced numerical model for the cellular uptake of random nanoparticles with membrane's mechano-adaptation", *in*: *International Journal for Numerical Methods in Biomedical Engineering* (202x), p. xx (cit. on p. 85).

[217] Sarah Iaquinta, Shahram Khazaie, Sylvain Fréour, and Frédéric Jacquemin, "Influence of the cell's reaction during the uptake of nanoparticles", *in*: *18th European Mechanics of Materials Conference*, 2022 (cit. on p. 85).

[218] Sarah Iaquinta, Shahram Khazaie, Éléna Ishow, Christophe Blanquart, Sylvain Fréour, and Frédéric Jacquemin, "Prise en compte de l'adaptation mécanique de la cellule lors de l'enveloppement de nanoparticules", *in*: *15ème Journées du Cancéropôle Grand Ouest*, 2021 (cit. on p. 85).

[219] Joshua P. Ferguson, Scott D. Huber, Nathan M. Willy, Esra Aygün, Sevde Goker, Tugba Atabey, and Comert Kural, "Mechanoregulation of clathrin-mediated endocytosis", *in*: *Journal of cell science* 130.*21* (2017), pp. 3631–3636 (cit. on p. 86).

[220] Bidisha Sinha et al., "Cells respond to mechanical stress by rapid disassembly of caveolae", *in*: *Cell* 144.*3* (2011), pp. 402–413 (cit. on p. 86).

[221] Renshuai Zhang, Xiaofei Qin, Fandong Kong, Pengwei Chen, and Guojun Pan, "Improving cellular uptake of therapeutic entities through interaction with components of cell membrane", *in*: *Drug Delivery* 26.*1* (2019), pp. 328–342 (cit. on p. 87).

[222] Mattia Serpelloni, Matteo Arricca, Claudia Bonanno, and Alberto Salvadori, "Modeling cells spreading, motility, and receptors dynamics: a general framework", *in*: *Acta Mechanica Sinica* 37.*6* (2021), pp. 1013–1030 (cit. on pp. 87, 197).

[223] Richard J. Cherry, "Protein mobility in membranes", *in*: *FEBS letters* 55.*1-2* (1975), pp. 1–7 (cit. on p. 87).

[224] Michael McCloskey and Mu-ming Poo, "Protein diffusion in cell membranes: some biological implications", *in*: *International review of cytology* 87 (1984), pp. 19–81 (cit. on p. 87).

[225] Hongyan Yuan, Ju Li, Gang Bao, and Sulin Zhang, "Variable nanoparticle-cell adhesion strength regulates cellular uptake", *in*: *Physical review letters* 105.*13* (2010), p. 138101 (cit. on p. 87).

[226] Geoffrey A. Head and Richard McCarty, "Vagal and sympathetic components of the heart rate range and gain of the baroreceptor-heart rate reflex in conscious rats", *in*: *Journal of the autonomic nervous system* 21.*2-3* (1987), pp. 203–213 (cit. on p. 88).

[227] Patricia K. Dorward, Walter Riedel, Sandra L. Burke, Judith Gipps, and Paul I. Korner, "The renal sympathetic baroreflex in the rabbit. Arterial and cardiac baroreceptor influences, resetting, and effect of anesthesia.", *in*: *Circulation Research* 57.*4* (1985), pp. 618–633 (cit. on p. 88).

[228] James H. Ricketts and Geoffrey A. Head, "A five-parameter logistic equation for investigating asymmetry of curvature in baroreflex studies", *in*: *American Journal of Physiology-Regulatory, Integrative and Comparative Physiology* 277.*2* (1999), R441–R454 (cit. on p. 88).

[229] Hassan Obeid, Alexandre Clément, Sylvain Fréour, Frédéric Jacquemin, and Pascal Casari, "On the identification of the coefficient of moisture expansion of polyamide-6: Accounting differential swelling strains and plasticization", *in*: *Mechanics of Materials* 118 (2018), pp. 1–10 (cit. on p. 88).

[230] Max D. Morris, "Factorial sampling plans for preliminary computational experiments", *in*: *Technometrics* 33.*2* (1991), pp. 161–174 (cit. on p. 91).

[231] Loic Le Gratiet, Claire Cannamela, and Bertrand Iooss, "A Bayesian approach for global sensitivity analysis of (multifidelity) computer codes", *in*: *SIAM/ASA Journal on Uncertainty Quantification* 2.*1* (2014), pp. 336–363 (cit. on p. 109).

[232] Vincent T. DeVita Jr. and Steven A. Rosenberg, "Two hundred years of cancer research", *in*: *New England Journal of Medicine* 366.*23* (2012), pp. 2207–2214 (cit. on p. 133).

[233] Jacques Ferlay, Murielle Colombet, Isabelle Soerjomataram, Donald M. Parkin, Marion Piñeros, Ariana Znaor, and Freddie Bray, "Cancer statistics for the year 2020: An overview", *in*: *International journal of cancer* 149.*4* (2021), pp. 778–789 (cit. on p. 133).

[234] Chris Händel et al., "Cell membrane softening in human breast and cervical cancer cells", *in*: *New Journal of Physics* 17.*8* (2015), p. 083008 (cit. on pp. 134, 137, 141, 142).

[235] David Needham, “Possible role of cell cycle-dependent morphology, geometry, and mechanical properties in tumor cell metastasis”, *in*: *Cell biophysics* 18.*2* (1991), pp. 99–121 (cit. on p. 135).

[236] Matthew J. Paszek and Valerie M. Weaver, “The tension mounts: mechanics meets morphogenesis and malignancy”, *in*: *Journal of mammary gland biology and neoplasia* 9.*4* (2004), pp. 325–342 (cit. on p. 135).

[237] Sanjay Kumar and Valerie M. Weaver, “Mechanics, malignancy, and metastasis: the force journey of a tumor cell”, *in*: *Cancer and Metastasis Reviews* 28.*1* (2009), pp. 113–127 (cit. on p. 135).

[238] Ralph Sinkus, J. Lorenzen, D. Schrader, M. Lorenzen, M. Dargatz, and D. Holz, “High-resolution tensor MR elastography for breast tumour detection”, *in*: *Physics in Medicine & Biology* 45.*6* (2000), pp. 1649–1664 (cit. on p. 135).

[239] Dimitrios Fotiadis, Simon Scheuring, Shirley A. Müller, Andreas Engel, and Daniel J. Müller, “Imaging and manipulation of biological structures with the AFM”, *in*: *Micron* 33.*4* (2002), pp. 385–397 (cit. on p. 135).

[240] Kozaburo Hayashi and Mayumi Iwata, “Stiffness of cancer cells measured with an AFM indentation method”, *in*: *Journal of the mechanical behavior of biomedical materials* 49 (2015), pp. 105–111 (cit. on p. 135).

[241] Małgorzata Lekka, Dorota Gil, Katarzyna Pogoda, Joanna Dulińska-Litewka, Robert Jach, Justyna Gostek, Olesya Klymenko, Szymon Prauzner-Bechcicki, Zbigniew Stachura, Joanna Wiltowska-Zuber, Krysztof Okoń, and Piotr Laidler, “Cancer cell detection in tissue sections using AFM”, *in*: *Archives of biochemistry and biophysics* 518.*2* (2012), pp. 151–156 (cit. on pp. 136, 141).

[242] Kenneth Langstreth Johnson, Kevin Kendall, and A. D. Roberts, “Surface energy and the contact of elastic solids”, *in*: *Proceedings of the royal society of London. A. mathematical and physical sciences* 324.*1558* (1971), pp. 301–313 (cit. on p. 138).

[243] Evan Evans and David Needham, “Attraction between lipid bilayer membranes in concentrated solutions of nonadsorbing polymers: comparison of mean-field theory with measurements of adhesion energy”, *in*: *Macromolecules* 21.*6* (1988), pp. 1822–1831 (cit. on pp. 138, 139, 141).

[244] Marie-Josee Colbert, “A novel approach to measurement of the adhesion strength of a single cell on a substrate”, PhD thesis, McMaster University, 2005 (cit. on pp. 139, 141).

[245] Alexander Buffone and Valerie M. Weaver, “Don’t sugarcoat it: How glycocalyx composition influences cancer progression”, *in*: *Journal of Cell Biology* 219.*1* (2020) (cit. on p. 139).

[246] Deborah Alford and Joyce Taylor-Papadimitriou, “Cell adhesion molecules in the normal and cancerous mammary gland”, *in*: *Journal of mammary gland biology and neoplasia* 1.*2* (1996), pp. 207–218 (cit. on p. 139).

[247] Mirjam C. Boelens, Anke van den Berg, Irma Vogelzang, Jelle Wesseling, Dirkje S. Postma, Wim Timens, and Harry J. M. Groen, “Differential expression and distribution of epithelial adhesion molecules in non-small cell lung cancer and normal bronchus”, *in*: *Journal of clinical pathology* 60.*6* (2007), pp. 608–614 (cit. on p. 139).

[248] J. Louise Jones, D. R. Critchley, and Rosemary A. Walker, “Alteration of stromal protein and integrin expression in breast—a marker of premalignant change?”, *in*: *The Journal of pathology* 167.*4* (1992), pp. 399–406 (cit. on p. 139).

[249] Richard O. Hynes, “Integrins: bidirectional, allosteric signaling machines”, *in*: *cell* 110.*6* (2002), pp. 673–687 (cit. on p. 139).

[250] Ensieh Farahani, Hirak K Patra, Jaganmohan R Jangamreddy, Iran Rashedi, Marta Kawalec, Rama K Rao Pariti, Petros Batakis, and Emilia Wiechec, “Cell adhesion molecules and their relation to (cancer) cell stemness”, *in*: *Carcinogenesis* 35.*4* (2014), pp. 747–759 (cit. on p. 139).

[251] Michael A. Hollingsworth and Benjamin J. Swanson, “Mucins in cancer: protection and control of the cell surface”, *in*: *Nature Reviews Cancer* 4.*1* (2004), pp. 45–60 (cit. on p. 140).

[252] Guang-Kui Xu, Jin Qian, and Jinglei Hu, “The glycocalyx promotes cooperative binding and clustering of adhesion receptors”, *in*: *Soft Matter* 12.*20* (2016), pp. 4572–4583 (cit. on p. 140).

[253] Matthew J. Paszek, Christopher C. DuFort, Olivier Rossier, Russell Bainer, Janna K. Mouw, Kamil Godula, Jason E Hudak, Jonathon N Lakins, Amanda C Wijekoon, Luke Cassereau, et al., “The cancer glycocalyx mechanically primes integrin-mediated growth and survival”, *in*: *Nature* 511.*7509* (2014), pp. 319–325 (cit. on p. 140).

[254] Yudie Zhang, Long Li, and Jizeng Wang, “Role of Ligand Distribution in the Cytoskeleton-Associated Endocytosis of Ellipsoidal Nanoparticles”, *in*: *Membranes* 11.*12* (2021), p. 993 (cit. on p. 149).

[255] Yongjian Ai, Ruoxiao Xie, Jialiang Xiong, and Qionglin Liang, “Microfluidics for biosynthesizing: from droplets and vesicles to artificial cells”, *in*: *Small* 16.*9* (2020), p. 1903940 (cit. on p. 151).

[256] David J. Gavaghan, Jonathan P. Whiteley, S. Jonathan Chapman, J. Michael Brady, and Pras Pathmanathan, “Predicting tumor location by modeling the deformation of the breast”, *in*: *IEEE Transactions on Biomedical Engineering* 55.*10* (2008), pp. 2471–2480 (cit. on p. 151).

[257] Wilbur A. Lam, Michael J. Rosenbluth, and Daniel A. Fletcher, “Chemotherapy exposure increases leukemia cell stiffness”, *in*: *Blood* 109.*8* (2007), pp. 3505–3508 (cit. on p. 152).

[258] Gaurav Sahay, Jong Oh Kim, Alexander V Kabanov, and Tatiana K. Bronich, “The exploitation of differential endocytic pathways in normal and tumor cells in the selective targeting of nanoparticulate chemotherapeutic agents”, *in*: *Biomaterials* 31.*5* (2010), pp. 923–933 (cit. on p. 152).

[259] Art B. Owen, “Variance components and generalized Sobol’indices”, *in*: *SIAM/ASA Journal on Uncertainty Quantification* 1.*1* (2013), pp. 19–41 (cit. on p. 157).

[260] Stefano Marelli and Bruno Sudret, “UQLab: A framework for uncertainty quantification in Matlab”, *in*: *Vulnerability, uncertainty, and risk: quantification, mitigation, and management*, 2014, pp. 2554–2563 (cit. on p. 159).

[261] Alexandre Janon, Thierry Klein, Agnes Lagnoux, Maëlle Nodet, and Clémentine Prieur, “Asymptotic normality and efficiency of two Sobol index estimators”, *in*: *ESAIM: Probability and Statistics* 18 (2014), pp. 342–364 (cit. on p. 159).

[262] Christos Lataniotis, Stefano Marelli, and Bruno Sudret, “UQLab 2.0 and UQCloud: open-source vs. cloud-based uncertainty quantification”, *in*: *SIAM Conference on Uncertainty Quantification (SIAM UQ 2022)*, ETH Zurich, Institute of Structural Engineering, 2022 (cit. on p. 159).

[263] Bertrand Iooss, Alexandre Janon, Gilles Pujol, B. Broto, K Boumhaout, S. Da Veiga, et al., “Sensitivity: global sensitivity analysis of model outputs”, *in*: *R package version* 1.*0* (2020) (cit. on p. 160).

[264] Velimir V. Vesselinov, Boian S. Alexandrov, and Daniel O’Malley, “Nonnegative tensor factorization for contaminant source identification”, *in*: *Journal of contaminant hydrology* 220 (2019), pp. 66–97 (cit. on p. 160).

[265] Saman Razavi, Anthony Jakeman, Andrea Saltelli, Clémentine Prieur, Bertrand Iooss, Emanuele Borgonovo, Elmar Plischke, Samuele Lo Piano, Takuya Iwanaga, William Becker, et al., “The future of sensitivity analysis: an essential discipline for systems modeling and policy support”, *in*: *Environmental Modelling & Software* 137 (2021), p. 104954 (cit. on p. 160).

SUPPLEMENTARY MATERIAL

The Python script, used to conduct the investigations presented in this manuscript, is available in the following Github repository (`https://github.com/SarahIaquinta/PhDthesis`).

DOCTORAT
BRETAGNE SCIENCES
LOIRE POUR L'INGENIEUR

Nantes
Université

Titre : Influence des propriétés mécaniques et géométriques de nanoparticules sur leur ingestion par les cellules cancéreuses

Mot clés : modélisation ; nanoparticule ; cancer ; mécano-adaptation ; métamodèle ; analyse de sensibilité

Résumé : Des différences de propriétés mécaniques entre les cellules saines et les cellules cancéreuses ont été récemment observées. Les performances des nanoparticules (NP), couramment utilisées pour délivrer des agents anticancéreux, pourraient donc être améliorées en prenant ce facteur en compte. L'objectif de cette thèse est d'identifier l'influence des propriétés mécaniques et géométriques de la NP et de la membrane cellulaire sur l'absorption cellulaire des NPs. Pour cela, un modèle, basé sur une approche énergétique de l'ingestion cellulaire des NPs, a été utilisé et enrichi en tenant compte de l'adaptation mécanique de la membrane lors de l'enveloppement des NP. Cette nouvelle fonctionnalité permet d'affiner les prédictions du modèle et de différencier les cellules saines et cancéreuses par la manière dont elles s'adaptent mécaniquement à leur enveloppement. Des analyses de sensibilité, conduites à partir de métamodèles, ont donc été menées, afin de quantifier l'influence des paramètres introduits, montrant que le rapport de forme de la NP et le délai d'adaptation mécanique ont le plus d'influence. Enfin, le modèle a été appliqué à un type de cancer spécifique, pour lequel les propriétés mécaniques du modèle ont été déterminées suite à une étude de la bibliographie.

Title: Influence of the mechanical and geometrical properties of nanoparticles on their uptake by cancer cells

Keywords: model; nanoparticle; cancer; mechano-adaptation; surrogate modeling; sensitivity analysis

Abstract: Differences in mechanical properties between healthy and cancerous cells have been recently observed. The performance of nanoparticles (NPs), commonly used to deliver anticancer agents, could therefore be improved by taking this factor into account. The objective of this thesis is to identify the influence of the mechanical and geometrical properties of the NP and the cell membrane on the cellular uptake of NPs. For this purpose, an energetic model of NPs cellular ingestion has been used and enriched by taking into account the mechanical adaptation of the membrane during the NPs wrapping. This new feature allows to refine the model predictions and to differentiate between healthy and cancer cells by the way they mechanically adapt to their wrapping. Sensitivity analyses, conducted from metamodels, were therefore carried out, in order to quantify the influence of the introduced parameters, showing that the aspect ratio of the NP and the mechanical adaptation delay have the most influence. Finally, the model was applied to a specific type of cancer, for which the mechanical properties of the model were determined as a result of a literature review.